

# Manipulating Bose-Einstein condensates with laser light

by

Shin Inouye

Submitted to the Department of Physics  
in partial fulfillment of the requirements for the degree of

Doctor of Philosophy

at the

MASSACHUSETTS INSTITUTE OF TECHNOLOGY

September 2001

© Massachusetts Institute of Technology 2001. All rights reserved.

Author .....  
Department of Physics  
June 7, 2001

Certified by.....  
Wolfgang Ketterle  
John D. MacArthur Professor of Physics  
Thesis Supervisor

Accepted by.....  
Thomas J. Greytak  
Professor of Physics, Associate Department Head for Education

# Manipulating Bose-Einstein condensates with laser light

by  
Shin Inouye

Submitted to the Department of Physics  
on June 7, 2001, in partial fulfillment of the  
requirements for the degree of  
Doctor of Philosophy

## Abstract

A dilute gas Bose-Einstein condensate was probed and manipulated by off-resonant laser beams.

Spontaneous and stimulated off-resonant light scatterings were studied experimentally. Stimulated, two-photon Bragg scattering was used for spectroscopic measurement of the mean-field energy and of the intrinsic momentum uncertainty of the condensate. The high momentum and energy resolution of this method allowed the determination of the coherence length of the condensate, which was shown to be equal to its size. Spontaneous, off-resonant Rayleigh scattering was studied by exposing an elongated condensate to a single off-resonant laser beam. Highly directional scattering of light and atoms was observed. This collective light scattering is shown to be directly analogous to Dicke superradiance, where the electronic coherence is replaced by the coherent center-of-mass motion of the atoms in the condensate.

Superradiant Rayleigh scattering was used to amplify atomic matter waves. The active medium was a Bose-Einstein condensate, pumped by off-resonant laser light (“Dressed condensate”). An atomic wave packet was amplified with a gain of 10 to 100. Phase-coherence of the amplifier was verified by observing the interference of the output wave with a reference wave packet. Optical properties of the dressed condensate were also characterized, focusing on the key role of long-lived matter wave gratings produced by interference between the condensate at rest and the recoiling atoms. The narrow bandwidth for the optical gain gave rise to an extremely slow group velocity of an amplified light pulse ( $\sim 1$  m/s).

The role of quantum statistics in these enhanced scatterings was studied. It was shown that the macroscopic occupation of a single quantum state is not necessary. These processes are in principle possible for fermionic or non-degenerate samples, provided the atomic ensemble has a sufficiently long coherence time.

By moving a focused, far off-resonant laser beam through a condensate, vortex excitations were created in a Bose-Einstein condensate. They were observed as dislocations in the interference fringes formed by the stirred condensate and a second unperturbed condensate. The technique was shown to be a powerful tool to study turbulent superfluid flow.

Thesis Supervisor: Wolfgang Ketterle  
Title: John D. MacArthur Professor of Physics

To Tamon, Kazuko, Ayako,

and Shinko.

## Acknowledgments

The results of my five years of research in MIT are presented in the rest of this dissertation. Here, I would like to acknowledge people who made this possible.

The biggest “thanks” goes to Professor Wolfgang Ketterle, who took the job of advising me. As all his previous students have pointed out, Wolfgang is a true group leader. His genuine interest in physics and his sincere attitude toward people created the special atmosphere inside the group, and I just loved working in that environment. Of course, he is also an extremely strong scientist and an excellent teacher. In fact, I am impressed by him for many different reasons throughout the past five years.

I also learned a lot from Professor Dave Pritchard. Conversations with him were always stimulating, whether the subject was on condensate experiments, or on the history of domestic animals.

Everyday life in the lab consists of close collaborations between postdocs and graduate students, and I benefited significantly throughout the years from these collaborations. Two former graduate students, Michael Andrews and Dallin Durfee, were great resources for me at the early stage of my research. Later, I found myself adopting many of Michael’s special style of research: a small notebook in the back pocket, Mike’s unit (in which the mass of sodium was  $1/17$ ), etc., which helped me increase the efficiency in the lab work. One of the most efficient people I worked with was Jörn Stenger, who was a kind person with a strong leadership. During the second half of my Ph.D. study, I had the privilege to work with Subhadeep Gupta, Tilman Pfau, Robert Löw, and Till Rosenband who are not only extremely nice people but also have a great enthusiasm for physics. The successes of most of the research presented here crucially depended on their dedication, especially Deep’s constant help during and between the runs, and innovative works from others (like “Tilman’s formula,” “Robert’s slit,” and “Till’s scanning beam,” etc.). I feel like I owe each of them a paper.

Although I did not have the chance to directly collaborate with some of the people in our group, the time we shared was priceless. My lab nickname “Shunty-Shin” was given to me by two of my great collaborators, Dan Stamper-Kurn and Ananth Chikkatur. The “Enrico Fermi” summer school in 1998, which I attended with them, was one of the best experience in my life. The list of other collaborators include Hans-Joachim Miesner, Axel Görlitz, Todd Gustavson, Aaron Leanhardt, and Kai Dieckmann from the “Old” lab; Dallin Durfee, Chris Kuklewicz, Chandra Raman, Robert Onofrio, Johnny Vogels, Charles Sestok, Jeff Gore, Michael Köhl, Kaiwen Xu, and Jamil Abo-Shaeer from the “New” lab; Zoran Hadzibabic, Claudiu Stan, and Martin Zwierlein from the Lithium lab; Erik Streed, Micah Boyd, Yoshio Torii, and Dominik Schneble from the Rubidium lab.

The “Ketterle group” was not the only resource I had at MIT. People in the larger AMO group at MIT were quite supportive, and I would like to express my gratitude for the support, especially from those who entered MIT together in 1996: Simon Rainville, Tony

Roberts, Steve Moss, and Chris Kuklewicz. RLE(Research Laboratory of Electronics) was another place where I felt the strength of a true team work. The help from Maxine Samuels, Gerry Power and Albert McGurl was literally vital to the success of my life at MIT. Also, I would like to say thank you to Carol Costa. Talking with her once in a while in her office was somehow relaxing to me.

I also would like to acknowledge people who supported my life outside the lab: Takaaki Koga, Isamu Kato, officers of JAM(Japanese Association of MIT), and all other friends.

Finally, it's time for my family. I would like to say thank you to my father Tamon for inspiring me to study abroad, my mother Kazuko and sister Ayako for moral support, and my wife Shinko for being next to me and encouraging me when I was facing challenges.

This work was supported by the National Science Foundation (NSF), the Office of Naval Research (ONR), the Army Research Office and the Joint Services Electronics Program (JSEP) of the Army Research Office (ARO), the National Aeronautics and Space Administration (NASA), and the David and Lucile Packard Foundation.

# Contents

<b>1</b>	<b>Introduction</b>	<b>12</b>
1.1	Realization of dilute gas Bose-Einstein Condensate (1995 ~)	12
1.1.1	Why is BEC interesting?	12
1.1.2	What is BEC?	13
1.2	My career as a Ph.D. student (1996 ~)	15
1.2.1	Projects in the old lab and my contributions	15
1.2.2	Outline of this thesis	16
1.3	History of BEC	17
1.3.1	Einstein’s prediction and response from liquid helium	17
1.3.2	The quest for BEC in dilute system	19
<b>2</b>	<b>Experimental setup</b>	<b>25</b>
2.1	Overview of the experimental setup	25
2.1.1	Zeeman slowing	26
2.1.2	Dark-SPOT	26
2.1.3	Polarization-gradient cooling	26
2.1.4	Magnetic trap	27
2.1.5	Rf-induced evaporation	27
2.1.6	Imaging	27
2.2	Laser system	28
2.3	Vacuum chamber	30
<b>3</b>	<b>Bragg scattering from a Bose-Einstein condensate</b>	<b>35</b>
3.1	Linewidth of an “atom laser”	35
3.2	Bragg scattering as a two-photon resonance	36
3.3	Finite-size broadening and effects of the mean-field	38
3.4	Higher order Bragg scattering	41
3.5	Other measurements of the coherence length of condensates	42
<b>4</b>	<b>Superradiant Rayleigh scattering from a Bose-Einstein condensate</b>	<b>44</b>
4.1	Directional matter waves produced by spontaneous scatterings	44

4.2	Dicke superradiance — emerging coherence . . . . .	47
4.3	<i>In-situ</i> monitoring of matter wave gratings . . . . .	48
<b>5</b>	<b>Matter wave amplification using a dressed Bose-Einstein condensate</b>	<b>53</b>
5.1	“Seeding” the superradiance . . . . .	53
5.2	Phase of the amplified matter wave . . . . .	55
<b>6</b>	<b>Optical properties of a dressed Bose-Einstein condensate</b>	<b>57</b>
6.1	Four-wave mixing of light and atoms . . . . .	57
6.2	Amplification of light in a dressed condensate . . . . .	60
6.3	Cross-section for optical gain and slow light . . . . .	60
6.4	Relation between optical gain and atomic gain . . . . .	62
6.5	Optical Bloch equations . . . . .	65
6.6	Optical probe of matter wave gain . . . . .	69
6.7	Single-atom and collective behavior . . . . .	70
<b>7</b>	<b>Does matter wave amplification work for fermions?</b>	<b>73</b>
<b>8</b>	<b>Imaging a vortex in a Bose-Einstein condensate</b>	<b>77</b>
8.1	A little personal introduction to vortex experiments . . . . .	77
8.2	Vortices in BEC . . . . .	78
<b>9</b>	<b>Conclusion and Outlook</b>	<b>82</b>
<b>A</b>	<b>Observation of Feshbach resonances in a Bose-Einstein condensate</b>	<b>84</b>
<b>B</b>	<b>Strongly Enhanced Inelastic Collisions in a Bose-Einstein Condensate near Feshbach Resonances</b>	<b>90</b>
<b>C</b>	<b>Bragg Spectroscopy of a Bose-Einstein condensate</b>	<b>95</b>
<b>D</b>	<b>Superradiant Rayleigh Scattering from a Bose-Einstein Condensate</b>	<b>101</b>
<b>E</b>	<b>Phase-coherent amplification of atomic matter waves</b>	<b>106</b>
<b>F</b>	<b>Amplification of Light and Atoms in a Bose-Einstein Condensate</b>	<b>111</b>
<b>G</b>	<b>Does matter wave amplification work for fermions?</b>	<b>116</b>
<b>H</b>	<b>Observation of vortex phase singularities in Bose-Einstein condensates</b>	<b>121</b>

# List of Figures

1-1	Typical images of Bose-Einstein condensates. . . . .	15
2-1	Relevant optical transitions of sodium. . . . .	29
2-2	Frequencies of beams generated from the dye-laser system. . . . .	29
2-3	Schematics of the oven assembly. . . . .	30
2-4	Schematics of the slower part. . . . .	31
2-5	Schematic of the main trapping chamber. . . . .	31
2-6	Ioffe-Pritchard trap with clover-leaf design. . . . .	32
2-7	Circuit diagram of the high-current setup. . . . .	33
2-8	Schematic of absorption and phase-contrast imaging. . . . .	34
3-1	Typical Bragg resonance curve for trapped condensates. . . . .	36
3-2	Schemes for high-resolution velocimetry . . . . .	37
3-3	Bragg resonances for a trapped condensate and after time-of-flight . . . . .	38
3-4	Bragg spectroscopy of a trapped condensate. . . . .	40
3-5	Kapitza-Dirac diffraction of a Bose-Einstein condensate. . . . .	41
3-6	Observation of elastic collision between the condensate and Bragg diffracted atoms. . . . .	43
4-1	Observation of superradiant Rayleigh scattering. . . . .	45
4-2	Build-up of a matter wave grating inside a condensate due to light scattering. . . . .	46
4-3	Dicke Superradiance from two atoms in excited states. . . . .	48
4-4	Dicke superradiance from an extended sample. . . . .	49
4-5	Observation of directional emission of light. . . . .	50
4-6	Matter wave amplification out of noise. . . . .	51
5-1	Demonstration of matter wave amplification. . . . .	54
5-2	Ramsey-type atom interferometer. . . . .	55
5-3	Phase coherent amplification of matter waves. . . . .	56
6-1	Amplification of light and atoms by off-resonant light scattering. . . . .	61
6-2	Pulse delay due to light amplification. . . . .	63

6-3	Gain and temporal behavior of light pulses propagating through a dressed condensate. . . . .	67
6-4	Rabi oscillations of atoms observed by monitoring the transmitted probe light intensity. . . . .	68
6-5	Pump-probe spectroscopy of a matter wave grating inside the condensate. .	70
6-6	Schematic diagram of the different regimes of a dressed condensate. . . . .	71
6-7	From single-atom Rabi oscillations to collective superradiance. . . . .	71
6-8	Comparison between two different methods to generate slow light. . . . .	72
7-1	Quantum statistics vs. coherence time. . . . .	75
8-1	Density and phase profile of a moving condensate with a vortex. . . . .	79
8-2	Schematic of the experiment. . . . .	79
8-3	Observation of the phase singularities due to vortices. . . . .	81

## Notations

- $A$  : cross-section of a condensate
- $a(\hat{a})$  : atomic field (operator)
- $a_{\text{sc}}$  : scattering length
- $b(\hat{b})$  : light field (operator)
- $C$  : coefficient of four-wave mixing Hamiltonian
- $c$  : speed of light
- $c_s$  : speed of sound in a condensate
- $d$  : atomic dipole matrix element
- $\mathcal{E}$  : (complex) electric field strength
- $G$  : growth rate of a matter wave
- $g$  : optical gain
- $|g\rangle$  : condensate ground state
- $k$  : wavevector of light.
- $k_{\text{F}}$  : wavevector associated with fermi momentum
- $k_{\text{th}}$  : wavevector associated with thermal energy
- $M$  : mass of (sodium) atoms.
- $m$  : magnetic quantum number
- $N$  : total number of atoms
- $N_0$  : number of atoms in a condensate
- $N_q$  : number of quasi-particles associated with momentum  $q$
- $n_k$  : number of photons in mode  $k$
- $n_{\text{p}}$  : number of photons in the probe beam mode
- $n(\omega)$  : (complex) index of refraction ( $n_1 + in_2$ )
- $\mathbf{q}$  : wavevector associated with the momentum transfer
- $R$  : Rayleigh scattering rate

$S(q)$  : static structure factor  
 $S(q, \omega)$  : dynamic structure factor  
 $s$  : size of the spin  
 $U_0$  :  $4\pi\hbar^2 a_{sc}/M$   
 $v$  : off-diagonal element of density matrix ( $2\text{Im}(\rho_{12})$ )  
 $v_g$  : group velocity of light  
 $w$  : population difference between two coupled states ( $\rho_{22} - \rho_{11}$ )  
 $\Gamma$  : natural linewidth of the atomic resonance  
 $\Gamma_2$  : linewidth of two-photon transition  
 $\Delta$  : detuning of light from the atomic resonance  
 $\epsilon_0$  : permittivity of vacuum  
 $\lambda$  ( $\lambda$ ) : wavelength of optical transition ( $\lambda = \lambda/2\pi$ )  
 $\mu$  : chemical potential of a condensate  
 $\rho$  : atomic density  
 $\rho_0$  : peak atomic density  
 $\rho_E$  : density of states  
 $\rho_n$  : normalized atomic density  
 $\hat{\rho}(q)$  : density matrix  
 $\sigma$  : scattering cross section  
 $\tau_D$  : delay time of a probe pulse  
 $\Omega$  : Rabi frequency of light  
 $\Omega'$  : Solid angle for radiation  
 $\Omega_0, \Omega_R$  : Two-photon Rabi frequencies  
 $\omega_0$  : angular frequency of optical transition  
 $\omega_q^B$  : frequency of quasi-particles with wave vector  $q$   
 $\omega_{\text{rec}}$  : recoil (angular) frequency,  $\hbar k^2/2M$   
 $\omega_x$  : trap frequency in  $x$ - direction

# Chapter 1

## Introduction

### 1.1 Realization of dilute gas Bose-Einstein Condensate (1995 ~)

#### 1.1.1 Why is BEC interesting?

The quantum nature of matter shows up when the number of particles becomes comparable to the number of accessible states in the system. Fermions start to show the effect of the Pauli-exclusion principle when the occupation numbers become on the order of unity. Lasers start lasing when the average number of (spontaneously-emitted) photons in the cavity exceeds one. Bosons start to “attract” each other by bosonic stimulation and form a macroscopic population in the ground state of the system — this is Bose-Einstein condensation (BEC), which is the topic of this thesis.

The realization of Bose-Einstein condensation in dilute atomic gases in 1995 [1, 2, 3] triggered a burst of research activity, which was almost impossible to foresee. Indeed, fifteen out of twenty issues of Physical Review Letters published this year (between January and May of 2001) contain more than one paper that has “Bose-Einstein condensate” explicitly in its title. Since there are so many articles on Bose-Einstein condensates, it is almost useless to search papers with the keywords “Bose-Einstein condensation,” except when one wants to see how many there are!

There are several reasons why dilute gas BEC has attracted so much interest. First, it has realized a long-sought “weakly interacting” superfluid to which the original concepts of quasi-particle and collective excitations are readily applicable. The study of superfluids was so far limited to liquid helium, whose properties are strongly modified by the interaction between atoms. For alkali condensates, the effect of interactions measured by the “quantum depletion” is typically 1% or less, whereas it is about 90% for liquid helium. Secondly, it has realized “coherent” matter waves which are only limited by Heisenberg uncertainty. This has enabled us to apply many of the concepts developed in the atom optics and quantum optics communities. I am still amazed by the fact that higher order coherence, non-linear wave mixing, solitons, and squeezing have all been realized within five years of the first realization

of BEC. Third, advanced technologies in manipulation and probing of the condensates enabled us to access desired states and measure precise values experimentally. The density profile of the condensate is easily accessible by *in-situ* or time-of-flight imaging, whereas the phase profile of the condensate can be accessed through interferometric techniques. Phase can be precisely “engineered” to generate desired quantum states. Even the interaction between atoms can be tuned by external fields. Aside from these, one might find other reasons “why” Bose-Einstein condensates are interesting to study. However, what drives us most might be still the fact that it is a “new” state of matter!

### 1.1.2 What is BEC?

#### How BEC forms

Before going into the details of BEC, I would like to give a simple description of how a BEC forms and what a BEC is. Rigorous derivation of following results can be found in textbooks on statistical mechanics, e.g. Ref. [4]. As was introduced in the previous section, it forms when the number of particles  $N$  becomes comparable to the number of states  $\sim (k_{\text{th}}L/2\pi)^3$ , where  $k_{\text{th}} = \sqrt{2\pi Mk_{\text{B}}T}/\hbar$  is the thermal deBroglie wavevector and  $L$  is the size of the system ( $M$  is the mass of the particle and  $T$  is the temperature). Using the deBroglie wavelength  $\lambda_{\text{dB}} = 2\pi/k_{\text{th}}$ , the condition for the onset of quantum effects can be described as follows:

$$\rho\lambda_{\text{dB}}^3 \sim 1 \quad (1.1)$$

where  $\rho$  is the density of the particle. The value on the left-hand side ( $\rho\lambda_{\text{dB}}^3$ ) is called phase-space density, and it shows how far the sample is from the quantum regime. By increasing the density or reducing the temperature of the ensemble, one can approach the quantum regime.

At high phase-space density, deviation from the classical distribution becomes noticeable and effects of quantum statistics set in. For bosons, multiple occupancy of a single state is allowed, and the occupation number follows the Bose-Einstein distribution function  $f_i$ :

$$f_i = \frac{1}{\exp(\frac{E_i - \mu}{k_{\text{B}}T}) - 1} \quad (1.2)$$

where  $\mu$  is the chemical potential. The number of particles accommodated in the thermal distribution  $N_{\text{th}}$  is given by integrating the density of states  $\rho_E$  weighted by this distribution function:

$$N_{\text{th}} = \int \frac{1}{\exp(\frac{E - \mu}{k_{\text{B}}T}) - 1} \rho_E(E) dE. \quad (1.3)$$

As the number of particles increases, the chemical potential  $\mu$  approaches zero (the single-particle ground state energy) from the negative side. Since  $\mu$  cannot be positive, maximum

number of particles allowed in Bose-Einstein distribution is determined by setting  $\mu = 0$ . The peculiar feature of Bose-Einstein distribution is that this is *finite*, say, for particles in a 3D box potential.

The remaining particles have to go somewhere, and the only choice in equilibrium is to join the lowest energy state, which is the ground state of the system. This is the Bose-Einstein condensation. This is a true quantum mechanical phase-transition, which does not depend on interaction between particles. For the case of particles in a 3D box, it takes place at phase-space density  $\rho\lambda_{\text{dB}}^3$  of 2.612.

### How BEC looks like

Although the condition for BEC phase-transition does not depend on interaction between atoms, the product (the condensate) is strongly affected by the interaction between atoms. The dilute-gas condensate can be well described by a macroscopic wavefunction (or order parameter)  $\psi(\vec{r})$ , which satisfies the Gross-Pitaevskii equation.

$$\left( -\frac{\hbar^2}{2M}\nabla^2 + V(\vec{r}) + \frac{4\pi\hbar^2 a_{\text{sc}}}{M}|\psi(\vec{r})|^2 \right) \psi(\vec{r}) = \mu\psi(\vec{r}) \quad (1.4)$$

where  $a_{\text{sc}}$  is the scattering length of atoms, which determines the sign and the strength of interaction. If the scattering length is negative, condensates with a large number of atoms are not allowed since it builds up local density maxima to reduce the overall energy. For sodium, the scattering length is positive, and large stable condensates can form at the minimum of the trapping potential  $V(\vec{r})$ . For typical experimental conditions, the effect of kinetic energy  $(-\hbar^2/2M)\nabla^2\psi(\vec{r})$  is small and the density profile of the condensate is well approximated by the ‘‘Thomas-Fermi’’ density distribution determined by the balance between the trapping potential and the interaction energy:

$$\rho(\vec{r}) = \frac{M}{4\pi\hbar^2 a_{\text{sc}}}(\mu - V(\vec{r})). \quad (1.5)$$

Typical images of a Bose-Einstein condensate are shown in Fig. 1-1 to help intuitive understandings of the readers. Fig. 1-1a shows density profiles of an atomic cloud as it crosses the phase-transition temperature. Strong anisotropy of the atomic cloud results from that of the trapping potential. The emergence of a dense core at the center of the trap is the signature of Bose-Einstein condensation. By reducing the temperature far below the transition temperature, one can achieve almost ‘‘pure’’ condensate, which contains  $\sim 10^7$  atoms and is  $\sim 20 \times 20 \times 250 \mu\text{m}$  in size. Fig. 1-1b shows typical ‘‘time-of-flight’’ images taken after shutting off the confinement potential and waiting a variable time afterwards. Difference between the thermal cloud and the condensate is evident from the shape of the expansion. Thermal clouds expand isotropically, whereas condensates expands anisotropically, since the interaction energy is released mainly in the direction of tight confinement. These images are our main window to the quantum world, and we often take hundreds of

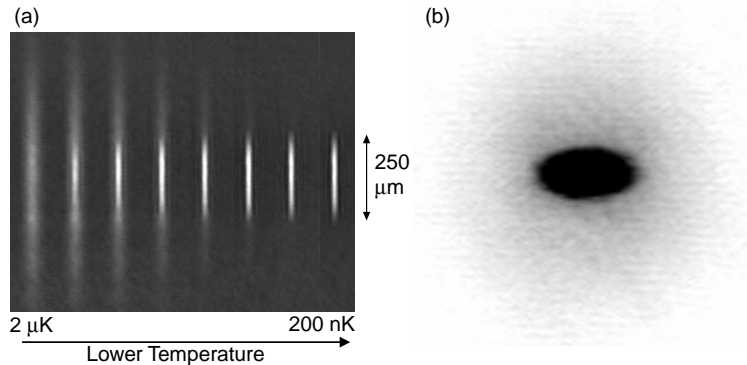


Figure 1-1: Typical images of Bose-Einstein condensates used for analyses. (a) *In-situ* images taken as the atomic cloud crosses the phase-transition temperature show the emergence of a dense core, which is the Bose-Einstein condensate. (b) A time-of-flight picture taken after releasing the atoms from the confinement potential shows a clear bi-modal feature, which is made of a condensate (inner black dot) and a thermal cloud (outside dilute cloud). The thermal cloud expands isotropically, reflecting the momentum distribution of atoms in the thermal distribution. The condensate expands anisotropically since the interaction energy is preferentially released in the direction of tight confinement.

images in a day, from the morning to the next early morning.

## 1.2 My career as a Ph.D. student (1996 ~)

### 1.2.1 Projects in the old lab and my contributions

All the research activities presented here was performed in the “old lab” in Prof. Wolfgang Ketterle’s group. From the beginning to the end, I tremendously benefited from the close collaboration within the group, which consists of highly innovative researchers, full of enthusiasm. Although each project was mainly carried out by two or three researchers in the lab, discussions at the group meetings and improvements and maintenance between the runs were also essential. The following is an effort to indicate my significant contributions to projects, and I have tried to be as objective as possible.

My research activity here in MIT started in the fall of 1996, when I joined the lab as a first year graduate student. It was just after dc magnetic trap was installed[5], but the interference between two condensates [6] had not yet been observed, and phase-contrast imaging was being tried out. After spending time on building cooling water circuits in the lab and also building several small and high current electronics, I joined the effort to observe vortices in the spring of 1997. After its failure, I split from the main effort of the lab, which was to develop an optical dipole trap for condensates [7], and set up the infrastructure for observing Feshbach resonances [8] (Appendix A). The resonance was observed in early 1998, and this is the first project that I made a significant contribution.

(The experiment itself was performed with two other collaborators.) After that, I teamed up with a postdoc and completed characterizing the Feshbach resonances [9] (Appendix B), and also investigated the ground state of optically trapped condensates with spin degrees of freedom [10]. Meanwhile, dynamic [11, 12] properties of magnetically trapped condensates, meta-stable [13] and transient [14] features of a spinor condensate, and the formation of a condensate [15, 16] were concurrently studied in the lab.

From the fall of 1998, we switched our focus from optical dipole traps to Bragg scattering of condensates [17] (Appendix C), which triggered a series of off-resonant light scattering experiments. Especially, the discovery of superradiant Rayleigh scattering [18] (Appendix D) led to phase-coherent matter wave amplification [19] (Appendix E). The topic was extended to the observation of light amplification in condensates [20] (Appendix F). Theoretical extension led to the discussion on the role of quantum statistics in amplification [21]. I served as the responsible person for these projects. Meanwhile, the structure factor [22] of the condensate and superfluidity of the condensate [23] were investigated by utilizing Bragg scattering as a tool for probing and manipulating the momentum state of condensates.

The most important development in the lab during the period of 2000-2001 was the construction of the new “science” chamber, which achieved Bose-Einstein condensation in February 2001. There were several parallel projects during that time, and I led the effort of observing the phase diffusion of the condensate. The project itself was not successful due to technical limitations, but the techniques developed there were adopted to the next project, which is the observation of vortices as a fringe dislocation [24] (Appendix H).

### 1.2.2 Outline of this thesis

In this dissertation, I decided to focus on projects after the fall of 1998, and mention only briefly the work before. This is because I wanted to maintain a clear focus in this dissertation. The main topic is the manipulation of the momentum and angular momentum of condensates by optical means, and I believe each project shown in the following chapters serve as good examples. The original papers on Feshbach resonances are attached in Appendices A and B with some comments on recent progress based on our work. I completely left the spinor work out of this thesis partly because it was already presented in the previous dissertation [25] in a beautiful integrated manner with various extensions. Other works in which I played a secondary role are also left out.

So the structure of this thesis is as follows. Concise summary of condensate physics and history is laid out in Chapter 1. In Chapter 2, our experimental apparatus is explained briefly. Chapters 3-8 form the most important part of this dissertation. The off-resonant light scattering experiments and vortex experiments are explained with emphasis on motivations, underlying physics and limitations. These chapters are not intended for providing information on (hyper)fine details of each experiment. I refer interested readers to original papers which are attached in appendices in chronological order. Conclusion and future

Theory	Experiments
<p><b>1923, deBroglie</b> Matter wave (<math>\lambda_{dB} = h/p</math>) [35].</p> <p><b>1924, Bose</b> Derivation of Planck distribution from photon statistics [36].</p> <p><b>1925, Einstein</b> Bose-Einstein condensation for massive particles [37].</p> <p><b>1926, Schrödinger</b> Schrödinger's wave equation.</p> <p><b>1926, Fermi</b> Fermi statistics [38].</p>	<p><b>1928, Keesom and Wolfke</b> Phase transition in liquid helium [39].</p>

outlook are discussed in Chapter 9.

### 1.3 History of BEC

Both theories and experiments of BEC are less than 100 years old: however, their histories involve many surprises and also deep thoughts on the quantum mechanical nature of matter, which were developed by many great physicists in the 20th century. They are also intimately related to many of the major experimental achievements in that century, such as superfluidity, superconductivity, and lasing. Readers interested in the history of the theories should refer to the biographies of Einstein [26] and London [27], and also a review by Griffin [28]. Current dilute gas BEC experiments can trace their conceptual roots through a series of experiments with hydrogen and laser-cooled atoms performed in the 1980's. The history of the hydrogen experiments was summarized by Greytak [29]. Experiments on the laser-cooled atoms were nicely described by Chu, Cohen-Tannoudji and Phillips in the Nobel lectures given in 1997 [30, 31, 32]. The efforts toward BEC were reviewed in detail by Cornell [33] and Ketterle [34]. Here, I will quickly review the field of BEC by focusing on when and how relevant theoretical concepts and experimental techniques were developed. Theoretical and experimental discoveries are shown in chronological tables. References are primarily shown in these tables rather than in the main body of the text.

#### 1.3.1 Einstein's prediction and response from liquid helium

In 1924, Bose re-derived the black-body radiation spectrum by treating the radiation field as "a photon gas" and applying a statistical argument to it. Einstein, one of the small number of physicists who knew about deBroglie's new idea of matter waves, considered applying the same statistics to massive particles. If particles were waves, they should obey the same

Theory	Experiments
<p><b>1938, London</b> Bose-Einstein condensation as an explanation for liquid helium (<math>T_{\text{BEC}} = 3.1\text{K}</math>) [40, 42].</p> <p><b>1938, Tisza</b> Two fluid model of liquid helium based on BEC (<math>\rho = \rho_{\text{normal}} + \rho_{\text{super}}</math>) [43, 44].</p> <p><b>1941, Landau</b> Two fluid model based on quantum hydrodynamics [45].</p>	<p><b>1938, Kapitza, Allen and Misener</b> The viscosity of helium II <math>\rightarrow 0</math> [46, 47].</p> <p><b>1938, Allen and Jones</b> Fountain effect [48].</p>

statistics as photons! He applied Bose-Einstein statistics to mono-atomic molecules and derived the Bose-Einstein distribution. He immediately noticed a peculiar feature of the distribution: at low temperature, it saturates. In other words, below a critical temperature, the number of particles in the thermal distribution is limited, and the remaining ones have to go to the lowest energy state. This was how the concept of Bose-Einstein condensation began.

Foundation of Quantum mechanics was laid out in the next few years. Fermi statistics was introduced and the relation between the statistics and the spin was clarified. However, in the meantime, Einstein’s prediction of condensation acquired “the reputation of having only a purely imaginary existence” [40]. Uhlenbeck, a leading experts in the kinetic theory at that time criticized Einstein’s prediction by arguing that it would not occur in finite systems. According to his comments, this criticism was accepted even by Einstein himself [41].

The situation quickly turned around in 1938, when the superfluid nature of liquid helium was observed. London knew that a year before, some issue of second-order phase transitions were clarified and Uhlenbeck had taken back his criticism on Einstein’s work. He also knew  $^4\text{He}$  was a boson and immediately put the two ideas together: *some sort of BEC was involved in the strange phase transition shown by superfluid  $^4\text{He}$* . As evidence, London noted that Einstein’s formula for the phase transition temperature ( $T_{\text{BEC}} = 3.1\text{K}$ ) gave a good estimate of the observed transition temperature ( $T_\lambda = 2.2\text{K}$ ).

Extending London’s work, Tisza developed the two-fluid model and explained all the experiments exhibiting superfluidity, usually involving the normal fluid and superfluid moving in opposite directions. His notion of superfluid was based on Bose-Einstein condensation as a microscopic model. However, soon Landau reproduced the two-fluid model starting from classical hydrodynamics and quantizing it. In his paper, Landau never mentioned the fact that  $^4\text{He}$  atoms were bosons, let alone the existence of a Bose condensate. He introduced the concept of collective excitations like second sound, which was later observed as a temperature oscillation. He assumed a phonon- and roton-branch of the quasi-particle ex-

citation spectrum to explain superfluid behavior, and they were later confirmed in neutron scattering experiments. This mixture of success (phonon-roton spectrum, second sound, ...) and failure (quantum hydrodynamics itself) of Landau's approach resulted in confusion about the role of BEC and a macroscopic wavefunction in liquid helium.

In the following years, the research on liquid helium was refined, but it was confronted with the strong interaction between atoms and gradually decoupled from the original idea of BEC. New tools like second quantization became available in the condensed-matter community, and it provided them with theoretical breakthroughs like the derivation of the phonon spectrum. Especially the era "1957-1965" was a quite fruitful period for the theoretical study of weakly interacting Bose-condensed gas system. Many important theorists attacked this hot topic at that moment, and "the final theoretical edifice is one of the great success stories in theoretical physics. However, until recently it was largely unknown since it was somewhat uncoupled from experiments... (Griffin, in Ref. [28])."

### 1.3.2 The quest for BEC in dilute system

Stimulated by the theoretical work, serious attempt to realize BEC in weakly interacting gas started in the 1960's. There were several directions: liquid helium, optically-excited excitons in semiconductors, and atomic gases. Liquid helium in vycor, a porous sponge-like glass, behaved like a dilute three-dimensional gas and showed features of condensation. Condensation of excitons (electron-hole pairs) in semiconductor ( $\text{Cu}_2\text{O}$ , also  $\text{CuCl}$ ) were also studied. With the advent of intense short pulse lasers, it became possible to achieve high density of excitons. Narrow photo luminescence spectra were observed [66], and superfluid behavior of excitons was also suggested, but still the condensation was not conclusive. The quest for BEC in dilute atomic gases, which is directly relevant to the topic of this thesis, is explained in the next two subsections.

#### Spin-polarized hydrogen

The first discussion of atomic hydrogen as a candidate for a dilute gas BEC was published by Hecht. He used the quantum theory of corresponding states to conclude that atomic hydrogen, prevented from recombining into molecules by a strong magnetic field, would remain a gas down to absolute zero of temperature. The idea was raised again later by Stwalley and Nosanow. They also pointed out that the presence of the interaction between the atoms could lead to the Bose condensate being a superfluid as well. A number of experimental groups began work in the field. Spin-polarized hydrogen was first stabilized by Silvera and Walraven in Amsterdam, and brought within a factor of 50 of condensing at MIT. However, it became increasingly clear that the walls of the cell causes severe limitations to the lifetime of the gas. Atoms could thermalize with a superfluid helium surface without becoming depolarized. However, as the temperature is lowered, the density

Theory	Experiments
<p><b>1947, Landau</b> The phonon-roton spectrum (assumption) [49].</p> <p><b>1947, Bogoliubov</b> Derivation of phonon spectrum [50].</p> <p><b>1953, Feynman</b> Many-body wavefunction <math>\Psi_N(r_1, r_2, \dots, r_N)</math>. Microscopic understanding of roton [53, 54].</p> <p><b>1956, Penrose and Onsager</b> Long Range Order, estimate of quantum depletion in liquid helium (<math>n_c \sim 0.08n</math>) [55].</p> <p><b>1957, Bardeen, Cooper and Schrieffer</b> BCS theory for superconductivity [56].</p> <p><b>1961, Pitaevskii</b> Gross-Pitaevskii equation for macroscopic wave function <math>\Psi(\mathbf{r}, t)</math> [57].</p>	<p><b>1946, Peshkov</b> Observation of second sound [51].</p> <p><b>1949, Abraham</b> No evidence for superfluidity of <math>^3\text{He}</math> down to 1 K [52].</p> <p><b>1958, Schawlow and Townes</b> Invention of laser [58].</p> <p><b>1959</b> Observation of phonon-roton spectrum using inelastic neutron scattering [59, 60].</p> <p><b>1961, Vinen</b> Observation of quantized circulation in helium [61].</p> <p><b>1974, Packard</b> Observation of vortex lattice [62].</p> <p><b>1983, Reppy</b> Helium absorbed on Vycor showed dilute Bose gas condensation [63, 64].</p> <p><b>1995, Cornell and Wieman, Hulet, Ketterle</b> Bose-Einstein condensation of dilute alkali gas [1, 2, 3].</p> <p><b>1997, Ketterle</b> Interference between two dilute gas Bose-Einstein condensates [6].</p> <p><b>1998, Greytak and Kleppner</b> Bose-Einstein condensation of atomic hydrogen [65].</p>

Spin-polarized hydrogen	Laser-cooled alkali atoms
<p><b>1959, Hecht</b> Atomic hydrogen would remain a gas down to absolute zero temperature [67]. (Also Stwalley and Nosanov, Ref. [68].)</p> <p><b>1980, Silvera and Walraven</b> Stabilization of spin-polarized hydrogen [73].</p> <p><b>1983, Hess</b> Phase-space density <math>\sim 1/50</math> [74].</p> <p><b>1986, Hess</b> Proposal of magnetic trapping plus evaporative cooling [75].</p> <p><b>1988, Doyle, Greytak, and Kleppner</b> Evaporatively cooled hydrogen (<math>\sim 3</math> mK) [76].</p>	<p><b>1975, Hänsch and Schawlow, Wineland and Dehmelt</b> Proposal of laser cooling [69, 70].</p> <p><b>1978, Wineland, Dehmelt</b> Laser cooling of ions [71, 72].</p> <p><b>1985, Phillips, Hall</b> Slowing of atomic beam [77, 78].</p> <p><b>1985, Phillips</b> Realization of a magnetic trap [79].</p> <p><b>1985, Chu and Ashkin</b> Optical molasses [80].</p> <p><b>1986, Chu and Ashkin</b> Dipole force trap [81].</p> <p><b>1987, Dalibard, Chu, and Pritchard</b> Realization of Magneto-Optical Trap(MOT) [82].</p> <p><b>1988, Phillips</b> Observation of sub-Doppler temperature [83].</p> <p><b>1988, Dalibard, Chu</b> Sisyphus cooling [84].</p>

of atoms absorbed on the surface increases to the point where the three-body rate *on the surface* becomes prohibitive.

Hess from MIT proposed an idea to circumvent this surface problem by introducing a magnetic trap. By using low-field seeking states of hydrogen atoms, it was possible to trap atoms at a local minimum of the magnetic field. Moreover, thermally isolated atoms in a magnetic trap were the perfect candidate for evaporative cooling. Most energetic atoms simply leave the trap from the edge, effectively cooling what remains in the trap. The only disadvantage was the heating due to the dipolar relaxation of low-field seeking states, which limits the maximum density (at the trap center) to a modest value.

By 1988, the MIT group had implemented these ideas and demonstrated the power of evaporative cooling. They obtained  $100\ \mu\text{K}$  at a density only a factor of five(!) too low for BEC [85]. Evaporative cooling was also performed in Amsterdam [86]. Both groups started to construct laser sources for improved measurements of density and temperature of the cloud. At the same time, many aspects of dilute gas BEC in an inhomogeneous potential were investigated in detail [87].

### Laser-cooled alkalis

Nobel lectures given by Chu and Phillips in 1997 show that both laureates were motivated by Ashkin's work in late 70s (Chu, Cohen-Tannoudji, and Phillips shared the Nobel prize in physics that year [30, 31, 32]). Ashkin's *dream* was to slow down an atomic beam using the radiation pressure of a laser beam, and then to trap them using a dipole force from focused laser beam(s), and he has proposed several schemes and done some proof-of-principle experiments with atomic beams [88, 89].

There was, however, a significant difficulty: atom traps were too shallow. Phillips wrote "Ion traps were deep enough to easily trap ions having temperatures well above room temperature, but none of the proposed neutral atom traps had depths of more than a few kelvin. Significant cooling was required before trapping would be possible, as Ashkin had outlined in his paper [88], and it was with this idea that I began." [32]

Soon he realized laser cooling is the way to go. In laser cooling, momentum is transferred from a laser beam to the atoms during light scattering. This mechanical effect of light is significant — deceleration could be on the order of  $10^5$  times the gravitational acceleration. By carefully selecting detuning of the light from the atomic resonance, atoms could be cooled to temperatures corresponding to the linewidth of optical transitions, typically less than 1 mK. Ions were already laser cooled at the University of Washington and at the NBS in Boulder. In the early 80s, interest for laser cooling of atoms was gradually increasing.

The late 80s were the heydays of laser-cooling. Ashkin's original "dreams" were realized one after another, and almost all the necessary tools were developed in this age. Scattering force from laser beams were used to cool both atomic beams and vapor, and atom traps were realized by using the dipole force or magnetic field potential. But probably the most

Towards the dilute gas BEC
----------------------------

**1989, Pritchard**

Rf-induced evaporation (proposal) [90].

**1990, Wieman**

Vapor-cell MOT [91].

**1993, Ketterle and Pritchard**

Dark SPOT MOT [92].

**1995, Cornell and Wieman, Hulet, Ketterle**

Observation of Bose-Einstein condensate [1, 2, 3].

**1998, Greytak and Kleppner**

Bose-Einstein condensation of atomic hydrogen [65].

important advance in this period was the invention of the magneto-optical trap (MOT), which became the workhorse of the ultracold atom community.

**The hybrid approach**

Rapid progress of laser cooling and evaporative cooling in late 80s gave the impression of these techniques might lead directly to BEC. Especially, the observed temperature in optical molasses was much lower than the theoretical limit, indicating a violation of Murphy's law in the field of laser cooling. However, by 1990, major limitations of laser cooling and trapping were identified. Random momentum fluctuations from the re-scattered photons limited the ultimate temperature in optical molasses to about a factor of ten above the recoil limit [84]. Sub-recoil cooling techniques, especially in three dimensions, were harder to implement, and required long cooling times. Trap loss arising from light assisted collisions limited the number of atoms in the trap [93], whereas absorption of scattered light resulted in an outward radiation pressure, weakening the trapping potential and limiting the density [94]. The peak phase-space density in laser cooling experiments has increased hardly at all for several years since 1989, remaining around  $10^{-5}$ . (See refs. [95, 96, 97, 98] for recent progress.)

In the end, the successful approach was to use laser cooling only as pre-cooling for magnetic trapping and evaporative cooling. Again, I refer interested readers to the articles by Cornell [33] and Ketterle [34]. There were several important advances towards achieving efficient evaporation. The Dark-SPOT trap was invented in MIT to enhance the density of atoms in MOT, and rf-induced evaporation was proposed and successfully implemented in magnetic traps. In 1995, three groups (JILA, Rice, MIT) observed BEC in three different species ( $^{87}\text{Rb}$ , Li, Na). Even in the year I am writing this thesis, this hybrid approach still remains the only route to BEC except for hydrogen, where an efficient laser source is not available for single-photon excitation.

The final approach to BEC of hydrogen atoms needed more than a simple optimization

of the cooling trajectory. In the case of hydrogen, the evaporation was forced by reducing the height of the magnetic field potential used for the confinement. Atoms were evaporated over a magnetic field saddlepoint at one end of the trap, and this scheme worked efficiently for atoms at higher temperature. However, at lower temperature, the efficiency of evaporation dropped since the radial motion of the trap decoupled from the axial motion of the trap: the escape time for atoms with high radial energy becomes very long. By solving this problem by implementing the rf-induced evaporation scheme that worked perfectly for alkali atoms, hydrogen atoms were Bose-condensed in 1998.

Bose-Einstein condensates of  $^{85}\text{Rb}$  atoms were produced in 2000 [99] based on a new tool established by condensate physics, i.e., Feshbach resonance [8]. Researchers in Boulder enhanced the elastic cross-section by tuning the scattering length of  $^{85}\text{Rb}$  atoms with external magnetic fields. The tuning of the scattering length was crucial for observing a condensate, since the scattering length of  $^{85}\text{Rb}$  atoms at low magnetic field was negative, prohibiting the production of large stable condensates.

Recently, metastable helium atoms were also Bose condensed [100, 101]. Atoms in the metastable state are characterized by their huge ( $\sim 20\text{ eV}$ ) internal energy. The release of this energy through collisions, or Penning ionization, can be strongly suppressed for a polarized sample due to the conservation of spin. The creation of condensate by evaporative cooling solely relies on this suppression. This condensate of atoms with large internal energy opens up a possibility to do condensate experiments with single-atom sensitivity.

## Chapter 2

# Experimental setup

In this chapter, I will briefly describe the apparatus which was used for our studies of Bose-Einstein condensates. The main apparatus consists of two parts: a dye-laser system and a stainless-steel chamber. Despite their rather old-fashioned appearance, these allowed us to do experiments without major interruptions for more than five years (1996-2001). This amazing robustness is a proof of the dedication and skill of our predecessors. For detailed description of their work, I refer the readers to the previous dissertations of Michael Joffe, Kendall Davis, Marc-Oliver Mewes, Michael Andrews, and Dan Stamper-Kurn.

Another approach to BEC employed by many experimental groups around the world is based on diode lasers and vapor cells. This type of setup is particularly suited for Rb, since good diode laser sources are available and vapor pressure is high at room temperatures. Review of this type of experimental apparatus can be found in Ref. [33] and references therein.

The structure of this chapter is as follows: first, an overview of the experiment is laid out focusing on experimental techniques used to achieve Bose-Einstein condensation. Next, the structure of each part of the apparatus is introduced. This part is intended to serve as a virtual lab tour, referring more to figures to provide an intuitive understanding of the experiments.

### 2.1 Overview of the experimental setup

Following are the six major techniques used to produce (and observe) Bose-Einstein condensates. The principle of each technique is summarized and shown together with requirements and important references. What is shown in the requirement sections mainly reflects the case of sodium, and may not be applicable to other cases. Figure of merit of each cooling step is summarized in the table at the end.

### 2.1.1 Zeeman slowing

**Principle** Laser cooling in the moving frame. Suppose atomic beam is illuminated by a red-detuned, counter propagating laser beam. Atoms with higher velocity scatter more photons, resulting in lower velocity. By increasing atomic resonance frequency by spatially varying magnetic field, one can slow down the atomic beam almost to rest.

**Requirements** Closed optical transition. Atomic beam and a circularly-polarized, red-detuned laser beam propagating in the opposite direction.

**References** Refs. [77, 102].

### 2.1.2 Dark-SPOT

**Pr.** By placing an atomic cloud in a quadrupole magnetic field and illuminating it with six red-detuned counter-propagating laser beams, one can achieve simultaneous Doppler cooling and trapping (magneto-optical trap, MOT). Helicity of each beam is chosen in a way so that any atom moved away from the center of the trap absorbs more photons from the beam pushing atoms back to the center of the trap. One can regard the MOT as six increasing-type Zeeman slowers attached in six directions. The density of the MOT is limited by radiation pressure and light-assisted collisions. By transferring atoms in an inner region to an other hyperfine state (“dark” state), these limitations can be avoided.

**Req.** Six red-detuned, counter-propagating laser beams and quadrupole magnetic field. Repumping beam only illuminating outer part of the atomic ensemble.

**Ref.** Refs. [82, 103, 104] for MOT, Ref. [92] for Dark-SPOT.

### 2.1.3 Polarization-gradient cooling

**Pr.** Circularly-polarized, counter-propagating laser beams with the same helicity provides spatially varying polarization, creating a periodic optical potential that differs for different magnetic sub-levels. As atoms propagate through this periodic structure, they are transferred between these states, each time losing kinetic energy corresponding to the difference between these two potentials. “Dark” version of polarization gradient cooling is possible by limiting the fraction of atoms in the “bright” state.

**Req.** Six counter-propagating laser beams. No magnetic field.

**Ref.** Ref. [84] for theory, Refs. [83, 105, 106] for experiments.

#### 2.1.4 Magnetic trap

**Pr.** Atoms in low-field seeking states can be trapped at the spatial minimum of the magnetic field, like the center of a quadrupole field. Loss due to spin-flips at the magnetic field zero (Majorana flops) can be avoided by employing non zero-crossing magnetic field configurations like the Ioffe-Pritchard trap.

**Req.** Ground-state magnetic moment of atoms. High power (electro-)magnets placed close to the trapping region.

**Ref.** Refs. [5, 79]

#### 2.1.5 Rf-induced evaporation

**Pr.** Atomic cloud can be evaporatively cooled by selectively removing energetic atoms from a trap and letting it re-thermalize through elastic collisions. Rf-induced spin flips for atoms in a magnetic trap is effective for achieving this cooling scheme.

**Req.** Tight-confining magnetic trap. High stability of bias magnetic field and precise rf ramp.

**Ref.** Refs. [107, 108]

#### 2.1.6 Imaging

**Pr.** Absorption imaging of ballistically expanded cloud was used for signature of condensation and momentum analyses. For in-situ imaging, phase shift of the probe beam due to the index of refraction of the condensate was imaged by shifting the phase of the unscattered probe beam by  $\pi/2$  and overlapping it with the scattered light (phase-contrast imaging).

**Req.** For absorption imaging, instantaneous magnetic field shut-off and synchronized digital camera. For phase-contrast imaging, a phase-plate is needed.

**Ref.** Refs. [1, 3] for absorption imaging for condensates, and Ref. [34] for phase-contrast imaging.

Through these several steps of cooling, the density of the sodium gas is kept around  $10^{11} \sim 10^{14} \text{ cm}^{-3}$ , whereas the temperature is lowered by more than a factor of  $10^8$ . Typical duration, number of atoms, density, temperature, and peak phase-space densities in each cooling step are as follows.

Stage	$t$	$N$	$\rho$	$T$	Phase-space density
Oven			$10^{14} \text{ cm}^{-3}$	500 K	$10^{-13}$
Zeeman slowing and Dark-SPOT	3 s	$10^{10}$	$5 \times 10^{11} \text{ cm}^{-3}$	1 mK	$10^{-7}$
Polarization-gradient cooling	5 ms	$10^{10}$	$10^{11} \text{ cm}^{-3}$	100 $\mu\text{K}$	$10^{-6}$
Magnetic trap (compression)	3.5 s	$3 \times 10^9$	$10^{11} \text{ cm}^{-3}$	160 $\mu\text{K}$	$10^{-6}$
Rf-evaporation to BEC	22 s	$10^7$	$10^{14} \text{ cm}^{-3}$	500 nK	$10^7$

The experimental apparatus used for realizing these cooling schemes is explained in the next sections.

## 2.2 Laser system

A dye-laser based laser system is necessary for sodium experiment, since the closed transition of sodium ( $F = 2 \rightarrow F' = 3$ , see Fig. 2-1) lies in D2 line (589 nm) where no efficient diode laser source is available. More than ten near-resonant laser beams were necessary for laser cooling, trapping and probing, and all of them were generated from a Coherent 899 ring dye laser using Rhodamine 6G dye. In order to increase the efficiency of the dye, the dye pressure was increased by more than a factor of 3 ( $P \leq 3 \text{ bar} \rightarrow 12 \text{ bar}$ ), and the nozzle for the dye jet was exchanged against a high-pressure nozzle (the old nozzle would have withstood high pressure, but created turbulence). Together with high intensity of the pumping laser (typically 9W), 1.6 W of single-mode continuous-wave laser light was obtained.

Combinations of acousto-optical modulators (AOM) and electro-optic modulators (EOM) were used to generate all the necessary frequencies needed for experiments (Fig. 2-2). Among these, trapping, repumping, and slowing laser beams are important during the initial loading of atoms into the MOT. The frequency of the slowing laser beam is detuned by  $\nu_{\text{slower}} = 1 \text{ GHz}$  from the closed transition to capture atoms from  $v_{\text{capture}} = \lambda \nu_{\text{slower}} \sim 600 \text{ m/s}$ . The repumping beam is tuned to the  $F = 1 \rightarrow F' = 2$  transition and used to bring “dark ( $F = 1$ )” atoms in the outer shell of the MOT back to the “bright ( $F = 2$ )” states. For the next 5 ms, the trapping beam is detuned by another 8 MHz and used for polarization gradient cooling. Other beams (as well as the quadrupole magnetic field) are switched off during the polarization gradient cooling and weak sidebands are added to the molasses beam to substitute for the repumping beam.

Typically, at the beginning of each run, we spent more than an hour (often several hours) optimizing the dye laser, optics on the laser table and around the main vacuum chamber. This alignment procedure was based on the bad day-to-day stability. Recently, it was significantly improved by installing several key commercial products. First, the pumping laser was changed from an argon ion laser (Sabre from Coherent) to a doubled Nd:YVO<sub>4</sub> laser (Millennia from Spectra Physics). This change from gas laser to solid-state

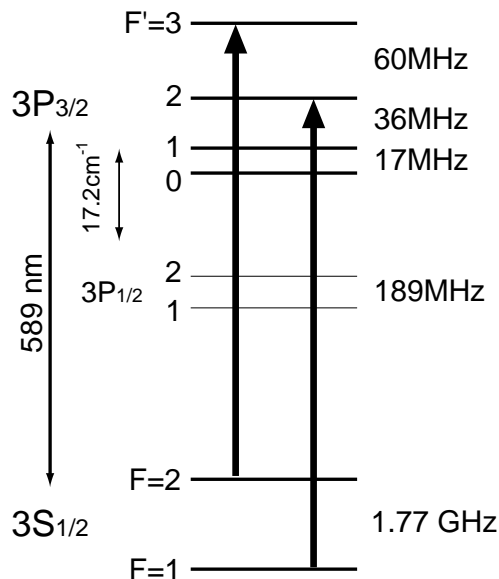


Figure 2-1: Main optical transitions of sodium. Shown are the total angular momentum  $F$  and energy separation between the states in frequency units. The  $F = 2 \rightarrow F' = 3$  closed transition is used for slowing and trapping. The lower hyperfine state ( $F = 1$ ) is used for storing atoms during the dark-SPOT trap phase. A laser beam tuned to  $F = 1 \rightarrow F' = 2$  transition is used to bring  $F = 1$  “dark” atoms back into  $F = 2$  “bright” states.

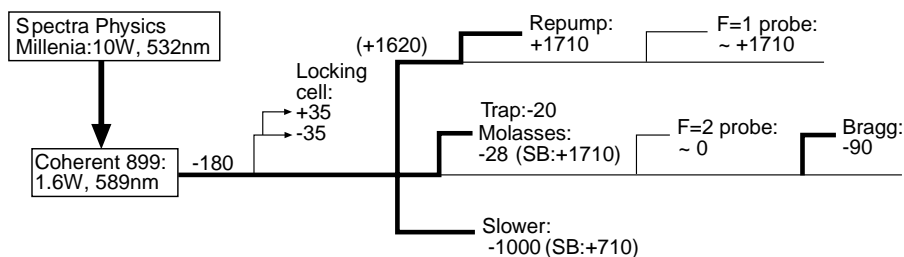


Figure 2-2: Frequencies of beams generated from the dye-laser system. Frequencies relative to the  $F = 2 \rightarrow F' = 3$  closed transition are shown. A doubled Nd:YVO<sub>4</sub> laser is used to excite dye laser based on Rhodamine 6G dye. The frequency of the dye laser is locked to a reference cavity, which is locked to the Doppler-free absorption signal from a sodium cell. All the frequencies, including the repumping beam which is 1.7 GHz away from the closed transition, are generated by acousto-optical modulators (AOM). Electro-optic modulators (EOM) are used to generate frequency sidebands (indicated as “SB”).

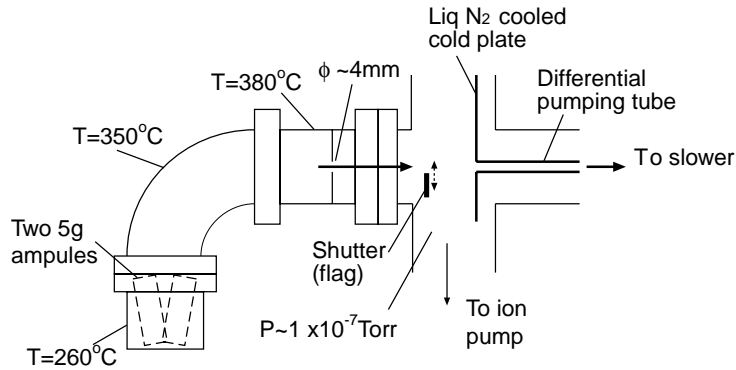


Figure 2-3: Schematics of the oven part.

pumping laser resulted in significant improvement in day-to-day stability of the dye laser beam profile. Secondly, optical fibers were installed instead of running laser beams through free space for 10 meters between the laser and the vacuum chamber. This installation has changed the description of all the optics alignment from “necessary” to “optional.”

## 2.3 Vacuum chamber

The following three figures (Fig. (2-3)-(2-5)) are the schematics of oven, slower, and trapping part of the vacuum chamber. Interested readers are encouraged to read detailed description in Michael Joffe’s thesis [109]. (However, there are a few modifications. The “cold screen” was removed, and the beam shutter is now placed at the oven side of the cold plate. The oven is now elbow-shaped as shown in Fig. 2-3, and more recently, a “cup” is attached at the bottom to shorten the time it takes for us to exchange sodium.)

Our oven (Fig. 2-3) is typically operated at  $260^{\circ}\text{C}$ , and the nozzle area is kept at higher temperature to prevent clogging. We load  $10\text{g}$  of sodium each time, and it lasts about 300 hours of running (Between the runs, the oven is cooled down to  $110^{\circ}\text{C}$ ). Most of the sodium atoms actually do not make it to the trap but simply pile up around the liquid  $\text{N}_2$  cooled cold plate. Every half a year, we disassemble the entire oven part and clean it out. Both keeping the oven pressure at or below  $1 \times 10^{-7}\text{Torr}$  and achieving a differential pumping factor of  $10^4$  through the 15-cm long,  $\phi = 4\text{mm}$  tube are necessary for maintaining  $1 \times 10^{-11}\text{Torr}$  in the main chamber, which is mandatory for 22-second evaporation. For this, the cold plate as well as the differential pumping tube was cooled down by liquid  $\text{N}_2$ . This liquid  $\text{N}_2$  cooling can be certainly avoided by improving the design of the differential pumping stage, and indeed new chambers developed in the next labs do not need liquid  $\text{N}_2$

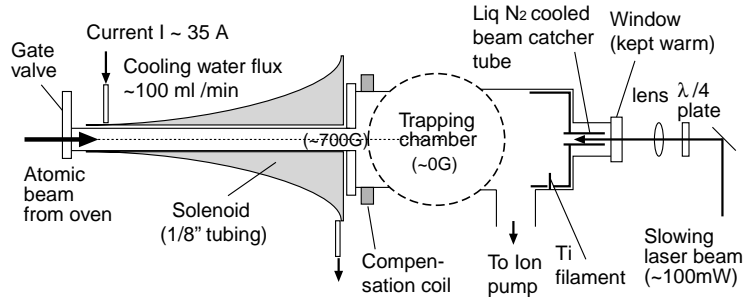


Figure 2-4: Schematics of the slower part. A high flux of  $10^{12}$  slow atoms per second was achieved with our increasing-field type slower.

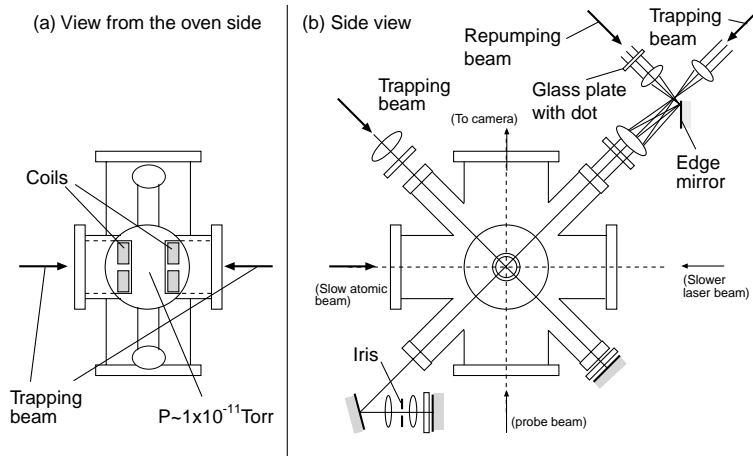


Figure 2-5: Schematic of the main trapping chamber. Both view from the oven (a) as well as the side view (b) are shown. The iris at the bottom is used to block the retro-reflection of the repumping beam.

cooling. The mechanical shutter is activated by sending in electric current to a relay placed inside the oven chamber. Compared to the design based on a mechanical feedthrough, this design has a certain advantage (for example, it is free from any backlashes which come with most of the feedthroughs), but it is less easy to service.

The atomic beam from the oven is decelerated by an increasing-field type Zeeman slower [110], which drives the  $F = 2, m_F = -2 \rightarrow F' = 3, m_{F'} = -3$  transition. The design of the slower is shown in Fig. 2-4. The typical power of the slowing laser beam is about 100 mW, and the diameter of the slowing laser beam is more than 3 cm at the view port and is focused down to the nozzle. The final velocity of the slowed atomic beam is  $\sim 30$  m/s, which corresponds to a kinetic energy of 1 K and well within the capture range of the MOT. The high flux of our slower ( $\sim 10^{12}$  atoms/s at 100 m/s and  $\sim 10^{11}$  atoms/s at 30 m/s, see [111]) enables us to load more than  $10^{10}$  atoms in  $1 \sim 2$  s.

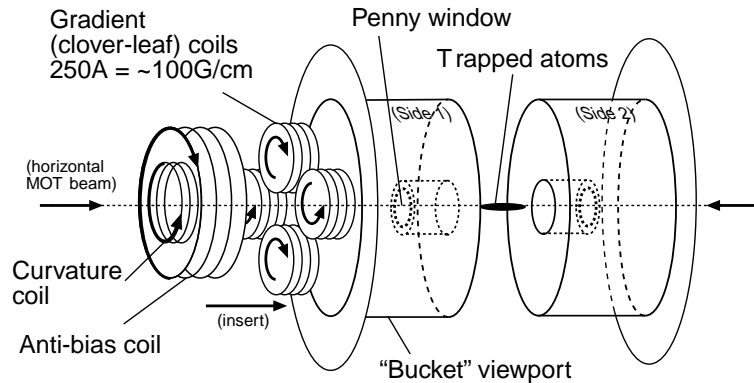


Figure 2-6: Ioffe-Pritchard trap with clover-leaf design. Radial linear confinement is produced by “clover-leaf” coils, whereas axial quadratic confinement is produced by Helmholtz “curvature” pairs. “Anti-bias” (Helmholtz pairs pointing in the opposite direction) is used to lower the bias field at the trapping center to increase the effective radial curvature at the bottom of the trap.

The rest of the cooling and imaging is done in the main trapping chamber (Fig. 2-5). Horizontal ports are used for slowing and two independent MOT beams. All of the four diagonal view ports are used for the (retro-reflected) MOT beams, and vertical view ports are mainly used for imaging. The repumping beam ( $\sim 30$  mW) is overlapped with one of the diagonal MOT beams by an edge mirror. The diameter of the MOT and repumping beams are more than 3 cm, and the intensity of each beam is on the order of the saturation intensity. The dark-SPOT trap was achieved by passing the repumping beam through a glass plate with a black dot, which was imaged into the trap center with an image size of  $\sim 10$  mm. Alignment of each beam is optimized by visually inspecting the shape of the trapped cloud and also the expansion during polarization-gradient cooling. The atomic cloud is quite sensitive to minute change in alignment of the MOT and repumping beams, and has allowed the development of several mysterious “voo-dooos.” This is illustrated by the fact that we quite often gain in the number of atoms in the MOT by unblocking the retro-reflection of the repumping beam and letting it back into the trap in an uncontrolled manner.

Tight confinement of the magnetic trap can be realized by placing electro-magnets close to the trapping region. However, installing high-power electro-magnets inside the vacuum chamber without compromising ultra-high vacuum is a difficult task. To get around this, we use “bucket” view ports, which are recessed closer to the trapping region (about 1/2 inch away, see Fig. 2-5(a) and also Fig. 2-6). A tight-confining, DC magnetic trap was realized by using a Ioffe-Prichard field configuration with clover-leaf coil design [5, 34]. Since the details of this magnetic trap is well described in previous dissertations [25, 112], I will only present schematic figures and typical operating conditions. Strong linear confinement

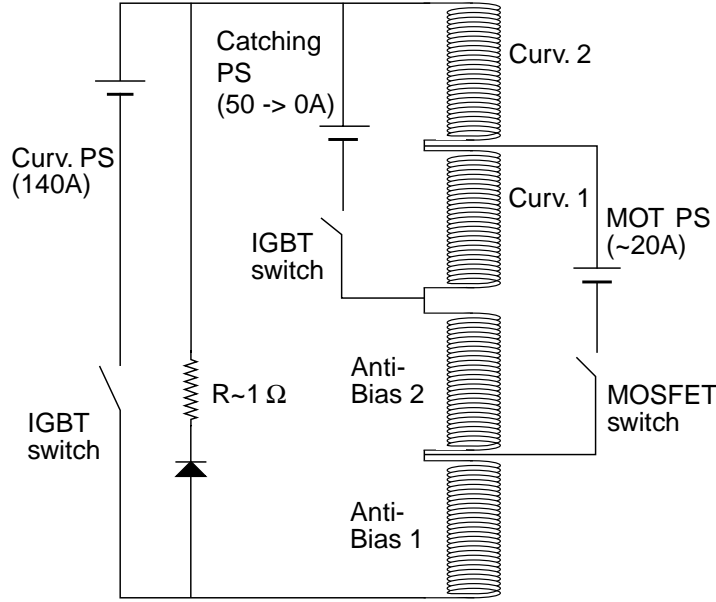


Figure 2-7: Circuit diagram of the high-current setup. Curv. 1 and Anti-bias 1 occupy one side of the trap, whereas curv. 2 and Anti-bias 2 occupy the other side of the trap. Resistor-diode pair, which ensures smooth shut-off of the trap can be replaced by varistors.

( $B'_r \sim 100 \text{ G/cm}$  at 250 A) in the radial direction is obtained from the field from clover-leaf coils, whereas modest quadratic confinement in the axial direction ( $B''_z \sim 120 \text{ G/cm}^2$  at 140 A) is available through Helmholtz coils (“curvature” coils). The linear radial confinement becomes quadratic at the bottom of the trap, and the field curvature is approximately proportional to  $B'_r{}^2/B_0$ , where  $B_0$  is the bias field at the bottom of the trap. By carefully aligning another Helmholtz pair in the other direction (“Anti-Bias” coil) and running current in series with the curvature coils, we can achieve a stable low bias field ( $B_0 \sim 1 \text{ G}$ ) at the position of the trap. For sodium atoms in the weak field seeking state in the lower hyperfine manifold ( $F = 1, m_F = -1$ ), this produces a radial trapping frequency  $\omega_r$  of  $2\pi \times 230 \text{ Hz}$ , and axial trapping frequency  $\omega_z$  of  $2\pi \times 17 \text{ Hz}$ .

The circuit diagram for the magnetic trap is shown in Fig. 2-7. Typically, one 5 kW ( $= 20 \text{ V} \times 250 \text{ A}$ ) DC power supply is used to run current through the clover-leaf coils, and one more unit is used to run current through both the curvature coils and anti-bias coils. The stability, ripple, and regulations of these switching power supplies are typically better than 0.1% in current control mode. Fast shut-off ( $\sim 20 \mu\text{s}$ ) of the trap is ensured by the combination of an IGBT switch and a resistor-diode pair, which dissipates the energy stored in the coils. Modification to the trapping potential is done by either controlling the power supply with an analog signal, or applying additional current to specific coils. For example, additional 50 A of current is applied to the curvature coils during the initial stage of the magnetic trap loading to reduce the tight confinement in the radial direction and

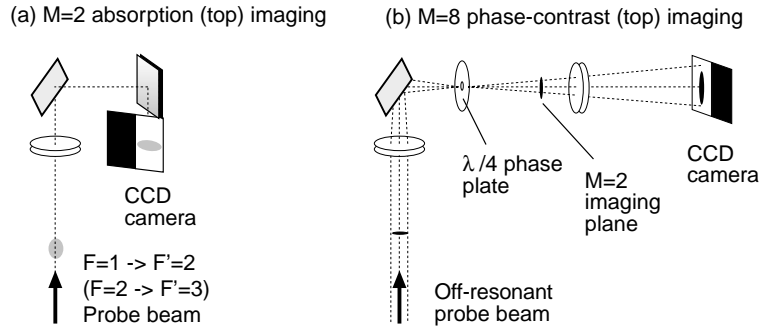


Figure 2-8: Schematic of absorption and phase-contrast imaging.

to achieve better mode-matching with the quasi-spherical MOT. Even the MOT is realized by constituting anti-Helmholtz coil using one coil from the curvature Helmholtz pair and another coil from the anti-bias pair.

We use time-of-flight absorption imaging and *in-situ* phase-contrast imaging for analyzing condensates. Typical setups are shown in Fig. 2-8. For most of the analysis, the number of atoms in specific momentum or spin (spatially separated by Stern-Gerlach magnet) states was determined from absorption images by integrating optical densities. Phase-contrast imaging is used when (a rapid sequence of) non-destructive images are necessary or *in-situ* images are needed for “micro-surgery” of condensates. Detailed description of our quantitative analysis of images can be found in Refs. [25, 34]

## Chapter 3

# Bragg scattering from a Bose-Einstein condensate

*This chapter summarizes the Bragg scattering from a Bose-Einstein condensate that was reported in the following publication:*

- *J. Stenger, S. Inouye, A.P. Chikkatur, D.M. Stamper-Kurn, D.E. Pritchard, and W. Ketterle, “Bragg Spectroscopy of a Bose-Einstein condensate,” Phys. Rev. Lett. **82** 4569 (1999). Included in Appendix C.*

### 3.1 Linewidth of an “atom laser”

What is the easiest way to determine the linewidth of laser light? The answer strongly depends on what is available in the lab, but one simple solution would be to use a diffraction grating. Due to the wave nature of light, the beam is diffracted only in the direction which satisfies the Bragg condition. The width of the angle is proportional to the linewidth  $\Delta\lambda$  and inversely proportional to the lattice spacings  $D$ . ( $\Delta\theta \sim n\Delta\lambda/D$ , where  $n$  is the diffraction order).

The same simple idea can be applied to determine the momentum distribution of a condensate. One can drop a condensate onto a mechanical grating and measure the diffraction efficiency as a function of the diffraction angle. However, installation of a mechanical grating inside the main vacuum chamber is not an ideal thing to do, since it requires considerable time to re-establish the ultra high vacuum that is essential for evaporative cooling. Also, the interaction time will be limited since any contact with its surface will result in the loss of atoms — atoms will either be heated up by the surface or stick to the surface.

Light gratings are an ideal tool for analyzing ultracold atoms. Two counter-propagating, off-resonant light beams produce an intensity grating whose periodicity is half the wavelength of the light. Instead of moving a condensate relative to the grating, we can *move* the grating by applying a small detuning between the two beams. The atoms in a condensate at

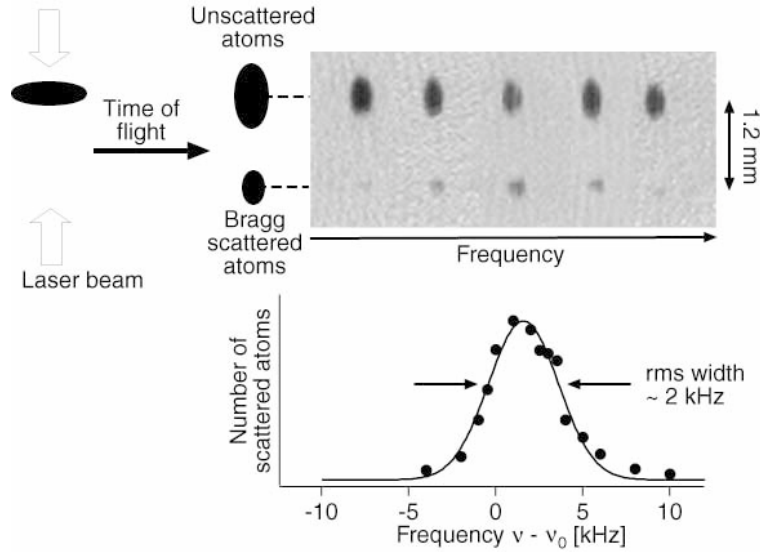


Figure 3-1: Typical Bragg resonance curve for trapped condensates. The fraction of atoms coupled out by the Bragg transition was determined from time-of-flight images, where recoiling atoms (lower spots) were clearly separated from condensates at rest (upper spots). It showed a narrow resonance when the difference frequency  $\nu$  between the two laser beams was varied around the recoil frequency  $\nu_0$  of the atoms.

rest absorb momentum from the periodic structure and start to move. The scattering takes place only if the velocity of atoms viewed from a moving frame of the grating is the same before and after the scattering. This is due to the conservation of energy in the moving frame and corresponds to the Bragg condition for matter waves. This resonance condition is sensitive to the initial motion of atoms and is broadened by the Doppler effect.

The efficiency of this diffraction can be determined by taking time-of-flight absorption images just after applying the “Bragg pulse” (the counter-propagating beams) to the condensate. The efficiency shows a resonance curve as a function of detuning between the two beams, which determines the velocity of the moving standing wave. Fig. 3-1 shows a typical Bragg resonance curve for trapped condensates, together with the geometry of the experiment. The direction of the standing wave was chosen to be perpendicular to the long axis of the condensate, which was horizontal in the image. This direction of momentum transfer was chosen to maximize the Heisenberg-limited momentum width, which will be discussed later. Atoms in a condensate are diffracted downward in the image by the standing wave moving in the same direction.

### 3.2 Bragg scattering as a two-photon resonance

It is important to notice that this diffraction can be also viewed as a stimulated Raman process between two momentum states. Absorption of a photon from a high frequency

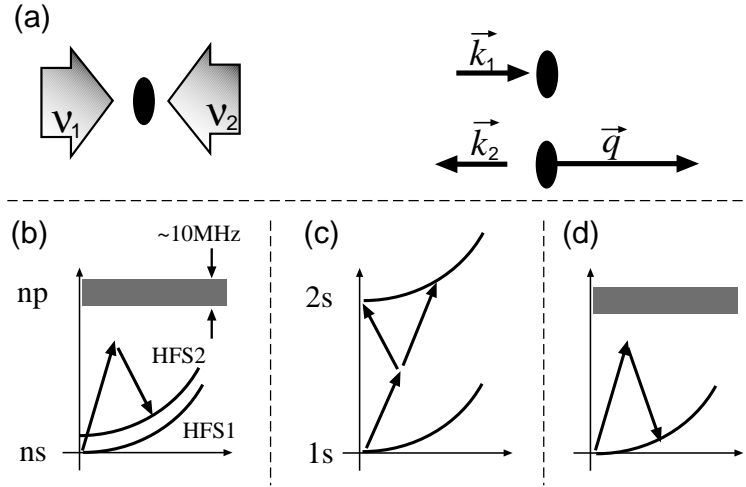


Figure 3-2: Schemes for high-resolution velocimetry using two-photon resonances. The momentum transfer  $\hbar\vec{q}$  and energy transfer  $h\nu$  due to the two-photon transition are given by wavevector and frequency differences between the two beams,  $\hbar\vec{q} = \hbar(\vec{k}_1 - \vec{k}_2) = 2\hbar k \sin(\theta/2)$  and  $h\nu = h(\nu_1 - \nu_2)$ , where  $\theta$  is the angle between the two laser beams (a). Narrow linewidth of the transition between different hyperfine states (Raman transition, (b)) and transition to a metastable excited states (c) were used for resolving small Doppler broadening due to the initial momentum spread of atoms. Bragg transition connects two momentum states of the same ground state (d) and is thus less sensitive to fluctuations of external stray fields.

beam followed by a stimulated emission to the other beam results in momentum and energy transfer to atoms in a condensate. This process only happens when it satisfies conservation of energy and momentum i.e., when the detuning of the two beams corresponds to the recoil frequency of atoms  $\omega_{\text{rec}} = \hbar q^2/2M$ , where  $q$  is the momentum transferred to the atoms.

Bragg scattering of atoms from a light grating was first demonstrated in 1988 [113] and has been used to manipulate atomic samples in atom interferometers [114], in deBroglie wave frequency shifters [115], and also to couple out or manipulate a Bose-Einstein condensate [116]. Small angle Bragg scattering, called recoil-induced resonances, has been used for thermometry of laser-cooled atoms [117]. Here, we use Bragg scattering as a spectroscopic technique to probe properties of the condensate.

Bragg scattering is not the only method that uses two-photon transitions for achieving subrecoil momentum resolution (Fig. 3-2). Raman transition between two ground-level hyperfine states was used to prepare a sample of atoms with a velocity spread of  $\sim 0.01 \hbar k$  [118]. A Doppler sensitive two-photon transition to a metastable state was used to identify the momentum spread of a Bose-Einstein condensate of hydrogen atoms [65]. Systematic effects like ac-stark shift is a major concern for using these optical transitions that involve *different* internal states. In the case of the Raman resonance, the effect of the ac-stark shift was avoided by using relatively large detuning from the atomic resonance: the ac-Stark shift for magnetic field insensitive transitions vanishes in the limit of  $\Delta$  large compared to

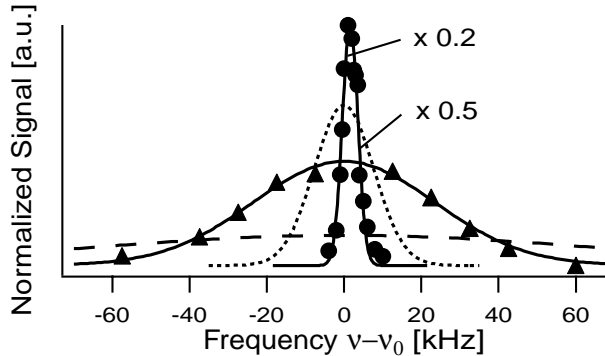


Figure 3-3: Bragg resonances for a trapped condensate (circles) and after 3 ms time-of-flight (triangles). For comparison, the momentum distributions of the ground state of the trapping potential (dotted curve) and of a  $1 \mu\text{K}$  cold, thermal cloud (dashed curve) are indicated. The heights of the curves for the trapped condensate and the ground state momentum distribution are scaled down as indicated in the figure. Figure taken from Ref. [17].

the hyperfine splitting. The Bragg resonance used here is completely insensitive to these external fields since both momentum states share the *same* internal state.

### 3.3 Finite-size broadening and effects of the mean-field

Fig. 3-3 shows typical spectra, taken both for a trapped condensate and after 3 ms time of flight. The rms width of the resonance for the ballistically expanding cloud is 20 kHz, which is much narrower than the 65 kHz wide distribution of a thermal cloud at the BEC transition temperature ( $1 \mu\text{K}$ ). Indeed, this sudden transition in velocity distribution in time-of-flight is the most popular method for identifying the phase transition. However, the signature of BEC observed by Bragg scattering is much more dramatic — the condensate resonance is more than 30 times narrower than the one of the thermal cloud. It is also important to notice that this width is even narrower than the momentum width of the ground state of the harmonic trap. Narrower momentum width indicates larger coherence length. This requirement from the Heisenberg uncertainty relation shows that Bragg scattering can be used to determine the coherence length of a condensate.

Repulsive interaction between atoms shifts and broadens the Bragg resonance, and precise determination of these values is essential for extracting the coherence length from the resonance width. Precisely speaking, the resonance condition is satisfied when the detuning between the two beams match the energy needed for exciting quasi-particle excitation with momentum  $\hbar q$ . For a weakly interacting homogeneous condensate, the dispersion relation of the quasi-particle excitation has the following form given by Bogoliubov:

$$\nu = \sqrt{\nu_{\text{rec}}^2 + 2\nu_{\text{rec}}\rho U_0/h} \quad (3.1)$$

where  $\rho U_0 = \rho 4\pi \hbar^2 a_{\text{sc}}/M$  is the chemical potential of a condensate and  $h\nu_{\text{rec}} = \hbar^2 q^2/2M$  is the recoil energy associated with the momentum  $q$ . If momentum transferred is smaller than the speed of sound (times the mass of atoms) of the condensate, the dispersion is linear (phonon excitation). For momentum larger than the speed of sound, the dispersion is quadratic and shifted up by amount equal to the chemical potential of the condensate.

$$\nu = \begin{cases} \frac{q}{2\pi} c_s & \hbar q \ll M c_s \\ \nu_{\text{rec}} + \rho U_0/h & \hbar q \gg M c_s \end{cases} \quad (3.2)$$

where  $c_s = \sqrt{\rho U_0/M}$  is the speed of sound in the condensate.

Our Bragg spectroscopy probes the free-particle regime, since the excitation by the Bragg transition has larger momentum than the speed of sound of the condensate. The resonance frequency shift is proportional to the local density of the condensate. Calculations show that the inhomogeneous density distribution due to the parabolic potential shifts the resonance by  $4\rho_0 U_0/h$  and broadens the resonance to an rms width of  $\Delta\nu_\rho = \sqrt{8/147}\rho_0 U_0/h$ . Since the chemical potential of our condensate is on the order of several kHz, this shift and broadening should be on the order of few kHz.

Both the (Doppler) broadening due to finite momentum width and mean-field interaction contribute to the resonance curve. While the exact calculation of the line shape requires detailed knowledge of the excitation wavefunctions, the total line shift and rms width can be calculated using sum rules and Fermi's Golden Rule. Thus, it can be rigorously shown that the total line shift remains  $4\rho_0 U_0/h$ , while the rms width of the resonance becomes  $\Delta\nu = \sqrt{\Delta\nu_p^2 + \Delta\nu_\rho^2}$  which is the quadrature sum of the Doppler and mean-field widths.

The narrow resonance of the trapped condensate was studied as a function of the condensate density and size. Fig. 3-4a demonstrates the linear dependence of the frequency shift on the density. The slope of the linear fit corresponds to  $(0.54 \pm 0.07)\rho_0 U_0/h$ , in agreement with the prediction of  $4\rho_0 U_0/7h \sim 0.57\rho_0 U_0/h$ . In fig 3-4b, the expected widths due to the mean field energy and the finite size of the condensate are shown for the two different trapping frequencies studied. The expected width due to the finite size of the condensate was determined by performing a Fourier transform to the wavefunction of a condensate and integrating it over the dimensions perpendicular to the momentum transfer [119]. The comparison between the measured resonance width after subtraction of the contribution of the mean field and the calculated effective rms width for the distribution,  $\Delta p_x \sim 1.58\hbar/x_0$ , shows excellent agreement, indicating that the coherence length of the condensate is equal to its size.

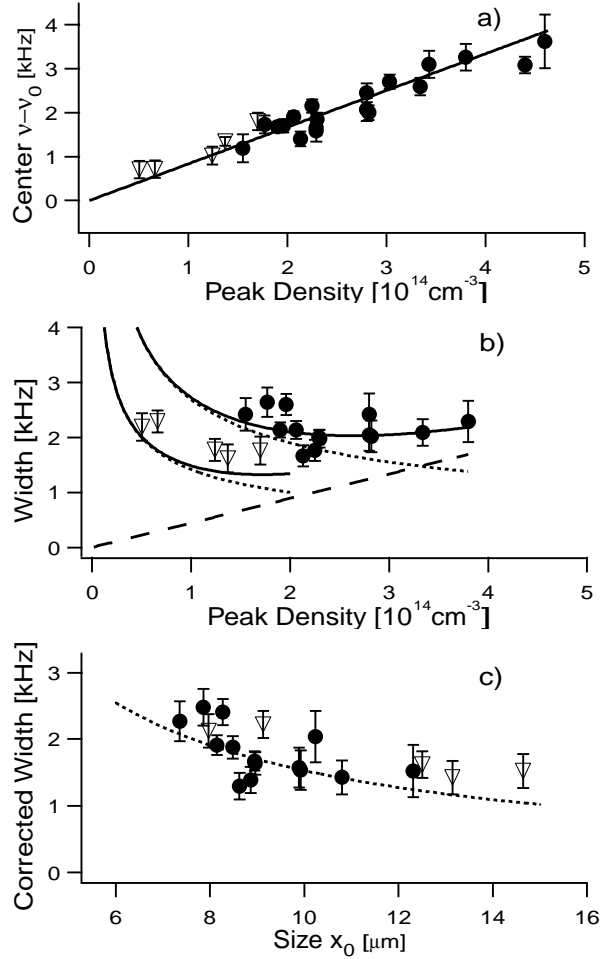


Figure 3-4: Bragg spectroscopy of a trapped condensate. Line shifts (a) and rms width (b) are shown for various densities and sizes of the condensate using two different radial trapping frequencies,  $\nu_x = (195 \pm 20) \text{ Hz}$  (circles), and  $\nu_x = (95 \pm 20) \text{ Hz}$ . The lines in (b) show the contributions of the mean-field energy (dashed) and due to the finite size (dotted, for both trapping frequencies) and their quadrature sum (solid lines). (c) displays the width after subtraction of the contribution of the mean field and the finite pulse duration and compares it with the prediction for the momentum uncertainty due to the finite size. The error bars are  $1\sigma$  errors of the Gaussian fits to the data. Figure taken from Ref. [17].

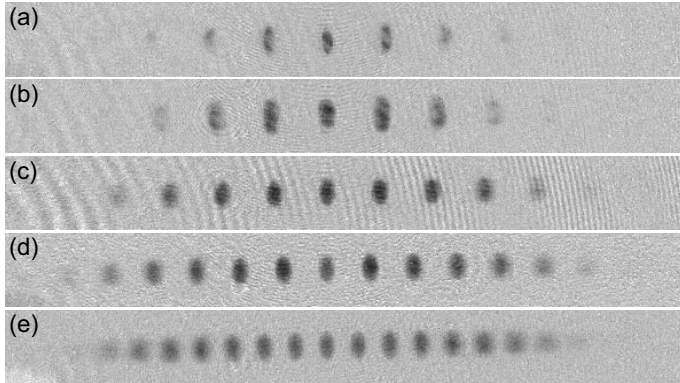


Figure 3-5: Kapitza-Dirac diffraction of a Bose-Einstein condensate. A red-detuned, standing wave of light was applied to condensates during time-of flight. The duration of the pulse was  $0.37 \mu\text{s}$ , which was factor of four shorter than the inverse of the recoil frequency ( $1.6 \mu\text{s}$ ). The density of the cloud at the time of diffraction was varied by changing the timing of the pulse. The delays of the pulse after the release of the cloud were 1 (a), 2 (b), 3 (c), 6 (d), and 10 (e) ms, which corresponds to the density of  $1.2$  (a),  $0.37$  (b),  $0.17$  (c),  $0.04$  (d), and  $0.02$  (e)  $\times 10^{14} \text{cm}^{-3}$ . The total time-of-flight was 20 ms. The intensity of each beam was  $200 \text{mW/cm}^2$ , and the detuning was 1.7 GHz. The field of view of each image is  $15 \text{mm} \times 1.7 \text{mm}$ .

### 3.4 Higher order Bragg scattering

Higher order Bragg diffraction could be ideal for high precision velocimetry, since it reduces the effect of inhomogeneous mean-field, which was contributing to about one half of the linewidth in the measurement shown in Fig. 3-4. The resonance condition for  $n$ th order Bragg diffraction is

$$n\hbar\omega = \frac{\hbar^2}{2M}(k + nq)^2 + \rho U_0 - \frac{\hbar^2}{2M}k^2 \quad (3.3)$$

where  $q$  is the momentum transfer. The condition simplifies to:

$$\omega = \frac{\hbar k}{M}q + n\omega_{\text{rec}} + \frac{1}{n} \frac{\rho U_0}{\hbar} \quad (3.4)$$

Both the shift and the width due to the mean field decrease as  $1/n$  as the order of Bragg scattering is increased.

Bragg spectroscopy using higher order Bragg scattering was pursued with the same experimental setup, but scaling the detuning between the two beams by a factor of  $n$  (“ $n\omega_{\text{rec}}$ ” in Eq. (3.4)). However, larger intensity and a longer pulse length were necessary for achieving similar diffraction efficiency, and it has resulted in severe loss of atoms due to spontaneous emission [116]. The transition probability for  $n$ th order Bragg diffraction is given by [114]

$$P_n = \sin^2 \left[ \frac{\Omega^{2n} \sqrt{\pi/2n}}{4^{2n-1} \Delta^n \omega_{\text{rec}}^{n-1} [(n-1)!]^2} t \right] \quad (3.5)$$

where  $t$  is the length of the pulse. Eq. (3.5) is valid for detunings  $\Delta$  much larger than the single beam Rabi frequency  $\Omega$ , and the linewidth of the optical transition,  $\Gamma$ . The probability for spontaneous emission varies as  $I/\Delta^2$ . The condition for realizing higher order Bragg scattering requires that  $I/\Delta$  be increased. Therefore, higher intensity  $I$  and larger detuning  $\Delta$  are necessary for keeping the Bragg diffraction rate higher than that of spontaneous emission.

For higher momentum transfer, collisional dephasing also starts to play a role, since the rate of collisions is proportional to the relative velocities between atoms. In order to illustrate this effect, a short ( $0.37\mu\text{s}$ ) standing wave laser pulse was applied to a condensate during time of flight and the maximum diffraction order was determined as a function of density. The density of the cloud was varied by changing the timing of the pulse.

Fig. 3-5 shows the density dependence of the number of diffraction orders. Third order diffraction ( $6\hbar k$  momentum transfer) was barely visible in the highest density cloud, whereas 7th order diffraction ( $14\hbar k$ ) was observed with the lowest density cloud. The two counter-propagating beams were parallel to the long axis of the condensate. Both the effect of Doppler broadening due to the motion in the axial direction and the effect of the mean field should be negligible in this experiment since the inverse of the pulse length (430 kHz) is far larger than those frequency widths.

This elastic scattering between atoms in different momentum states was nicely imaged in time-of-flight pictures taken after coupling out a fraction of atoms by Bragg diffraction. Fig. 3-6 shows the collision between the condensate at rest (lower black dot) and Bragg diffracted atoms (upper spot). Since the velocity of atoms after the Bragg diffraction is well within the  $s$ -wave regime ( $\sim 6\text{ cm/s}$ ) the momentum distribution of collided atoms shows a sphere in momentum space. This technique was used to study the suppression of elastic collision in the condensate due to superfluidity [23]. The observed “ $s$ -wave halo” is different from the “spontaneous emission circle” observed when condensate was illuminated with a single laser beam [116]. The number of atoms in the halo decreased as we reduced the number of Bragg diffracted atoms by changing the detuning between the two laser beams.

### 3.5 Other measurements of the coherence length of condensates

Several experiments have been performed to confirm the phase-coherence of a Bose-Einstein condensate [6, 17, 120, 121, 122]. Similarities and differences between these experiments were summarized in Ref. [25] from the view point of “near-field” and “far-field” measurement of the coherence length. In the “near-field” (or real space) measurements of the condensate phase, the phase of the wavefunction at two points were compared to each other by overlapping parts of the same condensate. This includes the interference between two Bose-Einstein condensate observed in 1997 [6], interference using Kapiza-Dirac pulses [120],

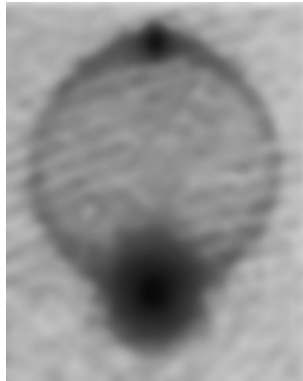


Figure 3-6: Observation of an elastic collision between the condensate (lower black dot) and Bragg diffracted atoms (upper spot). The image was taken after a time-of-flight of 30 ms, and shows the velocity distribution after the collision. The products of the collision are distributed over a sphere in momentum space, leading to the observed halo. The height of the image is 3.2 mm.

measurement of the spatial correlation function by rf-outcoupling [121], and the “auto-correlation” experiment by Bragg interferometry [122]. These measurements are sensitive to any local dislocations or discontinuities in phase profiles. In the Bragg spectroscopy explained here, phases of the wavefunction across the whole condensate was sampled at once, corresponding to observing the matter wave in the far field (or in momentum space). This method is not suited for identifying local structures in the phase profile, but ideal for identifying atoms in different “modes,” or quasi-particle excitations in the condensate. Suppose a condensate with vortex excitation is subjected to these studies. The “near-field” method will reveal the dislocation in the spatial phase profile, whereas Bragg spectroscopy detects atoms at finite velocities due to the flow field of a vortex.

Small angle Bragg scattering, where the transferred momentum is smaller than the speed of sound in the condensate, was used to probe the structure factor of the condensate in the small momentum limit [22]. The strength of the Bragg transition is proportional to the correlation of the scattered electrical field,  $\langle \mathcal{E}_S^\dagger(r_1, t_1) \mathcal{E}_S(r_2, t_2) \rangle$  [123]. Since the amplitude of the scattered electrical field is proportional to the local density, the strength of the two-photon transition is now proportional to  $\langle \rho(r_1, t_1) \rho(r_2, t_2) \rangle$ , which is the Fourier transform of the structure factor of the condensate.

## Chapter 4

# Superradiant Rayleigh scattering from a Bose-Einstein condensate

*This chapter describes the superradiant Rayleigh scattering from a Bose-Einstein condensate that was reported in the following publication:*

- *S. Inouye, A.P. Chikkatur, D.M. Stamper-Kurn, J. Stenger, D.E. Pritchard, and W. Ketterle, “Superradiant Rayleigh Scattering from a Bose-Einstein Condensate,” Science* **285**, 571 (1999). *Included in Appendix D.*

### 4.1 Directional matter waves produced by spontaneous scatterings

“Bose condensates scatter light differently.” This was what one of my colleagues came up with, when we were trying to summarize our work on superradiance with a single phrase. Another colleague of mine said “Try this at home!” when he was explaining this phenomenon to peer experimentalists. These two quotes show one of the main characteristics of this phenomenon: simplicity. Only a single off-resonant laser beam and a condensate are needed to observe this phenomenon. But the physics behind it is quite rich and requires a deep understanding of coherence and stimulation.

The most striking difference between normal Rayleigh scattering and superradiant Rayleigh scattering is the directionality of the scattering. The geometry of the setup is shown in Fig. 4-1. An elongated Bose-Einstein condensate was illuminated with a single off-resonant laser beam, traveling perpendicular to the long axis of the condensate (Fig. 4-1a). Atoms in a condensate absorb a photon from the laser beam and spontaneously emit a photon, receiving recoil momentum and energy (Fig. 4-1b). The direction of the spontaneous emission was expected to be random, leading to momentum diffusion and heating of the atomic cloud. This was confirmed by observing the momentum distribution of scattered atoms by taking time-of-flight images after the light pulse. Indeed, when the polarization of the

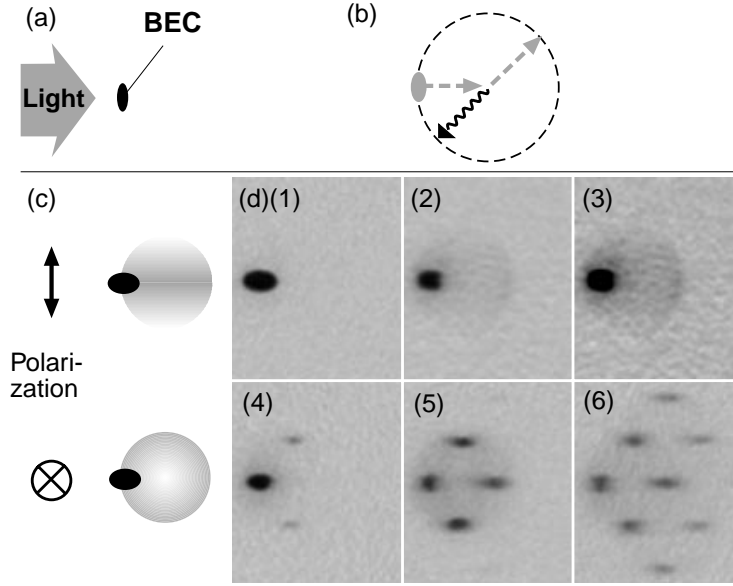


Figure 4-1: Observation of superradiant Rayleigh scattering. An elongated condensate was illuminated with a single off-resonant laser beam (a). The atomic momenta after the light scattering lie on a sphere centered at  $\hbar\vec{k}$  (b). The distribution shows the dipole pattern depending on the polarization of incoming beam (c). Shown in (d) are absorption images after 20 ms time-of-flight after their exposure to a laser pulse of variable duration. When the polarization was parallel to the long axis, normal Rayleigh scattering was observed (1-3). For perpendicular polarization, collective (superradiant) scattering lead to photons scattered predominantly along the axial direction, and atoms at 45 degrees(4-6), and evolved to repeated scattering for longer laser pulses (5,6). The pulse durations were 25 (1), 100 (2,3), 35 (4), 75 (5), 100  $\mu\text{s}$  (6). The field of view of each image is  $2.8 \times 3.3$  mm. The scattering angle appears larger than 45 degrees due to the angle of observation. All images use the same gray scale except for (3), which enhances the small signal of Rayleigh scattered atoms in (2). Figure taken from Ref. [18].

incident beam was parallel to the long axis of the condensate, the momentum distribution was isotropic, modified by the dipolar emission pattern(Fig. 4-1d(1-3)). However, when the polarization of the laser beam was perpendicular to the long axis of the condensate, highly directional beams of atoms were observed in time-of-flight images.

The observation of directional atomic beams strongly suggests the build-up of a high contrast matter wave grating in the condensate when these scattered atoms still overlapped with the condensate at rest. This build-up of the matter wave grating can be easily understood by following each step of the off-resonant Rayleigh scattering (Fig. 4-2). When a condensate is exposed to a laser beam with wave vector  $\mathbf{k}_0$ , it absorbs a photon from the laser beam and spontaneously emits a photon with wave vector  $\mathbf{k}_i$ , generating an atom with recoil momentum  $\hbar\mathbf{K}_j = \hbar(\mathbf{k}_0 - \mathbf{k}_i)$ (Fig. 4-2a,b). Because light propagates at a velocity about 10 orders of magnitude faster than the atomic recoil velocity, the recoiling atoms

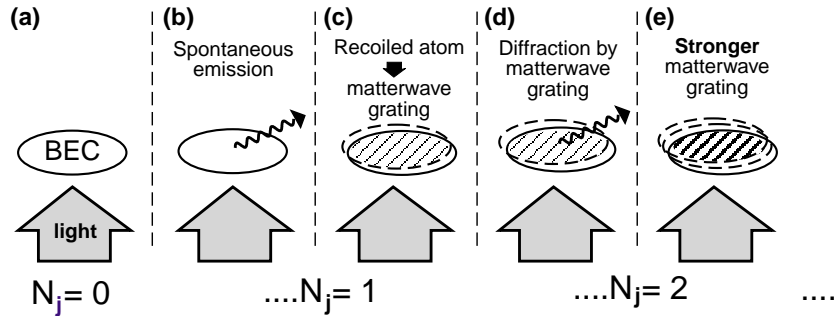


Figure 4-2: Build-up of matter wave grating inside a condensate due to light scattering. A condensate illuminated by a single laser beam (a) scatters a photon spontaneously (b). The scattered atom interferes with the condensate at rest and forms a matter wave grating (c). Diffraction of light by the matter wave grating (d) transfers more atoms into the recoil mode, leading to higher diffraction efficiency (e). As a result, the number of atoms in the recoil mode shows exponential growth.

remain with the volume of the condensate long after the photons have left and affect subsequent scattering events. They interfere with the condensate at rest to form a moving matter wave grating of wave vector  $\mathbf{K}_j$ , which diffracts the laser beam into the phase-matching direction, i.e. the *same* direction  $\mathbf{k}_i$  again (Fig. 4-2c,d). This diffraction is a self-amplifying process because every diffracted photon creates another recoiling atom that increases the amplitude of the matter wave grating (Fig. 4-2e).

Because each scattered photon creates a recoiling atom, the diffraction efficiency of the gratings gives the growth rate of each matter wave mode. The diffraction efficiency is proportional to the square of the depth of the density modulation, and therefore to the number of atoms in the recoil mode  $N_j$ . This implies an exponential growth of  $N_j$ , as long as one can neglect the depletion of the condensate at rest. The angular dependence of the gain can be understood as follows. Given the same contrast of the grating, one can show that the *intensity* of the scattered light in the phase-matching direction does not depend on the shape of the condensate. However, the *total intensity* of the scattered light, or the rate of scattering, is largest when the phase-matching direction of photon emission is along the long axis of the condensate, since the condition is fulfilled over a wider solid angle due to the finite size of the condensate.

The gain equation for the number of atoms in recoil mode  $j$  can be either obtained from the semi-classical treatment shown above, or from a fully quantum mechanical treatment based on second-quantization and Fermi's Golden Rule.

$$\dot{N}_j = R N_0 \frac{\sin^2 \theta_j}{8\pi/3} \Omega'_j (N_j + 1). \quad (4.1)$$

Here,  $R$  is the rate for single-atom Rayleigh scattering, which is proportional to the laser intensity. The angular term reflects the dipolar emission pattern with  $\theta_j$  being the

angle between the polarization of the incident light and the direction of emission. The solid angle factor  $\Omega'_j \sim \lambda^2/A_j$  depends on the angle of photon emission through  $A_j$ , which is the cross-sectional area of the condensate perpendicular to the direction of photon emission.

Eq. 4.1 now describes both the normal Rayleigh scattering at a constant rate  $\Sigma\dot{N}_j = RN_0$  when  $N_j \ll 1$  and exponential gain of the  $j$ th recoil mode once  $N_j$  becomes non-negligible. Initially, the angular distribution of the scattered light follows the single-atom spontaneous (dipolar) emission pattern but can become highly anisotropic when stimulation by the atomic field becomes important.

## 4.2 Dicke superradiance — emerging coherence

This build-up of coherence in an atomic ensemble through spontaneous photon emission is analogous to the superradiance discussed by Dicke [124, 125, 126]. He first considered spontaneous emission from two excited atoms. If the spacing between these two atoms is smaller than the wavelength, the two dipoles are *in phase* after the first photon emission, resulting in a factor of two larger spontaneous emission rate for the second photon emission compared to the single-atom rate. If the spacing between the two atoms is larger than the wavelength, the phase relationship between the dipoles does not have to be symmetric any more, but it introduces a strong correlation between the direction of the first and the second photon emission. Consider angular distribution of spontaneously emitted photons from two excited state atoms separated by  $2.5\lambda$ . If the first emitted photon was found in one of the “nodes” of the radiation pattern from dipoles oscillating in phase, the probability distribution of the direction of the second photon emission is given by the solid line in Fig. 4-3, since the wave function after the first photon emission is in an anti-symmetric state.

These correlations between the successive photon emission is further pronounced in superradiance from extended samples (Fig. 4-4). For an anisotropic sample, the strength of the correlation is largest when photons are emitted along its longest axis (“end-fire mode”). As a result, highly directional light beams come out from incoherently excited, elongated samples of atoms. The light beam has the same property as a laser beam and was called “coherence-brightened laser”, but its coherence is maintained by the phase relationship between the dipoles, not by recycling photons in a cavity.

The full analogy between the Dicke superradiance discussed above and the superradiant Rayleigh scattering observed here can be summarized as follows. The condensate at rest “dressed” by the off-resonant laser beam corresponds to the electronically excited state in the Dicke state. It is important to notice that we are not referring to the fraction of atoms in electronically excited state in the dressed condensate. The dressed condensate can decay by spontaneous emission to a state with photon recoil, corresponding to the ground state. The rate of superradiant emission in Dicke’s treatment is proportional to the square of an oscillating macroscopic dipole moment. In the present case, the radiated intensity is

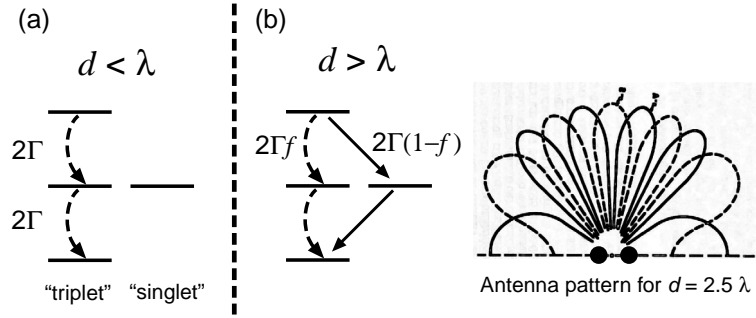


Figure 4-3: Dicke Superradiance from two atoms in excited states, separated by distances smaller or larger than the wavelength of radiation. If the two atoms are spaced closer than the wavelength (a), the two dipoles oscillates *in phase* after the first photon emission and thus couples strongly to the radiation field. If two atoms are separated by more than the wavelength (b), the dipoles can acquire either *in phase* (probability  $f$ ) or *out of phase* (probability  $1-f$ ) oscillation as a result of the first photon emission, and this phase difference affects the direction of the second photon emission. In case of two atoms separated by  $d = 2.5\lambda$ , if the first photon is emitted into one of the nodes of the dotted line (the radiation pattern from two dipoles in phase), it indicates out of phase oscillation of the dipoles, and the probability distribution of the second photon emission is given by the solid line (the radiation pattern from two dipoles oscillating out of phase).

proportional to the matter wave interference pattern between the condensate and recoiling atoms.

### 4.3 *In-situ* monitoring of matter wave gratings

The directional scattering of light was verified by directing the light onto a CCD camera that was positioned out of focus of the imaging system, and observing the angular distribution of photons emitted around the axial direction (Fig. 4-5a). The images consisted of bright spots with angular widths equal to the diffraction limit for a source with a diameter of  $\sim 14\mu\text{m}$ . Typical images showed more than one such spot, and their pattern changed randomly under the same experimental condition. This large run to run variation arises from the amplification of initial quantum fluctuations as verified by detailed numerical simulations in Ref. [127].

By replacing the camera with a photomultiplier, a time-resolved measurement of the scattered light intensity was obtained (Fig. 4-5b). Simple Rayleigh scattering would give a constant signal during the square-shaped incident pulse. Instead, we observed a fast rise and a subsequent decay consistent with a stimulated process.

Measurement at variable laser intensities showed a threshold for the onset of superradiance and a shorter rise time for higher laser intensities. This behavior can be accounted for by introducing a loss term  $\Gamma_2$ :

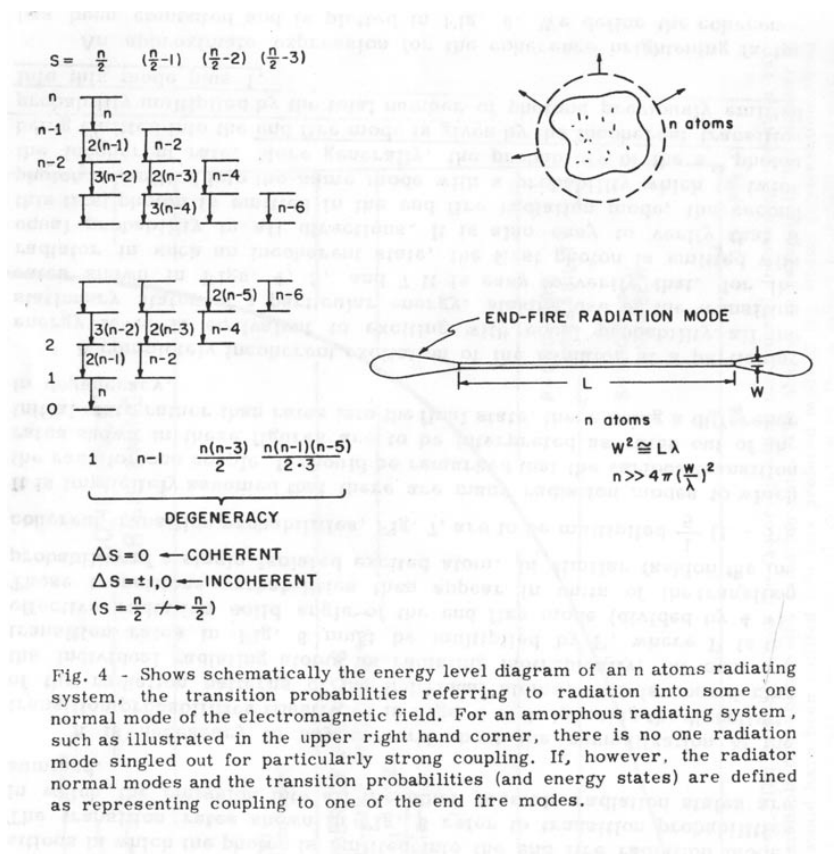


Figure 4-4: Dicke superradiance from an extended sample. For a spherical cloud of atoms, there is no special mode of radiation and superradiance happens in an omni-directional manner. For a pencil-shaped cloud, strong coupling between the dipoles in the cloud and the “end-fire” mode results in enhanced (superradiant) emission of light in the axial direction. Figure taken from Ref. [125]

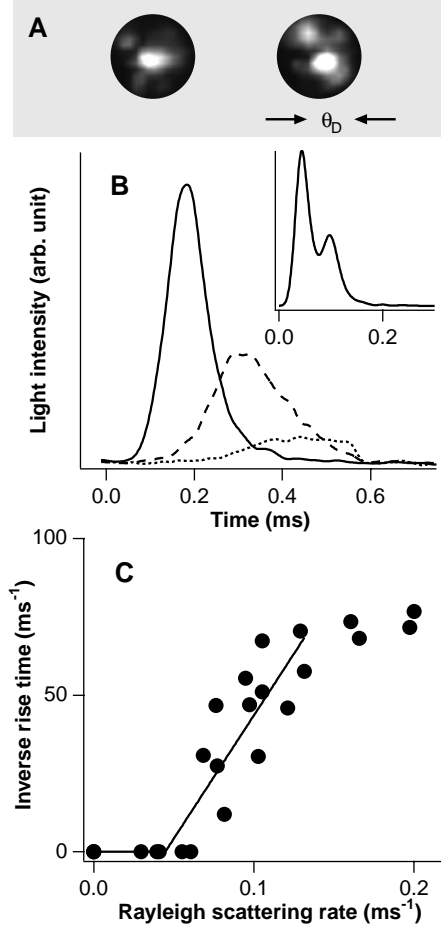


Figure 4-5: Observation of directional emission of light. (A) The angular pattern of the emitted light along the axial direction showed a few bright spots with an angular width  $\theta_D$  ( $1/e^2$  diameter) of  $107 \pm 20$  mrad, corresponding to the diffraction limited angle of an object of  $\sim 14 \mu\text{m}$  in diameter. The images were integrated over the entire duration of the light pulse. (B) The temporal evolution of the light intensity showed a strong initial increase characteristic of a stimulated process. For higher laser power, the pulse was shorter and more intense. The laser intensities were 3.8 (solid line), 2.4 (dashed line), and 1.4  $\text{mW}/\text{cm}^2$  (dotted line), and the duration was  $550 \mu\text{s}$ . The inset shows a double-peak in the temporal signal when the laser intensity was about  $15 \text{mW}/\text{cm}^2$ , which was above the threshold for sequential superradiant scattering. The photomultiplier recorded the light over an angle of 200 mrad around the axial direction. (C) The dependence of the inverse initial rise time on the Rayleigh scattering rate shows a threshold for the stimulated process. The solid curve is a straight-line fit. Figure taken from Ref. [18].

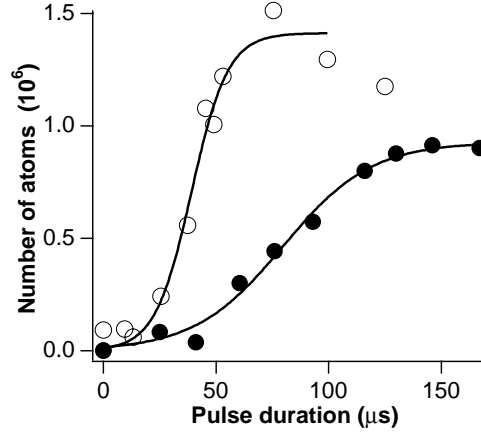


Figure 4-6: “Matter wave amplification out of noise.” Shown is the number of atoms in one of the superradiant peaks vs. duration of the laser pulse. An intense atomic pulse was formed by amplification of spontaneous scattering. The initial number of atoms in the condensate at rest was  $2 \times 10^7$ , and the laser intensities were about 25 (filled circles) and  $45 \text{ mW/cm}^2$  (open circles). The solid lines are guides to the eye. Figure taken from Ref. [18].

$$\dot{N}_j = (G_j - \Gamma_2)N_j \quad (4.2)$$

where  $G_j = RN_0 \sin^2 \theta_j \Omega_j' / (8\pi/3)$  is the gain coefficient. We determined the exponential rate  $(G_j - \Gamma_2)$  by fitting the initial rise in the light intensity. The inverse rise time  $\dot{N}_j/N_j$  versus the Rayleigh scattering rate  $R$  is shown in Fig. 4-5c. The slope gives  $G_j/R$ , and the offset determines the loss  $\Gamma_2$ . The agreement between the calculated value for  $G_j/R \sim 890$  and the result of the simple linear fit (790) is better than the uncertainty in the Rayleigh scattering rate (40%).

The offset in Fig. 4-5c determines the threshold for superradiance and yields  $1/\Gamma_2 = 35 \mu\text{s}$ . This decoherence rate of the matter wave grating was measured in Chapter 3 as a Bragg resonance width. The observed FWHM of about 5 kHz yields a decoherence rate of  $32 \mu\text{s}$ , in good agreement with the value shown above\*.

The rise of the number of atoms in the superradiant peak (Fig. 4-6) can be regarded as matter wave amplification seeded by quantum fluctuations. The input-output characteristic and phase-coherence of this process was studied in the next section.

Dicke superradiance is based on the coherence of the emitting system, but it does not require quantum degeneracy. The necessity of the bosonic nature of the atoms, or the possibility of using fermionic atoms to observe superradiant Rayleigh scattering and other matter wave amplification phenomena is discussed in detail in Chapter 7. Here, I only

---

\*There, the recoil atoms propagated perpendicular to the long axis of the condensate. The “finite-size” contribution to the line broadening was therefore twice that of the present geometry

point out that although quantum degeneracy is not needed for observing these phenomena, it affects the threshold for amplification in a major manner. The condition for superradiance is that the gain exceed the losses or that the superradiant decay time is shorter than any decoherence time. Above the BEC transition temperature, thermal Doppler broadening results in a 30 times shorter decoherence time than for a condensate. Furthermore, the larger size of the thermal cloud reduces the solid angle  $\Omega'_j$  and therefore the gain by factor of 10. Thus, the threshold for superradiance in a thermal cloud is several orders of magnitude higher than for a condensate. No signs of superradiant scattering were observed above  $T_c$ ; rather, the sudden appearance of superradiant emission was a sensitive indicator for reaching the phase transition.

It is often emphasized that “spontaneous” phenomena are truly quantum mechanical and different from “coherent” phenomena, which can be explained by classical physics. The study of superradiance shows that this boundary is somewhat arbitrary. On the one hand, superradiance is collectively enhanced *spontaneous* emission. The build up of the matter wave grating corresponds to the enhancement of correlation (or increased fluctuations), which causes the enhancement of the spontaneous scattering. (There is no grating like structure in the expectation value of the density profile.) However, as it was shown at the beginning of this chapter, a classical interpretation of this enhancement is possible if we introduce the notion of quantum fluctuation, which triggers the buildup of a macroscopic matter wave grating. Once the grating is there, the grating evolves “coherently” without help from the “spontaneous” nature of scattering. This interesting aspect of correlation functions in quantum mechanics will show up again in Chapter 7, where we discuss the role of quantum statistics.

## Chapter 5

# Matter wave amplification using a dressed Bose-Einstein condensate

*This chapter focuses on the experiment reported in the following publication:*

- *S. Inouye, T. Pfau, S. Gupta, A.P. Chikkatur, A. Görlitz, D.E. Pritchard, and W. Ketterle, “Phase-coherent amplification of atomic matter waves,” Nature, **402**, 641 (1999). Included in Appendix E.*

### 5.1 “Seeding” the superradiance

Although coherent atomic beams have been produced, matter wave amplification has not been directly observed prior to our work. Several schemes had been proposed in the past from the viewpoint of realizing matter wave analog of optical lasers [128, 129, 130, 131]. However, due to severe requirements for experimental conditions, none of them had been realized.

Matter wave amplification differs from light amplification in one important aspect. Since the total number of atoms is conserved (in contrast to photons), the active medium of a matter wave amplifier has to include a reservoir of atoms. One also needs a coupling mechanism which transfers atoms from the reservoir to the input mode while conserving energy and momentum. Amplification is realized if the transfer mechanism is accelerated by the build-up of atoms in the final state and irreversibility of the process is ensured by some form of dissipation.

In the last chapter, we studied how spontaneous Rayleigh scattering from a condensate leads to the buildup of directional matter waves. As it was pointed out towards the end of the last chapter, this buildup can be regarded as matter wave amplification (!) seeded by the initial spontaneous scattering. The active medium is a Bose-Einstein condensate dressed by an off-resonant laser beam. The momentum required to transfer atoms from the condensate at rest to the input mode was provided by light scattering. It amplifies input

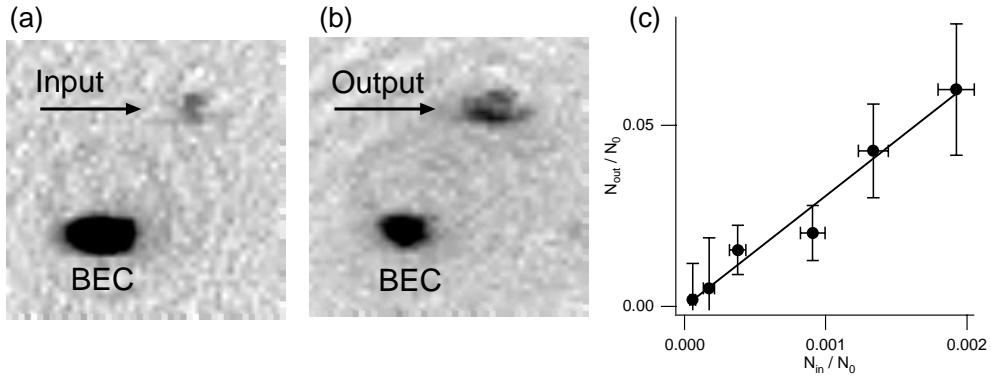


Figure 5-1: Input-output characteristics of the matter wave amplifier. (a,b) Typical time-of-flight absorption images demonstrating matter wave amplification. The number of atoms after amplification pulse (upper right spot in (b)) is clearly larger than what was seeded to the amplifier (a), showing gain for matter waves. No recoiling atoms are discernible in the case of amplification without the input. The size of the images is  $2.2 \text{ mm} \times 2.2 \text{ mm}$ . (c) Output of the amplifier as a function of the number of atoms at the input. A straight-line fit shows a number gain of 30.

matter waves within the momentum range which can be reached by scattering a photon from the dressing beam. The process is irreversible since the scattered photon quickly leaves the dressed condensate. This amplification process can be observed more directly by providing a variable input and measuring the amplitude and phase of the output matter wave.

Input matter waves with a well defined momentum were generated by exposing the condensate to a pulsed optical standing wave which transferred a small fraction of the atoms into a recoil mode by Bragg diffraction [17, 116]. The geometry of the light beams is shown in Fig. 5-2, and the intensity of the beams were kept below the threshold for superradiance. Amplification of the input matter wave was realized by applying an intense pump pulse along the direction of the radial Bragg beam for the next  $20 \mu\text{s}$  with a typical intensity of  $40 \text{ mW}/\text{cm}^2$ . The number of atoms in the recoil mode was determined by suddenly switching off the trap and observing the ballistically expanding using resonant absorption imaging.

Fig. 5-1 shows the input-output characteristics of the amplifier. The number of output atoms is an order of magnitude larger than the number of input atoms, clearly demonstrating the amplification of matter waves. The gain can be controlled by the intensity of the pump pulse (see Eq. 4.1) and typically varied between 10 and 100. Fig. 5-1c shows the observed linear relationship between the atom numbers in the input and the amplified output with a number gain of 30.

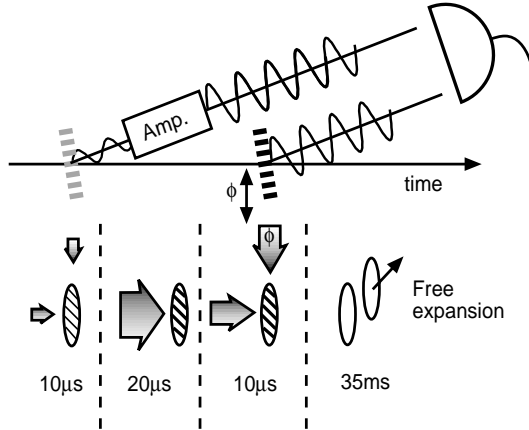


Figure 5-2: Experimental scheme for observing phase coherent matter wave amplification. A small-amplitude matter wave was split off the condensate by applying a pulse of two off-resonant laser beams (Bragg pulse). This input matter wave was amplified by passing it through the condensate pumped by a laser beam. The coherence of the amplified wave was verified by observing its interference with a reference matter wave, which was produced by applying a second (reference) Bragg pulse to the condensate. The interference signal was observed after 35 ms of ballistic expansion. Note that the polarization of the radial beam was perpendicular to the long axis of the condensate ( $\theta = \pi/2$ ). Extinction of the axial beam during the amplifying pulse was better than  $10^{-8}$ . Figure taken from Ref. [19] .

## 5.2 Phase of the amplified matter wave

The phase of the amplified matter wave was determined by an interferometric technique (Fig. 5-2). For this, a reference matter wave was split off the condensate in the trap in the same manner as the first (input) wave. The phase of the reference matter wave was scanned by shifting the phase of the rf signal that drove the acousto-optic modulator generating the axial Bragg beam. We then observed the interference between the reference and the amplified matter waves by measuring the number of atoms in the recoil mode.

Fig. 5-3 shows the interference signal between the amplified input and the reference matter wave as the reference phase was scanned. When the input was comparable in intensity to the reference matter wave, high contrast fringes were observed even without amplification (Fig. 5-3a). Fringes were barely visible, when the input was about 40 times weaker in population (Fig. 5-3b). After amplification, we regained a large visibility(Fig. 5-3c). This increase in visibility proves the coherent nature of the matter wave amplification process.

The visibility was studied as a function of the number of atoms in the recoil mode. If we characterize the two interfering matter waves by their atom numbers  $N_i$  and normalized wavefunctions  $\psi_i$ , then the visibility  $V$  of the interference pattern is given by

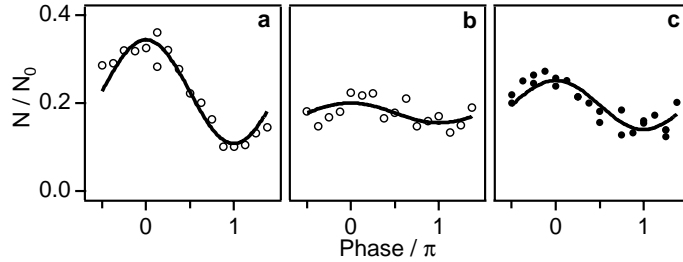


Figure 5-3: Phase coherent amplification of matter waves. Shown is the number of atoms  $N$  in the recoil mode versus the relative phase between the two Bragg pulses. (a) Interference between two matter waves of almost equal intensity yielded a high contrast fringe (visibility  $V = 52\%$ ). (b) When the intensity of the first matter wave was decreased by a factor of 40, the visibility  $V$  dropped to the noise level ( $< 15\%$ ). (c) By switching on the amplifier, a large visibility was regained ( $V = 31\%$ ). Figure taken from Ref. [19].

$$V = \frac{2 \langle \psi_1 | \psi_2 \rangle \sqrt{N_1 N_2}}{N_1 + N_2} \quad (5.1)$$

$$\sim 2 \langle \psi_1 | \psi_2 \rangle \sqrt{N_1 / N_2} \quad (N_1 \ll N_2) \quad (5.2)$$

Without amplification, the observed visibility was in good agreement with Eq. 5.2, assuming  $\langle \psi_1 | \psi_2 \rangle \sim 1$  for the overlap factor. With amplification, the visibility increased by a factor of about two over a wide range of input matter wave intensities under the same conditions which gave a number gain of 30 (Fig. 5-1). Since the visibility increases as  $\sqrt{N_1}$  (Eq. 5.2), this implies a “coherent matter wave gain” of at least four. The discrepancy with the number gain of 30 may be due to a distortion of the input matter wave during amplification which would reduce the overlap factor  $\langle \psi_1 | \psi_2 \rangle$ . Indeed, the shape of the amplified matter wave looked distorted after the 35 ms of time-of-flight. This indicates a wavefront distortion of the amplified matter wave which can be parameterized by introducing an overlap factor of  $\sqrt{4/30} = 0.4$  in Eq. 5.2.

This experiment can also be regarded as a demonstration of an active atom interferometer. It realizes a two-pulse atom interferometer [132] with phase-coherent amplification in one of the arms. Such active interferometers may be advantageous for precise measurements of phase shifts in highly absorptive media, e.g., for measurements of the index of (matter wave) refraction when a condensate passes through a gas of atoms or molecules [133]. Since the most accurate optical gyroscopes involve active interferometers [134], atom amplification might also play a role in future matter-wave gyroscopes [135].

## Chapter 6

# Optical properties of a dressed Bose-Einstein condensate

The following section is a chapter of the following review paper.

- Wolfgang Ketterle and Shin Inouye, “Collective enhancement and suppression in Bose-Einstein condensates.” *Special issue of Comptes rendus de l’académie des sciences, Série IV - Physique Astrophysique, in print; e-print cond- mat/010142429*

This chapter was my responsibility. It describes the optical properties of a dressed Bose-Einstein condensate that was first reported in the following publication:

- S. Inouye, R. F. Löw, S. Gupta, T. Pfau, A. Görlitz, T.L. Gustavson, D.E. Pritchard, and W. Ketterle, “Amplification of Light and Atoms in a Bose-Einstein Condensate,” *Phys. Rev. Lett.* **85**, 4225 (2000). Included in Appendix F.

### 6.1 Four-wave mixing of light and atoms

When a condensate scatters a photon, the scattering is described by the Hamiltonian

$$\mathcal{H}' = C \sum_{k,l,m,n} \hat{b}_l^\dagger \hat{a}_n^\dagger \hat{b}_k \hat{a}_m \delta_{l+n-k-m}. \quad (6.1)$$

Here  $\hat{b}_k$  ( $\hat{b}_k^\dagger$ ) is the destruction (creation) operator for photons, and  $\hat{a}_k$  ( $\hat{a}_k^\dagger$ ) is the destruction (creation) operator for atomic plane waves of wavevector  $\mathbf{k}$ . The strength of the coupling is parametrized by the coefficient  $C$  (which in general may depend on the momentum transfer), and the  $\delta$  function guarantees momentum conservation (with an uncertainty of  $\hbar/D$ , where  $D$  is the dimension of the condensate). The coupling can be regarded as four-wave mixing of two atomic fields and two electromagnetic fields.

When an atom is illuminated by two strong laser beams in a  $\Lambda$  configuration similar to Fig. 6-1b, the electronically excited state can be adiabatically eliminated for sufficiently

large detuning  $\Delta$ . The coupling matrix element between the two atomic ground states is  $\hbar\Omega_R/2$ , where  $\Omega_R$  is the two-photon Rabi frequency. This Rabi frequency can be expressed by the (complex) electric field strength  $\mathcal{E}_{1,2}$  of the two laser beams:  $\Omega_R = \Omega_1\Omega_2 \cos \phi/2\Delta$ , where  $\Omega_{1,2} = \mathcal{E}_{1,2}d/\hbar$  are the Rabi frequencies of the individual laser beams with the atomic dipole matrix element  $d$ .  $\phi$  is the angle between the axes of polarization of the two laser beams. The two-photon Rabi frequency  $\Omega_R$  can be rewritten as

$$\Omega_R = d^2\mathcal{E}_1\mathcal{E}_2 \cos \phi/2\hbar^2\Delta. \quad (6.2)$$

Using the Hamiltonian in Eq. 6.1, the coupling matrix element squared is  $|C|^2n_1n_2$  where  $n_{1,2}$  are the photon numbers in the two beams. The two-photon Rabi frequency  $\Omega_R$  is given by

$$(\hbar\Omega_R/2)^2 = |C|^2n_1n_2. \quad (6.3)$$

Expressing the number  $n_1$  of photons with angular frequency  $\omega_0$  in a volume  $V$  by the complex electric field strength  $E_1$

$$n_1 = \epsilon_0|\mathcal{E}_1|^2V/2\hbar\omega_0, \quad (6.4)$$

and comparing to Eq. 6.2 we obtain for the coupling constant  $C$  between the two modes

$$C = \frac{\omega_0d^2 \cos \phi}{2\epsilon_0V\Delta}. \quad (6.5)$$

Another simple limit of the Hamiltonian in Eq. 6.1 is the situation when atoms are illuminated by a single laser beam in mode 1. Then the diagonal term  $C\hat{b}_1^\dagger\hat{a}_0^\dagger\hat{b}_1\hat{a}_0$  gives rise to the AC Stark shift. With the photon number  $n_1$ , the AC Stark shift  $\Delta E$  of an atom is  $\Delta E = Cn_1$ . Using Eqs. 6.4 and 6.5 with  $\cos \phi = 1$  one obtains the well known result,  $\Delta E = d^2\mathcal{E}_1^2/4\hbar\Delta$ .

The four-wave mixing Hamiltonian (Eq. 6.1) applies to interactions of a condensate both with light and atoms. By introducing proper ‘‘C’’ for atom-atom interaction, we can draw analogies. The AC Stark shift corresponds to the mean field interaction between impurity atoms and the condensate. The scattering of atoms into empty modes by the four-wave mixing between the atoms gave rise to the usual elastic collision rate. Similarly, the scattering of photons into empty modes by the four-wave mixing between light and atoms results in Rayleigh scattering which we want to discuss now in more detail.

Rayleigh scattering rate  $R$  can be obtained from Fermi’s Golden Rule:

$$R = \frac{2\pi}{\hbar}|C|^2n_1\delta(E_k - E_{k-q} - \hbar\omega_q^0). \quad (6.6)$$

The scattering rate per solid angle  $d\gamma_{\text{scatt}}/d\Omega'$  is given by integrating this equation over all

final states using the density of states per energy interval and solid angle

$$\frac{d\rho_E}{dE d\Omega'} = \frac{V\omega_0^2}{(2\pi c)^3 \hbar}. \quad (6.7)$$

Using Eqs. 6.4, 6.5 one obtains

$$\frac{d\gamma_{\text{scatt}}}{d\Omega'} = \frac{2\pi}{\hbar} |C|^2 n_1 \frac{d\rho_E}{dE d\Omega'} = \frac{\omega_0^3 E_1^2 d^4 \cos^2 \phi}{32\pi^2 \hbar^3 c^3 \epsilon_0 \Delta^2}. \quad (6.8)$$

With the expression for the natural linewidth  $\Gamma$

$$\Gamma = \frac{d^2 \omega_0^3}{3\pi \epsilon_0 \hbar c^3}, \quad (6.9)$$

this simplifies to

$$\frac{d\gamma_{\text{scatt}}}{d\Omega'} = \frac{3 \cos^2 \phi}{8\pi} \frac{\Omega_1^2}{4\Delta^2} \Gamma = \frac{3 \sin^2 \theta}{8\pi} R, \quad (6.10)$$

where we have defined the Rayleigh rate  $R$

$$R = \frac{\Omega_1^2}{4\Delta^2} \Gamma. \quad (6.11)$$

$\theta$  denotes the angle between the linear polarization of the incident light and the direction of the scattered light. For each scattering angle  $\theta$  there are two polarizations of the scattered light. One is orthogonal to the incident polarization, thus  $\cos \phi = 0$  in Eq. 6.5, and it doesn't contribute. The density of states in Eq. 6.7 was therefore defined for only one polarization. The other polarization is in the plane of the incident polarization and the scattering direction, thus  $\cos \phi = \sin \theta$ .  $R$  was defined in Eq. 6.11 in such a way that integration of Eq. 6.10 over the whole solid angle gives  $\gamma_{\text{scatt}} = R$ .

Below, we will need another useful expression for the two-photon Rabi frequency  $\Omega_R$ . We use Eq. 6.3, assume that one laser beam is a weak probe beam with photon number  $n_p$ , express the photon number of the other (strong) beam by its Rayleigh scattering rate and obtain

$$\Omega_R^2 = 6\pi R \lambda^2 c n_p / V. \quad (6.12)$$

Generally, the optical (or atomic) gratings are moving. As a result, the diffracted atoms (or photons) have an energy different from that of the incident particles. However, one can always transform to a moving frame where the grating is stationary and there is no energy transfer in the scattering process. The frequency shift due to the moving grating can therefore be regarded as the Doppler shift related to the Galilean transformation between the two frames.

## 6.2 Amplification of light in a dressed condensate

A dressed condensate (Fig. 6-1), a condensate illuminated by laser light, was used as an atom amplifier. Now we develop this picture further. Rayleigh scattering produces scattered photons and recoiling atoms. In the dressed atom picture, this is described as the decay of the dressed condensate into a photon and recoiling atom, or in other words, the dressed condensate can spontaneously emit pairs of photons and atoms. The amplification of atoms discussed in the previous sections solely focuses on the recoiling atoms “emitted” by the dressed condensate. Although recoiling atoms and scattered photons are emitted in pairs, the photons leave the condensate almost instantaneously and there is no significant population build-up. Formally, one can adiabatically eliminate the light field from coupled equations and obtain the gain equation for the matter waves.

On the other hand, the dressed condensate should act also as an amplifier for light. An input optical field should stimulate Rayleigh scattering processes which results in photons scattered into the input mode. Our recent experiments on optical amplification in a BEC [20] required a more general description of the interplay between optical and matter wave amplification.

On the following pages, we present a general discussion of four-wave mixing of light and atoms. We first start simply with the gain cross-section for the light and a complex index of refraction. The recoiling atoms enter the picture in two stages, first within the framework of Heisenberg equations in the undepleted-pump approximation, and then using optical Bloch equations.

## 6.3 Cross-section for optical gain and slow light

The physical picture behind the optical gain of the dressed condensate is as follows: if a very weak probe beam is injected into the dressed condensate, it acts together with the dressing beam as a pair of Bragg beams and creates recoiling atoms. This process transfers photons from the dressing beam into the probe beam. At higher gain, the recoiling atoms become significant. They move out of the condensate (or decohere) on a time scale  $\Gamma_2^{-1}$  which is the inverse of the linewidth of the Bragg transition. In steady state, the number of recoiling atoms  $N_q$  in the volume of the condensate is proportional to the intensity of the probe light. Those recoiling atoms interfere with the condensate at rest and form a diffraction grating which diffracts the dressing beam into the path of the probe light resulting in amplification of the probe light (Fig. 6-1).

An expression for the gain can be derived in analogy to a fully inverted two-level system with dipole coupling which would have a gain cross-section of  $6\pi\lambda^2$  for radiation with wavelength  $\lambda(= 2\pi\lambda)$ . For the Raman-type system in Fig. 6-1b, the gain is reduced by the excited state fraction,  $R/\Gamma$  (where  $R$  is the Rayleigh scattering rate for the dressing beam and  $\Gamma$  is the linewidth of the single-photon atomic resonance) and increased by  $\Gamma/\Gamma_2$ , the

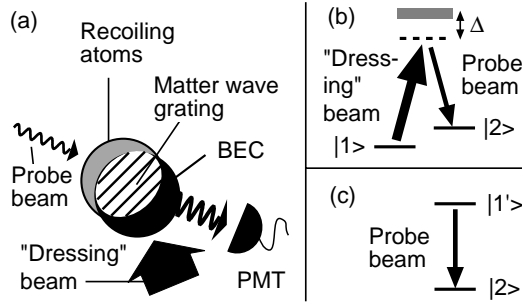


Figure 6-1: Amplification of light and atoms by off-resonant light scattering. (a) The fundamental process is the absorption of a photon from the “dressing” beam by an atom in the condensate (state  $|1\rangle$ ), which is transferred to a recoil state (state  $|2\rangle$ ) by emitting a photon into the probe field. The intensity in the probe light field was monitored by a photomultiplier. (b) The two-photon Raman-type transition between two motional states ( $|1\rangle, |2\rangle$ ) gives rise to a narrow resonance. (c) The dressed condensate is the upper state ( $|1'\rangle$ ) of a two-level system, and decays to the lower state (recoil state of atoms,  $|2\rangle$ ) by emitting a photon. Figure is taken from Ref. [20]

ratio of the linewidths of the single-photon and two-photon Bragg resonances. Thus the expected cross-section for gain is

$$\sigma_{\text{gain}} = 6\pi\lambda^2 \frac{R}{\Gamma_2}. \quad (6.13)$$

The lineshape of the optical gain is that of the two-photon Bragg resonance. Due to the long coherence time of a condensate, it has a very narrow linewidth. Such a narrow band gain is accompanied by a slow group velocity of light. This can be described by a complex index of refraction  $n(\omega) = n_1(\omega) + in_2(\omega)$ .

For a Lorentzian resonance curve with FWHM of  $\Gamma_2$  for the gain, the complex index of refraction is

$$n(\omega) = n_\infty + \frac{g'}{\delta + i} = n_\infty + \frac{g'\delta}{1 + \delta^2} - \frac{g'i}{1 + \delta^2} \quad (6.14)$$

where  $n_\infty$  is the background index of refraction,  $g'$  denotes the strength of the resonance, and  $\delta = (\omega - \omega_0)/(\Gamma_2/2)$  is the normalized detuning from the resonance at  $\omega_0$ . The imaginary part of Eq. 6.14 has the usual Lorentzian lineshape.

The real and imaginary parts of the index of refraction are connected by Kramers-Kronig relations. For the special case above of a Lorentzian lineshape the gain and dispersion at resonance are connected by

$$\left. \frac{dn_1}{d\omega} \right|_{\omega=\omega_0} = -\frac{2}{\Gamma_2} n_2 \Big|_{\omega=\omega_0}. \quad (6.15)$$

A steep slope of the (real part of) the index of refraction gives rise to a slow group velocity of light

$$v_g = \frac{c}{\omega(dn_1/d\omega) + n_1}. \quad (6.16)$$

Eqs. 6.15 and 6.16 imply a simple relationship between the gain and delay time for an optical pulse. The amplitude of an optical pulse at frequency  $\omega_0$  which propagates through a medium with the index of refraction  $n$  of length  $l$  is amplified by a factor

$$g = \exp(-n_2\omega_0 l/c). \quad (6.17)$$

When the first term in the denominator of Eq. 6.16 is dominant, the delay time  $\tau_D$  of the pulse is

$$\tau_D = \frac{l}{v_g} \approx l \frac{\omega_0}{c} \frac{dn_1}{d\omega} = \frac{2 \ln g}{\Gamma_2}. \quad (6.18)$$

This equation provides a simple relationship between a narrow band gain and pulse delay [136]. A non-inverted absorptive two-level system gives rise to “superluminal” pulse propagation [137].

For the experimental study of the optical gain, a condensate was illuminated (“dressed”) with a single off-resonant laser beam and probed with another laser beam, which was red-detuned by 91 kHz to satisfy the Bragg resonance condition. Both the dressing beam and the probe beam were in the plane perpendicular to the long axis of the condensate, and intersected at an angle of 135 degrees. The probe beam, which propagated parallel to the axis of imaging, was much larger than the condensate size. In order to block all the light that did not pass through the condensate, a slit was placed at an intermediate imaging plane. The light transmitted by the slit was recorded with a photomultiplier. The polarization of each beam was set parallel to the long axis of the condensate to suppress superradiance to other recoil modes [18].

Fig. 6-2 shows that light pulses were delayed by about  $20 \mu\text{s}$  across the  $20 \mu\text{m}$  wide condensate corresponding to a group velocity of 1 m/s. This was one order of magnitude slower than any value reported at the time of our first publication (See Ref. [138] and references therein. See Refs. [139, 140] for progresses after our report). Fig. 6-2b presents the experimental verification of the relationship between gain and delay time (Eq. 6.18).

## 6.4 Relation between optical gain and atomic gain

Both the optical gain  $g$  (Eqs. 6.13 and 6.17) and the matter wave gain  $G$  (Eq. 4.2) have the same origin, stimulated Rayleigh scattering. Therefore, the two gain coefficients should be related. The expression for  $G$  (Eq. 4.2) involves a solid angle factor  $\Omega'_q$  which is proportional to  $\lambda^2/A$ . To be consistent with the optical Bloch equation (to be discussed below) we use now  $2\lambda^2/A$  for  $\Omega'_q$  and obtain

$$G = \frac{RN_0}{A} \frac{3}{4\pi} \lambda^2 = (\rho_0 l \sigma_{\text{gain}}/2) \Gamma_2. \quad (6.19)$$

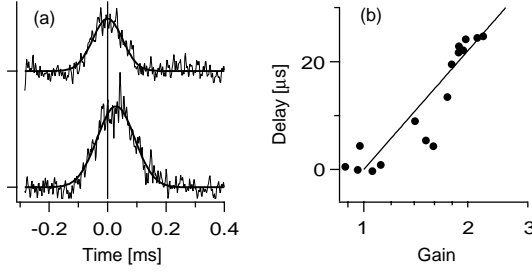


Figure 6-2: Pulse delay due to light amplification. (a) About  $20 \mu\text{s}$  delay was observed when a Gaussian pulse of about  $140 \mu\text{s}$  width and  $0.11 \text{ mW}/\text{cm}^2$  peak intensity was sent through the dressed condensate (bottom trace). The top trace is a reference taken without the dressed condensate. Solid curves are Gaussian fits to guide the eyes. (b) The observed delay was proportional to the logarithm of the observed gain. Figure is taken from Ref. [20].

The gain  $g$  for the amplitude of the optical field is

$$g = \exp(\rho_0 l \sigma_{\text{gain}}/2) = \exp(G/\Gamma_2) \approx 1 + \frac{G}{\Gamma_2} \quad (6.20)$$

with the last equation being an approximation for small gain. However, Eq. 6.20 cannot be universally valid. When the gain  $G$  is above the threshold for superradiance,  $G > \Gamma_2$  (Eq. 4.2) the optical gain should diverge: a single recoiling atom created by the probe light and dressing light is exponentially amplified and creates a huge matter wave grating which will diffract the dressing light into the probe light path, thus amplifying the probe light by a divergent factor. Indeed, as we will derive below, Eq. 6.20 is only valid at small values of  $G/\Gamma_2$ .

If we can neglect the depletion of the dressed condensate and the dressing laser beam we can simplify the interaction Hamiltonian in Eq. 6.1 to

$$\mathcal{H}' = C'(\hat{a}^\dagger \hat{b}^\dagger + \hat{a} \hat{b}). \quad (6.21)$$

Here,  $\hat{a}(\hat{b})$  indicates the atomic (light) field to be amplified, but the following derivation is completely symmetric between the two fields. This Hamiltonian is a standard down-conversion Hamiltonian. Here it describes the down-conversion of the dressed condensate into photons and recoiling atoms. Considering only two modes neglects propagation effects in the amplification. The coefficient  $C'$  defines the time constant of the amplification and is proportional to the amplitude of the dressing beam and the square root of the number of atoms in the condensate. The Heisenberg equations of motions are

$$i\dot{\hat{a}} = [\hat{a}, \mathcal{H}'] = C'\hat{b}^\dagger, \quad (6.22)$$

$$i\dot{\hat{b}}^\dagger = [\hat{b}^\dagger, \mathcal{H}'] = -C'\hat{a}. \quad (6.23)$$

This leads to exponential growth of  $\hat{a}$  and  $\hat{b}$  (proportional to  $\exp(C't)$ ). However, to describe the physical situation in the experiments, one has to allow for damping by introducing  $\Gamma_a(\Gamma_b)$  as phenomenological damping time constants for  $\hat{a}(\hat{b})$ . We also include source terms (input fields) and approximate the operators by  $c$  numbers:

$$\begin{aligned}\dot{a} &= -\frac{\Gamma_a}{2}(a - a_0) - iC'b^*, \\ \dot{b}^* &= iC'a - \frac{\Gamma_b}{2}(b^* - b_0^*).\end{aligned}\tag{6.24}$$

The solutions show relaxation ( $C'^2 \leq \Gamma_a\Gamma_b/4$ ) or exponential growth ( $C'^2 \geq \Gamma_a\Gamma_b/4$ ) depending on the strength of the coupling relative to the damping rates. The “gain” below the threshold can be defined as  $a(t \rightarrow \infty)/a_0$  for atoms (assuming  $b_0 = 0$ ) and as  $b(t \rightarrow \infty)/b_0$  for light (assuming  $a_0 = 0$ ), yielding

$$g = \frac{a(t \rightarrow \infty)}{a_0} = \frac{b(t \rightarrow \infty)}{b_0} = \frac{\Gamma_a\Gamma_b/4}{(\Gamma_a\Gamma_b/4) - C'^2}.\tag{6.25}$$

The fact that the two gain coefficients are equal is a general property of parametric amplification where two kinds of particles are produced in pairs.

In the limiting case that one field is strongly damped (e.g. that light quickly escapes from the system,  $\Gamma_b \gg \Gamma_a$ ), one can adiabatically eliminate this field from the coupled equation (assuming no photon input ( $b_0^* = 0$ ))

$$b^* = \frac{2iC'}{\Gamma_b}a\tag{6.26}$$

and obtain a single gain equation for  $a$ . The gain equation for the atom field is

$$\dot{a} = -\frac{\Gamma_a}{2}(a - a_0) + \frac{2C'^2}{\Gamma_b}a.\tag{6.27}$$

In the absence of damping, the atom number would increase exponentially with a rate constant  $4C'^2/\Gamma_b$  which we therefore identify with the atom gain rate coefficient  $G$  in Eq. 6.19. This can be shown explicitly using  $C'^2 = |C|^2 N_0 n_k / \hbar^2$  and setting the mode volume  $V = AL$ , where  $A$  is the cross section of the condensate. The axial length  $L$  could be the condensate length  $l$ , but will cancel out. Eqs. 6.3 and 6.12 yield  $4C'^2/\Gamma_b = 2Gc/L\Gamma_b$  which equals  $G$  when we set the decay rate  $\Gamma_b/2$  equal to the photon transit time  $c/L$ . We can then rewrite the gain calculated above as

$$g = \frac{\Gamma_a}{\Gamma_a - 4C'^2/\Gamma_b} = \frac{\Gamma_a}{\Gamma_a - G}.\tag{6.28}$$

For the dressed condensate, we identify  $\Gamma_a$  with  $\Gamma_2$ . As expected, at the threshold to superradiance ( $G = \Gamma_2$ ), the (steady-state) gain for both light and matter waves diverges.

The gain can be rewritten as

$$g = \Gamma_2/(\Gamma_2 - G) = 1 + G/(\Gamma_2 - G). \quad (6.29)$$

In the low gain limit, this yields the same result as Eq. 6.20. The comparison with Eq. 6.20 shows that the effect of the coupled equations is to replace the two-photon linewidth  $\Gamma_2$  in Eq. 6.20 by the dynamic coherence decay rate  $\Gamma_2 - G$ . Since propagation effects have been excluded, we can't expect to obtain the exponential factor in Eq. 6.20, but rather the linearized form. The expansion

$$g = 1 + (G/\Gamma_2) + (G/\Gamma_2)^2 + \dots \quad (6.30)$$

describes the transition from (linear) single-atom gain to (nonlinear) collective gain.

## 6.5 Optical Bloch equations

The discussion in the previous two sections assumed that the condensate is undepleted—i.e., we calculated properties of a condensate with all the atoms in the initial dressed state. However, the presence of the dressing light and the probe light depletes the condensate. Furthermore, the calculated amplification coefficients are only valid in a quasi-steady state regime which is usually preceded by transient behavior. A correct interpretation of the experimental results required a more complete description of the dynamics of the system which will be developed in this section using optical Bloch equations.

We proceed in two steps. In the limit of weak optical gain (or strong probe laser intensity), we will use the ordinary optical Bloch equations where the laser fields are treated as constant. Later we will introduce an additional equation for the dynamics of the probe light. The condensate at rest ( $|1\rangle$ ) and the atoms in the recoil state ( $|2\rangle$ ) are treated as a two-level system coupled by the four-wave mixing Hamiltonian which gives rise to a two-photon Rabi frequency  $\Omega_R$  (Eq. 6.2). The coherence between those two states decays at a rate  $\Gamma_2/2$ . Assuming constant  $\Omega_R$ , the optical Bloch equations at resonance take the following simple form

$$\dot{v} = -\frac{\Gamma_2}{2}v - \Omega_R w \quad (6.31)$$

$$\dot{w} = \Omega_R v \quad (6.32)$$

where  $v = 2 \text{Im}(\rho_{12})$  represents the amplitude of the matter wave grating ( $\rho_{ij}$  is the atomic density matrix) and  $w = \rho_{22} - \rho_{11}$  is the population difference between the two states [141].

The eigenvalues of the matrix

$$\begin{pmatrix} -\Gamma_2/2 & -\Omega_R \\ \Omega_R & 0 \end{pmatrix} \quad (6.33)$$

are  $\lambda_{\pm} = -\Gamma_2/4 \pm \sqrt{(\Gamma_2/4)^2 - \Omega_R^2}$ . In the limits of large and small laser intensities one obtains

$$\lambda_{\pm} = \begin{cases} -\frac{\Gamma_2}{4} \pm i\Omega_R & \Gamma_2/4 \ll \Omega_R \\ -\frac{\Gamma_2}{2}, -\frac{2\Omega_R^2}{\Gamma_2} & \Gamma_2/4 \gg \Omega_R \end{cases}. \quad (6.34)$$

This means that at high intensities the system exhibits damped oscillations—Rabi oscillations between the two levels. At low intensities, there is relaxation in two steps: The coherence is damped with a rate of  $\Gamma_2/2$ , followed by depletion of atoms in the condensate, which happens at a rate of  $2\Omega_R^2/\Gamma_2$ . It is in this temporal window ( $2/\Gamma_2 < t < \Gamma_2/2\Omega_R^2$ ) that the perturbative treatment with the complex index of refraction applies. For longer times, the condensate becomes depleted and the assumption that most of the atoms are in the initial dressed state is no longer valid.

The optical Bloch equations can be analytically solved for a step function input. With the initial condition that at time  $t = 0$  all the atoms are in the condensate at rest ( $w(t = 0) = -1$ ,  $v(t = 0) = 0$ ) one obtains

$$v(t) = \begin{cases} \frac{\Omega_R}{\sqrt{\Omega_R^2 - (\Gamma_2/4)^2}} \exp(-\frac{\Gamma_2}{4}t) \sin\left(\sqrt{\Omega_R^2 - (\Gamma_2/4)^2}t\right) & \Omega_R \geq \frac{\Gamma_2}{4} \\ \frac{\Omega_R}{\sqrt{(\Gamma_2/4)^2 - \Omega_R^2}} \exp(-\frac{\Gamma_2}{4}t) \sinh\left(\sqrt{(\Gamma_2/4)^2 - \Omega_R^2}t\right) & \Omega_R \leq \frac{\Gamma_2}{4} \end{cases} \quad (6.35)$$

simplifying in the limit of small probe laser intensity ( $\Omega_R \ll \Gamma_2/4$ ) to

$$v(t) \approx \frac{2\Omega_R}{\Gamma_2} \left( -\exp(-\frac{\Gamma_2}{2}t) + \exp(-\frac{2\Omega_R^2}{\Gamma_2}t) \right) \quad (6.36)$$

$$= \frac{2\Omega_R}{\Gamma_2} \left( -\exp(-\frac{\Gamma_2}{2}t) + 1 \right) \quad t \ll \Gamma_2/\Omega_R^2. \quad (6.37)$$

By reducing the probe power, the Rabi oscillations slow down and become overdamped and a (quasi-)steady state gain is obtained. Inserting Eq. 6.36 into Eq. 6.32 one obtains the transition rate  $N_0\dot{w}/2 = N_0\Omega_R v/2$  which is the number of photons per unit time emitted by the dressed condensate. To obtain the gain one has to normalize by the input photon flux  $cn_p/l$  where  $n_p$  is the number of photons in the condensate. The amplitude gain is then (assuming small gain)

$$g = 1 + \frac{N_0\Omega_R l}{4cn_p} v. \quad (6.38)$$

Using the asymptotic behavior of Eq. 6.37 ( $v(t) \approx 2\Omega_R/\Gamma_2$ ), Eq. 6.12 for  $\Omega_R$  and Eq. 6.13 one obtains  $g = 1 + \rho_0\sigma_{\text{gain}}l/2$  which agrees with Eqs. 6.20 and 6.29 in the low-intensity limit. Eq. 6.38 thus has the correct asymptotic limit, but it also describes transient behavior when the general solution for  $v(t)$  (Eq. 6.35) is used. Theoretical traces based on Eq. 6.38 are directly compared to the experimental results in Fig. 6-3.

In the experiment, we used long square probe pulses for the probe light (Fig. 6-3). When the dressing beam was suddenly switched off, a sudden change in the observed probe

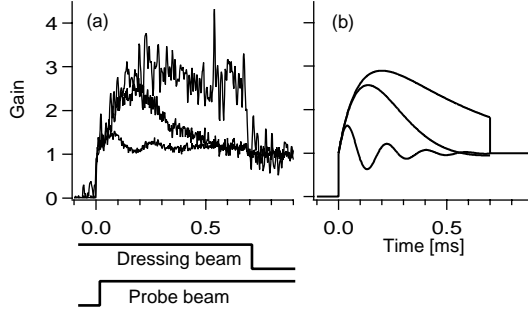


Figure 6-3: Gain and temporal behavior of light pulses propagating through a dressed condensate. (a) Observed probe pulse output from a dressed condensate. The probe light intensities were  $5.7 \text{ mW/cm}^2$  (bottom),  $1.5 \text{ mW/cm}^2$  (middle),  $0.10 \text{ mW/cm}^2$  (top), while the dressing beam intensity was  $5 \text{ mW/cm}^2$ , which was just below the threshold for super-radiance. The plotted signals were normalized by the incident probe intensity and show the gain for the probe light. (b) Calculated probe light output for typical experimental parameters. Rabi oscillations develop into steady state gain as the intensity of the probe light is reduced. Figure is taken from Ref. [20].

light intensity was evidence for optical gain. At the lowest probe intensity, the depletion of atoms in the condensate was negligible and a clear step at the switch off was observed, corresponding to a gain of  $\approx 2.8$ . The initial rise time of  $\approx 100 \mu\text{s}$  is the coherence time of the dressed condensate. At high probe laser power we observed Rabi oscillations in the transmitted probe light. Note that all the traces were normalized by the probe beam intensity, and the oscillatory trace at the bottom was obtained at the highest probe beam intensity. The oscillations reflect simple two-level Rabi oscillations of atoms between the two motional states driven by the two-photon Bragg coupling.

When the probe laser frequency was detuned from the two-photon resonance, the frequency of the Rabi oscillations increased (Fig. 6-4). Optical Bloch equations with detuning [141] predict oscillations at

$$\Omega_{\text{eff}} = \sqrt{\Omega_R^2 + \Delta\omega^2} \quad (6.39)$$

where  $\Delta\omega$  is the detuning, in agreement with observations.

For large optical gain, the Rabi frequency  $\Omega_R$  increases during the pulse and the above treatment is no longer valid. Therefore, we derive now a second equation which treats the Rabi frequency as a dynamic variable. The population transfer to the recoil state ( $\dot{w}$ ) results in an increase of the number of the probe beam photons inside the condensate volume

$$\dot{n}_p = c(n_p^0 - n_p)/l + N_0\dot{w}/2, \quad (6.40)$$

where  $l$  is the length of the condensate with  $N_0$  atoms and  $cn_p^0/l$  is the input photon flux. Without gain, the steady-state number of photons in the condensate volume would be  $n_p^0$ . Eq. 6.40 neglects propagation effects of the light by replacing the non-uniform electric field

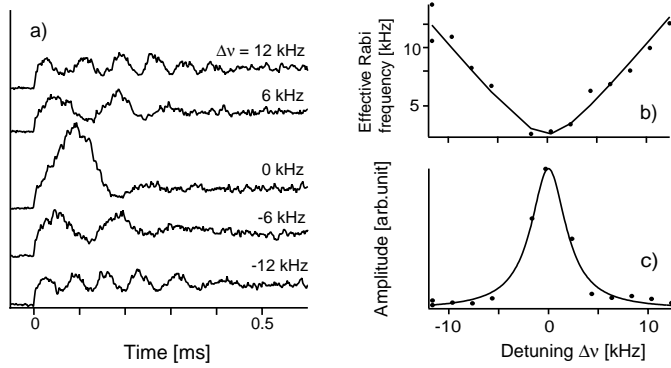


Figure 6-4: Rabi oscillations of atoms observed by monitoring the transmitted probe light intensity. a) Rabi oscillations for different detunings of the probe light from the two-photon resonance. b) Observed frequencies of Rabi oscillation versus detuning. The solid line is a fit to Eq. 6.39. c) Amplitude of the oscillations versus detuning. The solid line is a Lorentzian fit with a linewidth of about 4 kHz.

by an average value (such a “mean-field model” is only qualitative, see [142]).

Replacing the photon number by the Rabi frequency (Eq. 6.12) leads to

$$2\Omega_R \dot{\Omega}_R = \frac{c}{l}(\Omega_0^2 - \Omega_R^2) + \frac{N_0 R 6\pi \lambda^2 c}{2V} \Omega_R v \quad (6.41)$$

where  $\Omega_0$  is the two-photon Rabi frequency due to the input probe beam and the dressing beam. For small gain, we approximate  $\Omega_0^2 - \Omega_R^2 \approx 2\Omega_R(\Omega_0 - \Omega_R)$ . This approximation should retain the qualitative features of the coupled light-atom system even when the small gain approximation is no longer quantitative. Indeed, we will obtain results consistent with our previous treatment (Eq. 6.29) which was not limited to small gain. Using Eq. 6.19 for the atom gain  $G$  we obtain

$$\dot{\Omega}_R = \frac{c}{l}(\Omega_0 - \Omega_R + \frac{G}{2}v) \quad (6.42)$$

This equation together with Eqs. 6.31 and 6.32 forms a set of coupled equations describing the combined dynamics of the atom and light fields. The situation is analogous to the optical laser, where the atomic polarization and the electric field inside the cavity are coupled. However, the role of atoms and light is reversed: in the optical laser, the cavity lifetime is usually longer than the coherence time of the atomic polarization, whereas in our case the extremely long coherence time of the condensate dominates. This would correspond to the bad cavity limit of the optical laser which is usually not realized (see [143] and references therein).

Assuming rapid relaxation of the light field ( $\dot{\Omega}_R = 0$  in Eq. 6.42) leads to

$$\Omega_R = \Omega_0 + \frac{G}{2}v. \quad (6.43)$$

Inserting this into Eqs. 6.31 and 6.32 adiabatically eliminates the light field. This treatment is more general than the Heisenberg equations above, where we had neglected condensate depletion. To check for consistency, we now assume an undepleted condensate ( $w = -1$ ) and obtain

$$\dot{v} = \frac{G - \Gamma_2}{2}v + \Omega_0. \quad (6.44)$$

Below the threshold for superradiance, ( $G \leq \Gamma_2$ ),  $v$  relaxes with a time constant of  $2/(\Gamma_2 - G)$  to  $v = 2\Omega_0/(\Gamma_2 - G)$ . This and Eq. 6.43 show that the gain  $g$  for the probe beam is

$$g = 1 + \frac{G}{\Gamma_2 - G} \quad (6.45)$$

in agreement with Eq. 6.29.

## 6.6 Optical probe of matter wave gain

The matter wave grating formed inside the condensate is responsible for both atomic and optical gain. We now briefly describe experiments where the dynamics of the matter wave grating could be directly observed by monitoring the probe light. We first created a matter wave grating with a Bragg pulse and then observed its time evolution by monitoring the diffracted dressing beam. The initial seed pulse was 100  $\mu\text{s}$  long and transferred about 5% of the atoms to the recoil state.

At lower intensities for which atom amplification was negligible, the grating showed a simple decay (Fig. 6-5). At higher intensities, collective gain started to compensate the loss, and at intensities above a threshold, net amplification was observed. The initial growth rate (Fig. 6-5) followed the linear dependence on the intensity of the dressing beam ( $\propto (G - \Gamma_2)$ ) predicted by Eq. 6.44 and Refs. [18, 127]. The net growth of the matter wave grating was studied previously by observing an increase in the number of recoiling atoms in time-of-flight images [19], whereas Fig. 6-5 was obtained by monitoring the dynamics of amplification *in situ* by observing light instead of atoms.

Extrapolating the decay rate in Fig. 6-5 to zero intensity of the dressing beam gives the decay rate of the matter wave grating  $\Gamma_2$  of  $(100 \mu\text{s})^{-1}$ , in fair agreement with the linewidth of the Bragg excitation process observed previously [17]. This observation of the decay of the matter-wave grating can be regarded as pump-probe spectroscopy of quasi-particles in the condensate. The seeding Bragg pulse created the quasi-particles (in this case condensate excitations in the free-particle regime). One can control the momentum of the excited quasi-particles by the angle between the laser beams. This could be used to excite phonon-like quasiparticles [22], and their lifetimes could be determined with the pump-probe scheme presented here.

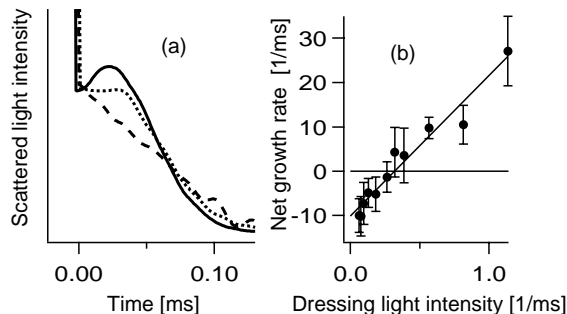


Figure 6-5: Pump-probe spectroscopy of a matter wave grating inside the condensate. (a) First, approximately 5 % of atoms were transferred to the recoil state by the two-photon Bragg transition. Then the dynamics of the matter wave grating was observed *in situ* by illuminating the grating with off-resonant dressing light and monitoring the diffracted light intensity. All traces were normalized to the same diffracted light intensity at  $t = 0$ . The dressing beam intensity was 2.9 mW/cm<sup>2</sup> (bottom), 5.7 mW/cm<sup>2</sup> (middle), 13 mW/cm<sup>2</sup> (top). (b) The initial growth rate of the grating vs. light intensity shows the threshold for net gain. The intensity of the dressing beam is given in units of the single-atom Rayleigh scattering rate. Figure is taken from Ref. [20].

## 6.7 Single-atom and collective behavior

The optical gain studied above clearly showed the transition from single-atom gain (the first term in the expansion in Eq. 6.30) to collective gain. Varying the intensities of probe and dressing light allows for the study of different physical regimes. At low dressing light intensity, below the superradiant threshold, one encounters single-atom behavior, at high intensity the system shows collective superradiance. The probe laser intensity determines whether the system shows oscillatory or steady state response, as derived above using optical Bloch equations. Fig. 6-6 summarizes the different regimes.

Probe light traces showing the transition from Rabi oscillations to superradiance are presented in Fig. 6-7. As a function of the dressing light intensity, the damped Rabi oscillations become faster and almost suddenly turn into a giant superradiant pulse.

Previously, recoil related gain based on single-atom phenomena (Recoil Induced Resonances) was observed in cold cesium atoms [117]. Collective gain due to the formation of a density grating was discussed as a possible gain mechanism for lasing action [144] (named CARL—Coherent Atomic Recoil Laser) and pursued experimentally [145, 146] with ambiguous results (see [147] and the discussion in [148, 149]). Our experiments clearly identify the two regimes and their relationship.

The dressed condensate is a clean, model system for discussing optical and atom-optical properties. The observed slow group velocity of the probe laser pulse can be directly related to the dynamics of the amplification process. The optical amplification can be described as a reflection of the dressing light by a matter wave grating. The initial delay time in the

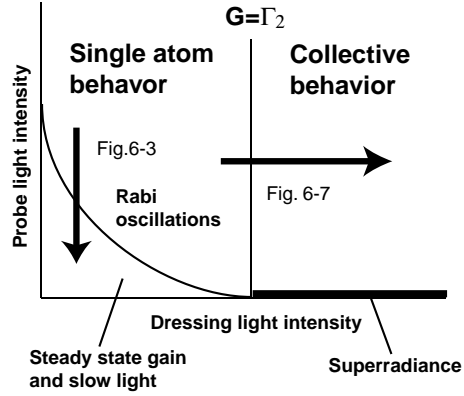


Figure 6-6: Schematic diagram of the different regimes of a dressed condensate. Depending on the intensities of the dressing and the probe beams, the dressed condensate occupies different physical regimes. Single atom and collective behavior are separated by the threshold to superradiance ( $G = \Gamma_2$ , Eq. 4.2).

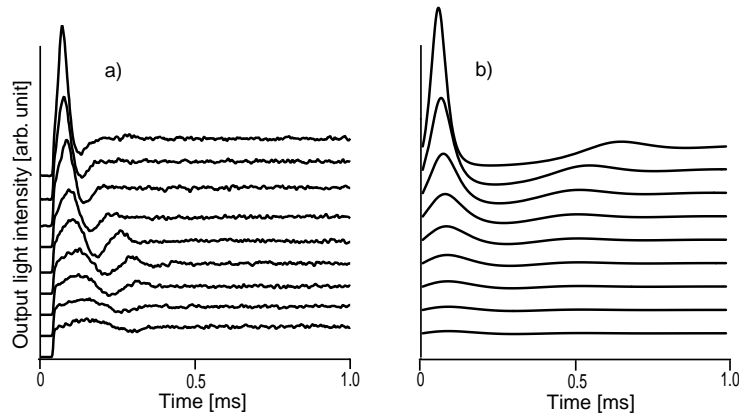


Figure 6-7: From single-atom Rabi oscillations to collective superradiance. a) The dressing beam intensity was increased from 2.7, 3.8, 6.1, 9.1, 14.1, 21.3, 32.7, 49.5 to 76  $\text{mW}/\text{cm}^2$  (bottom to top). The probe beam intensity was kept at 5  $\text{mW}/\text{cm}^2$ . b) Numerical solution of the nonlinear optical Bloch equations (Eqs. 6.42, 6.31 and 6.32). Plotted is  $\Omega_R^2$  for the same experimental parameters as in a).

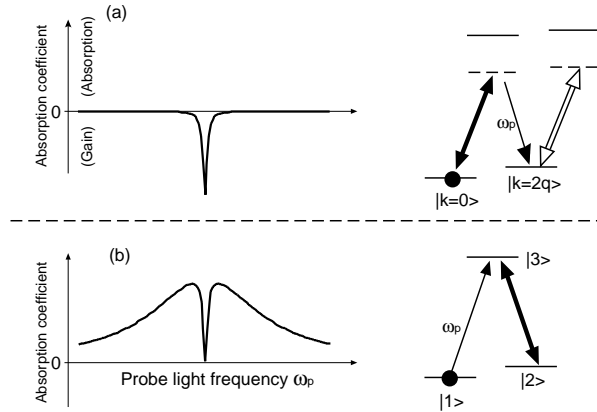


Figure 6-8: Comparison between two different methods to generate slow light. (a) Narrow-band optical amplification using a two-photon resonance. (b) Electromagnetically induced transparency.

amplification of optical pulses is the time necessary to build up the (quasi-)steady state matter wave grating. When the input pulse is switched off, the matter wave grating still exists and diffracts the pump light (as observed in Fig. 6-5) creating the trailing edge of the transmitted light pulse. Thus, the slow speed of light is simply related to the slow build-up and decay of quasi-particles which we were able to monitor directly. In this microscopic picture, all photons propagate with the vacuum speed of light  $c$ , the slow group velocity is only a phenomenological description of the center-of-mass propagation of the amplified pulse. This description leads to the same number of photons inside the condensate. Slow light pulses are compressed by a factor  $c/v_g$ , but the electric field strength is unchanged [150, 151]. Therefore, the product of the total number of photons within the pulse and the transit time is constant.

Recent demonstrations of slow group velocities for light focused on electromagnetically induced transparency (EIT) in a three-level  $\Lambda$  system [138]. This system features a narrow dip in a broad absorption feature. In our system, the broad absorption line is missing. Since the propagation of resonant laser pulses is mainly determined by the narrow feature (which determines  $dn_1/d\omega$ ), both systems show analogous behavior (see Fig. 6-8). Indeed, if one would add a broad-band absorber to the narrow-band amplifier, one would create the same index of refraction as in the EIT scheme.

Although both schemes involve three levels in a  $\Lambda$  configuration (Fig. 6-8), there are major differences. The amplification scheme does not have a dark state because it has off-resonant couplings to other momentum states which are indicated in Fig. 6-8. In the amplification scheme the strong pump pulse connects the initially populated state to the excited state in a far off-resonant way. In the EIT scheme the strong coupling laser drives the other leg of the  $\Lambda$  transition and is on resonance.

## Chapter 7

# Does matter wave amplification work for fermions?

*This chapter discusses the role of quantum statistics on off-resonant light scattering experiments, which was reported in the following publication:*

- *Wolfgang Ketterle and Shin Inouye, “Does matter wave amplification work for fermions?” Phys. Rev. Lett. **86**, 4203 (2001). Included in appendix G*

At the end of the discussion on superradiant Rayleigh scattering in Chapter 4, I briefly mentioned that Bose-Einstein condensates are not necessary for observing the phenomenon. In principle, thermal clouds (“Boltzmannons”) or even an ensemble of fermionic atoms can be used for the same experiments presented in previous chapters (4-6). However, this conclusion is not obvious at first sight, and the following chapter is dedicated to clarifying this interesting but subtle matter.

In Chapter 4, superradiant Rayleigh scattering was fully described by the “gain” equation for matter waves (Eq. 4.1):

$$\dot{N}_j = R \frac{\sin^2 \theta_j}{8\pi/3} \Omega_j' N_0 (N_j + 1) \quad (7.1)$$

It shows that the rate of Rayleigh scattering, which is proportional to the number of atoms in the initial momentum state ( $N_0$ ), is bosonically stimulated by atoms in the recoil state  $N_j$  and shows exponential growth when  $N_j \gg 1$ . This quantum mechanical form of the gain equation for matter waves rather indicates the opposite conclusion: *macroscopic* population of the final state is necessary for *bosonic stimulation* that drives the observed amplification. Moreover, the notion of “matter wave amplification” becomes unclear for fermions, since the number of fermionic atoms in a single mode cannot exceed one.

However, at the same time, we introduced the idea of Dicke superradiance and showed one-to-one correspondence between those two forms of superradiance. Just as a reminder,

the “dressed” condensate corresponds to the electronically excited state in Dicke superradiance. It can decay by spontaneous emission to a state with photon recoil, corresponding to the ground state. Now, it is important to note that the rate of superradiant emission in Dicke’s treatment is exactly the same as the bosonically stimulated rate in the accelerated scattering. In other words, “bosonic stimulation” is already included in the superradiance picture.

The correspondence goes as follows. Dicke regarded the two-level atom as a spin  $1/2$  system and introduced angular momentum quantum numbers. In this subspace, a fully symmetric state of  $N_0 (= N_1 + N_2)$  atoms has spin  $s = N_0/2$  and magnetic quantum number  $m = (N_1 - N_2)/2$ . The squared matrix element for the transition  $|s, m\rangle \rightarrow |s, m-1\rangle$  induced by the ladder operator  $S_-$  is  $(s-m+1)(s+m)$ . Expressing this by initial occupation numbers  $N_1$  and  $N_2$ , one obtains  $N_1(N_2 + 1)$  retrieving the formula of bosonic enhancement. Thus, the collective enhancement in our superradiance and matter wave amplification only based on the superradiant (or symmetric) coupling between atoms and the radiation field, which keeps atoms in cooperative ( $s = N_0/2$ ) states.

Now, all the known properties of Dicke’s case are applicable to our previous experiments. For example, it does not depend on statistics of particles explicitly. Quantum statistics is completely irrelevant for Dicke superradiance experiments. Moreover, the atomic sample does not have to be made of a single species. The only requirement is that each particle couple to the radiation field in the same manner. Then it is fundamentally impossible to distinguish which atom has radiated the last photon, and the collective enhancement can take place. However, this last statement raises an important question: how precise is the requirement? What will happen if the transition frequencies were slightly different from atom to atom, but those differences were smaller than the inverse of the observation time?

The condition for the phenomenon to happen can be summarized as follows: **the accelerated scattering takes place when it can be finished within the coherence time of the atomic ensemble.** The difference in frequency does not matter if the associated coherence time ( $\tau_{\text{coh}} = 1/\Gamma_2$ ) is longer than the collective scattering time ( $1/G$ ). Any difference between atoms can lead to the reduction of coherence time: maybe the atoms are simply different species, or they are the same species but in different momentum states. All these effects are now parameterized by a single quantity, the coherence time  $\tau_{\text{coh}}$ .

So the question whether the same experiments are possible with fermions is synonymous with whether the same long coherence time can be achieved with a fermionic sample. At least in principle, one can prepare a fermionic system with infinite coherence time by starting out with a cloud which is in a single momentum state along the  $\hat{z}$  axis, but occupies many momentum states along  $\hat{x}$  and  $\hat{y}$ . With a Bragg pulse transferring momentum  $q\hat{z}$ , one can prepare a system which shows collective behavior for scattering particles or light with momentum transfer  $q\hat{z}$  with an infinite coherence time (Fig. 7-1 c). In this ensemble, the scattering is between the states  $|k_z = 0\rangle \otimes |k_x, k_y\rangle$  and  $|k_z = q\rangle \otimes |k_x, k_y\rangle$ . Therefore,

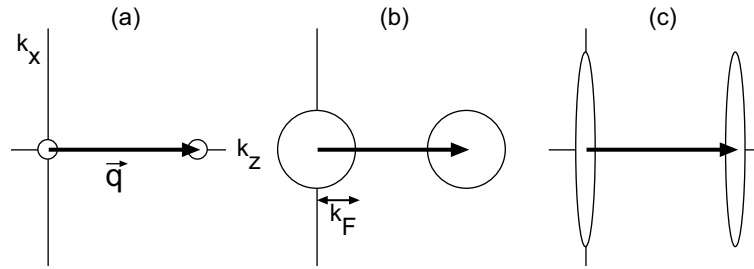


Figure 7-1: Momentum transfer  $\vec{q}$  (a) to a Bose-Einstein condensate, (b) to a Fermi sea, and (c) to a momentum squeezed degenerate Fermi cloud. Shown are the populated states vs. the  $k$ -vector. The momentum spread  $k_F$  of the Fermi sea introduces Doppler broadening of the transition and a finite coherence time, whereas the coherence time in (a) and (c) is much longer due to a small momentum spread in the  $z$ -direction and could in principle be infinite. Figure taken from Ref. [21].

we have enhanced scattering into the  $|k_z = q\rangle$  quantum state, but the atoms may differ in other quantum numbers. What matters is only the symmetrization of the many-body wavefunction along  $\hat{z}$ . The other quantum numbers ensure that there is no conflict with the Pauli blocking for fermionic systems. This is analogous to the separation of electronic wavefunctions into a symmetric part (e.g. the spin part) and an antisymmetric part (e.g. the spatial part) where the coupling to an external field (e.g. electron spin resonance experiment) only depends on the symmetric part.

So if one comes back to the initial question “Is matter wave amplification possible for fermions?” then the answer is yes, if the system is prepared in a cooperative state and the amplification is faster than the coherence time. However, this amplification does not pile up atoms in a single quantum state, but rather in states which are in the same (or approximately the same) momentum state along  $\hat{z}$ , but differ in other quantum numbers. Therefore, this amplification can be regarded as amplification of a density modulation or as amplification of spatial bunching of atoms. Alternatively, one can regard the density modulation as a collective excitation of the system which involves bosonic quasi-particles (e.g. phonons). Superradiance and four-wave mixing (both with bosons and fermions) can then be ascribed to bosonic stimulation by those quasi-particles.

The phase-coherent matter wave amplification for fermions would start with a short Bragg pulse which puts some of the atoms into a recoil state which is then amplified. This superposition of two momentum states creates a matter wave grating. This can be regarded as the interference pattern of each atom with itself with all the individual interference patterns being exactly in phase. Matter wave amplification occurs when a single laser beam is diffracted off this grating increasing the amplitude of each atom to be in the recoiling state. Therefore, the matter wave amplification scheme of refs. [19, 152] would work for fermions, provided the whole process can be done in the short coherence time of the fermionic matter wave grating.

Of course, there is a fundamental difference between bosons and fermions which is reflected in the symmetry of the total wavefunction. A bosonic system with two macroscopically occupied quantum states is *always* in a fully symmetric and maximally cooperative state. In other words, if two independent Bose condensates cross each other, there is always a macroscopic interference pattern (as observed experimentally [6]). It is this density modulation which can be amplified by the dynamic diffraction discussed here. If two beams of fermions overlap, there is no macroscopic interference, unless the two beams were prepared in a symmetric way, e.g. by generating one of the beams by a Bragg pulse from the other one.

## Chapter 8

# Imaging a vortex in a Bose-Einstein condensate

*In this chapter, I present the experiment on observation of vortex excitations in a Bose-Einstein condensate reported in the following preprint:*

- *S. Inouye, S. Gupta, T. Rosenband, A.P. Chikkatur, A. Görlitz, T.L. Gustavson, A.E. Leanhardt, D.E. Pritchard, and W. Ketterle, “Observation of vortex phase singularities in Bose-Einstein condensates,” submitted to Phys. Rev. Lett. . Available as an e-print (cond-mat/0104444), and also included in Appendix H.*

### 8.1 A little personal introduction to vortex experiments

The first project I pursued in the “old lab” was observation of vortices in BEC, which was one of the few projects that completely failed in our lab in these five years. Michael Andrews (senior graduate student at that moment, now in Bell Labs) and I teamed up in 1997 and tried to observe centrifugal holes made by vortex excitations. Several excitation schemes were experimentally investigated, but no holes were observed in the time-of-flight images for three months, and the project was terminated. Having this experience in mind, I chose observation of the phase profile of the vortex as my last project in this lab, closing a full circle. This is a good way to see if the integral along my research experiences during my Ph.D. years is zero or has some finite value.

The technique to observe vortices is as important as the technique to generate vortices. The detection scheme we used in this experiment was already discussed in 1997 [153]. Long, straight fringes due to the interference between two Bose-Einstein condensates observed in late 1996 [6] constitute the base-line of this experiment. There, the two condensates were produced by dividing a magnetic trap with a light sheet, and they were overlapped during time-of-flight. Several people pointed out that fringes should show characteristic fork-like structure if one of the condensates contains a vortex excitation [154, 153, 155].

The interference technique works best if only one of the condensates contains vortex excitations. The other condensate, which serves as a reference, should have a flat phase all across it. The way we tried to excite vortices in 1997 relied on the shift of the magnetic trap center by additional bias fields, which exerts a force not only onto the “sample” condensate, but also onto the “reference” condensate.

This time, vortices were created by moving a laser beam through one of the condensates. This is a technique developed in the “new lab,” where superfluidity of condensates was investigated. In the new lab experiment, heating or deformation of the condensate induced by the stirring was measured as a function of the velocity of the stirrer [156, 157]. Both measurements showed onset of dissipation at about one tenth of the speed of sound of the condensate. Numerical simulations based on the Gross-Pitaevskii eq. indicate nucleation of vortex-pairs at this critical velocity [158]. Interferometric detection of the flow pattern should give a definite answer to the cause of dissipation.

## 8.2 Vortices in BEC

Vortices in a Bose-Einstein condensate was first observed in JILA, when they introduced a phase-winding into a two-component BEC by combining an ac-Stark shift from a rotating laser beam and a coherent rf-transition [159]. Vortices were also produced in ENS Paris [160], and also later in MIT [161] by rotating a deformed trapping potential. In most of the work at these places, vortices were identified by observing the density depletion at the cores. The velocity field was inferred indirectly, with the exception of the work at Boulder [159]. The flow of the superfluid is given by the gradient of the phase  $\phi(\vec{r})$  of the wavefunction  $\psi(\vec{r}) = \sqrt{\rho(\vec{r})} \exp(i\phi(\vec{r}))$ :

$$\vec{v}_s(\vec{r}) = \frac{\hbar}{M} \nabla \phi(\vec{r}), \quad (8.1)$$

Interferometric detection of the phase profile of the condensate leads to visualization of the turbulent flow of the superfluid.

The line integral of Eq. (8.1) around a closed path gives the quantization of circulation:

$$\int \vec{v}(\vec{r}) \cdot d\vec{r} = \frac{\hbar}{m} (\phi(\vec{r}_f) - \phi(\vec{r}_i)). \quad (8.2)$$

If the path is singly connected, there is no circulation. If the path is multiply connected (like around a vortex core) the circulation can take values  $nh/m$  (integer multiples of  $h/m$ ), since the phase is only defined modulo  $2\pi$ . As a result, the phase accumulated between two points A and B can be different depending on the path (Fig. 8-1). The integer quantum number  $n$  is called the charge of the vortex. When the phase gradient is integrated along a path to the left of the vortex (path ACB), the accumulated phase differs by  $2n\pi$  from the path to the right (ADB).

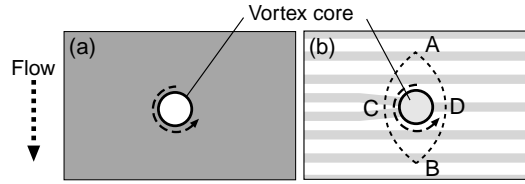


Figure 8-1: Density (a) and phase (b) profile of a moving condensate with singly-charged ( $n = 1$ ) vortex. The density profile shows the vortex core, whereas the phase pattern features a fork-like dislocation at the position of the vortex. Interference between two initially separated, freely expanding condensates produces exactly the same pattern as shown in (b), if one of the condensates contains a vortex. Figure taken from Ref. [24] .

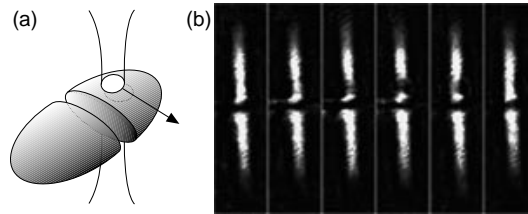


Figure 8-2: Schematic (a) and phase-contrast images (b) of the condensates used for the experiment. A blue-detuned laser beam (not shown in the figure) was focused into a light sheet separating the two condensates in the magnetic trap. Another tightly focused laser beam was swept through one of the condensates (the upper one in image (b)) to excite vortices. The intensity of each laser beam was a factor of four higher than in the experiments to enhance the depleted regions in the images. The images in (b) have a field of view of  $100 \mu\text{m} \times 380 \mu\text{m}$ . For each image, the stirrer was advanced from left to right by  $5 \mu\text{m}$ . Figure taken from Ref. [24] .

The fork-like structure in interference fringes comes from this difference in phase evolution between the two sides of the vortex. When two condensates with relative velocity  $v$  overlap, the total density shows straight interference fringes with a periodicity  $h/mv$ . If one of the condensates contains a vortex of charge  $n$ , there are  $n$  more fringes on one side of the singularity than on the other side (Fig. 8-1b). An observation of this fork-like dislocation in the interference fringes is a clear signature of a vortex.

The schematic of the experiment is shown in Fig. 8-2. The double-well potential was created by adding a potential hill at the center of a cigar-shaped magnetic trap. For this, blue-detuned far off-resonant laser light (532 nm) was focused to form an elliptical light sheet and was aligned to the center of the magnetic trap with the long axis of the sheet perpendicular to the long axis of the condensate. After two condensates each containing  $\sim 1 \times 10^6$  atoms were formed in the double-well potential, we swept a second blue-detuned laser beam through one of the condensates using an acousto-optical deflector (Fig. 8-2). After sweeping the beam once across the condensate, the magnetic and optical fields were

switched off and the two condensates expanded and overlapped during 41 ms time-of-flight. The atoms were then optically pumped into the  $F = 2$  hyperfine ground state for  $80 \mu\text{s}$  and subsequently probed for  $20 \mu\text{s}$  by absorption imaging tuned to the  $F = 2$  to  $F' = 3$  cycling transition.

Images of interfering condensates show a qualitative difference between stirred (Fig. 8-3(b-d)) and unperturbed states (Fig. 8-3(a)). Fork-like structures in the fringes were often observed for stirred condensates, whereas unperturbed condensates always showed straight fringes. The charge of the vortices can be determined from the fork-like pattern. In Fig. 8-3(b), vortices were excited in the condensate on top, and the higher number of fringes on the left side indicates higher relative velocity on this side, corresponding to counterclockwise flow. Fig. 8-3(c) shows a vortex of opposite charge. The double fork observed in Fig. 8-3(d) represents the phase pattern of a vortex pair. Multiply charged vortices, which are unstable against the break-up into singly charged vortices, were not observed.

For interferometric detection of vortices, other schemes have also been discussed. The one employed here uses a separate condensate as a local oscillator. The other alternative is to split, shift and recombine a single condensate with vortices. In this case, the interference pattern is more complicated because all singularities and distortions appear twice. The simulations in Ref. [162] show that the self-interference technique produces more complicated fringe patterns. After completion of this work, we learned that this second technique was used in ENS, Paris to observe the phase pattern of a single vortex [163].

By varying the speed of the laser beam sweep, we determined the velocity dependence of the vortex nucleation process. The study suggests that the nucleation of vortices requires a velocity of  $\sim 0.5 \mu\text{m/ms}$ , corresponding to a Mach number  $v_c/c_s \sim 0.08$ , consistent with a previous measurement [157].

The interferometric technique used here is a sensitive way to assess whether a condensate has the assumed ground state wave function which is characterized by a uniform phase. By delaying the release of the atoms from the trap by a variable amount of time, we can study the relaxation of the condensate towards its ground state. It was observed that the condensate completely recovers its uniform phase after 50 – 100 ms. Vortices disappeared after  $\sim 30$  ms.

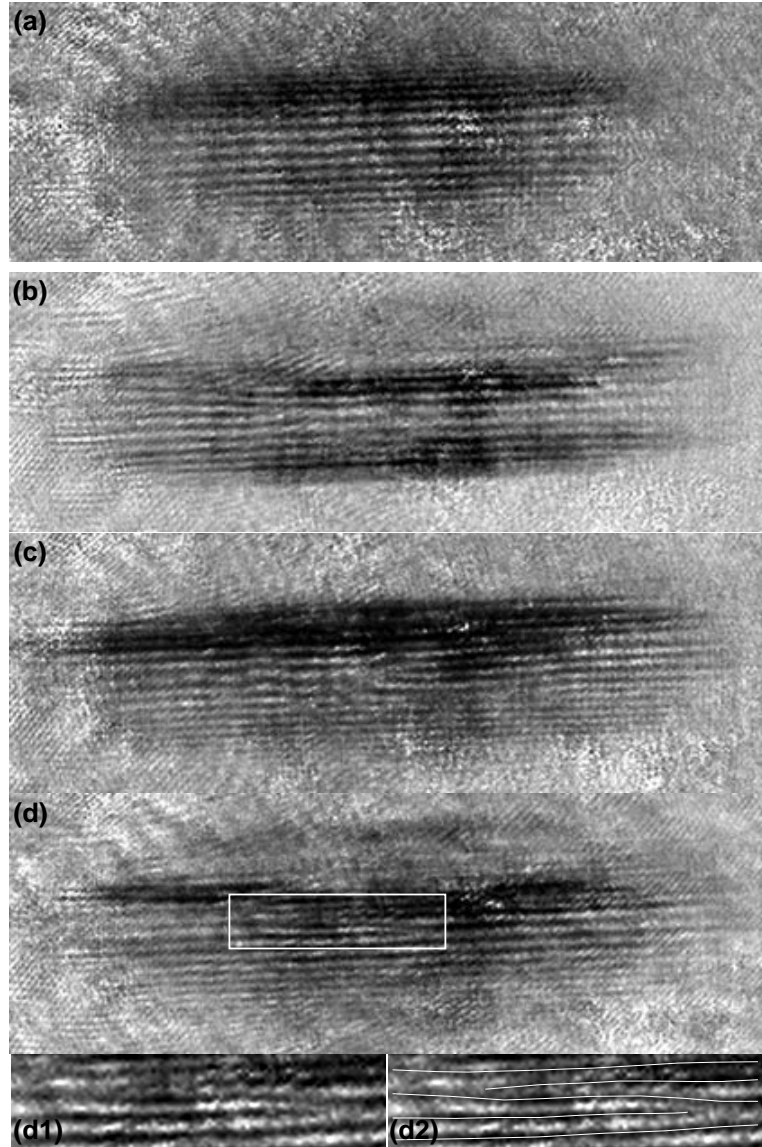


Figure 8-3: Observation of the phase singularities of vortices created by sweeping a laser beam through a condensate. Without the sweep, straight fringes of  $\sim 20 \mu\text{m}$  spacings were observed (a), while after the sweep, fork-like dislocations appeared (b-d). The speed of the sweep was  $1.1 \mu\text{m}/\text{ms}$ , corresponding to a Mach number of  $\sim 0.18$ . The field of view of each image is  $1.1 \text{ mm} \times 0.38 \text{ mm}$ . Fig. (d) shows a pair of dislocations with opposite circulation characteristic of a vortex pair. At the bottom, magnified images of the fork-like structures are shown (d1) with lines to guide the eye (d2). The orientation of the condensates is the same as in Fig. 8-2(b). Figure taken from Ref. [24] .

## Chapter 9

# Conclusion and Outlook

In this dissertation, interaction between coherent light and coherent atoms was studied in detail. Matter wave gratings played an important role throughout the work. I would like to summarize the off-resonant scattering experiments first, and then the work on vortex excitations.

The unifying concept behind the four off-resonant light scattering experiments is four wave mixing between light and atoms. Light can be diffracted by matter wave gratings, and atoms can be diffracted by light gratings. The latter regime (Bragg spectroscopy) was used to measure coherence properties of a condensate with spectroscopic precision. The measured narrow linewidth of the two-photon process shows that the coherence length of a condensate is equal to its size.

It was found that the long coherence time of a Bose-Einstein condensate gave rise to superradiance based on coherent external motion of atoms. The underlying physics is light diffraction from a matter wave grating, which builds up atoms in a recoil mode. An important idea introduced here is the “dressed condensate,” which describes a condensate illuminated by a single off-resonant laser beam. This is a gain medium for matter waves and light fields. Amplification of both atomic and light fields were experimentally realized. It was also shown that a long coherence time, rather than the macroscopic occupation of a single quantum state is most important to these phenomena.

The idea of a “dressed condensate” opened up several possibilities. One of the most notable applications is the creation of entangled atom-photon pairs [164]. Superradiance can be regarded as amplified parametric down-conversion of a dressed condensate. Nowadays the most popular technique for generating entangled photon pairs is spontaneous parametric down-conversion in a nonlinear crystal. By driving a dressed condensate below the threshold for superradiance, entangled atom-photon pairs can be generated.

From a practical point of view, the most important result in this dissertation is the realization of matter wave amplification. This parametric amplifier is easy to realize and control. The gain is proportional to the “dressing” light intensity, which can be as low as  $1 \text{ mW/cm}^2$  for our conditions. The only obvious disadvantage is its narrow bandwidth

— the dressed condensate can only amplify atoms within the momentum range that can be reached by scattering a photon from the dressing beam. The amplifier works best for matter waves with a well-defined momentum.

In the vortex experiment, vortex excitations in Bose-Einstein condensates were studied using an interferometric technique. Vortices were excited by moving a laser beam across the condensate, and they were clearly imaged as topological singularities. This technique is suited for the study of complicated flowfield of superfluids, e.g. when multiple vortices with opposite charges are present.

There are many issues of vortex physics that remain unexplored, including vortices in two-dimensional condensates (condensates in lower dimensions were recently realized in our laboratory [165]), pinning of vortices by additional laser beams, and interactions between vortices. This work has proven that an atomic physics technique, matter wave interferometry, is a powerful tool to probe the nucleation of vortices, a problem of many-body physics. This is yet another example of the successful interplay between atomic physics and condensed matter physics, which has been a main stay of BEC research. I am sure that this collaboration will bear many interesting fruits in the future.

## Appendix A

# Observation of Feshbach resonances in a Bose-Einstein condensate

This appendix includes the following paper [8]: S. Inouye, M.R. Andrews, J. Stenger, H.-J. Miesner, D.M. Stamper-Kurn, and W. Ketterle, “Observation of Feshbach resonances in a Bose-Einstein condensate,” *Nature* **392**, 151 (1998).

This work has received a lot of attention for the following three reasons. First, the scattering length was modified by an external magnetic field, opening up new possibilities for the study and manipulation of Bose-Einstein condensates. Second, anomalous trap losses observed at these resonances imposed a new challenge to the collisional physics community. Third, the position of the Feshbach resonances gave a unique opportunity to determine molecular interaction parameters. Relevant new results are listed below.

- Bose-Einstein condensates of  $^{85}\text{Rb}$  atoms were produced [99]. A Feshbach resonance was used to change the sign of the scattering length (which is negative at zero bias field) to a positive value and stabilize a condensate with large number of atoms. Collapse of a large condensate as well as condensates in the hydrodynamic regime were realized by modulating the scattering length.
- More than 25 Feshbach resonances were found in Cs, which led to the unambiguous and accurate determination of Cs ultracold collision properties [166]
- (Studies on trap-losses are summarized in the next appendix (Appendix B).)

Optically induced Feshbach resonances were also observed [167]. The scattering properties were varied by changing either the intensity or the detuning of a laser tuned near a photoassociation transition to a molecular state in the dimer. Feshbach resonances were

also studied intensively in connection with the production of a condensate of diatomic molecules [168, 169].

# Observation of Feshbach resonances in a Bose–Einstein condensate

S. Inouye\*, M. R. Andrews\*†, J. Stenger\*, H.-J. Miesner\*, D. M. Stamper-Kurn\* & W. Ketterle\*

\* Department of Physics and Research Laboratory of Electronics, Massachusetts Institute of Technology, Cambridge, Massachusetts 02139, USA

**It has long been predicted that the scattering of ultracold atoms can be altered significantly through a so-called ‘Feshbach resonance’. Two such resonances have now been observed in optically trapped Bose–Einstein condensates of sodium atoms by varying an external magnetic field. They gave rise to enhanced inelastic processes and a dispersive variation of the scattering length by a factor of over ten. These resonances open new possibilities for the study and manipulation of Bose–Einstein condensates.**

Bose–Einstein condensates of atomic gases offer new opportunities for studying quantum-degenerate fluids<sup>1–5</sup>. All the essential properties of Bose condensed systems—the formation and shape of the condensate, the nature of its collective excitations and statistical fluctuations, and the formation and dynamics of solitons and vortices—are determined by the strength of the atomic interactions. In contrast to the situation for superfluid helium, these interactions are weak, allowing the phenomena to be theoretically described from ‘first principles’. Furthermore, in atomic gases the interactions can be altered, for instance by employing different species, changing the atomic density, or, as in the present work, merely by varying a magnetic field.

At low temperatures, the interaction energy in a cloud of atoms is proportional to the density and a single atomic parameter, the scattering length  $a$  which depends on the quantum-mechanical phase shift in an elastic collision. It has been predicted that the scattering length can be modified by applying external magnetic<sup>6–10</sup>, optical<sup>11,12</sup> or radio-frequency<sup>13</sup> (r.f.) fields. Those modifications are only pronounced in a so-called ‘Feshbach resonance’<sup>14</sup>, when a quasibound molecular state has nearly zero energy and couples resonantly to the free state of the colliding atoms. In a time-dependent picture, the two atoms are transferred to the quasibound state, ‘stick’ together and then return to an unbound state. Such a resonance strongly affects the scattering length (elastic channel), but also affects inelastic processes such as dipolar relaxation<sup>6,7</sup> and three-body recombination. Feshbach resonances have so far been studied at much higher energies<sup>15</sup> by varying the collision energy, but here we show that they can be ‘tuned’ to zero energy to be resonant for ultracold atoms. The different magnetic moments of the free and quasibound states allowed us to tune these resonances with magnetic fields, and as a result, minute changes in the magnetic field strongly affected the properties of a macroscopic system.

Above and below a Feshbach resonance, the scattering length  $a$  covers the full continuum of positive and negative values. This should allow the realization of condensates over a wide range of interaction strengths. By setting  $a \approx 0$ , one can create a condensate with essentially non-interacting atoms, and by setting  $a < 0$  one can make the system unstable and observe its collapse. Rapid tuning of an external magnetic field around a Feshbach resonance will lead to sudden changes of the scattering length. This opens the way to studies of new dynamical effects such as novel forms of collective oscillations or the sudden collapse of a large condensate when the scattering length is switched from positive to negative<sup>16</sup>.

## Theoretical predictions

Calculations for Feshbach resonances in external magnetic fields have been reported for the lower hyperfine states of the atoms Li (ref. 8), K (ref. 10), Na (ref. 8), Rb (ref. 9) and Cs (refs 6, 7). They are typically spaced by several hundred gauss, and for Li and Na occur outside the range where states in the lower hyperfine manifold are weak-field-seeking and can be magnetically trapped. Recent experimental efforts to observe Feshbach resonances have concentrated on <sup>87</sup>Rb (ref. 17) and on <sup>85</sup>Rb (ref. 18 and C. E. Wieman, personal communication) where Feshbach resonances have been predicted at relatively low magnetic fields<sup>9</sup>. However, our recently demonstrated all-optical confinement of a Bose condensate<sup>19</sup> opened the possibility of observing Feshbach resonances for strong-field-seeking states which cannot be trapped in a d.c. magnetic trap. The optical trapping potential is unaffected by magnetic fields and is independent of the hyperfine ground state. We report here the observation of two Feshbach resonances of sodium in a strong-field-seeking state.

Several Feshbach resonances in sodium are caused by quasibound hyperfine states of the second highest vibrational level,  $v = 14$ , of the triplet potential of the sodium dimer. The lowest magnetic field value  $B_0$  for a strong Feshbach resonance in sodium was predicted to lie in the range  $760 < B_0 < 925$  G (B. J. Verhaar and F. A. van Abeelen, personal communication). It occurs in collisions between atoms in the lowest hyperfine state  $|m_s = -1/2, m_l = +3/2\rangle$ , which correlates with the  $|F = 1, m_F = +1\rangle$  state at low fields ( $S, I$  and  $F$  are the usual quantum numbers for the electronic, nuclear and total spin, respectively). This Feshbach resonance is due to a quasibound molecular state  $|S = 1, m_s = +1, I = 1, m_l = +1\rangle$ . A much weaker resonance due to a  $|S = 1, m_s = +1, I = 3, m_l = +1\rangle$  state (which is almost degenerate with the other quasibound state) was predicted to occur 50 to 75 G below.

Near a Feshbach resonance, the scattering length  $a$  should vary dispersively as a function of magnetic field  $B$  (ref. 8):

$$a = \bar{a} \left( 1 - \frac{\Delta}{B - B_0} \right) \quad (1)$$

where  $\Delta$  parametrizes the width of the resonance at  $B = B_0$ , and  $\bar{a}$  is the scattering length outside the resonance. For sodium,  $\bar{a}$  was found spectroscopically to be 2.75 nm at zero field, and increases to the triplet scattering length of 4.5 nm (ref. 20) at high magnetic fields. The widths  $\Delta$  for the strong and weak resonance were predicted to be 1 G and 0.01 G, respectively (B. J. Verhaar and F. A. van Abeelen, personal communication).

† Present address: Bell Laboratories, Lucent Technologies, Murray Hill, New Jersey 07974, USA.

**Experimental set-up**

Bose–Einstein condensates in the  $|F = 1, m_F = -1\rangle$  state were produced as in our previous work by laser cooling, followed by evaporative cooling in a magnetic trap<sup>21</sup>. The condensates were transferred into an optical dipole trap formed at the focus of an infrared laser beam<sup>19</sup>. Atoms were then spin-flipped with nearly 100% efficiency to the  $|F = 1, m_F = +1\rangle$  state with an adiabatic r.f. sweep while applying a 1 G bias field. Without large modifications of our magnetic trapping coils, we could provide bias fields of up to  $\sim 1,200$  G, but only by using coils producing axial curvature<sup>21</sup>, which for high-field-seeking states generated a repulsive axial potential. At the highest magnetic fields, this repulsion was stronger than the axial confinement provided by the optical trap. To prevent the atoms from escaping, two ‘end-caps’ of far-off-resonant blue-detuned laser light were placed at the ends of the condensate, creating a repulsive potential, and confining the atoms axially (Fig. 1a). For this, green light at 514 nm from an argon-ion laser was focused into two sheets about  $200\ \mu\text{m}$  apart. The focus of the optical trap was placed near the minimum of the bias field in order to minimize the effect of the destabilizing magnetic field curvature. The axial trapping potential at high fields was approximately ‘W’-shaped (Fig. 1b), and had a minimum near one of the end-caps as observed by phase-contrast imaging<sup>22</sup> (Fig. 1c, d).

The calibration factor between the current (up to  $\sim 400$  A) in the coils and the magnetic bias field was determined with an accuracy of 2% by inducing r.f. transitions within the  $|F = 1\rangle$  ground-state hyperfine manifold at about 40 G. Additionally, an optical resonance was found around 1,000 G, where the Zeeman shift equalled the probe light detuning of about 1.7 GHz and led to a sign-reversal of the phase-contrast signal. These two calibrations agreed within their uncertainties.

The condensate was observed in the trap directly using phase-contrast imaging<sup>22</sup> or by using time-of-flight absorption imaging<sup>1,2,21</sup>. In the latter case, the optical trap was suddenly switched off, and the magnetic bias field was shut off 1–2 ms later to ensure that the high-field value of the scattering length was responsible for the acceleration of the atoms. After ballistic expansion of the condensate (either 12 or 20 ms), the atoms were optically pumped into the  $|F = 2\rangle$  ground state and probed using resonant light driving the cycling transition. The disk-like expansion of the

cloud and the radial parabolic density profile were clear evidence for the presence of a Bose condensed cloud.

**Locating the resonances**

When the magnetic field is swept across a Feshbach resonance one would expect to lose a condensate due to an enhanced rate of inelastic collisions (caused either by the collapse in the region of negative scattering length or by an enhanced rate coefficient for inelastic collisions). This allowed us to implement a simple procedure to locate the resonances: we first extended the field ramp until the atoms were lost and then used successively narrower field intervals to localize the loss. This procedure converged much faster than a point-by-point search. As we could take many non-destructive phase-contrast images during the magnetic field ramp, the sharp onset of trap loss at the resonance was easily monitored (Fig. 1c, d).

The most robust performance was obtained by operating the optical dipole trap at 10 mW laser power focused to a beam waist of  $6\ \mu\text{m}$ , resulting in tight confinement of the condensate and therefore rather short lifetimes owing to three-body recombination<sup>19</sup>. This required that the magnetic field be ramped up in two stages: a fast ramp at a rate of  $\sim 100\ \text{G ms}^{-1}$  to a value slightly below that expected for a Feshbach resonance, followed by a slow ramp at a rate between 0.05 and  $0.3\ \text{G ms}^{-1}$  to allow for detailed observation. Near 907 G, we observed a dramatic loss of atoms, as shown in Figs 1c and 2a. This field value was reproducible to better than 0.5 G and had a calibration uncertainty of  $\pm 20$  G.

To distinguish between an actual resonance and a threshold for trap loss, we also approached the resonance from above. Fields above the Feshbach resonance were reached by ramping at a fast rate of  $200\ \text{G ms}^{-1}$ , thus minimizing the time spent near the resonance and the accompanying losses. The number of atoms above the resonance was typically three times smaller than below. Approaching the resonance from above, a similarly sharp loss phenomenon was observed about 1 G higher in field than from below (Fig. 2a), which roughly agrees with the predicted width of the resonance. A second resonance was observed  $54 \pm 1$  G below the first one, with the observed onset of trap loss at least a factor of ten sharper than for the first. As the upper resonance was only reached by passing through the lower one, some losses of atoms were unavoidable; for example, when the lower resonance was crossed at  $2\ \text{G ms}^{-1}$ ,

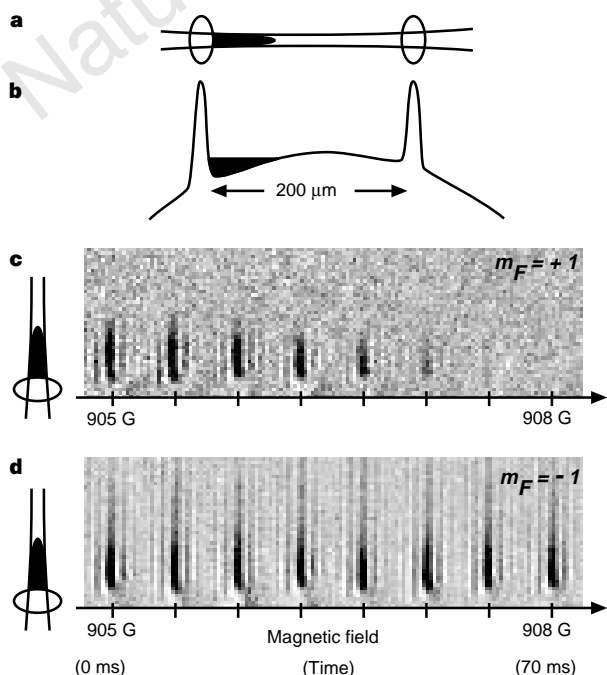


**Figure 1** Observation of the Feshbach resonance at 907 G using phase-contrast imaging in an optical trap. A rapid sequence (100 Hz) of non-destructive, *in situ* phase-contrast images of a trapped cloud (which appears black) is shown. As the magnetic field was increased, the cloud suddenly disappeared for atoms in the  $|m_F = +1\rangle$  state (see images in **c**), whereas nothing happened for a cloud in the  $|m_F = -1\rangle$  state (images in **d**). The height of the images is  $140\ \mu\text{m}$ . A diagram of the optical trap is shown in **a**. It consisted of one red-detuned laser beam providing radial confinement, and two blue-detuned laser beams acting as end-caps (shown as ovals). The minimum of the magnetic field was slightly offset from the centre of the optical trap. As a result, the condensate (shaded area) was pushed by the magnetic field curvature towards one of the end-caps. The axial profile of the total potential is shown in **b**.

about 80% of the atoms were lost. This, coupled with the stability and finite programming speed of the power supplies, limited the ramp rates to those given above.

The observation of twin resonances separated by  $54 \pm 1$  G, with the weaker one at lower field, exactly matches the theoretically predicted pattern and thus strongly confirms our interpretation. No resonance phenomena were observed in the  $|m_F = -1\rangle$  state at any field up to 1,000 G, in agreement with theory which predicted resonances for this state only at much higher fields.

### Changing the scattering length

The trap loss measurements easily located the Feshbach resonances. To measure the variation of the scattering length around these resonances, we determined the interaction energy of a trapped condensate. This was done by suddenly switching off the trap, allowing the stored interaction energy to be converted into the kinetic energy of a freely expanding condensate and measuring it by time-of-flight absorption imaging<sup>1,2,21</sup>. The interaction energy is proportional to the scattering length and the average density of the condensate  $\langle n \rangle$ :

$$E_I/N = \frac{2\pi\hbar^2}{m} a \langle n \rangle \quad (2)$$

where  $N$  is the number of condensed atoms of mass  $m$ . For a large condensate the kinetic energy in the trap is negligible (Thomas–Fermi limit), and  $E_I$  is equal to the kinetic energy  $E_K$  of the freely expanding condensate  $E_K/N = mv_{\text{rms}}^2/2$ , where  $v_{\text{rms}}$  is the root-mean-square velocity of the atoms. For a three-dimensional har-

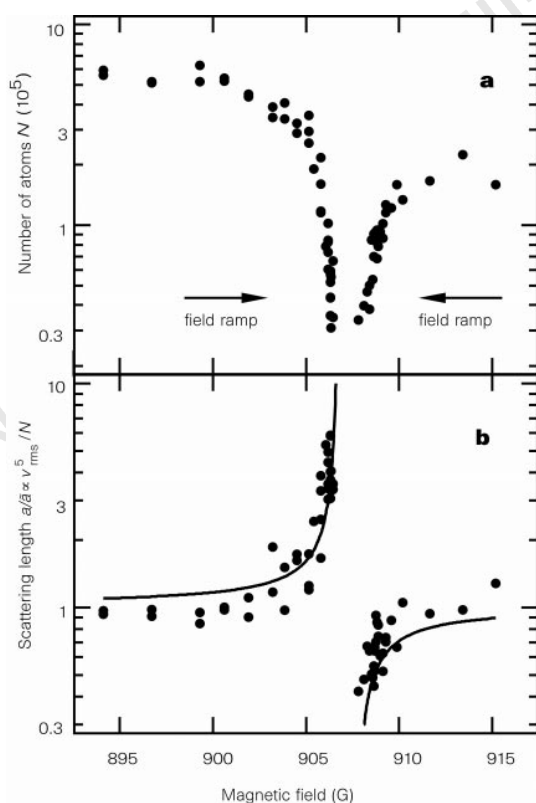


**Figure 2** Observation of the Feshbach resonance at 907 G using time-of-flight absorption imaging. **a**, Number of atoms in the condensate versus magnetic field. Field values above the resonance were reached by quickly crossing the resonance from below and then slowly approaching from above. **b**, The normalized scattering length  $a/\bar{a} \propto v_{\text{rms}}^5/N$  calculated from the released energy, together with the predicted shape (equation (1), solid line). The values of the magnetic field in the upper scan relative to the lower one have an uncertainty of  $<0.5$  G.

monic oscillator potential one finds  $\langle n \rangle \propto N(Na)^{-3/5}$  (ref. 23) (We note that, for a general power-law potential  $\Sigma_i c_i x_i^{p_i}$ , one obtains  $\langle n \rangle \propto N(Na)^{k-1}$ , where  $k = 1/(1 + \Sigma_i 1/p_i)$ ). Thus, the value of the scattering length scales as:

$$a \propto \frac{v_{\text{rms}}^5}{N} \quad (3)$$

Both  $v_{\text{rms}}$  and  $N$  can be directly evaluated from absorption images of freely expanding condensates. For a cigar-shaped condensate the free expansion is predominantly radial, and so the contribution of the axial dimension to  $v_{\text{rms}}$  could be neglected. The quantity  $v_{\text{rms}}^5/N$  (equation (3)), normalized to unity outside the resonance, should be identical to  $a/\bar{a}$  (equation (1)). This quantity was measured around the resonance at 907 G and is shown in Fig. 2b together with the theoretical prediction of a resonance with width  $\Delta = 1$  G. The data clearly displays the predicted dispersive shape and shows evidence for a variation in the scattering length by more than a factor of ten.

We now discuss the assumptions for equation (3) and show that it is approximately valid for our conditions. (1) We assumed that the condensate remains in equilibrium during the magnetic field ramp. This is the case if the adiabatic condition  $\dot{a}/a \ll \omega_i$  holds for the temporal change of the scattering length<sup>16</sup>, and a similar condition for the loss of atoms (the  $\omega_i$  are the trapping frequencies). For the condensate's fast radial dynamics ( $\omega_r \approx 2\pi \times 1.5$  kHz) this condition is fulfilled, whereas for the slower axial motion ( $\omega_z \approx 2\pi \times 0.1$  kHz) it breaks down close to or within the resonance. In this case the density would approach the two-dimensional scaling  $N(Na)^{-1/2}$ , but the values for  $a/\bar{a}$  (Fig. 2b) would differ by at most 50%. (2) The second assumption was a three-dimensional harmonic trap. If the axial potential has linear contributions, the density scales instead like  $N(Na)^{-2/3}$  resulting in at most a 50% change for  $a/\bar{a}$ . (3) We assumed that contributions of collective excitations to the released energy were small. Axial striations were observed in free expansion for both  $|m_F = +1\rangle$  and  $|m_F = -1\rangle$  atoms (probably created by the changing potential during the fast magnetic field ramp). However, the small scatter of points outside the resonance in Fig. 2b, which do not show any evidence of oscillations, suggests that the contribution of excitations to the released energy is negligible. (4) We assumed a sudden switch-off of the trap and ballistic expansion. The inhomogeneous bias field during the first 1–2 ms of free expansion accelerated the axial expansion, but had a negligible effect on the expansion of the condensate in the radial direction, which was evaluated for Fig. 2b.

None of the corrections (1)–(4) discussed above affect our conclusion that the scattering length varies dispersively near a Feshbach resonance. More accurate experiments should be done with a homogeneous bias field. In addition, an optical trap with larger volume and lower density would preclude the need to ramp the field quickly because three-body recombination would be reduced.

The trap losses observed around the Feshbach resonances merit further study as they might impose practical limits on the possibilities for varying the scattering length. An increase of the dipolar relaxation rate near Feshbach resonances has been predicted<sup>6,7</sup>, but for atoms in the lowest hyperfine state no such inelastic binary collisions are possible. Therefore, the observed trap loss is probably due to three-body collisions. In this case the loss rate is characterized by the coefficient  $K_3$ , defined as  $\dot{N}/N = -K_3 \langle n^2 \rangle$ . So far, there is no theoretical work on  $K_3$  near a Feshbach resonance. An analysis based on Fig. 2 shows that  $K_3$  increased on both sides of the resonance, because the loss rate increased while the density decreased or stayed constant. In any case, the fact that we observed Feshbach resonances at high atomic densities ( $\sim 10^{15} \text{ cm}^{-3}$ ) strongly enhanced this loss process, which can be avoided with a condensate at lower density in a modified optical trap. Control of the bias field with a precision better than  $\sim 10^{-4}$  will be necessary to achieve negative or extremely large values of the scattering length in a stable way.

## articles

### A tunable condensate

We have observed two Feshbach resonances for Bose–Einstein condensates of sodium through the abrupt loss of atoms, and obtained strong evidence for a dispersive variation of the scattering length by a factor of more than ten. ‘Tuning’ of the scattering length should become an important tool for ‘designing’ atomic quantum gases with novel properties; for example, to create ideal Bose–Einstein condensates with nearly zero scattering length, and to obtain a detailed picture of the collapse of a condensate with negative scattering length, which is so far not fully understood. Tuning the scattering length can also be used to vary interactions between different species<sup>24</sup> and thus control the phase diagram of multi-component condensates, possibly switching from interpenetrating superfluids to phase separation<sup>25</sup>. Feshbach resonances may also be important in atom optics, for modifying the atomic interactions in an atom laser, or more generally, for controlling nonlinear coefficients in atom optics with coherent beams of atoms. □

Received 18 February; accepted 19 February 1998.

1. Anderson, M. H., Ensher, J. R., Matthews, M. R., Wieman, C. E. & Cornell, E. A. Observation of Bose–Einstein condensation in a dilute atomic vapor. *Science* **269**, 198–201 (1995).
2. Davis, K. B. *et al.* Bose–Einstein condensation in a gas of sodium atoms. *Phys. Rev. Lett.* **75**, 3969–3973 (1995).
3. Bradley, C. C., Sackett, C. A. & Hulet, R. G. Bose–Einstein condensation of lithium: Observation of limited condensate number. *Phys. Rev. Lett.* **78**, 985–989 (1997).
4. Georgia Southern University BEC home page, <http://amo.phy.gasou.edu/bec.html>.
5. Bradley, C. C., Sackett, C. A., Tollett, J. J. & Hulet, R. G. Evidence of Bose–Einstein condensation in an atomic gas with attractive interactions. *Phys. Rev. Lett.* **75**, 1687–1690 (1995).
6. Tiesinga, E., Moerdijk, A. J., Verhaar, B. J. & Stoof, H. T. C. Conditions for Bose–Einstein condensation in magnetically trapped atomic cesium. *Phys. Rev. A* **46**, R1167–R1170 (1992).
7. Tiesinga, E., Verhaar, B. J. & Stoof, H. T. C. Threshold and resonance phenomena in ultracold ground-state collisions. *Phys. Rev. A* **47**, 4114–4122 (1993).
8. Moerdijk, A. J., Verhaar, B. J. & Axellson, A. Resonances in ultracold collisions of <sup>6</sup>Li, <sup>7</sup>Li and <sup>23</sup>Na. *Phys. Rev. A* **51**, 4852–4861 (1995).

9. Vogels, J. M. *et al.* Prediction of Feshbach resonances in collisions of ultracold rubidium atoms. *Phys. Rev. A* **56**, R1067–R1070 (1997).
10. Boesten, H. M. J. M., Vogels, J. M., Tempelaars, J. G. C. & Verhaar, B. J. Properties of cold collisions of <sup>39</sup>K atoms and of <sup>41</sup>K atoms in relation to Bose–Einstein condensation. *Phys. Rev. A* **54**, R3726–R3729 (1996).
11. Fedichev, P. O., Kagan, Yu., Shlyapnikov, G. V. & Walraven, J. T. M. Influence of nearly resonant light on the scattering length in low-temperature atomic gases. *Phys. Rev. Lett.* **77**, 2913–2916 (1996).
12. Bohn, J. L. & Julienne, P. S. Prospects for influencing the scattering lengths with far-off-resonant light. *Phys. Rev. A* **56**, 1486–1491 (1997).
13. Moerdijk, A. J., Verhaar, B. J. & Nagtegaal, T. M. Collisions of dressed ground-state atoms. *Phys. Rev. A* **53**, 4343–4351 (1996).
14. Feshbach, H. A unified theory of nuclear reactions. II. *Ann. Phys.* **19**, 287–313 (1962).
15. Bryant, H. C. *et al.* Observation of resonances near 11 eV in the photodetachment cross-section of the H<sup>+</sup> ion. *Phys. Rev. Lett.* **38**, 228–230 (1977).
16. Kagan, Yu., Surkov, E. L. & Shlyapnikov, G. V. Evolution and global collapse of trapped Bose condensates under variations of the scattering length. *Phys. Rev. Lett.* **79**, 2604–2607 (1997).
17. Newbury, N. R., Myatt, C. J. & Wieman, C. E. s-wave elastic collisions between cold ground-state <sup>87</sup>Rb atom. *Phys. Rev. A* **51**, R2680–R2683 (1995).
18. Courteille, P. & Heinzen, D. Paper presented at *SPIE Photonics West*, 24–30 Jan., San Jose, California (1998).
19. Stemper-Kurn, D. M. *et al.* Optical confinement of a Bose–Einstein condensate. *Phys. Rev. Lett.* (in the press).
20. Tiesinga, E. *et al.* A spectroscopic determination of scattering lengths for sodium atom collisions. *J. Res. Natl. Inst. Stand. Technol.* **101**, 505–520 (1996).
21. Mewes, M.-O. *et al.* Bose–Einstein condensation in a tightly confining d.c. magnetic trap. *Phys. Rev. Lett.* **77**, 416–419 (1996).
22. Andrews, M. R. *et al.* Propagation of sound in a Bose–Einstein condensate. *Phys. Rev. Lett.* **79**, 553–556 (1997).
23. Baym, G. & Pethick, C. J. Ground-state properties of magnetically trapped Bose-condensed rubidium gas. *Phys. Rev. Lett.* **76**, 6–9 (1996).
24. van Abeelen, F. A., Verhaar, B. J. & Moerdijk, A. J. Sympathetic cooling of <sup>6</sup>Li atoms. *Phys. Rev. A* **55**, 4377–4381 (1997).
25. Ho, T.-L. & Shenoy, V. B. Binary mixtures of Bose condensates of alkali atoms. *Phys. Rev. Lett.* **77**, 3276–3279 (1996).

**Acknowledgements.** We thank J. M. Vogels for discussions, A. P. Chikkatur for experimental assistance, and B. J. Verhaar and F. A. van Abeelen for providing updated theoretical predictions. We also thank D. Kleppner, D. E. Pritchard and R. A. Rubenstein for a critical reading of the manuscript. This work was supported by the Office of Naval Research, NSF, Joint Services Electronics Program (ARO), and the David and Lucile Packard Foundation. J.S. acknowledges support from the Alexander von Humboldt-Foundation, and D.M.S.-K. was supported by the JSEP graduate fellowship program.

Correspondence and requests for materials should be addressed to W.K.

# YOURS TO HAVE AND TO HOLD BUT NOT TO COPY

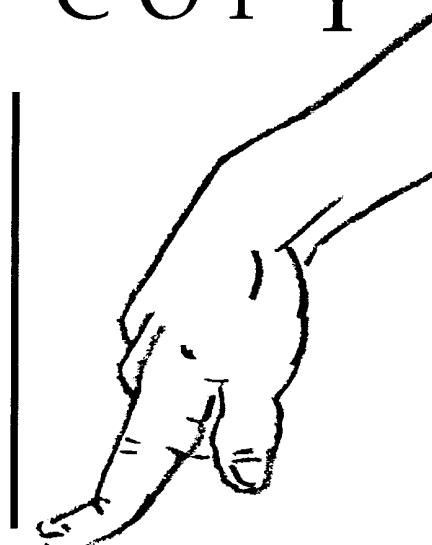
The publication you are reading is protected by copyright law. This means that the publisher could take you and your employer to court and claim heavy legal damages if you make unauthorised infringing photocopies from these pages.

Photocopying copyright material without permission is no different from stealing a magazine from a newsagent, only it doesn't seem like theft.

The Copyright Licensing Agency (CLA) is an organisation which issues licences to bring photocopying within the law. It has designed licensing services to cover all kinds of special needs in business, education, and government.

If you take photocopies from books, magazines and periodicals at work your employer should be licensed with CLA.

Make sure you are protected by a photocopying licence.



The Copyright Licensing Agency Limited  
90 Tottenham Court Road, London W1P 0LP

Telephone: 0171 436 5931  
Fax: 0171 436 3986

## Appendix B

# Strongly Enhanced Inelastic Collisions in a Bose-Einstein Condensate near Feshbach Resonances

This appendix includes the following preprint [9]: J. Stenger, S. Inouye, M.R. Andrews, H.-J. Miesner, D.M. Stamper-Kurn, and W. Ketterle, “Strongly Enhanced Inelastic Collisions in a Bose-Einstein Condensate near Feshbach Resonances,” *Phys. Rev. Lett.* **82**, 2422 (1999).

Several proposals have been made on the origin of these extraordinary large trap losses reported in this publication. They include a “two-body” mechanism where the formation of a molecular condensate of quasi-bound atom pairs was considered [170, 171], and a “three-body” mechanism where the deactivation of the resonant molecular state by interaction with a third condensate atom was considered [172, 173]. The decay rates near the Feshbach resonance were also experimentally studied in detail with  $^{85}\text{Rb}$  [174].

## Strongly Enhanced Inelastic Collisions in a Bose-Einstein Condensate near Feshbach Resonances

J. Stenger, S. Inouye, M. R. Andrews,\* H.-J. Miesner, D. M. Stamper-Kurn, and W. Ketterle  
*Department of Physics and Research Laboratory of Electronics, Massachusetts Institute of Technology,  
 Cambridge, Massachusetts 02139*  
 (Received 24 September 1998)

The properties of Bose-Einstein condensed gases can be strongly altered by tuning the external magnetic field near a Feshbach resonance. Feshbach resonances affect elastic collisions and lead to the observed modification of the scattering length. However, as we report here, the observed rate of inelastic collisions was strongly enhanced in a sodium Bose-Einstein condensate when the scattering length was tuned to both larger or smaller values than the off-resonant value. These strong losses impose severe limitations for using Feshbach resonances to tune the properties of Bose-Einstein condensates. [S0031-9007(99)08767-0]

PACS numbers: 03.75.Fi, 05.30.-d, 32.80.Pj, 65.50.+m

Most of the properties of Bose-Einstein condensates in dilute alkali gases are dominated by two-body collisions, which can be characterized by the  $s$ -wave scattering length  $a$ . The sign and the absolute value of the scattering length determine, e.g., stability, internal energy, formation rate, size, and collective excitations of a condensate. Near a Feshbach resonance the scattering length varies dispersively [1,2] covering the whole range of positive and negative values. Thus it should be possible to study strongly interacting, weakly or noninteracting, or collapsing condensates [3], all with the same alkali species and experimental setup.

A Feshbach resonance occurs when the energy of a molecular (quasi-) bound state is tuned to the energy of two colliding atoms by applying an external magnetic field. Such resonances have been observed in a Bose-Einstein condensate of Na ( $F = 1, m_F = +1$ ) atoms at 853 and 907 G [4,5], and in two experiments with cold clouds of  $^{85}\text{Rb}$  ( $F = 2, m_F = -2$ ) atoms at 164 G [6]. In the sodium experiment, the scattering length  $a$  was observed to vary dispersively as a function of the magnetic field  $B$ , in agreement with the theoretical prediction [2]:

$$a = a_0 \left( 1 + \frac{\Delta}{B_0 - B} \right), \quad (1)$$

where  $a_0$  is the off-resonant scattering length, and  $\Delta$  characterizes the width of the resonance.

In this Letter we report on the observation of a broad Feshbach resonance in sodium in the  $F = 1, m_F = -1$  state at 1195 G, and we investigate the strong inelastic processes accompanying all three sodium resonances, which result in a rapid loss of atoms while approaching or crossing the resonances with the external magnetic field. The losses show an unpredicted dependence on the external magnetic field and impose strong constraints on future experiments exploiting the tunability of the scattering length.

The experimental setup is very similar to that described in [4]. Magnetically trapped condensates in the  $F = 1, m_F = -1$  state were transferred into an optical trap

consisting of a focused far off-resonant infrared laser beam [7]. The atoms could be transferred to the  $m_F = +1$  state by an rf pulse in a 1 G bias field. For the studies of the Feshbach resonances, bias fields of up to 1500 G were applied with ramp speeds of up to 1000 G/ms. Inhomogeneities in the bias field exerted a force mainly in the axial direction. To prevent atoms from escaping, green light from an argon-ion laser was focused into two light sheets at the ends of the cigar shaped condensates, forming repulsive light barriers. The resulting trapping frequencies were around 1500 Hz radially and 150 Hz axially. The trap losses were studied by ramping the bias field with different ramp speeds to various field values near the resonances. The atoms were probed in ballistic expansion after suddenly switching off the optical trap. The magnetic field was switched off 2 ms later to ensure that the high field value of the scattering length was responsible for the acceleration of the atoms. After 7–25 ms free expansion the atoms were optically pumped into the  $F = 2$  state and observed in absorption using the cycling transition in a small bias field of 0.5 G.

The number of atoms  $N$ , the scattering length  $a$ , and the mean density  $\langle n \rangle$  could be obtained from the absorption images.  $N$  is calculated from the integrated optical density. The mean-field energy  $2\pi\hbar^2 a \langle n \rangle / m$  is converted into kinetic energy  $m v_{\text{rms}}^2 / 2$  after switching off the trap. The root-mean-square velocity  $v_{\text{rms}}^2$  can be extracted from the size of the cloud after the time of flight. As discussed in Ref. [4], the mean density  $\langle n \rangle$  is proportional to  $N(Na)^{-3/5}$  for a three-dimensional harmonic oscillator potential, and thus the scattering length  $a$  scales as

$$a \sim \frac{v_{\text{rms}}^5}{N}. \quad (2)$$

Normalized to unity far away from the resonance,  $v_{\text{rms}}^5 / N$  is equal to  $a/a_0$ . The proportionality factor in Eq. (2) involves the mean trapping frequency which was not accurately measured. However, we can obtain absolute values by multiplying the normalized scattering length

with the theoretical value of  $a_0$ . The off-resonance scattering length  $a_0 = 2.75$  nm of sodium at zero field increases to the triplet scattering length  $a_0 = a_T = 3.3$  nm [8] at the high fields of the resonances. Using this value, the mean density is obtained from the root-mean-square velocity

$$\langle n \rangle = \frac{m^2 v_{\text{rms}}^2}{4\pi \hbar^2 a}. \quad (3)$$

The peak density  $n_0$  is given by  $n_0 = (7/4)\langle n \rangle$  in a parabolic potential.

The experimental results for the 907 and 1195 G resonances are shown in Fig. 1. The number of atoms, the normalized scattering length, and the density are plotted versus the magnetic field. The resonances can be identified by enhanced losses. The 907 G resonance could be approached from higher field values by crossing it first with very high ramp speed. This was not possible for the 1195 G resonance due to strong losses, and also not for the 853 G resonance due to its proximity to the 907 G resonance and the technical difficulty of suddenly reversing the magnetic field ramp. For the 907 G resonance the dispersive change in  $a$  can clearly be identified. The solid lines correspond to the predicted shapes with width parameters  $\Delta = 1$  G in Fig. 1(b), and  $\Delta = -4$  G in Fig. 1(e). The negative width parameter for the 1195 G resonance reflects the decreasing scattering length when the resonance is approached from the low field side. The uncertainties of the positions are mainly due to uncertainties of the magnetic field calibration.

The time dependent loss of atoms from the condensate can be parametrized as

$$\frac{\dot{N}}{N} = - \sum_i K_i \langle n^{i-1} \rangle, \quad (4)$$

where  $K_i$  denotes an  $i$ -body loss coefficient, and  $\langle n \rangle$  the spatially averaged density. In general, the density  $n$  depends on the number of atoms  $N$  in the trap, and the loss curve is nonexponential. One-body losses—e.g., due to background gas collisions or spontaneous light scattering—are negligible under our experimental conditions. An increase of the dipolar relaxation rate (two-body collisions) near Feshbach resonances has been predicted [1]. However, for sodium in the lowest energy hyperfine state  $F = 1, m_F = +1$  binary inelastic collisions are not possible. Collisions involving more than three atoms are not expected to contribute. Thus the experimental study of the loss processes focuses on the three-body losses around the  $F = 1, m_F = +1$  resonances, while both two- and three-body losses must be considered for the  $F = 1, m_F = -1$  resonance.

Figures 1(c) and 1(f) show a decreasing or nearly constant density when the resonances were approached. Thus the enhanced trap losses can be explained only with increasing coefficients for the inelastic processes. The quantity  $\dot{N}/N\langle n^2 \rangle$  is plotted versus the magnetic field in Fig. 2 for both the 907 G and the 1195 G resonances. Assuming that mainly three-body collisions cause the trap losses, these plots correspond to the coefficient  $K_3$ . For the 907 G (1195 G) resonance, the off-resonant value of  $\dot{N}/N\langle n^2 \rangle$  is about 20 (60) times larger than the value for  $K_3$  measured at low fields [7]. Close to the resonances, the loss coefficient strongly increases both when tuning the

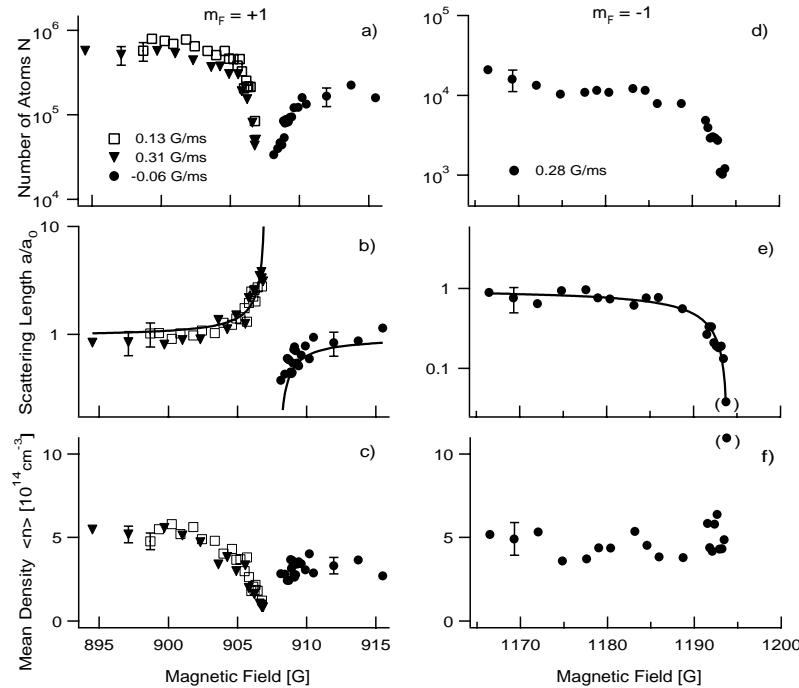


FIG. 1. Number of atoms  $N$ , normalized scattering length  $a/a_0$ , and mean density  $\langle n \rangle$  versus the magnetic field near the 907 and 1195 G Feshbach resonances. The different symbols for the data near the 907 G resonance correspond to different ramp speeds of the magnetic field. All data were extracted from time-of-flight images. The errors due to background noise of the images, thermal atoms, and loading fluctuations of the optical trap are indicated by single error bars in each curve.

scattering length larger or smaller than the off-resonant value. Since the density is nearly constant near the 1195 G resonance, the data can also be interpreted by a two-body coefficient  $K_2 = \dot{N}/N\langle n \rangle$  with an off-resonant value of about  $30 \times 10^{-15} \text{ cm}^3/\text{s}$ , increasing by a factor of more than 50 near the resonance. The contribution of the two processes cannot be distinguished by our data. However, dipolar losses are much better understood than three-body losses. The off-resonant value of  $K_2$  is expected to be about  $10^{-15} \text{ cm}^3/\text{s}$  [9] in the magnetic field range around the Feshbach resonances, suggesting that the three-body collisions are the dominant loss mechanism also for the 1195 G resonance.

The data analysis following Eqs. (2) and (3) is based on two major assumptions: the Thomas-Fermi approximation in which the kinetic energy is small compared to the mean-field energy, and the assumption that the atoms maintain the equilibrium density distribution during the change of the scattering length. The Thomas-Fermi approximation is well justified for all data points with  $a/a_0 > 1$ . For  $a/a_0 < 1$  close to the resonances, the mean-field energy of the condensates is only a few times larger than the level spacing in the trap. This leads to an overestimate of the density and thus to an underestimate of  $K_3$  for the data points with smallest scattering length. The ramp speeds of the magnetic field were chosen low enough to ensure adiabaticity, characterized by the condition  $\dot{a}/a \ll \omega_i$  [3], where  $\omega_i = 2\pi\nu_i$  are the trapping frequencies. Only for the data point closest to the 1195 G resonance (in parentheses) this condition is not fulfilled. Indeed, the scattering length  $a/a_0$  [Fig. 1(b)] and the quantity

$\dot{N}/N\langle n^2 \rangle$  [Fig. 2(a)] are independent of the ramp speeds, supporting the assumption of adiabaticity.

The observed increase and the magnetic field dependence of the three-body collision rate is not accounted for by any theory. Two theoretical treatments suggested that the rate coefficient  $K_3$  should vary monotonically with the scattering length following some power law. Fedichev *et al.* [10] derived the universal relation  $K_3 = 3.9\hbar a^4/2m$ . This prediction was in fairly good agreement with measurements in rubidium [11] and sodium [7] in low magnetic fields, even though it is not clear that the assumptions are valid in these experiments. By considering the breakup of a dimer by a third atom as the inverse process of recombination, Moerdijk *et al.* [12] suggested that the recombination rate is proportional to  $a^2$ . Although the assumptions of those theories might not be fulfilled near Feshbach resonances, they raised the hope that loss rates should not increase in the region of the Feshbach resonance where the scattering length is small. However, for scattering lengths smaller than  $a_0$  a substantial increase of the coefficient  $K_3$  was observed. Thus, these measurements show the need for a more accurate theoretical treatment of ultracold three-body collisions.

Another way to characterize the losses is a rapid sweep across the resonances. We determined the fraction of atoms which were lost in sweeping through the 853 G resonance and the 907 G resonance at different ramping speeds [13]. For this, the optical trap and the magnetic field were suddenly switched off, either before or after crossing the resonance, and the number of atoms was determined from absorption images as before.

Figure 3 shows the fraction of lost atoms as a function of the inverse ramp speed. Using the width of 1 G for the 907 G resonance, this implies that 70% of all atoms are lost in one microsecond. Across the 853 G resonance 70% of all atoms are lost at a ramp speed of 1 G/400  $\mu\text{s}$ . Assuming a universal behavior near Feshbach resonances, this implies that the strength of the 853 G resonance is four hundred times weaker than of the 907 G resonance. Since the width  $\Delta$  of the Feshbach resonance is proportional to the coupling strength between the two involved molecular states [2], a width of 0.0025 for the 853 G resonance is estimated. A theoretical prediction for the widths of the 907 G and the 853 G resonances are 1 and 0.01 G, respectively [14].

The loss of 70% of the atoms in only one microsecond cannot be explained by the usual picture of inelastic collisions. Because of the very small kinetic energy of Bose-Einstein-condensed atoms, which is of order  $\frac{\hbar^2}{2m}(\frac{n}{N})^{2/3}$  [15], the travel distance of an atom in 1  $\mu\text{s}$  is less than 1 nm under our conditions, much smaller than the mean distance between the atoms,  $d \approx n^{-1/3} \approx 100 \text{ nm}$ . Loss by two- or three-body collisions should then be limited to the small fraction of atoms which happen to be very close to other atoms. Possible explanations for the observed large losses are the divergence of the scattering

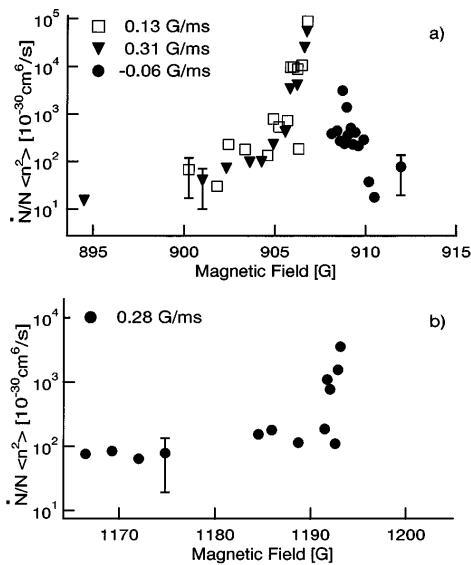


FIG. 2. Rate coefficients for inelastic collisions near Feshbach resonances.  $\dot{N}/N\langle n^2 \rangle$  is plotted versus the magnetic field. The time derivative  $\dot{N}$  was calculated from neighboring points without smoothing the data.

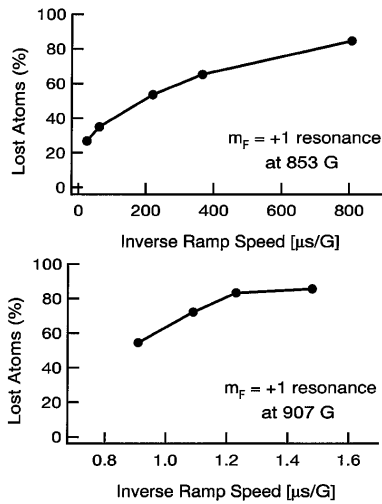


FIG. 3. Fraction of lost atoms after crossing the Feshbach resonances at 853 and 907 G for different inverse ramp speeds of the magnetic field.

length which allows for extremely long-range interactions between atoms, the formation of a molecular condensate, as recently proposed [16], or the impulsive excitation of solitons [17] when the region of negative scattering length is crossed. All suggested explanations require new concepts in many-body theory.

In conclusion, we have reported on the observation of a new,  $F = 1, m_F = -1$  Feshbach resonance at 1195 G in sodium, and we have investigated the enhanced trap losses accompanying all three resonances observed so far. The scattering length could be altered in the range of  $0.2 \leq a/a_0 \leq 5$ . The three-body loss coefficient  $K_3$  increased for both larger and smaller scattering length by up to more than 3 orders of magnitude. Those losses show that the density of the sodium samples must be reduced well below  $10^{14} \text{ cm}^{-3}$  for further studies exploiting the tunability of the scattering length near Feshbach resonances.

Our sweep experiments revealed that approaching a Feshbach resonance from the high magnetic field side is strongly affected by trap loss while crossing the resonance. The new  $m_F = -1$  resonance at 1195 G is well suited for studies of Bose-Einstein condensates with zero or negative scattering length, since this region is on the low field side of the resonance and can be directly approached without crossing any resonance.

So far, the physics of gaseous Bose-Einstein condensates has been very well described including only binary interactions between the atoms [15]. Feshbach resonances might open the possibility to study physics beyond this approximation which breaks down when the scattering length diverges, and also for very small scattering lengths when one has to consider higher order terms in the atomic interactions. Feshbach resonances may also lead to new inelastic processes. The observed losses of atoms near

Feshbach resonances indicate molecular and many-body physics which is not yet accounted for by any theory.

This work was supported by the Office of Naval Research, NSF, Joint Services Electronics Program (ARO), NASA, and the David and Lucile Packard Foundation. J. S. would like to acknowledge support from the Alexander von Humboldt Foundation.

\*Present address: Lucent Technologies, Murray Hill, NJ 07974.

- [1] E. Tiesinga, B. J. Verhaar, and H. T. C. Stoof, Phys. Rev. A **47**, 4114 (1993); E. Tiesinga, A. J. Moerdijk, B. J. Verhaar, and H. T. C. Stoof, Phys. Rev. A **46**, R1167 (1992).
- [2] A. J. Moerdijk, B. J. Verhaar, and A. Axelsson, Phys. Rev. A **51**, 4852 (1995).
- [3] Y. Kagan, E. L. Surkov, and G. V. Shlyapnikov, Phys. Rev. Lett. **79**, 2604 (1997).
- [4] S. Inouye, M. R. Andrews, J. Stenger, H.-J. Miesner, D. M. Stamper-Kurn, and W. Ketterle, Nature (London) **392**, 151 (1998).
- [5] Although  $F$  is a good quantum number only in small magnetic fields, in our case it unambiguously defines the states at high fields together with  $m_F$ .
- [6] P. Courteille, R. S. Freeland, D. J. Heinzen, F. A. van Abeelen, and B. J. Verhaar, Phys. Rev. Lett. **81**, 69 (1998); E. A. Cornell and C. E. Wieman (private communication).
- [7] D. M. Stamper-Kurn, M. R. Andrews, A. P. Chikkatur, S. Inouye, H.-J. Miesner, J. Stenger, and W. Ketterle, Phys. Rev. Lett. **80**, 2027 (1998).
- [8] C. J. Williams (private communication).
- [9] H. M. J. M. Boesten, A. J. Moerdijk, and B. J. Verhaar, Phys. Rev. A **54**, R29 (1996).
- [10] P. O. Fedichev, M. W. Reynolds, and G. V. Shlyapnikov, Phys. Rev. Lett. **77**, 2921 (1996).
- [11] E. A. Burt, R. W. Ghrist, C. J. Myatt, M. J. Holland, E. A. Cornell, and C. E. Wieman, Phys. Rev. Lett. **79**, 337 (1997).
- [12] A. J. Moerdijk, H. M. J. M. Boesten, and B. J. Verhaar, Phys. Rev. A **53**, 916 (1996).
- [13] The maximum ramp speed was 1000 G/ms. The switch-off time of the magnetic field was much shorter than a millisecond. The time between the crossing of the 853 G (907 G) resonance and the trap switch off was in the range of 1–20 ms (100–400  $\mu\text{s}$ ). The atom density had already dropped by a factor of at least ten for the 907 G resonance and more than 100 for the 853 G resonance before crossing the resonance again during the switch off. Thus additional losses of atoms during the switch-off of the magnetic field can be neglected.
- [14] F. A. v. Abeelen and B. J. Verhaar (private communication).
- [15] A. S. Parkins and D. F. Walls, Phys. Rep. **303**, 1 (1998); F. Dalfovo, S. Giorgini, L. P. Pitaevskii, and S. Stringari, Rev. Mod. Phys. (to be published).
- [16] E. Timmermans, P. Tommasini, R. Côté, M. Hussein, and A. Kerman, Phys. Rev. Lett. (to be published); cond-mat/9805323.
- [17] W. Reinhardt (private communication).

## Appendix C

# Bragg Spectroscopy of a Bose-Einstein condensate

This appendix includes the following paper [17]: J. Stenger, S. Inouye, A.P. Chikkatur, D.M. Stamper-Kurn, D.E. Pritchard, and W. Ketterle, “Bragg Spectroscopy of a Bose-Einstein condensate,” *Phys. Rev. Lett.* **82**, 4569 (1999).

# PHYSICAL REVIEW LETTERS

VOLUME 82

7 JUNE 1999

NUMBER 23

## Bragg Spectroscopy of a Bose-Einstein Condensate

J. Stenger, S. Inouye, A. P. Chikkatur, D. M. Stamper-Kurn, D. E. Pritchard, and W. Ketterle  
*Department of Physics and Research Laboratory of Electronics, Massachusetts Institute of Technology,  
Cambridge, Massachusetts 02139*  
(Received 11 January 1999)

Properties of a Bose-Einstein condensate were studied by stimulated, two-photon Bragg scattering. The high momentum and energy resolution of this method allowed a spectroscopic measurement of the mean-field energy and of the intrinsic momentum uncertainty of the condensate. The coherence length of the condensate was shown to be equal to its size. Bragg spectroscopy can be used to determine the dynamic structure factor over a wide range of energy and momentum transfers. [S0031-9007(99)09356-4]

PACS numbers: 03.75.Fi, 32.80.Pj

The first evidence for Bose-Einstein condensation (BEC) in dilute gases was obtained by a sudden narrowing of the velocity distribution as observed for ballistically expanding clouds of atoms [1]. Indeed, most textbooks describe Bose-Einstein condensation as occurring in momentum space [2]. However, the dominant contribution to the observed momentum distribution of the expanding condensate was the released interaction energy (mean-field energy). In this paper, we present a direct measurement of the true momentum distribution of a trapped Bose-Einstein condensate, which was significantly narrower than that observed by time of flight. Furthermore, since the size of a trapped condensate with repulsive interactions is larger than the trap ground state, the momentum distribution was also narrower than that of the trap ground state. Indeed, we show that the momentum distribution of a trapped condensate is Heisenberg-uncertainty limited by its finite size, i.e., that the coherence length of the condensate is equal to its physical size.

Subrecoil momentum resolution has been previously achieved by resolving the Doppler width of a Raman transition between different hyperfine states [3] or of a two-photon transition to a metastable excited state [4]. Here we use Bragg scattering where two momentum states of the *same* ground state are connected by a stimulated two-photon process. This process can be used to probe density fluctuations of the system and thus to measure

directly the dynamic structure factor  $S(\mathbf{q}, \nu)$ , which is the Fourier transform of the density-density correlation function and is central to the theoretical description of many-body systems [5,6]. In contrast to measuring  $S(\mathbf{q}, \nu)$  with inelastic neutron scattering as in superfluid helium [7], or using inelastic light scattering [8,9], Bragg scattering as used here is a stimulated process which greatly enhances resolution and sensitivity.

Bragg scattering of atoms from a light grating was first demonstrated in 1988 [10] and has been used to manipulate atomic samples in atom interferometers [11], in de Broglie wave frequency shifters [12], and also to couple out or manipulate a Bose-Einstein condensate [13]. Small angle Bragg scattering, called recoil-induced resonances, has been used for thermometry of laser-cooled atoms [14]. In this work we establish Bragg scattering as a spectroscopic technique to probe properties of the condensate. We refer to it as Bragg spectroscopy [15] in analogy to Raman spectroscopy which involves different *internal* states.

The absorption of  $N$  photons from one laser beam and stimulated emission into a second laser beam constitutes an  $N$ th order Bragg scattering process. The momentum transfer  $\mathbf{q}$  and energy transfer  $h\nu$  are given by  $|\mathbf{q}| = 2N\hbar k \sin(\vartheta/2)$  and  $\nu = N\Delta\nu$ , where  $\vartheta$  is the angle between the two laser beams with wave vector  $k$  and frequency difference  $\Delta\nu$ .

For noninteracting atoms with initial momentum  $\hbar\mathbf{k}_i$ , the resonance is given by the Bragg condition  $h\nu = q^2/2m + \hbar\mathbf{k}_i \cdot \mathbf{q}/m$ , which simply reflects energy and momentum conservation for a free particle. The second term is the Doppler shift of the resonance and allows the use of Bragg resonances in a velocity-selective way [13,14].

For a weakly interacting homogeneous condensate at density  $n$ , the dispersion relation has the Bogoliubov form [2]

$$\nu = \sqrt{\nu_0^2 + 2\nu_0 nU/h}, \quad (1)$$

where  $nU = n4\pi\hbar^2 a/m$  is the chemical potential, with  $a$  and  $m$  denoting the scattering length and the mass, respectively, and  $h\nu_0 = q^2/2m$ . For energies  $h\nu \gg nU$ , as probed in this paper, the spectrum is particlelike:

$$\nu \approx \nu_0 + nU/h. \quad (2)$$

The mean-field shift  $nU/h$  reflects the exchange term in the interatomic interactions: a particle with momentum  $\mathbf{q}$  experiences *twice* the mean-field energy as a particle in the condensate [2]. We use this property to determine the condensate mean-field energy spectroscopically. This is similar to the mean-field shift due to interactions with an electronically excited state which was used to identify BEC in atomic hydrogen [4].

The inhomogeneity of a trapped condensate adds two features which broaden the resonance. First, the finite size of the condensate implies a distribution of momenta which broadens the Bragg resonance due to the Doppler sensitivity of the excitation. In the Thomas-Fermi approximation, the condensate wave function  $\psi(x, y, z)$  in a harmonic trapping potential is  $[\psi(x, y, z)]^2 = n_0[1 - (x/x_0)^2 - (y/y_0)^2 - (z/z_0)^2]$ , where  $n_0$  denotes the peak density. The radii of the condensate  $(x_0, y_0, z_0)$  are given by  $x_0 = \sqrt{2n_0U/m(2\pi\nu_x)^2}$  (similar for  $y_0, z_0$ ), where  $\nu_i$  are the trapping frequencies. The distribution of momenta  $p_x$  along the  $x$  axis is given by the square of the Fourier transform of the wave function [16]

$$|\psi(p_x)|^2 \sim [J_2(p_x x_0/\hbar)/(p_x x_0/\hbar)^2]^2 \quad (3)$$

where  $J_2$  denotes the Bessel function of order 2. This distribution is similar to a Gaussian and has an rms width of  $\Delta p_x = \sqrt{21/8} \hbar/x_0$ . Thus, the corresponding Doppler broadening of the Bragg resonance  $\Delta\nu_p = \sqrt{21/8} q/2\pi m x_0$  is inversely proportional to the condensate size  $x_0$  and does not depend explicitly on the number of atoms.

Second, the Bragg resonance is also broadened and shifted by the inhomogeneous density distribution of the trapped condensate. The parabolic condensate wave function gives the (normalized) density distribution  $(15n/4n_0)\sqrt{1 - n/n_0}$ . The simplest model for the spectroscopic line shape  $I_n(\nu)$  due to the inhomogeneous density assumes that a volume element with density  $n$

leads to a line shift  $nU/h$  [Eq. (2)]:

$$I_n(\nu) = \frac{15h(\nu - \nu_0)}{4n_0U} \sqrt{1 - \frac{h(\nu - \nu_0)}{n_0U}}. \quad (4)$$

The effect of the inhomogeneous condensate density is thus to shift the line from the free-particle resonance  $\nu_0$  by  $4n_0U/7h$  (first moment), and to broaden the resonance to an rms width of  $\Delta\nu_n = \sqrt{8/147} n_0U/h$ . In contrast to the finite-size Doppler broadening, the mean-field broadening depends only on the maximum density, but not explicitly on the size.

In our experiments, both the finite-size and mean-field broadening mechanisms had to be considered. While the exact calculation of the line shape requires detailed knowledge of the excitation wave functions, the total line shift and rms width can be calculated using sum rules and Fermi's Golden Rule. Thus, it can rigorously be shown that the total line shift remains  $4n_0U/7h$ , while the rms width of the resonance becomes  $\Delta\nu = \sqrt{\Delta\nu_p^2 + \Delta\nu_n^2}$  which is the quadrature sum of the Doppler and mean-field widths [17].

We produced magnetically trapped, cigar-shaped Bose-Einstein condensates as in previous work [18]. In order to study the resonance as a function of density and size, we prepared condensates using two different sets of trapping frequencies and varied the number of atoms by removing a variable fraction using the rf output coupler [19]. The density of the condensate was determined from the expansion of the cloud in time of flight and the size from the atom number and the trapping frequencies [18]. Bragg scattering was performed by using two counterpropagating beams aligned perpendicularly to the weak axis of the trap. Spectra were taken by pulsing on the light shortly before switching off the trap and determining the number of scattered atoms as a function of the frequency difference between the two Bragg beams. Since the kinetic energy of the scattered atoms was much larger than the mean-field energy, they were well separated from the unscattered cloud after a typical ballistic expansion time of 20 ms. Center frequencies and widths were determined from Gaussian fits to the spectra.

The duration, intensity, and detuning of the Bragg pulses were chosen carefully. The instrumental resolution is limited by the pulse duration  $\delta t_{\text{pulse}}$  due to its Fourier spectrum, in our case requiring  $\delta t_{\text{pulse}} > 250 \mu\text{s}$  for sub-kHz resolution. The maximum pulse duration of  $500 \mu\text{s}$  was chosen to be less than one quarter of the trap period by which time the initially scattered atoms would come to rest and thus would be indistinguishable from the unscattered atoms in time of flight. The light intensity was adjusted to set the peak excitation efficiency to about 20%. Sufficient detuning was necessary to avoid heating of the sample. The ratio of the two-photon rate  $\omega_R^2/4\Delta$  to the spontaneous scattering rate  $\omega_R^2\Gamma/2\Delta^2$  is  $\Gamma/2\Delta$ , where  $\omega_R$  denotes the single beam

Rabi frequency,  $\Delta$  the detuning, and  $\Gamma$  the natural linewidth. Spontaneous scattering was negligible for the chosen detuning of 1.77 GHz below the  $3S_{1/2} F = 1 \rightarrow 3P_{3/2} F = 2$  transition.

The relative detuning of the two Bragg beams was realized in two ways. In one scheme, a beam was split and sent through two independent acousto-optical modulators driven with the appropriate difference frequency, and then overlapped in a counterpropagating configuration. Alternatively, a single beam was modulated with two frequencies separated by the relative detuning and backreflected. Both methods were insensitive to frequency drifts of the laser since the Bragg process only depends on the relative frequency of the two beams, which was controlled by rf synthesizers. The second method simultaneously scattered atoms in the  $+x$  and  $-x$  directions and was thus helpful to identify center-of-mass motion of the cloud. We estimate that residual vibrational noise broadened the line by less than 1 kHz. This resolution corresponds to a velocity resolution of 0.3 mm/s or 1% of the single-photon recoil. At a radial trapping frequency of 200 Hz, this required that the trapped condensate vibrate with an amplitude less than 0.2  $\mu\text{m}$ .

Figure 1 shows typical spectra, taken both for a trapped condensate and after 3 ms time of flight when the mean-field energy was fully converted into kinetic energy. The rms width of the resonance for the ballistically expanding cloud is 20 kHz, which is much narrower than the 65 kHz wide distribution of a thermal cloud at 1  $\mu\text{K}$ , a typical value for the BEC transition temperature under our conditions. We could not measure the thermal distribution with the same pulse duration as for the condensate since the fraction of scattered atoms was too small due to the broad resonance. The spectra for the thermal cloud and the expanding condensate correspond to the spatial distributions observed by absorption imaging after sufficiently long time of flight. With this technique, the BEC tran-

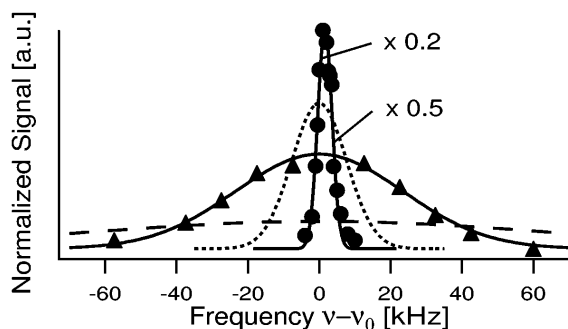


FIG. 1. Bragg resonances for a trapped condensate (circles) and after 3 ms time of flight (triangles). For comparison, the momentum distributions of the ground state of the trapping potential (dotted curve) and of a 1  $\mu\text{K}$  cold, thermal cloud (dashed curve) are indicated. The heights of the curves for the trapped condensate and the ground state momentum distribution are scaled down as indicated in the figure.

sition is indicated by a sudden narrowing of the time-of-flight distribution by a factor of 3. Using Bragg spectroscopy, the signature of BEC is much more dramatic—the condensate resonance is more than 30 times narrower than of the thermal cloud, and indeed narrower than that of the ground state of the trap.

Figure 2 traces the broadening of the Bragg resonance from about 2 to 20 kHz (rms width) after releasing a condensate from the trap as the mean-field interaction energy is converted into kinetic energy. After 3 ms, the momentum distribution of the cloud reached its asymptotic velocity width and expanded ballistically thereafter. Castin and Dum [20] considered the expansion of a cigar-shaped condensate in the Thomas-Fermi approximation and found that the velocity distribution should be parabolic with a maximum velocity  $v_x$  which grows as  $v_x = v_\infty 2\pi\nu_x t / \sqrt{1 + (2\pi\nu_x t)^2}$ , where  $v_\infty = 2\pi\nu_x x_0$ . To compare with our data, we combined in quadrature the Doppler width predicted by this velocity distribution, the mean-field width, and the finite-size width (assuming the size of the condensate grows as  $x(t) = x_0 \sqrt{1 + (2\pi\nu_x t)^2}$  [20]). As shown in Fig. 2, the agreement with our measurement is excellent.

The narrow resonance of the trapped condensate (Fig. 1) was studied as a function of the condensate density and size. Figure 3a demonstrates the linear dependence of the frequency shift on the density. The slope of the linear fit corresponds to  $(0.54 \pm 0.07)n_0 U/h$ , in agreement with the prediction of  $4n_0 U/7h$ . In Fig. 3b, the expected widths due to the mean-field energy and finite size are shown for the two different trapping frequencies studied. The data agree well with the solid lines, which represent the quadrature sum of the two contributions. To demonstrate the finite-size effect the same data are shown in Fig. 3c after subtracting the mean-field broadening and the finite pulse-length broadening (0.5 kHz). The linewidths are consistent with the expected  $1/x_0$  dependence. Even without these corrections the measured linewidths are within 20% of the value expected due to the Heisenberg-uncertainty limited momentum distribution (Fig. 3b).

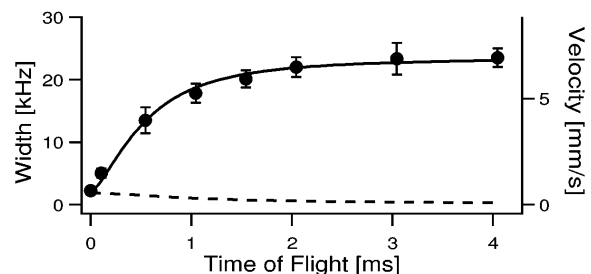


FIG. 2. Mean-field acceleration of a condensate released from the trap. Shown is the increase of the rms width of the Bragg resonance during the expansion. The solid line is the theoretical prediction [20] using the trap frequency  $\nu_x = 195$  Hz. The dashed line represents the contributions of mean-field energy and finite size to the total width.

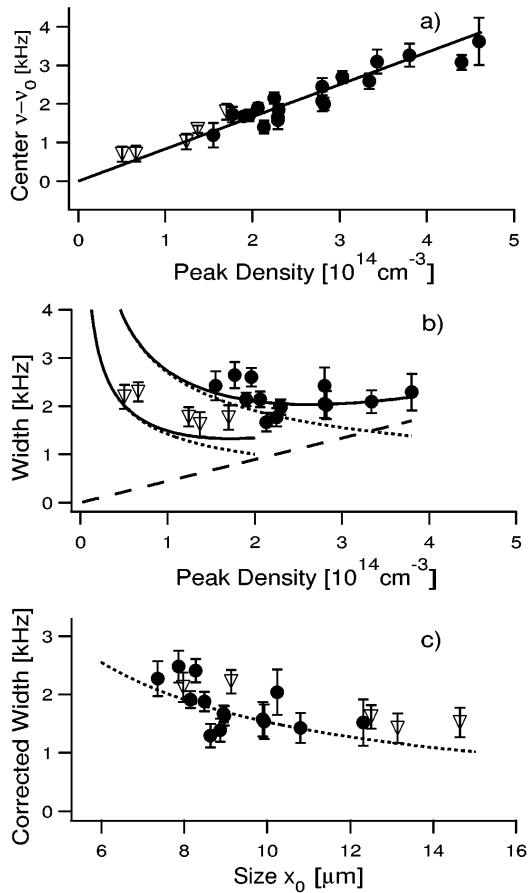


FIG. 3. Bragg spectroscopy of a trapped condensate. Line shifts (a) and rms widths (b) are shown for various densities and sizes of the condensate using two different radial trapping frequencies,  $\nu_x = (195 \pm 20)$  Hz (circles), and  $\nu_x = (95 \pm 20)$  Hz (triangles). The lines in (b) show the contributions of the mean-field energy (dashed) and due to the finite size (dotted, for both trapping frequencies) and their quadrature sum (solid lines). (c) displays the width after subtraction of the contribution of the mean field and the finite pulse duration and compares it with the prediction for the momentum uncertainty due to the finite size. The error bars are  $1\sigma$  errors of the Gaussian fits to the data.

The momentum spread of the condensate is limited by its coherence length  $x_c$  which, in the case of long-range order, should be equal to the size  $x_0$  of the condensate. Our results show that  $x_c \approx x_0$  in the radial direction of the trap, thus providing a quantitative measure of the long-range coherence observed earlier by interfering two condensates [21]. In particular, our measurements indicate that the condensate does not have phase fluctuations on this length scale, i.e., that it does not consist of smaller quasicondensates with random relative phases. It would be interesting to measure the coherence length during the formation of the condensate, e.g., after suddenly quenching the system below the BEC transition

temperature [22], and to observe the disappearance of phase fluctuations.

In this work we have energy resolved the response of the condensate to a momentum transfer of two photon recoils, constituting a measurement of the dynamic structure factor  $S(\mathbf{q}, \nu)$  for this value of  $\mathbf{q}$ . Different momentum transfers are possible by changing the angle between the Bragg beams and/or the order  $N$  of the Bragg transition, thus enabling measurements of  $S(\mathbf{q}, \nu)$  over a wide range of parameters. At low momentum transfer, the line shape is dominated by the mean-field energy and by phononlike collective excitations, whereas at high momentum transfers, the linewidth mainly reflects the momentum distribution of individual atoms. This is analogous to neutron scattering in liquid helium, where slow neutrons were used to observe the phonon and roton part of the dispersion curve, and fast neutrons were used to determine the zero-momentum peak of the condensate [7]. While we have observed higher-order Bragg scattering up to third order in the trapped condensate using higher laser intensities, its spectroscopic use was precluded by severe Rayleigh scattering, and would require larger detuning from the atomic resonance.

The use of inelastic light scattering to determine the structure factor of a Bose-Einstein condensate was discussed in several theoretical papers [8,9]. It would require the analysis of scattered light with kHz resolution and suffers from a strong background of coherently scattered light [9]. Bragg spectroscopy has distinct advantages because it is a stimulated, background-free process in which the momentum transfer and energy are predetermined by the laser beams rather than postdetermined from measurements of the momentum and energy of the scattered particle.

In conclusion, we have established Bragg spectroscopy as a new tool to measure properties of a condensate with spectroscopic precision. We have demonstrated its capability to perform high-resolution velocimetry by resolving the narrow momentum distribution of a trapped condensate and by observing the acceleration phase in ballistic expansion. Since the momentum transfer can be adjusted over a wide range, Bragg spectroscopy can be used to probe such diverse properties as collective excitations, mean-field energies, coherence properties, vortices, and persistent currents.

This work was supported by the Office of Naval Research, NSF, Joint Services Electronics Program (ARO), NASA, and the David and Lucile Packard Foundation. A.P.C. would like to acknowledge support from NSF, D.M.S.-K. from the JSEP, and J.S. from the Alexander von Humboldt Foundation.

[1] M.H. Anderson *et al.*, Science **269**, 198 (1995); K.B. Davis *et al.*, Phys. Rev. Lett. **75**, 3969 (1995).

- 
- [2] K. Huang, *Statistical Mechanics* (Wiley, New York, 1987), 2nd ed.
- [3] M. Kasevich *et al.*, Phys. Rev. Lett. **66**, 2297 (1991).
- [4] D.G. Fried *et al.*, Phys. Rev. Lett. **81**, 3811 (1998); T. C. Killian *et al.*, *ibid.* **81**, 3807 (1998).
- [5] T. J. Greytak, in *Quantum Liquids*, edited by J. Ruvalds and T. Regge (North-Holland, New York, 1978).
- [6] A. Griffin, *Excitations in a Bose-Condensed Liquid* (Cambridge University Press, Cambridge, 1993).
- [7] P. Sokol, in *Bose-Einstein Condensation*, edited by A. Griffin, D.W. Snoke, and S. Stringari (Cambridge University Press, Cambridge, 1995); P. Nozieres and D. Pines, *The Theory of Quantum Liquids* (Addison-Wesley, Reading, 1994).
- [8] J. Javanainen, Phys. Rev. Lett. **75**, 1927 (1995); R. Graham and D. Walls, Phys. Rev. Lett. **76**, 1774 (1996); A. S. Parkins and D.F. Walls, Phys. Rep. **303**, 1 (1998), and references therein.
- [9] H.D. Politzer, Phys. Rev. A **55**, 1140 (1996).
- [10] P.J. Martin, B.G. Oldaker, A.H. Miklich, and D.E. Pritchard, Phys. Rev. Lett. **60**, 515 (1988).
- [11] D.M. Giltner, R.W. McGowan, and S.A. Lee, Phys. Rev. Lett. **75**, 2638 (1995).
- [12] S. Bernet *et al.*, Phys. Rev. Lett. **77**, 5160 (1996).
- [13] M. Kozuma *et al.*, Phys. Rev. Lett. **82**, 871 (1999).
- [14] J.-Y. Courtois, G. Grynberg, B. Lounis, and P. Verkerk, Phys. Rev. Lett. **72**, 3017 (1994).
- [15] P.R. Berman and B. Bian, Phys. Rev. A **55**, 4382 (1997).
- [16] G. Baym and C.J. Pethick, Phys. Rev. Lett. **76**, 6 (1996).
- [17] D.M. Stamper-Kurn (to be published).
- [18] M.-O. Mewes *et al.*, Phys. Rev. Lett. **77**, 416 (1996).
- [19] M.-O. Mewes *et al.*, Phys. Rev. Lett. **78**, 582 (1997).
- [20] Y. Castin and R. Dum, Phys. Rev. Lett. **77**, 5315 (1996).
- [21] M.R. Andrews *et al.*, Science **275**, 637 (1997).
- [22] H.-J. Miesner *et al.*, Science **279**, 1005 (1998); D.M. Stamper-Kurn *et al.*, Phys. Rev. Lett. **81**, 2194 (1998).

## Appendix D

# Superradiant Rayleigh Scattering from a Bose-Einstein Condensate

This appendix includes the following paper [18]: S. Inouye, A.P. Chikkatur, D.M. Stamper-Kurn, J. Stenger, D.E. Pritchard, W. Ketterle, “Superradiant Rayleigh Scattering from a Bose-Einstein Condensate,” *Science* **285**, 571 (1999).

## REPORTS

opposed to 19,000 to 23,000 years in the insolation record), indicating a more complicated relation (15, 16).

Our results demonstrate that embedded within the long-term climatic changes were much finer scale variations at sub-Milankovitch time scales (Fig. 2). We therefore propose that, in addition to the climatic changes associated with the linear response to the orbital forcing, a nonlinear response at sub-Milankovitch frequencies may have been responsible for the initiation of the NHG. Perhaps an incremental increase in amplitude and frequency of these sub-Milankovitch oscillations across the transition resulted in a shortening of the length of time between subsequent cold stages. This would have reduced the time for climatic "recovery" between each cycle, thereby providing a mechanism for the buildup of large terrestrial ice

sheets. Thus, a combination of factors at different time scales within a nonlinear framework may be responsible for the changes leading to the NHG.

### References and Notes

1. L. J. Lourens and F. J. Hilgen, *Quat. Int.* **40**, 43 (1997).
2. M. E. Raymo, D. Hodell, E. Jansen, *Paleoceanography* **7**, 645 (1992).
3. G. H. Haug and R. Tiedemann, *Nature* **393**, 673 (1998).
4. X. S. Li *et al.*, *Geophys. Res. Lett.* **25**, 915 (1998).
5. W. F. Ruddimann and J. E. Kutzbach, *J. Geophys. Res.* **94**, 18409 (1989).
6. M. E. Raymo, W. F. Ruddimann, P. N. Froelich, *Geology* **16**, 649 (1988).
7. M. A. Maslin, X. S. Li, M. F. Loutre, A. Berger, *Quat. Sci. Rev.* **17**, 411 (1998).
8. K. J. Willis, A. Kleczkowski, S. J. Crowhurst, *Nature* **397**, 685 (1999).
9. C. Ravasz, *Annu. Rep. Hung. State Geol. Inst.* **1974** (1974), p. 221.
10. M. Hajós, *Annu. Rep. Hung. State Geol. Inst.* **1988** (1989), p. 5.

11. N. J. Shackleton, M. A. Hall, D. Pate, in *Proceedings of the Ocean Drilling Program, Scientific Results*, N. G. Pisias, T. R. Janecek, A. Palmer-Julson, T. H. van Andel, Eds. (Ocean Drilling Program, College Station, TX, 1995), vol. 138, pp. 337-355.
12. M. A. Maslin, G. H. Haug, M. Sarnthein, R. Tiedemann, *Geol. Rundsch.* **85**, 452 (1996).
13. G. Kukla, *Boreas* **1**, 63 (1972).
14. J. Laskar, F. Joutel, F. Boudin, *Astron. Astrophys.* **270**, 522 (1993).
15. T. K. Hagelberg, G. Bond, P. deMenocal, *Paleoceanography* **9**, 545 (1994).
16. A. Berger and M. F. Loutre, *Science* **278**, 1476 (1997).
17. D. B. Percival and A. T. Walden, *Spectral Analysis for Physical Applications* (Cambridge Univ. Press, Cambridge, 1993).
18. This work was supported by a Royal Society University Research Fellowship (K.J.W.), a King's College Senior Research Fellowship (A.K.), Biotechnology and Biological Sciences Research Council (K.M.B. and C.A.G.), a Royal Society Leverhulme Trust Senior Research Fellowship (C.A.G.), and St. Hugh's College Oxford Higher Studies Fund (payment for color of Fig. 1), which we gratefully acknowledge.

4 January 1999; accepted 7 June 1999

# Superradiant Rayleigh Scattering from a Bose-Einstein Condensate

S. Inouye,\* A. P. Chikkatur, D. M. Stamper-Kurn, J. Stenger, D. E. Pritchard, W. Ketterle

Rayleigh scattering off a Bose-Einstein condensate was studied. Exposing an elongated condensate to a single off-resonant laser beam resulted in the observation of highly directional scattering of light and atoms. This collective light scattering is caused by the coherent center-of-mass motion of the atoms in the condensate. A directional beam of recoiling atoms was built up by matter wave amplification.

Rayleigh scattering, the scattering of a photon off an atom, is the most elementary process involving atoms and light. It is responsible for the index of refraction of gases, the blue sky, and resonance fluorescence. This process can be divided into absorption of a photon and subsequent spontaneous emission. Photon scattering imparts a recoil momentum to the atom. Because of the random nature of spontaneous emission, the direction of the recoil is random, leading to momentum diffusion and heating of the atomic motion.

With the realization of Bose-Einstein condensation (BEC) (1), it is now possible to study the interactions of coherent light with an ensemble of atoms in a single quantum state. The high degree of spatial and temporal coherence of a condensate was confirmed in several experiments (2, 3). This raises the important question of whether the coherent

external motion of the atoms can alter the interactions between atoms and light. Here we show that the long coherence time of a Bose-Einstein condensate introduces strong correlations between successive Rayleigh scattering events. The scattering of photons leaves an imprint in the condensate in the form of long-lived excitations that provide a positive feedback and lead to directional Rayleigh scattering.

The gain mechanism for Rayleigh scattering from a condensate can be derived semiclassically. When a condensate of  $N_0$  atoms is exposed to a laser beam with wave vector  $\mathbf{k}_0$  and scatters a photon with wave vector  $\mathbf{k}_j$ , an atom [or quasi-particle, also called momentum side mode in (4)] with recoil momentum  $\hbar\mathbf{K}_j = \hbar(\mathbf{k}_0 - \mathbf{k}_j)$ , where  $\hbar$  is Planck's constant divided by  $2\pi$ , is generated. Because light propagates at a velocity about 10 orders of magnitude greater than the atomic recoil velocity (3 cm/s for sodium), the recoiling atoms remain within the volume of the condensate long after the photons have left and affect subsequent scattering events. They interfere with the condensate at rest to form a

moving matter wave grating of wave vector  $\mathbf{K}_j$ , which diffracts the laser beam into the phase-matching direction  $\mathbf{k}_j$  ( $= \mathbf{k}_0 - \mathbf{K}_j$ ). This diffraction is a self-amplifying process because every diffracted photon creates another recoiling atom that increases the amplitude of the matter wave grating.

When  $N_j$  recoiling atoms with momentum  $\hbar\mathbf{K}_j$  interfere with  $N_0$  condensate atoms at rest, the density modulation comprises  $N_{\text{mod}} = 2\sqrt{N_0 N_j}$  atoms. The light scattered by these atoms interferes constructively in the phase-matching direction with a total power  $P$  of

$$P = \hbar\omega_j R \frac{N_{\text{mod}}^2}{4} \quad (1)$$

$$f_j = \frac{\sin^2\theta_j}{8\pi/3} \Omega_j \quad (2)$$

Here,  $R$  is the rate for single-atom Rayleigh scattering, which is proportional to the laser intensity, and  $\omega$  is the frequency of the radiation. The angular term in Eq. 2 reflects the dipolar emission pattern with  $\theta_j$  being the angle between the polarization of the incident light and the direction of emission. Because of the finite size of the sample, the phase-matching condition is fulfilled over the solid angle  $\Omega_j \sim \lambda^2/A$ , where  $A$  is the cross-sectional area of the condensate perpendicular to the direction of the light emission and  $\lambda$  is the optical wavelength. More rigorously,  $\Omega_j$  is given by the usual phase-matching integral for superradiance in extended samples (5):

$$\Omega_j = \int d\Omega(\mathbf{k}) \left| \int \tilde{\rho}(\mathbf{r}) e^{i(\mathbf{k}_j - \mathbf{k}) \cdot \mathbf{r}} d\mathbf{r} \right|^2 \quad (3)$$

where  $|\mathbf{k}| = |\mathbf{k}_j|$  and  $\tilde{\rho}(\mathbf{r})$  is the normalized spatial density distribution in the condensate ( $\int \tilde{\rho}(\mathbf{r}) d\mathbf{r} = 1$ ).

Because each scattered photon creates a

Department of Physics and Research Laboratory of Electronics, Massachusetts Institute of Technology, Cambridge, MA 02139, USA.

\*To whom correspondence should be addressed. E-mail: sinouye@mit.edu

## REPORTS

recoiling atom, we obtain the growth rate for  $N_j$  from  $P/\hbar\omega$ :

$$\dot{N}_j = G_j N_j \quad (4)$$

This equation predicts exponential growth of  $N_j$  with the small-signal gain  $G_j = RN_0 f_j \sim R \sin^2 \theta_j D_j$ , where  $D_j \sim \rho_0 \lambda^2 l_j$  is the resonant optical density for a condensate with an atomic density  $\rho_0$  and a length  $l_j$  along the axis of emission. Therefore, for an anisotropic Bose condensate, the gain is largest when the light is emitted along its longest axis [the “end-fire mode” (6)]. Equation 4 is valid in the absence of decoherence and predicts the buildup of highly anisotropic Rayleigh scattering from a nonspherical sample of atoms.

For the experimental study of directional Rayleigh scattering, elongated Bose-Einstein condensates were prepared in a magnetic trap (7). The trapped condensates were about 20  $\mu\text{m}$  in diameter  $d$  and 200  $\mu\text{m}$  in length  $l$  and contained several million sodium atoms in the  $F = 1$  hyperfine ground state. The condensate was exposed to a single off-resonant laser pulse that was red-detuned by 1.7 GHz from the  $3S_{1/2}, F = 1 \rightarrow 3P_{3/2}, F = 0, 1, 2$  transition. The beam had a diameter of a few millimeters, propagated at an angle of  $45^\circ$  to the vertical axis, and intersected the elongated condensate perpendicular to its long axis (Fig. 1A). Typical laser intensities were between 1 and 100  $\text{mW}/\text{cm}^2$ , corresponding to Rayleigh scattering rates of  $4.5 \times 10^1$  to

$4.5 \times 10^3 \text{ s}^{-1}$  and the pulse duration between 10 and 800  $\mu\text{s}$ . To probe the momentum distribution of scattered atoms, we suddenly turned off the magnetic trap immediately after the light pulse and imaged the ballistically expanding cloud after 20- to 50-ms time of flight using resonant probe light propagating vertically onto a charge-coupled device (CCD) camera.

The momentum distributions of atoms after light scattering (Fig. 1B, to G) showed a marked dependence on the polarization of the incident laser beam. For polarization parallel to the long axis of the elongated condensate ( $\theta_j = 0$ ), light emission into the end-fire mode was suppressed, and the distribution of atoms followed the dipolar pattern of normal Rayleigh scattering. For perpendicular polarization ( $\theta_j = \pi/2$ ), photons were predominantly emitted along the long axis of the condensate, and the recoiling atoms appeared as highly directional beams propagating at an angle of  $45^\circ$  with respect to this axis (8).

A fully quantum-mechanical treatment reproduces the semiclassical result (Eq. 4) except that  $\dot{N}_j$  is replaced by  $\dot{N}_j + 1$ :

$$\dot{N}_j = RN_0 \frac{\sin^2 \theta_j}{8\pi/3} \Omega_j (N_j + 1) \quad (5)$$

Equation 5 now describes both normal Rayleigh scattering at a constant total rate  $\Sigma \dot{N}_j = RN_0$  when  $N_j \ll 1$  and exponential gain of the  $j$ th recoil mode once  $\dot{N}_j$  becomes

nonnegligible. Initially, the angular distribution of the scattered light follows the single-atom spontaneous (dipolar) emission pattern but can become highly anisotropic when stimulation by the atomic field becomes important (9, 10).

This phenomenon is analogous to the superradiance discussed by Dicke (6). He showed that the optical emission of incoherently excited atoms can be highly directional. The key feature of superradiance (or superfluorescence) (11) is that spontaneous emission is not a single-atom process but a collective process of all atoms, leaving the atoms in a coherent superposition of ground and excited states (12). The condensate at rest “pumped” by the off-resonant laser corresponds to the electronically excited state in the Dicke case. It can decay by a spontaneous Raman process to a state with photon recoil (corresponding to the ground state). The rate of superradiant emission in Dicke’s treatment is proportional to the square of an oscillating macroscopic dipole moment. In the present case, the radiated intensity is proportional to the square of the contrast of the matter wave interference pattern between the condensate and the recoiling atoms.

A characteristic feature of superradiance is an accelerated decay of the initial state. In our experiment, normal exponential decay and the superradiant decay could be directly compared by tracing the number of atoms remaining in the condensate at rest after exposure to light of different polarizations. For parallel polarization, we observed a simple exponential decay with the expected Rayleigh scattering rate (Fig. 2). For perpendicular polarization, the end-fire mode was active, and the condensate decayed nonexponentially with a strongly accelerated superradiant rate.

To verify the directional emission of light, we observed the scattered light by directing it

**Fig. 1.** Observation of superradiant Rayleigh scattering. **(A)** An elongated condensate is illuminated with a single off-resonant laser beam. Collective scattering leads to photons scattered predominantly along the axial direction and atoms at  $45^\circ$ . **(B to G)** Absorption images after 20-ms time of flight show the atomic momentum distribution after their exposure to a laser pulse of variable duration. When the polarization was parallel to the long axis, superradiance was suppressed, and normal Rayleigh scattering was observed (B to D). For perpendicular polarization, directional superradiant scattering of atoms was observed (E to G) and evolved to repeated scattering for longer laser pulses (F and G). The pulse durations were 25 (B), 100 (C and D), 35 (E), 75 (F), and 100 (G)  $\mu\text{s}$ . The field of view of each image is 2.8 mm by 3.3 mm. The scattering angle appears larger than  $45^\circ$  because of the angle of observation. All images use the same color scale except for (D), which enhances the small signal of Rayleigh scattered atoms in (C).

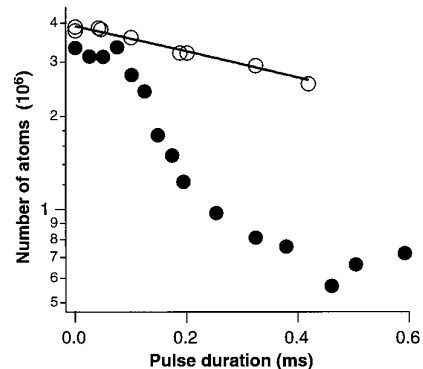
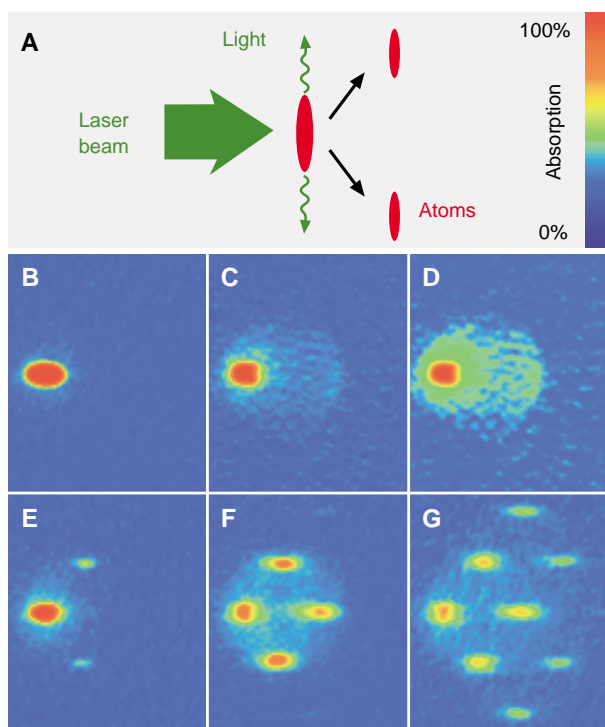


**Fig. 2.** The decay of atoms in the condensate at rest showed the normal exponential decay for parallel polarization (○) and faster superradiant decay for perpendicular polarization (●). The laser intensities (13  $\text{mW}/\text{cm}^2$ ) and oscillation strengths were equal in both cases.

## REPORTS

onto a CCD camera (Fig. 3A). The camera was positioned out of focus of the imaging system, so that the images represent the angular distribution of photons emitted around the axial direction. The images consisted of bright spots with angular widths equal to the diffraction limit for a source with a diameter of  $\sim 14 \mu\text{m}$ . Typical images showed more than one such spot, and their pattern changed randomly under the same experimental conditions. The observation of a few spots is consistent with a Fresnel number  $F = \pi d^2/$

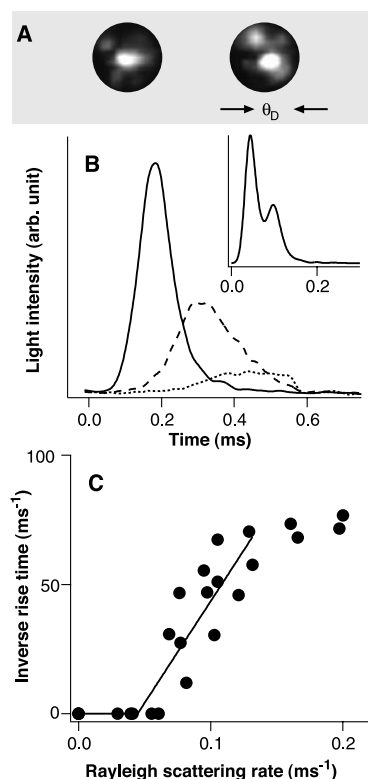


**Fig. 3.** Observation of directional emission of light. (A) The angular pattern of the emitted light along the axial direction showed a few bright spots with an angular width  $\theta_0$  ( $1/e^2$  diameter) of  $107 \pm 20$  mrad, corresponding to the diffraction-limited angle of an object of  $\sim 14 \mu\text{m}$  in diameter. The images were integrated over the entire duration of the light pulse. (B) The temporal evolution of the light intensity showed a strong initial increase characteristic of a stimulated process. For higher laser power, the pulse was shorter and more intense. The laser intensities were 3.8 (solid line), 2.4 (dashed line), and 1.4 (dotted line)  $\text{mW}/\text{cm}^2$ , and the duration was 550  $\mu\text{s}$ . The inset shows a double peak in the temporal signal when the laser intensity was about 15  $\text{mW}/\text{cm}^2$ , which was above the threshold for sequential superradiant scattering. The photomultiplier recorded the light over an angle of 200 mrad around the axial direction. (C) The dependence of the inverse initial rise time on the Rayleigh scattering rate shows a threshold for the stimulated process. The solid curve is a straight-line fit.

$4\lambda$  slightly larger than 1, implying that the geometric angle  $d/l$  is larger than the diffraction angle  $\lambda/d$ .  $F > 1$  leads to multimode superradiance (11) because there is now more than one end-fire mode.

By replacing the camera with a photomultiplier, a time-resolved measurement of the scattered light intensity was obtained (Fig. 3B). Simple Rayleigh scattering would give a constant signal during the square-shaped laser pulse. Instead, we observed a fast rise and a subsequent decay consistent with a stimulated process.

Measurements at variable laser intensities showed a threshold for the onset of superradiance and a shorter rise time for higher laser intensities. This behavior can be accounted for by adding a loss term  $L_j$  in Eq. 4:

$$\dot{N}_j = (G_j - L_j)N_j \quad (6)$$

We determined the exponential rate  $(G_j - L_j)$  by fitting the initial rise in the light intensity. At early times, the depletion of the condensate is negligible and  $G_j$  and  $L_j$  are constants. The inverse rise time  $\dot{N}/N$  versus the Rayleigh scattering rate  $R$ , which was measured by "switching off" the superradiance by changing to parallel polarization, is shown in Fig. 3C. The slope gives  $G_j/R$ , and the offset determines the loss  $L_j$ . The agreement between the calculated value for  $G_j/R \sim 890$  (with  $\Omega_j \sim 1.9 \times 10^{-4}$  and  $N_0 = 4.7 \times 10^6$ ) and the result of the simple linear fit (790) is better than the uncertainty in the Rayleigh scattering rate (40%). The offset in Fig. 3C determines the threshold for superradiance and yields  $1/L_j = 35 \mu\text{s}$ .

The rate of decoherence  $L_j$  for the superradiance indicates the decay of the matter wave interference. This decoherence has been studied separately by stimulated Rayleigh scattering (or Bragg spectroscopy) (3), where the linewidth of the Bragg resonance

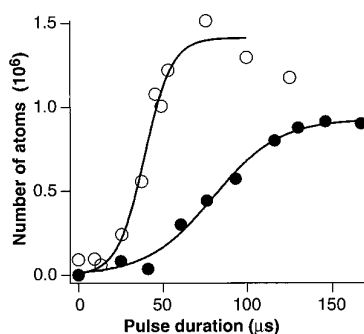


**Fig. 4.** Observation of "matter wave amplification." Shown is the number of atoms in one of the superradiant peaks versus duration of the laser pulse. An intense atomic pulse was formed by amplification of spontaneous scattering. The initial number of atoms in the condensate at rest was  $2 \times 10^7$ , and the laser intensities were about 25 (●) and 45 (○)  $\text{mW}/\text{cm}^2$ . The solid lines are guides to the eye.

resulted from Doppler and mean-field broadening. The observed full width at half-maximum of about 5 kHz yields a decoherence time of 32  $\mu\text{s}$ , in good agreement with the value shown above (13, 14).

For higher laser powers, a distinct change in both the momentum pattern of the atoms (Fig. 1, F and G) and the photomultiplier traces (Fig. 3B) was observed. The atomic pattern showed additional momentum peaks that can be explained as a sequential scattering process in which atoms in the initial momentum peak undergo further superradiant scattering (15). These processes are time-delayed with respect to the primary process and showed up as a second peak in the time-resolved photomultiplier traces (Fig. 3B). This "cascade" of superradiant scattering processes does not exist in the two-level superradiance systems studied so far.

Superradiance is based on the coherence of the emitting system, but it does not require quantum degeneracy. The condition for superradiance is that the gain exceed the losses or that the superradiant decay time be shorter than any decoherence time (11). Above the BEC transition temperature  $T_c$ , thermal Doppler broadening results in a 30 times shorter decoherence time than for a condensate. Furthermore, the larger size of the thermal cloud reduces the solid angle  $\Omega_j$  and therefore the gain by a factor of 10. Therefore, the threshold for superradiance in a thermal cloud is several orders of magnitude higher than for a condensate. No signs of superradiant scattering were observed above  $T_c$ ; rather, the sudden appearance of superradiant emission was a sensitive indicator for reaching the phase transition.

The rise of the number of atoms in the superradiant peak (Fig. 4) can be regarded as single-pass matter wave amplification. Recently, Law and Bigelow considered such an amplifier formed by passing input atoms through a condensate (16). The condensate atoms are transferred into the input atomic mode by bosonic stimulation, assisted by spontaneously scattered photons from a coupling laser that ensures momentum conservation and irreversibility of the gain process. Our experiment realized this geometry except for the fact that the input atoms were created spontaneously. The observed peak of recoiling atoms can thus be regarded as amplified vacuum fluctuations.

An atom cloud with a small excited state admixture can act as a gain medium for both matter waves and light, and we have observed the matter wave amplification. If the emitted light is allowed to build up in a cavity, an optical laser is realized (17). Similarly, the buildup of the matter wave field in an atom cavity can lead to an atom laser (18).

In conclusion, we have studied the interaction between coherent light and coherent atoms. The long coherence time of a Bose-

## REPORTS

Einstein condensate gave rise to superradiance based on coherent external motion. The extremely low threshold in light intensity ( $\sim 1 \text{ mW/cm}^2$  for our conditions) should be taken into account in BEC experiments that use optical probing and manipulation with off-resonant light. The simultaneous superradiant emission of light and atoms emphasizes the symmetry between atom lasers and optical lasers.

### References and Notes

1. M. H. Anderson, J. R. Ensher, M. R. Matthews, C. E. Wieman, E. A. Cornell, *Science* **269**, 198 (1995); K. B. Davis *et al.*, *Phys. Rev. Lett.* **75**, 3969 (1995); C. C. Bradley, C. A. Sackett, R. G. Hulet, *ibid.* **78**, 985 (1997); D. G. Fried *et al.*, *ibid.* **81**, 3811 (1998).
2. M. R. Andrews *et al.*, *Science* **275**, 637 (1997); D. S. Hall, M. R. Matthews, C. E. Wieman, E. A. Cornell, *Phys. Rev. Lett.* **81**, 1543 (1998); B. P. Anderson and M. A. Kasevich, *Science* **282**, 1686 (1998).
3. J. Stenger *et al.*, *Phys. Rev. Lett.* **82**, 4569 (1999).
4. M. G. Moore and P. Meystre, *Phys. Rev. A* **59**, R1754 (1999).
5. N. E. Rehler and J. H. Eberly, *ibid.* **3**, 1735 (1971).
6. R. H. Dicke, in *Proceedings of the Third International Congress on Quantum Electronics*, P. Grivet and N. Bloembergen, Eds. (Columbia Univ. Press, New York, 1964), pp. 35–54.
7. M.-O. Mewes *et al.*, *Phys. Rev. Lett.* **77**, 416 (1996).
8. One can emphasize the symmetry of the atomic and optical fields by describing the process in the moving frame of the excited atoms that have absorbed one laser photon. Because the total momentum is zero in this frame, photons and atoms are emitted into opposite directions, preferentially along the long axis of the elongated cloud. Transforming back into the laboratory frame results in preferential emission of light still along the long axis but of atoms at  $45^\circ$ .
9. H.-J. Miesner *et al.*, *Science*, **279**, 1005 (1998).
10. The probability for reabsorption of scattered light was less than 3% and could be neglected. Optical amplification is accounted for by treating all the atoms as a single quantum mechanical system.
11. N. Skribanowitz, I. P. Herman, J. C. MacGillivray, M. S. Feld, *Phys. Rev. Lett.* **30**, 309 (1973); R. Bonifacio and L. A. Lugiato, *Phys. Rev. A* **11**, 1507 (1975); Q. H. F. Vrehen and H. M. Gibbs, in *Topics in Current Physics* **27**, R. Bonifacio, Ed. (Springer-Verlag, Berlin, 1982), pp. 111–147; M. Gross and S. Haroche, *Phys. Rep.* **93**, 301 (1982).
12. R. H. Dicke, *Phys. Rev.* **93**, 99 (1954).
13. In (3), the recoiling atoms propagated perpendicular to the long axis of the condensate. The "finite size" contribution to the Doppler broadening was therefore twice that of the present geometry.
14. Elastic collisions at a maximum rate of  $\sim 2 \text{ kHz}$  do not contribute substantially to  $L_y$ , although they reduce the number of atoms in the superradiant peak by  $\sim 50\%$ .
15. Stimulated Raman scattering and four-wave mixing between matter waves [see L. Deng *et al.*, *Nature* **398**, 218 (1999)] may couple the different recoil modes and further affect the momentum distribution.
16. C. K. Law and N. P. Bigelow, *Phys. Rev. A* **58**, 4791 (1998).
17. This is called the coherent atomic recoil laser. See R. Bonifacio and L. De Salvo, *Nucl. Instrum. Methods Phys. Res. A* **341**, 360 (1994); M. G. Moore and P. Meystre, *Phys. Rev. A* **58**, 3248 (1998); P. R. Berman, *ibid.* **59**, 585 (1999); M. G. Moore, O. Zobay, P. Meystre, <http://xxx.lanl.gov/abs/cond-mat/9902293>.
18. M. Olshanii, Y. Castin, J. Dalibard, in *Proceedings of the XII Conference on Laser Spectroscopy*, M. Inguscio, M. Allegrini, A. Sasso, Eds. (World Scientific, New York, 1995), pp. 7–12; H. M. Wiseman and M. J. Collett, *Phys. Lett. A* **202**, 246 (1995); U. Janicke and M. Wilkens, in *Topics on Ultracold Atoms and BEC* **7**, K. Burnett, Ed. (Optical Society of America, Washington, DC, 1997), pp. 38–47.
19. We thank C. E. Kulewicz for experimental assistance,

D. A. Kokorowski for critical reading of the manuscript, and H. M. Gibbs, P. Meystre, J. H. Eberly, E. M. Wright, and M. S. Feld for helpful discussions. This work was supported by the Office of Naval Research, NSF, Joint Services Electronics Program (Army Research Office), NASA, and the David and Lucile Pack-

ard Foundation. A.P.C. acknowledges support from NSF, D.M.S.-K. from the Joint Services Electronics Program Graduate Fellowship Program, and J.S. from the Alexander von Humboldt-Foundation.

27 April 1999; accepted 28 June 1999

# The U.S. Carbon Budget: Contributions from Land-Use Change

R. A. Houghton,\* J. L. Hackler, K. T. Lawrence

The rates at which lands in the United States were cleared for agriculture, abandoned, harvested for wood, and burned were reconstructed from historical data for the period 1700–1990 and used in a terrestrial carbon model to calculate annual changes in the amount of carbon stored in terrestrial ecosystems, including wood products. Changes in land use released  $27 \pm 6$  petagrams of carbon to the atmosphere before 1945 and accumulated  $2 \pm 2$  petagrams of carbon after 1945, largely as a result of fire suppression and forest growth on abandoned farmlands. During the 1980s, the net flux of carbon attributable to land management offset 10 to 30 percent of U.S. fossil fuel emissions.

The rate at which carbon is accumulating in terrestrial ecosystems in the United States is uncertain, as are the mechanisms responsible for the current sink. Estimates based on measured changes in wood volumes (forest inventories) (1–3) range between  $0.079$  and  $0.280$  petagrams of carbon per year ( $\text{Pg C year}^{-1}$ ). An estimate, based on atmospheric and oceanic data and models, and including southern Canada, calculated a sink of  $1.7 \pm 0.5 \text{ Pg C year}^{-1}$  (4). Neither of these approaches identifies the mechanisms responsible for the sink (5). In contrast, although the changes in carbon associated with land-use change do not define the total net flux of carbon between land and atmosphere, they represent the portion of the flux that can be attributed to direct human activity, and it is this portion that is addressed by the United Nations Framework Convention on Climate Change and by the Kyoto Protocol. In this report, we estimate the annual flux of carbon in the United States attributable to changes in land use.

Our approach is based on two types of information: rates of land-use change and changes per hectare in carbon that follow a change in land use. We considered the conversion of natural ecosystems to croplands (cultivated) and pastures (not cultivated), the abandonment of croplands and pastures, harvest of industrial wood and fuel wood, and fire management, that is, the area annually

burned by wildfires. Rates of agricultural clearing and abandonment and rates of wood harvest were obtained directly from the U.S. Department of Agriculture (USDA) for the period since 1945 (6) and largely from the U.S. Bureau of Census (7) for the period between 1700 and 1945. Areas burned each year were obtained from wildfire statistics of the U.S. Forest Service (8) for the period after 1930 and from pre-European burning rates (9) modified by settlement and logging practices for the years 1700–1930 (10). A more detailed description of the data, sources, and assumptions can be found elsewhere (11, 12).

We divided the United States into seven geographic regions (each region including two to five natural ecosystems) for a total of 13 different ecosystems, not including croplands and pastures. The areas and carbon stocks of ecosystems in 1700 were determined from both natural areas (13) and current ecosystems (14). The fractions of vegetation left alive, killed, and burned as a result of human activity and fire were defined for each type of land use and ecosystem. The efficiency of industrial wood harvest increased through time, so that more wood was removed per hectare and less left as slash (dead vegetation) (15, 16). Rates of forest growth after harvest, fire, and agricultural abandonment and rates of decay of organic matter for each ecosystem were obtained from the ecological literature (17). Changes in soil carbon included only the losses that resulted from cultivation and the reaccumulations that followed abandonment of cultivated land. These per hectare rates of carbon loss and accumulation after changes in land

Woods Hole Research Center, Post Office Box 296, Woods Hole, MA 02543, USA.

\*To whom correspondence should be addressed. E-mail: rhoughton@whrc.org

## Appendix E

# Phase-coherent amplification of atomic matter waves

This appendix includes the following paper [19]: S. Inouye, T. Pfau, S. Gupta, A.P. Chikkatur, A. Görlitz, D.E. Pritchard, and W. Ketterle, “Phase-coherent amplification of atomic matter waves,” *Nature* **402**, 641 (1999).

3. Girvin, S. M. & MacDonald, A. H. in *Perspectives in Quantum Hall Effects* (eds Das Sarma, S. & Pinczuk, A.) 161–224 (Wiley, New York, 1996).
4. Giuliani, G. F. & Quinn, J. J. Spin-polarization instability in a tilted magnetic field of a two-dimensional electron gas with filled Landau levels. *Phys. Rev. B* **31**, 6228–6232 (1985).
5. Jungwirth, T., Shukla, S. P., Smrčka, L., Shayegan, M. & MacDonald, A. H. Magnetic anisotropy in quantum Hall ferromagnets. *Phys. Rev. Lett.* **81**, 2328–2331 (1998).
6. Zheng, L., Radtke, R. J. & Das Sarma, S. Spin-excitation-instability-induced quantum phase transitions in double-layer quantum Hall systems. *Phys. Rev. Lett.* **78**, 2453–2456 (1997).
7. Das Sarma, S., Sachdev, S. & Zheng, L. Double-layer quantum Hall antiferromagnetism at filling fraction  $\nu = 2/m$  where  $m$  is an odd integer. *Phys. Rev. Lett.* **79**, 917–920 (1997).
8. MacDonald, A. H., Rajaraman, R. & Jungwirth, T. Broken symmetry ground states in  $\nu = 2$  bilayer quantum Hall systems. *Phys. Rev. B* **60**, 8817–8826 (1999).
9. Eisenstein, J. P. *Perspectives in Quantum Hall Effects* (eds Das Sarma, S. & Pinczuk, A.) 58–70 (Wiley, New York, 1996).
10. Daneshvar, A. J. et al. Magnetisation instability in a two-dimensional system. *Phys. Rev. Lett.* **79**, 4449–4452 (1997).
11. Pellegrini, V. et al. Collapse of spin excitations in quantum Hall states of coupled electron double layers. *Phys. Rev. Lett.* **78**, 310–313 (1997).
12. Pellegrini, V. et al. Evidence of soft-mode quantum phase transitions in electron double layers. *Science* **281**, 799–802 (1998).
13. Sawada, A. et al. Phase transition in the  $\nu = 2$  bilayer quantum Hall state. *Phys. Rev. Lett.* **80**, 4534–4537 (1998).
14. Sachdev, S. *Quantum Phase Transitions* (Cambridge Univ. Press, 1999).
15. Sondhi, S. L., Girvin, S. M., Carini, J. P. & Shahar, D. Continuous quantum phase transitions. *Rev. Mod. Phys.* **69**, 315–333 (1997).
16. MacDonald, A. H., Platzman, P. M. & Boebinger, G. S. Collapse of integer Hall gaps in a double-quantum-well system. *Phys. Rev. Lett.* **65**, 775–778 (1990).
17. Cho, H. et al. Hysteresis and spin transitions in the fractional quantum Hall effect. *Phys. Rev. Lett.* **81**, 2522–2525 (1998).

**Acknowledgements**

We thank M. Bichler for technical support during sample growth, and G. F. Giuliani for discussions. The work at Scuola Normale Superiore was funded in part by MURST. The work at Indiana University was supported by the NSF, and at Institute of Physics ASCR by the Ministry of Education of the Czech Republic and the Grant Agency of the Czech Republic.

Correspondence and requests for materials should be addressed to V. Piazza (e-mail: piazza@cmp.sns.it).

.....  
**Phase-coherent amplification of atomic matter waves**

**S. Inouye, T. Pfau, S. Gupta, A. P. Chikkatur, A. Görlitz, D. E. Pritchard & W. Ketterle**

*Department of Physics and Research Laboratory of Electronics, Massachusetts Institute of Technology, Cambridge, Massachusetts 02139, USA*

.....  
**Atomic matter waves, like electromagnetic waves, can be focused, reflected, guided and split by currently available passive atom-optical elements. However, the key for many applications of electromagnetic waves lies in the availability of amplifiers. These active devices allow small signals to be detected, and led to the development of masers and lasers. Although coherent atomic beams have been produced<sup>1–4</sup>, matter wave amplification has not been directly observed. Here we report the observation of phase-coherent amplification of atomic matter waves. The active medium is a Bose–Einstein condensate, pumped by light that is far off resonance. An atomic wave packet is split off the condensate by diffraction from an optical standing wave, and then amplified. We verified the phase coherence of the amplifier by observing interference of the output wave with a reference wave packet. This development provides a new tool for atom optics and atom interferometry, and opens the way to the construction of active matter-wave devices.**

Matter-wave amplification differs from light amplification in one important respect. Because the total number of atoms is conserved (in contrast to photons), the active medium of a matter-wave amplifier has to include a reservoir of atoms. Also needed is a

coupling mechanism that transfers atoms from the reservoir to the input mode while conserving energy and momentum. Amplification is realized if the transfer mechanism is accelerated by the build-up of atoms in the final state and inversion is maintained between the initial and final states.

It is convenient to use a Bose–Einstein condensate with its high phase-space density to realize matter-wave amplification, although in principle it is not necessary<sup>1–4</sup>. This is analogous to the situation in optics where coherent light is used for pumping parametric amplifiers. The momentum required to transfer atoms from the condensate at rest to the input mode can be provided by light scattering. As was discussed in refs 5 and 6, a condensate pumped by an off-resonant laser acts as a matter-wave amplifier. It can amplify input matter waves within the momentum range that can be reached by scattering a single pump photon. Energy is conserved because the scattered light has lower frequency.

The inversion in this matter-wave amplifier is most apparent in the ‘dressed atom’ picture, where the condensate at rest and the pump light field form an upper state that can decay into recoiling atoms and scattered photons. The escape of the photons maintains inversion, allowing, in principle, a complete transfer of the condensate atoms into the recoil mode.

The gain process can be explained in a semiclassical picture. The input matter wave of wavevector  $\mathbf{K}_j$  interferes with the condensate at rest, and forms a moving matter-wave grating; this grating diffracts the pump light with wavevector  $\mathbf{k}_0$  into the momentum and energy conserving direction  $\mathbf{k}_i = (\mathbf{k}_0 - \mathbf{K}_j)$ . The momentum imparted by the photon scattering is absorbed by the matter-wave grating by coherently transferring an atom from the condensate into the recoil mode, which is the input mode. The diffraction efficiency of the grating is proportional to the square of the depth of the density modulation, and therefore to the number of atoms in the input mode,  $N_j$ . This implies an exponential growth of  $N_j$  (as long as one can neglect the depletion of the condensate at rest).

The amplification of atoms in a recoil mode  $j$  follows a gain equation<sup>7,8</sup>

$$\dot{N}_j = (G_j - L_j)N_j \tag{1}$$

with the gain coefficient

$$G_j = RN_0 \frac{\sin^2 \theta_j}{8\pi/3} \Omega_j \tag{2}$$

Here  $R$  is the rate for single-atom Rayleigh scattering which is proportional to the pump light intensity,  $N_0$  is the number of atoms in the condensate at rest,  $\theta_j$  is the angle between the polarization of the incident light and the direction of the scattered light, and  $\Omega_j$  is the phase-matching solid angle for scattering into mode  $j$ . The loss term  $L_j$  describes the decoherence rate of the matter-wave grating and determines the threshold for exponential growth (see ref. 7 for details). We have recently observed the build-up of superradiant emission due to this gain, and have confirmed the salient features of the model presented above. Previous theoretical discussions of this system had assumed an optical cavity into which the pump light is scattered<sup>5,6</sup>, but our experiment<sup>7</sup> showed that cigar-shaped condensates have sufficient gain for axial light emission, even in free space. In our observation of superradiance, there were no input atoms, and the build-up of a macroscopic matter wave was initiated by spontaneous scattering. Here we characterize the amplification process by providing a variable input and measuring the amplitude and phase of the amplified matter wave.

Cigar-shaped Bose–Einstein condensates of a few million sodium atoms in the  $F = 1$ ,  $m_F = -1$  state were produced in a magnetic trap using the standard techniques of laser cooling and evaporative cooling<sup>9</sup>. The condensate was 200  $\mu\text{m}$  in length and 18  $\mu\text{m}$  in diameter. Input matter waves with a well defined momentum were generated by exposing the condensate to a pulsed optical standing wave which transferred a small fraction of the atoms ( $10^{-4}$  to  $10^{-2}$ ) into a recoil mode by Bragg diffraction<sup>10,11</sup>. The

## letters to nature

frequencies of both laser beams were red-detuned by 1.7 GHz from the  $3S_{1/2}, F = 1 \rightarrow 3P_{3/2}, F = 0, 1, 2$  transition, and the intensities were kept below the threshold for superradiant Rayleigh scattering<sup>7</sup>. The geometry of the light beams is shown in Fig. 1. The beam which was perpendicular to the long axis of the condensate (the radial beam) was blue-detuned by 50 kHz relative to the axial beam. This detuning fulfills the Bragg resonance condition; that is, it corresponds to the kinetic energy of the recoiling atoms. The broadening of the Bragg resonance by the finite pulse length (10  $\mu$ s) was small enough to prevent the off-resonant excitation of other diffraction orders.

Amplification of the input matter wave was realized by applying an intense pump pulse along the direction of the radial Bragg beam for the next 20  $\mu$ s with a typical intensity of 40 mW cm<sup>-2</sup>. The number of atoms in the recoil mode was determined by suddenly switching off the trap and observing the ballistically expanding cloud of atoms after 35 ms using resonant absorption imaging. After the expansion, the condensate and the recoiling atoms were fully separated (Fig. 2a–c).

Figure 2 shows the input–output characteristics of the amplifier. The number of input atoms was below the detection limit of our absorption imaging (Fig. 2a) and was determined from a calibration of the Bragg process at high laser powers, where the diffracted atoms were clearly visible in the images. For short pulses, the diffraction efficiency was quadratic in the laser power, as expected. The amplification pulse alone, although above the threshold for superradiance<sup>7</sup>, did not generate a discernible signal of atoms in the recoil mode (Fig. 2b). When the weak input matter wave was added, the amplified signal was clearly visible (Fig. 2c). The gain was controlled by the intensity of the pump pulse (see equation (2)) and typically varied between 10 and 100. Figure 2d shows the observed linear relationship between the atom numbers in the input and the amplified output with a number gain of 30.

The phase of the amplified matter wave was determined with an interferometric technique. For this, a reference matter wave was split off the condensate in the trap in the same manner as the first (input) wave. The phase of the reference matter wave was scanned by shifting the phase of the radio-frequency signal that drove the acousto-optic modulator generating the axial Bragg beam. We then observed the interference between the reference and the amplified matter waves by measuring the number of atoms in the recoil mode.

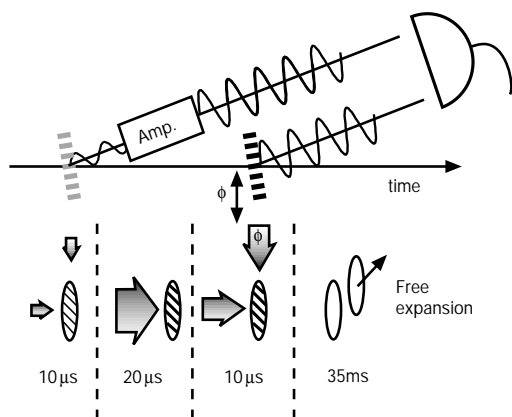


**Figure 1** Experimental scheme for observing phase-coherent matter-wave amplification. A small-amplitude matter wave was split off the condensate by applying a pulse of two off-resonant laser beams (Bragg pulse). This input matter wave was amplified by passing it through the condensate pumped by a laser beam. The coherence of the amplified wave was verified by observing its interference with a reference matter wave, which was produced by applying a second (reference) Bragg pulse to the condensate. The interference signal was observed after 35 ms of ballistic expansion. Note that the polarization of the radial beam was perpendicular to the long axis of the condensate ( $\theta = \pi/2$ ). Extinction of the axial beam during the amplifying pulse was better than  $10^{-8}$ .

If we characterize the two interfering matter waves by their atom numbers  $N_i$  and normalized wavefunctions  $\psi_i$ , then the visibility  $V$  of the interference pattern is given by:

$$V = \frac{2\langle\psi_1|\psi_2\rangle\sqrt{N_1N_2}}{N_1 + N_2} \quad (3)$$

$$\sim 2\langle\psi_1|\psi_2\rangle\sqrt{N_1/N_2} \quad (N_1 \ll N_2) \quad (4)$$

This simple description is valid for small transfer efficiencies of the Bragg pulses ( $N_i \ll N_0$ ). A more general description treats the two Bragg pulses as a Ramsey-type matter-wave interferometer<sup>12</sup>, where the phase of the matter-wave grating (formed by the recoiling atoms and the condensate) is compared with the phase of the standing-wave light grating used for the second Bragg transition. This treatment reproduces equation (3), where  $N_1$  is replaced by  $N_1(1 - N_2/N_0)$  and  $N_2$  by  $N_2(1 - N_1/N_0)$ .

In Fig. 3 we show the interference signal between the amplified input and the reference matter wave as the reference phase was scanned. When the amplitude of the input was comparable to that of the reference matter wave, high-contrast fringes were observed even without amplification (Fig. 3a). When the input was about 40 times weaker in population, fringes were barely visible (Fig. 3b). After amplification, we regained a large visibility (Fig. 3c). This increase in visibility proves the coherent nature of the matter-wave amplification process.

The visibility was studied as a function of the number of input atoms (Fig. 4). Since amplification did not produce any observable phase shift, the visibility could be measured by comparing the number of atoms in the recoil mode at constructive and destructive phases. Without amplification, the visibility increased with the number of input atoms in fair agreement with equation (3), assuming  $\langle\psi_1|\psi_2\rangle \sim 1$  for the overlap factor. With amplification (under the same conditions which gave a number gain of 30 (Fig. 2)), the visibility increased by a factor of about two over a

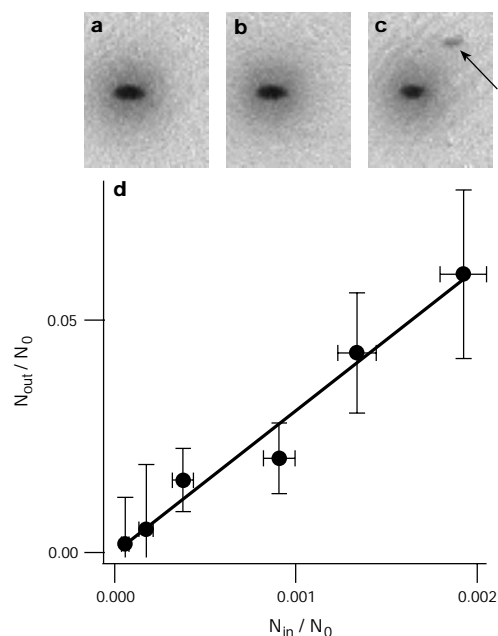


**Figure 2** Input–output characteristics of the matter-wave amplifier. **a–c**, Typical time-of-flight absorption images demonstrating matter-wave amplification. The output of the seeded amplifier (**c**) is clearly visible, as indicated by the arrow, whereas no recoiling atoms are discernible in the case without amplification (**a**) or amplification without the input (**b**). The size of the images is 2.8 mm  $\times$  2.3 mm. **d**, Output of the amplifier as a function of the number of atoms at the input. A straight-line fit shows a number gain of 30. Note that the same data set as in Fig. 4 was used. The total number of amplified atoms was determined by measuring the increase in the offset of the obtained interference fringes discussed below.

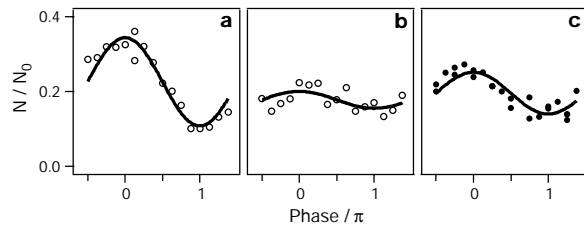


**Figure 3** Phase-coherent amplification of matter waves. Shown is the number of atoms  $N$  in the recoil mode (normalized by the initial number of atoms in the condensate  $N_0$ ) versus the relative phase between the two Bragg pulses. **a**, Interference between two matter waves of almost equal intensity yielded a high contrast fringe (visibility  $V = 52\%$ ). **b**, When the intensity of the first matter wave was decreased by a factor of 40, the visibility  $V$  dropped to the noise level ( $< 15\%$ ). **c**, By switching on the amplifier, a large visibility was regained ( $V = 31\%$ ).

wide range of input intensities. Since for a small number of atoms  $N_1$ , the visibility increases as  $\sqrt{N_1}$  (equation (4)), this implies a “coherent matter-wave gain” of at least four. The discrepancy from the number gain of 30 may be due to a distortion of the input matter wave during its amplification which would reduce the overlap factor  $\langle \psi_1 | \psi_2 \rangle$ . Indeed, the shape of the amplified matter wave looked distorted after the 35 ms of ballistic expansion. This indicates a wavefront distortion of the amplified matter wave which can be parametrized by introducing an overlap factor of  $\sqrt{4/30} = 0.4$  in equation (3), but this effect requires further study. No distortion was seen at short times (1.5 ms) after the amplification (as observed by phase-contrast imaging). This and a simple model suggest that the spatially non-uniform gain is not the dominant cause of the non-ideal visibility.

The interference between the (amplified) signal and the reference matter wave was measured in a two-pulse interferometer where the delay time between the pulses was kept shorter than the coherence time of the two-photon Bragg process ( $\sim 40 \mu\text{s}$ ; ref. 7). The coherence time can be determined by the linewidth of the Bragg resonance<sup>11</sup>, or by the decay rate of the Ramsey fringe visibility<sup>12</sup>. In the absence of mean-field broadening, it is proportional to the spatial extent of the condensate divided by the recoil velocity<sup>11,12</sup>.

We deliberately studied the matter-wave amplification in the small-signal limit. We chose a low density of the condensate, a small number of input atoms, and rather low gain in order to avoid additional complexities such as elastic collisions and repeated superradiant scattering<sup>7</sup>. The density of the condensate was adjusted to be less than  $2 \times 10^{14} \text{ cm}^{-3}$  by limiting the number of condensed atoms. The average number of (incoherent) elastic collisions occurring between the two Bragg pulses was less than 0.05 per recoiling atom, and should be negligible.

The input matter waves were generated in perfect spatial overlap with the condensate by Bragg pulses. In further experiments, we have also observed the single-pass amplification of input atomic wave packets which were initially spatially separated from the condensate. This was achieved by letting the input wave packet oscillate in the trapping potential for half an oscillation period before applying the amplification light pulse. As the wave packet passed through the pumped condensate at rest, amplification was clearly observed.

The matter-wave amplifier that we have demonstrated amplifies only the recoil states that can be populated by normal Rayleigh scattering. Their momentum is located on a sphere with radius  $|\hbar\mathbf{k}_0|$  centred at the incoming photon momentum ( $\hbar\mathbf{k}_0$ ). We have achieved perfect momentum matching by using the radial beam for the Bragg process as the pump beam for the amplification process. Ultimately, the momentum bandwidth of the amplification process should be given by the momentum uncertainty of the condensate, which is roughly Planck’s constant divided by the size of the condensate.

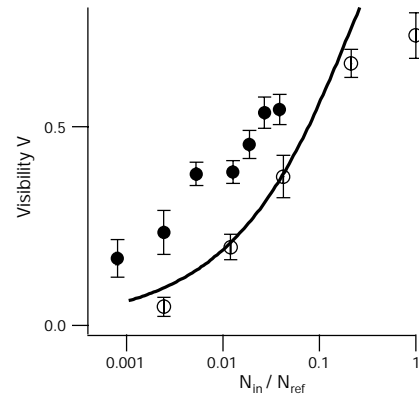


**Figure 4** Visibility of interference with and without amplification. The visibility of the interference pattern between input (output) and the reference matter wave is shown with open (filled) circles as a function of the input number of atoms  $N_{in}$  (normalized by the population of the reference matter wave  $N_{ref}$ ). The solid line is the expected visibility from equation (3), assuming an overlap factor of unity. The intensity of the amplification pulse was  $40 \text{ mW cm}^{-2}$ .

The amplification process studied in this work is based on bosonic stimulation: if  $N$  bosons occupy a given state, the transition rates into that state are proportional to  $N + 1$ . Some experiments have seen such accelerated transition rates without observing phase coherence<sup>7,13,14</sup>. A study of the formation of the condensate showed evidence for bosonic stimulation in the elastic scattering of atoms into the condensate<sup>13</sup>, an irreversible process establishing thermal equilibrium. The recently demonstrated four-wave mixing of atoms<sup>14</sup> also relied on bosonic stimulation of atom–atom collisions, but in this case as a coherent process mediated by the mean field.

Bosonic stimulation has been discussed as the gain mechanism of atom lasers, either based on evaporation or optical pumping<sup>1–4</sup>. In these discussions, the idea was to start with a thermal cloud of low phase-space density and create a large population in a single matter-wave mode. Our experiments exploited the high phase-space density of a condensate to realize a high matter-wave gain. In principle, we could have used an optically pumped thermal cloud as a gain medium, but the gain would have been extremely small due to the large Doppler broadening.

Our experiment can also be regarded as a demonstration of an active atom interferometer. It realizes a two-pulse atom interferometer<sup>15</sup> with phase-coherent amplification in one of the arms. Such active interferometers may be advantageous for precise measurements of phase shifts in highly absorptive media; for example, measurements of the index of (matter wave) refraction when a condensate passes through a gas of atoms or molecules<sup>16</sup>. As the most accurate optical gyroscopes involve active interferometers<sup>17</sup>, atom amplification might also play a role in future matter-wave gyroscopes<sup>18</sup>.

*Note added in proof:* M. Kozuma has informed us that related work has been done at the University of Tokyo. □

Received 9 November; accepted 18 November 1999.

- Holland, M., Burnett, K., Gardiner, C., Cirac, J. & Zoller, P. Theory of an atom laser. *Phys. Rev. A* **54**, R1757–R1760 (1996).
- Olshani, M., Castin, Y. & Dalibard, J. in *Proc. XII Conf. on Laser Spectroscopy* (eds Inguscio, M., Allegrini, M. & Sasso, A.) 7–12 (World Scientific, New York, 1995).
- Spreeuw, R. J. C., Pfau, T., Janicke, U. & Wilkens, M. Laser-like scheme for atomic-matter waves. *Eur. Phys. Lett. B* **32**, 469–474 (1995).
- Wiseman, H. M. & Collett, M. J. An atom laser based on dark-state cooling. *Phys. Lett. A* **202**, 246–252 (1995).
- Law, C. K. & Bigelow, N. P. Amplifying an atomic wave signal using a Bose-Einstein condensate. *Phys. Rev. A* **58**, 4791–4795 (1998).
- Moore, M. G. & Meystre, P. Optical control and entanglement of atomic Schrödinger fields. *Phys. Rev. A* **59**, R1754–R1757 (1999).
- Inouye, S. *et al.* Superradiant Rayleigh scattering from a Bose-Einstein condensate. *Science* **285**, 571–574 (1999).

## letters to nature

- Moore, M. G. & Meystre, P. Theory of superradiant scattering of laser light from Bose-Einstein condensates. Preprint cond-mat/9905425 at (<http://xxx.lanl.gov>) (1999).
- Mewes, M.-O. *et al.* Bose-Einstein condensation in a tightly confining dc magnetic trap. *Phys. Rev. Lett.* **77**, 416–419 (1996).
- Kozuma, M. *et al.* Coherent splitting of Bose-Einstein condensed atoms with optically induced Bragg diffraction. *Phys. Rev. Lett.* **82**, 871–875 (1999).
- Stenger, J. *et al.* Bragg spectroscopy of a Bose-Einstein condensate. *Phys. Rev. Lett.* **82**, 4569–4573 (1999).
- Hagley, E. W. *et al.* Measurement of the coherence of a Bose-Einstein condensate. *Phys. Rev. Lett.* **83**, 3112–3115 (1999).
- Miesner, H.-J. *et al.* Bosonic stimulation in the formation of a Bose-Einstein condensate. *Science* **279**, 1005–1007 (1998).
- Deng, L. *et al.* Four-wave mixing with matter waves. *Nature* **398**, 218–220 (1999).
- Berman, P. R. (ed.) *Atom Interferometry* (Academic, New York, 1997).
- Schmiedmayer, J. *et al.* Index of refraction of various gases for sodium matter waves. *Phys. Rev. Lett.* **74**, 1043–1047 (1995).
- Stedman, G. E. *et al.* Ring-laser tests of fundamental physics and geophysics. *Rep. Prog. Phys.* **60**, 615–688 (1997).
- Gustavson, T. L., Bouyer, P. & Kasevich, M. A. Precision rotation measurements with an atom interferometer gyroscope. *Phys. Rev. Lett.* **78**, 2046–2049 (1997).

### Acknowledgements

We thank D. M. Stamper-Kurn for discussions. This work was supported by the Office of Naval Research, NSF, Joint Services Electronics Program, ARO, NASA, and the David and Lucile Packard Foundation. A.P.C. was supported by NSF, A.G. by DAAD, and T.P. by the Alexander von Humboldt Foundation.

Correspondence and requests for materials should be addressed to S.I. (e-mail: [sinouye@mit.edu](mailto:sinouye@mit.edu)).

## Weaker Gulf Stream in the Florida Straits during the Last Glacial Maximum

Jean Lynch-Stieglitz\*, William B. Curry† & Niall Slowey‡

\* Department of Earth and Environmental Sciences, Lamont-Doherty Earth Observatory, Palisades, New York 10964, USA

† Woods Hole Oceanographic Institution, Woods Hole, Massachusetts 02543, USA

‡ Department of Oceanography, Texas A & M University, College Station, Texas 77843, USA

As it passes through the Florida Straits, the Gulf Stream consists of two main components: the western boundary flow of the wind-driven subtropical gyre and the northward-flowing surface and intermediate waters which are part of the 'global conveyor belt', compensating for the deep water that is exported from the North Atlantic Ocean<sup>1</sup>. The mean flow through the Straits is largely in geostrophic balance and is thus reflected in the contrast in seawater density across the Straits<sup>2</sup>. Here we use oxygen-isotope ratios of benthic foraminifera which lived along the ocean margins on the boundaries of the Florida Current during the Last Glacial Maximum to determine the density structure in the water and thereby reconstruct transport through the Straits using the geostrophic method—a technique which has been used successfully for estimating present-day flow<sup>3</sup>. Our data suggest that during the Last Glacial Maximum, the density contrast across the Florida Straits was reduced, with the geostrophic flow, referenced to the bottom of the channel, at only about two-thirds of the modern value. If the wind-driven western boundary flow was not lower during the Last Glacial Maximum than today, these results indicate a significantly weaker conveyor-belt component of the Gulf Stream compared to present-day values. Whereas previous studies based on tracers suggested that deep waters of North Atlantic origin were not widespread during glacial times, indicating either a relatively weak or a shallow overturning cell, our results provide evidence that the overturning cell was indeed weaker during glacial times.

The Florida Current, which flows through the Florida Straits (Fig. 1), is the southernmost part of the Gulf Stream. The average northward transport of the Florida Current is fairly well constrained by modern measurement at 30–32 Sv, and shows a seasonal variation with a range of 4.6 Sv as well as considerable variability on shorter timescales<sup>4</sup>. Schmitz and McCartney<sup>1</sup> assign an uncertainty of only 5% to the mean annual transport value of 31 Sv. The transport at the Florida Current includes 13 Sv of flow from the South Atlantic which travels northward in the Gulf Stream to the North Atlantic and ultimately compensates for the export of North Atlantic Deep Water (NADW). The other 17 Sv compensate for southward-flowing upper waters from the eastern portion of the wind-driven North-Atlantic subtropical gyre<sup>1</sup>. The strong tilts in the surfaces of constant temperature and density within the Florida Straits reflect the geostrophic adjustment of the density surfaces in the presence of the large velocities (Fig. 2a and b). The contrast in temperature and density across the Florida Current is large, and is well represented in the  $\delta^{18}\text{O}$  of benthic foraminifera living in this region.

We can use the  $\delta^{18}\text{O}$  from the calcite tests of foraminifera to estimate density because both the  $\delta^{18}\text{O}$  of calcite ( $\delta^{18}\text{O}_{\text{calcite}}$ ) and density increase as a result of increasing salinity or decreasing temperature. The dependence of seawater density on salinity and temperature is well known and will be constant throughout the ocean and through geological time. The dependence of  $\delta^{18}\text{O}$  of foraminifera on the temperature of calcification is also fairly well constrained. The fractionation between calcite precipitated inorganically and the water in which it forms increases by about 0.2‰ for every 1 °C decrease in temperature<sup>5</sup>, and the isotopic composition of calcitic benthic foraminifera in the genera *Planulina* and *Cibicides* show the same fractionation as measured in the experiments with inorganic calcite<sup>3</sup>. The relationship between  $\delta^{18}\text{O}_{\text{calcite}}$  and salinity is more complex. The  $\delta^{18}\text{O}_{\text{calcite}}$  reflects the  $\delta^{18}\text{O}$  of the water in which the foraminifera grew. The  $\delta^{18}\text{O}$  of sea water ( $\delta^{18}\text{O}_{\text{water}}$ ) primarily reflects patterns of evaporation and freshwater influx to the surface of the ocean. Because salinity also reflects these patterns, salinity and  $\delta^{18}\text{O}_{\text{water}}$  are often well correlated in the ocean. Although the exact relationship varies in different areas of the surface ocean<sup>6</sup>, the vast majority of surface and warm subsurface waters ( $T > 5\text{ °C}$ ) in the ocean have salinity and  $\delta^{18}\text{O}_{\text{water}}$  values which scatter around a linear trend<sup>3</sup>. For times in the geological past, our ability to reconstruct density from the  $\delta^{18}\text{O}_{\text{calcite}}$

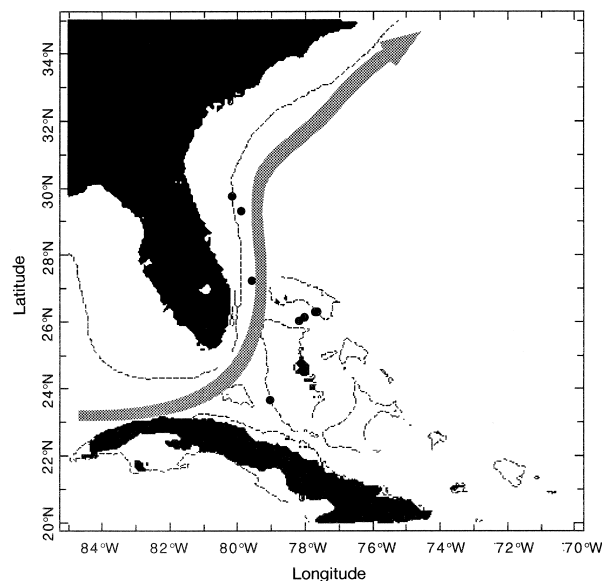


Figure 1 Location of sediment cores used in this study. The path of the Gulf Stream is indicated with the shaded arrow, and the depth of the 200-m isobath with a dashed line.

## Appendix F

# Amplification of Light and Atoms in a Bose-Einstein Condensate

This appendix includes the following paper [20]: S. Inouye, R.F. Low, S. Gupta, T. Pfau, A. Görlitz, T.L. Gustavson, D.E. Pritchard, and W. Ketterle, “Amplification of Light and Atoms in a Bose-Einstein Condensate,” *Phys. Rev. Lett.* **85**, 4225 (2000).

## Amplification of Light and Atoms in a Bose-Einstein Condensate

S. Inouye, R. F. Löw, S. Gupta, T. Pfau, A. Görlitz, T. L. Gustavson, D. E. Pritchard, and W. Ketterle

*Department of Physics and Research Laboratory of Electronics, Massachusetts Institute of Technology, Cambridge, Massachusetts 02139*

(Received 27 June 2000)

A Bose-Einstein condensate illuminated by a single off-resonant laser beam (“dressed condensate”) shows a high gain for matter waves and light. We have characterized the optical and atom-optical properties of the dressed condensate by injecting light or atoms, illuminating the key role of long-lived matter wave gratings produced by the condensate at rest and recoiling atoms. The narrow bandwidth for optical gain gave rise to an extremely slow group velocity of an amplified light pulse ( $\sim 1$  m/s).

PACS numbers: 03.75.Fi, 42.50.Ct, 42.50.Gy

The field of atom optics is based on profound analogies between electromagnetic waves and matter waves. Both light and atoms can be amplified by bosonic stimulation, and this has led to the optical laser and the atom laser, respectively. Recently, Bose-Einstein condensates illuminated by an off-resonant laser beam (“dressed condensates”) were used to realize phase-coherent amplification of matter waves [1,2]. The amplification process involved the scattering of a condensate atom and a laser photon into an atom in a recoil mode and a scattered photon. This four-wave mixing process between two electromagnetic fields and two Schrödinger fields became a self-amplifying process above a threshold laser intensity, leading to matter wave gain. However, the symmetry between light and atoms indicates that a dressed condensate should not only amplify injected atoms, but also injected light.

In this paper, we focus on the optical properties of a dressed condensate above and below the threshold for the matter wave amplification. The optical gain below the threshold has a narrow bandwidth due to the long coherence time of a condensate. This resulted in an extremely slow group velocity for the amplified light. Above the threshold, we observed nonlinear behavior in the optical gain. This is due to the buildup of a macroscopic matter wave grating inside the condensate and was observed *in situ* by a pump-probe measurement.

Figure 1a shows the basic light scattering process. An atom scatters a photon from the laser beam (called “dressing beam”) into another mode and receives the corresponding recoil momentum and energy. Injection of atoms or light turns this *spontaneous* process into a *stimulated* process. If atoms are injected, they form a matter wave grating (an interference pattern with the condensate at rest) and this grating diffracts light. The diffraction transfers recoil momentum and energy to the atoms, which results in a growth of the grating and therefore the number of atoms in the recoil mode—this is the intuitive picture for atom gain. If probe light is injected, it forms a moving standing wave with the dressing beam, and this light grating diffracts atoms. This diffraction transfers photons into the probe beam mode, resulting in optical gain.

For low dressing beam intensity, the probe beam gain is due to the two-photon gain of individual atoms (Fig. 1b). By introducing the dressed atom picture [3], the optical gain can be understood as the gain of a fully inverted two-level system (Fig. 1c). The atoms in the condensate and the photons in the dressing beam form a dressed condensate, corresponding to the upper state ( $|1'\rangle$ ). The lower state is the recoil state of atoms ( $|2\rangle$ ) and the dressed condensate can “decay” to the lower state by emitting a photon into the probe beam mode. A fully inverted two-level system with dipole coupling would have a gain cross section of  $6\pi\lambda^2$  for radiation with wavelength  $\lambda [= (2\pi)\lambda]$ . For the Raman-type system in Fig. 1b, the gain is reduced by the excited state fraction,  $R_D/\Gamma$  (where  $R_D$  is the Rayleigh scattering rate for the dressing beam and  $\Gamma$  is the linewidth of the single-photon atomic resonance) and increased by  $\Gamma/\Gamma_2$ , the ratio of the linewidths of the single-photon and two-photon Bragg resonances. Thus the expected cross section for gain is

$$\sigma_{\text{gain}} = 6\pi\lambda^2 \frac{R_D}{\Gamma_2}, \quad (1)$$

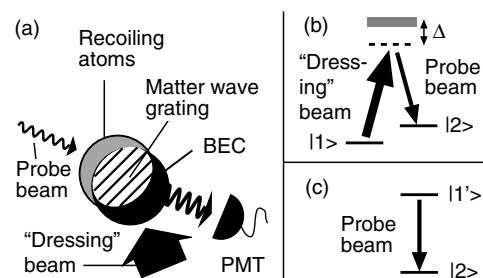


FIG. 1. Amplification of light and atoms by off-resonant light scattering. (a) The fundamental process is the absorption of a photon from the “dressing” beam by an atom in the condensate (state  $|1\rangle$ ), which is transferred to a recoil state (state  $|2\rangle$ ) by emitting a photon into the probe field. The intensity in the probe light field was monitored by a photomultiplier. (b) The two-photon Raman-type transition between two motional states ( $|1\rangle, |2\rangle$ ) gives rise to a narrow resonance. (c) The dressed condensate is the upper state ( $|1'\rangle$ ) of a two-level system, and decays to the lower state (recoil state of atoms,  $|2\rangle$ ) by emitting a photon.

which is proportional to the intensity of the dressing beam. A Bose–Einstein condensate has a very narrow two-photon resonance width  $\Gamma_2$  of only a few kHz. The residual linewidth stems from the loss of overlap between the two motional states and from the inhomogeneous density distribution [4].

A gain with narrow bandwidth causes a slow group velocity of light. The gain represents the imaginary part of the complex index of refraction. A sharp peak in the gain implies a steep dispersive shape for the real part of the index of refraction  $n(\omega)$ . This results in a small value of the group velocity  $v_g$

$$v_g = \frac{c}{n + \omega \frac{dn}{d\omega}}, \quad (2)$$

and in large pulse delays. More precisely, a narrow-band gain feature with gain  $g$  and width  $\gamma$  leads to an amplified pulse with a delay time of  $\tau_D = (\ln g)/\gamma$ .

For the experimental study of optical properties of a dressed condensate, elongated Bose–Einstein condensates consisting of several million sodium atoms in the  $F = 1$ ,  $m_F = -1$  state were prepared in a magnetic trap [5]. The condensate was illuminated (“dressed”) with a single laser beam that was red-detuned by 1.7 GHz from the  $3S_{1/2}, F = 1 \rightarrow 3P_{3/2}, F = 0, 1, 2$  transition. Both the dressing beam and the probe beam were in the plane perpendicular to the long axis of the condensate, and intersected at an angle of  $135^\circ$ . The probe beam was red-detuned from the dressing beam by 91 kHz, which was determined to be the resonance frequency for the two-photon Bragg transition. This small frequency difference between the two light beams was realized by deriving both beams from a common source, and then passing

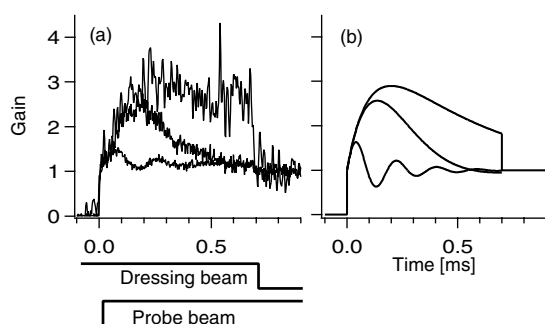


FIG. 2. Gain and temporal behavior of light pulses propagating through a dressed condensate. (a) Observed probe pulse output from a dressed condensate. The probe light intensities were  $5.7 \text{ mW/cm}^2$  (bottom),  $1.5 \text{ mW/cm}^2$  (middle),  $0.10 \text{ mW/cm}^2$  (top), while the dressing beam intensity was  $5 \text{ mW/cm}^2$ , which was just below the threshold for superradiance. The plotted signals were normalized by the incident probe intensity and show the gain for the probe light. (b) Calculated probe light output for the experimental parameters in (a). Rabi oscillations develop into steady-state gain as the intensity of the probe light is reduced.

them through two separate acousto-optical modulators that were driven with separate frequency synthesizers. The probe beam, which propagated parallel to the axis of imaging, was a few millimeters in diameter and much larger than the condensate, which was  $20 \mu\text{m}$  in diameter and  $200 \mu\text{m}$  in length. In order to block all the light that did not pass through the condensate, a  $25 \mu\text{m} \times 100 \mu\text{m}$  slit was placed at an intermediate imaging plane where the condensate was 2 times magnified. The light transmitted by the slit was recorded with a photomultiplier. The polarization of each beam was set parallel to the long axis of the condensate to suppress superradiance to other recoil modes [6].

The main results of this paper are shown in Figs. 2 and 3. In order to measure the gain of the dressed condensate, we used long square probe pulses during which the dressing beam was switched off (Fig. 2). At the lowest probe intensity, the depletion of atoms in the condensate was negligible and a clear step at the switch off was observed, corresponding to a gain of  $\sim 2.8$ . The initial rise time  $\sim 100 \mu\text{s}$  is the coherence time of the dressed condensate.

The square pulse response observed in Fig. 2a already indicates long pulse delays. The distortion of the pulse is due to the large frequency bandwidth contained in the square pulse. This was avoided by modifying the pulse shape to be Gaussian, but keeping the peak intensity of the probe beam at the same level. Figure 3a shows that such pulses were delayed by about  $20 \mu\text{s}$  across the  $20 \mu\text{m}$  wide condensate corresponding to a group velocity of  $1 \text{ m/s}$ . This is, to the best of our knowledge, 1 order of magnitude smaller than any other value published thus far [7].

At high probe laser power we observed Rabi oscillations in the transmitted probe light (Fig. 2). Note that all the traces were normalized by the probe beam intensity, and the oscillatory trace at the bottom was obtained at the highest probe beam intensity. They reflect simple two-level

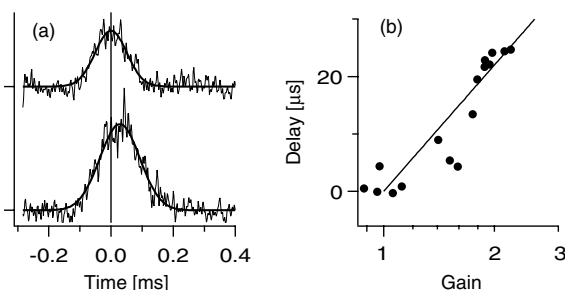


FIG. 3. Pulse delay due to light amplification. (a) About  $20 \mu\text{s}$  delay was observed when a Gaussian pulse of about  $140 \mu\text{s}$  width and  $0.11 \text{ mW/cm}^2$  peak intensity was sent through the dressed condensate (bottom trace). The top trace is a reference taken without the dressed condensate. Solid curves are Gaussian fits to guide the eyes. (b) The observed delay  $\tau_D$  is proportional to  $(\ln g)$ , where  $g$  is the observed gain.

Rabi oscillations of atoms between states  $|1\rangle$  and  $|2\rangle$  (Fig. 1b) driven by the two-photon Bragg coupling.

The transition from Rabi oscillations to steady-state gain can be described by optical Bloch equations. The two-level system  $|1\rangle$  and  $|2\rangle$  is coupled with the two-photon Rabi frequency  $\Omega = \Omega_D \Omega_p / 2\Delta$  where  $\Omega_D (\Omega_p)$  is the Rabi frequency of the dressing (probe) beam and  $\Delta$  is the detuning of the beams from the atomic resonance. The Bloch equations for atoms at the two-photon resonance take the following simple form:

$$\dot{v} = -\frac{\Gamma_2}{2} v - \Omega w, \quad (3)$$

$$\dot{w} = \Omega v, \quad (4)$$

where  $v = 2 \text{Im}(\rho_{12})$  represents the amplitude of the matter wave grating ( $\rho_{ij}$  is the atomic density matrix) and  $w = \rho_{22} - \rho_{11}$  is the population difference between the two states.

Figure 2b shows the calculated probe output for a step function input. Assuming constant  $\Omega$  (valid for small optical gain), the solutions of the optical Bloch equations show either Rabi oscillation ( $\Omega \gg \Gamma_2/2$ ) or damped behavior ( $\Omega \ll \Gamma_2/2$ ). By reducing the probe power, the Rabi oscillations slow down, and a (quasi-)steady-state gain is obtained in the limit that they are slower than the damping time. It is in this regime that the perturbative treatment with the complex index of refraction applies. Note that for longer times ( $\gg \Gamma_2/\Omega^2$ ) the condensate becomes depleted.

For large optical gain, the Rabi frequency  $\Omega$  increases during the pulse and the above treatment is no longer valid. The population transfer to the recoil state ( $\dot{w}$ ) results in an increase of the number of the probe beam photons inside the condensate volume:  $\dot{n}_p = c(n_p^0 - n_p)/l + N_0 \dot{w}/2$ , where  $l$  is the length of the condensate with  $N_0$  atoms and  $cn_p^0/l$  is the input photon flux. This equation neglects propagation effects of the light by replacing the nonuniform electric field by an average value [8]. Replacing the photon number by the Rabi frequency  $\Omega^2 = R_D 6\pi \lambda^2 cn_p/V$  ( $V$  is the volume of the condensate), we obtain

$$\dot{\Omega} = \frac{c}{l} \left( \Omega^0 - \Omega + \frac{G}{2} v \right), \quad (5)$$

where  $\Omega^0$  is the two-photon Rabi frequency due to the input probe beam and the dressing beam, and  $G$  is defined by  $G = N_0 R_D 6\pi \lambda^2 / 2A$  ( $A$  is the cross section of the condensate perpendicular to the probe beam). The coupled equations (3) and (5) between the light and matter wave grating are analogous to the optical laser, where the atomic polarization and the electric field inside the cavity are coupled. However, the roles of atoms and light are reversed: in the optical laser, the cavity lifetime is usually longer than the coherence time of the atomic polarization, whereas in our case the extremely long coherence time of the condensate dominates.

Adiabatically eliminating the light [ $\dot{\Omega} = 0$  in Eq. (5)] and neglecting condensate depletion ( $w = -1$ ), we are led to

$$\dot{v} = \frac{G - \Gamma_2}{2} v + \Omega^0. \quad (6)$$

Above the threshold for superradiance ( $G \geq \Gamma_2$ ), the matter wave grating builds up exponentially. Below the threshold, it relaxes with a time constant of  $2/(\Gamma_2 - G)$ , providing a gain for the probe light field of

$$1 + \frac{G}{\Gamma_2 - G} = 1 + \frac{n_0 \sigma_{\text{gain}} l}{2} \frac{\Gamma_2}{\Gamma_2 - G}, \quad (7)$$

where  $n_0$  is the condensate density. In the low intensity limit, Eq. (7) reproduces the two-photon gain discussed above [Eq. (1)]. Equation (7) shows that the effect of the coupled equations is to replace the two-photon linewidth  $\Gamma_2$  in Eq. (1) by the ‘‘dynamic’’ coherence decay rate  $\Gamma_2 - G$ . The expansion of the optical gain  $1 + G/(\Gamma_2 - G) = 1 + (G/\Gamma_2) + (G/\Gamma_2)^2 + \dots$  shows the transition from (linear) single-atom gain to (nonlinear) collective gain. At the onset of superradiance, the optical gain diverges.

We studied this transition by first creating a matter wave grating with a Bragg pulse (using the dressing and probe beams), and then observing its time evolution by monitoring the diffracted dressing beam.

The grating showed a simple decay at lower dressing beam intensities (Fig. 4a) [9]. At higher intensities, collective gain started to compensate the loss, and at intensities above a threshold, net amplification was observed. The initial growth rate (Fig. 4b) followed the linear dependence on the intensity of the dressing beam [ $\propto (G - \Gamma_2)$ ] predicted by Eq. (6) and Refs. [6,10]. The net growth of the matter wave grating corresponds to atom amplification which was studied previously by observing an increase in the number of recoiling atoms in time-of-flight images [1]. Here we have monitored the dynamics of amplification *in situ* by observing light instead of atoms.

Extrapolating the decay rate in Fig. 4b to zero intensity of the dressing beam, we obtained the decay time of the matter wave grating  $\Gamma_2$  of 100  $\mu\text{s}$ , in fair agreement with the linewidth of the Bragg excitation process observed previously [4].

Recent demonstrations of slow group velocities for light focused on electromagnetically induced transparency in a three-level lambda system [7]. This system features a narrow dip in a broad absorption feature. In our system, the broad absorption line is missing. Since the propagation of resonant laser pulses is mainly determined by the narrow feature, both systems show analogous behavior. In the past, ‘‘superluminal’’ pulse propagation was observed in noninverted, absorptive two-level systems [11]. Our scheme realizes the opposite case of gain and slow pulse propagation [12].

The dressed condensate studied in this paper is a clean, model system for discussing optical and atom-optical

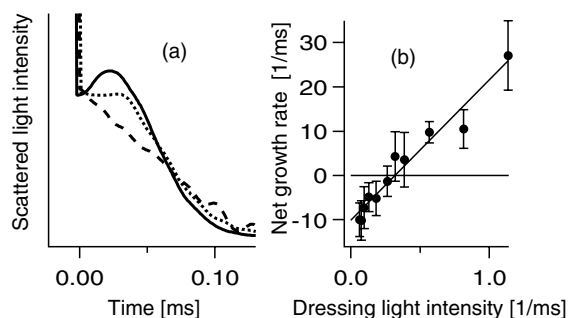


FIG. 4. Pump-probe spectroscopy of a matter wave grating inside the condensate. (a) First, approximately 5% of atoms were transferred to the recoil state by a  $100 \mu\text{s}$  long Bragg pulse. Then the dynamics of the matter wave grating was observed *in situ* by illuminating the grating with off-resonant light and monitoring the diffracted light intensity. All traces were normalized to the same diffracted light intensity at  $t = 0$ . The dressing beam intensity was  $2.9 \text{ mW/cm}^2$  (bottom),  $5.7 \text{ mW/cm}^2$  (middle), and  $13 \text{ mW/cm}^2$  (top). (b) The initial growth rate of the grating vs light intensity shows the threshold for net gain. The intensity of the dressing beam is given in units of the single-atom Rayleigh scattering rate.

properties. The optical amplification can be described as a reflection of the dressing light by a matter wave grating. The initial delay time in the amplification of optical pulses is the time necessary to build up the (quasi-)steady-state matter wave grating. The trailing edge of the transmitted light pulse reflects the slow decay of quasiparticles. Thus, the slow speed of light is simply related to the buildup and decay of quasiparticles which we were able to monitor directly.

The optical gain studied above clearly showed the transition from single-atom gain to collective gain. Previously, recoil related gain based on single-atom phenomena (recoil induced resonances) was observed in cold cesium atoms [13]. Collective gain due to the formation of a density grating was discussed as a possible gain mechanism for lasing action [14] (named CARL—coherent atomic recoil laser) and pursued experimentally [15] with ambiguous results (see [16] and the discussion in [17]). Our experiments clearly identify the two regimes and their relationship.

Our observation of the decay of the matter wave grating can be regarded as pump-probe spectroscopy of quasiparticles in the condensate. The seeding Bragg pulse created the condensate excitations in the free-particle regime. By controlling the angle between the laser beams, one

can also excite phononlike quasiparticles [18]. Thus, the pump-probe scheme presented here could be directly applied to the study of their lifetimes.

In conclusion, we have characterized the optical and atom-optical properties of a dressed condensate. The simple process of Rayleigh scattering gave rise to a rich variety of phenomena including steady-state gain, Rabi oscillations, collective gain, and slow group velocities. We have also introduced a pump-probe technique to study the lifetime of quasiparticles in a condensate.

We thank D. M. Stamper-Kurn for critical reading of the manuscript and A. P. Chikkatur for experimental assistance. This work was supported by the ONR, NSF, ARO, NASA, and the David and Lucile Packard Foundation. A. G. acknowledges support from DAAD and T. P. from the Alexander von Humboldt Foundation.

- [1] S. Inouye *et al.*, *Nature (London)* **402**, 641 (1999).
- [2] M. Kozuma *et al.*, *Science* **286**, 2309 (1999).
- [3] C. Cohen-Tannoudji, J. Dupont-Roc, and G. Grynberg, *Atom-Photon Interactions* (Wiley, New York, 1992).
- [4] J. Stenger *et al.*, *Phys. Rev. Lett.* **82**, 4569 (1999).
- [5] M.-O. Mewes *et al.*, *Phys. Rev. Lett.* **77**, 416 (1996).
- [6] S. Inouye *et al.*, *Science* **285**, 571 (1999).
- [7] L. V. Hau *et al.*, *Nature (London)* **397**, 594 (1999); M. M. Kash *et al.*, *Phys. Rev. Lett.* **82**, 5229 (1999); D. Budker *et al.*, *ibid.* **83**, 1767 (1999).
- [8] This “mean-field model” is only qualitative. See M. Gross and S. Haroche, *Phys. Rep.* **93**, 301 (1982).
- [9] Because the line shape of the Bragg resonance for the condensate atoms is not Lorentzian, the decay curve is not strictly exponential.
- [10] M. G. Moore and P. Meystre, *Phys. Rev. Lett.* **83**, 5202 (1999).
- [11] S. Chu and S. Wong, *Phys. Rev. Lett.* **48**, 738 (1982).
- [12] L. Casperson and A. Yariv, *Phys. Rev. Lett.* **26**, 293 (1971).
- [13] J.-Y. Courtois *et al.*, *Phys. Rev. Lett.* **72**, 3017 (1994).
- [14] R. Bonifacio and L. De Salvo, *Nucl. Instrum. Methods Phys. Res., Sect. A* **341**, 360 (1994).
- [15] G. L. Lippi *et al.*, *Phys. Rev. Lett.* **76**, 2452 (1996); P. R. Hemmer *et al.*, *ibid.* **77**, 1468 (1996).
- [16] W. J. Brown *et al.*, *Phys. Rev. A* **55**, R1601 (1997).
- [17] M. G. Moore, and P. Meystre, *Phys. Rev. A* **59**, R1754 (1999); P. R. Berman, *ibid.* **59**, 585 (1999).
- [18] D. M. Stamper-Kurn *et al.*, *Phys. Rev. Lett.* **83**, 2876 (1999).

## Appendix G

# Does matter wave amplification work for fermions?

This appendix includes the following paper [21]: Wolfgang Ketterle and Shin Inouye, “Does matter wave amplification work for fermions?” *Phys. Rev. Lett.* **86**, 4203 (2001).

## Does Matter Wave Amplification Work for Fermions?

Wolfgang Ketterle and Shin Inouye

*Department of Physics and Research Laboratory of Electronics, Massachusetts Institute of Technology,  
Cambridge, Massachusetts 02139*

(Received 16 August 2000)

We discuss the relationship between bosonic stimulation, density fluctuations, and matter wave gratings. It is shown that enhanced stimulated scattering, matter wave amplification, and atomic four-wave mixing do not require macroscopic occupation of a single quantum state. These processes are in principle possible for fermionic or nondegenerate samples, if they are prepared in a cooperative state. In practice, there are limitations due to short coherence times.

DOI: 10.1103/PhysRevLett.86.4203

PACS numbers: 03.75.Fi, 34.50.-s, 67.90.+z

*Introduction.*—The realization of Bose-Einstein condensation in atoms has made it possible to study the phenomenon of bosonic stimulation for massive particles. Superradiance of atoms [1], four-wave mixing [2], and matter wave amplification [3,4] were described as processes which are bosonically stimulated, i.e., their rates are proportional to  $(N + 1)$ , where  $N$  is the number of identical bosons in the final state. These experimental achievements have raised the question of whether these processes are inherently connected to bosonic systems.

We have recently pointed out that atomic superradiance does not depend on Bose-Einstein statistics and would occur for thermal atoms or even for fermions, although with much shorter coherence times [1], and similar arguments should apply to four-wave mixing. These suggestions have stirred a controversy among researchers. This note will reconcile the different physical descriptions. The central result is that the stimulated processes mentioned above do not rely on quantum statistics, but rather on symmetry and coherence.

In this note, we identify clearly the physical process behind bosonically stimulated scattering. We show that the presence of a macroscopically occupied state increases the density fluctuations of the system, and bosonically enhanced scattering is simply the diffraction of particles from these density fluctuations. The first parts of this paper establish the equivalence of bosonically enhanced scattering, diffraction, and superradiance, which will then be applied to fermionic systems.

*Scattering theory.*—It is useful to summarize basic aspects of the theory of scattering of light or particles from an arbitrary system. These textbook results simply follow from lowest order perturbation theory (Fermi's Golden Rule). The double differential cross section can be decomposed into two factors  $\frac{d^2\sigma}{d\Omega d\omega} = \left(\frac{d\sigma}{d\Omega}\right)_{\text{single}} S(q, \omega)$ . The first one is the differential cross section for the scattering by a single particle (e.g., the Rayleigh cross section for far-off resonant light scattering), the second one is the dynamic structure factor (van Hove or scattering function)  $S(q, \omega)$  which is the Fourier transform of the density-density correlation function:  $S(q, \omega) =$

$(1/2\pi) \int dt e^{i\omega t} \langle \hat{\rho}(q, t) \hat{\rho}^\dagger(q, 0) \rangle$  where  $\hat{\rho}(q)$  is the Fourier transform of the particle density operator (see, e.g., [5]).

For a noninteracting system of bosons,  $S(q, \omega)$  can be expressed using the single-particle states  $|i\rangle$  with energy  $E_i$  and occupation numbers  $N_i$ :

$$S(q, \omega) = S_0(q) \delta(\omega) + \sum_{i \neq j} |\langle j | e^{iqr} | i \rangle|^2 N_i (N_j + 1) \times \delta[\omega - (E_j - E_i)/\hbar]. \quad (1)$$

The factor  $(N_j + 1)$  reflects bosonic stimulation by the occupation of the final state. The elastic term  $S_0(q)$  describes coherent elastic scattering or diffraction and is simply the square of the Fourier transform of the density  $S_0(q) = |\langle \rho^\dagger(q) \rangle|^2 = |\sum N_i \langle i | e^{iqr} | i \rangle|^2$ .

*A simple example.*—It is instructive to apply this formalism to a system of noninteracting bosons which has macroscopic occupation in two momentum states with momentum  $\pm \hbar k$ . If the initial state is a Fock state  $|+k\rangle^{N_+} |-k\rangle^{N_-}$ , we find that, apart from forward scattering, the dominant term in  $S(q, \omega)$  is the bosonically enhanced scattering between those two (degenerate) states,  $S(q, \omega) = [N^2 \delta_{q,0} + N_+(N_- + 1) \delta_{q,-2k} + N_-(N_+ + 1) \delta_{q,2k}] \delta(\omega)$  where the Kronecker symbol  $\delta_{q,p}$  implies  $q = p$  within the wave vector resolution  $\approx 1/L$  of a finite volume with length  $L$ . Alternatively, we can assume the initial state to be a coherent superposition state  $|i\rangle^N$  with the eigenstate  $|i\rangle = c_+ |+k\rangle + c_- |-k\rangle$  and  $|c_\pm|^2 = N_\pm/N$  and  $N = N_+ + N_-$ . Now, the dominant contribution to  $S(q, \omega)$  comes from  $S_0(q) = N^2 \delta_{q,0} + N^2 |c_+|^2 |c_-|^2 [\delta_{q,2k} + \delta_{q,-2k}]$  which is equivalent to the Fock state case when the difference between  $N_\pm$  and  $N_\pm + 1$  can be neglected in the limit of large occupation numbers.

This equivalence between Fock states and coherent superposition states has been extensively discussed in the context of two interfering Bose-Einstein condensates [6–8] and also with regard to optical coherences [9]. Those papers show that, in many situations, a Fock state is equivalent to an ensemble of coherent states with arbitrary phase.

Experimental interrogation determines the phase and reduces the ensemble to a single coherent state with a phase which will vary from experiment to experiment. For large occupation numbers, one can therefore regard the Fock state as an initial state which has not yet “declared its phase,” and, in many cases, for the convenience of calculations, replace the Fock state by a coherent superposition state with an arbitrarily chosen phase.

However, on first sight, the physical interpretation is different. In the Fock state formulation, the enhanced scattering results from a macroscopic occupation number in a single quantum state, whereas for the coherent superposition state, the scattering is simple diffraction by a sinusoidally modulated density distribution with an amplitude proportional to  $N|c_+c_-|$ . This density modulation acts as a diffraction grating for incident light or particles and has a diffraction efficiency proportional to the square of the amplitude. Such a density modulation does not require bosonic atoms. It can, for example, be imprinted into thermal or fermionic clouds by subjecting them to a suitable optical standing wave. The equivalence of these two descriptions points towards one of the major conclusions of this paper, namely macroscopic population of bosonic states is not necessary for enhanced scattering.

The previous discussion assumed scattering between two degenerate momentum states  $|\pm k\rangle$ . A simple Galilean transformation generalizes this to two arbitrary momentum states  $|k_\pm\rangle$  with energies  $E_\pm$ . Now the standing wave moves with a velocity  $\hbar(k_+ + k_-)/2m$  where  $m$  is the mass of the atoms, and the enhanced scattering appears at  $\hbar\omega = \pm(E_+ - E_-)$  instead of at  $\omega = 0$ .

*Enhancement of fluctuations.*—The general results of statistical physics presented above emphasize that enhanced scattering *must* be related to enhanced density fluctuations. Therefore, bosonic enhancement of a scattering rate is either due to a density modulation  $\langle\rho(q)\rangle$  (in the coherent superposition description) or due to density fluctuations (in the Fock state description)—the latter can be regarded as a density modulation with an unknown phase. This relation allows a more intuitive answer to the question of why there is bosonic enhancement when two atoms 1 and 2 collide in the presence of a condensate with  $N_0$  atoms. The standard answer would be that the symmetry of the wave function enhances the scattering rate into the condensate and into some other state 3 by a factor of  $(N_0 + 1)$ . An equivalent answer is that the condensate interferes with atom 2 (or 1) and creates a density grating with an amplitude proportional to  $N_0^{1/2}$ , which diffracts atom 1 (or 2) into state 3. The grating absorbs this momentum transfer by transferring the atom in state 2 (or 1) into the condensate. Therefore, *bosonic stimulation can be regarded as heterodyne amplification of density fluctuations* where the condensate acts as the local oscillator.

*Dicke superradiance.*—We now want to establish the connection between bosonic enhancement and Dicke superradiance. This will formally introduce the enhance-

ment factor  $(N + 1)$  for nonbosonic systems. A system of  $N$  atoms in two states  $|\pm\rangle$  is conveniently described with the formalism introduced by Dicke to discuss superradiance in two-level atoms [10]. It should be emphasized that the only assumption in this treatment is that the  $N$  atoms couple identically to the probe field (the electromagnetic field or some incident particle beam), i.e., that they have the same transition frequency and matrix element without any assumption of quantum statistics. For example, in magnetic resonance experiments, the Dicke treatment would apply to different atomic species with the same value of the magnetic moment.

Dicke regarded the two-level atom as a spin  $1/2$  system and introduced angular momentum quantum numbers. In this subspace, a fully symmetric state of  $N$  atoms has spin  $s = N/2$  and magnetic quantum number  $m = (N_+ - N_-)/2$ . The squared matrix element for the transition  $|s, m \pm 1\rangle \rightarrow |s, m\rangle$  induced by the ladder operator  $S_\mp$  is  $(s \pm m + 1)(s \mp m)$ . Expressing this by initial occupation numbers  $N_\pm$ , one obtains  $N_\pm(N_\mp + 1)$  [11–13], retrieving the formula of bosonic enhancement. For a given  $N$  and  $m$ , the transition rates are largest for the state with  $s = N/2$  which is therefore called the state of maximum cooperativity.

Such a system will couple to the probe field in a superradiant way (i.e., with an up to  $N$  times enhanced transition rate). In the Bloch vector picture, its dynamics is described as the precession of a macroscopic spin vector with length  $s = N/2$ . This spin vector decays in a time  $1/\Gamma$  where  $\Gamma$  is the total (homogeneous and inhomogeneous) linewidth of the transition  $|+\rangle \rightarrow |-\rangle$ . Collective superradiant behavior can be observed only at times shorter than  $1/\Gamma$ .

*Matter wave gratings and fermions.*—Dicke’s formalism is usually applied to one-photon transitions between internal states, but here we use it to discuss scattering, i.e., a two-photon transition between two momentum states  $|k_\pm\rangle$ . Let us first assume that we have an ideal Bose-Einstein condensate in the  $k = 0$  momentum state. Light scattering between momentum states  $k = 0$  and  $k = q$  has an infinite coherence time for a noninteracting condensate of infinite size (Fig. 1a). For a thermal (nondegenerate) cloud of atoms with thermal momentum spread  $\hbar k_{th} \ll \hbar q$  the transition frequencies for the transfer of momentum  $\hbar q$  are Doppler broadened by  $\Gamma = \hbar k_{th} q/m$ . For times shorter than  $1/\Gamma$  the system will behave collectively like the Bose condensed system, i.e., a probe beam would induce transitions between the  $k = 0$  and  $k = q$  momentum states at a rate proportional to  $N_{k=0}(N_{k=q} + 1)$  where  $N_{k=0,q}$  refers to the total number of atoms in states with momentum around  $k = 0, q$ .

Once we have distributed the particles over many initial states, indistinguishability and quantum statistics do not play any role. Therefore, the only modification for a Fermi degenerate cloud is to replace  $k_{th}$  with the Fermi wave vector  $k_F$  in the expression for the inhomogeneous broadening (Fig. 1b). Because of the assumption  $\hbar k_F \ll \hbar q$ , Pauli

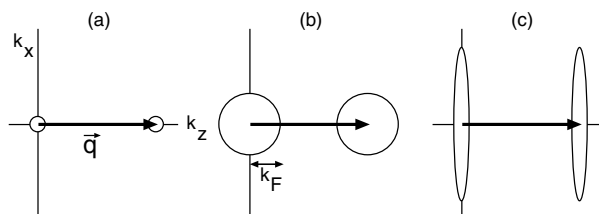


FIG. 1. Momentum transfer  $\vec{q}$  (a) to a Bose-Einstein condensate, (b) to a Fermi sea, and (c) to a momentum squeezed degenerate Fermi cloud. Shown are the populated states vs the  $k$  vector. The momentum spread  $k_F$  of the Fermi sea introduces Doppler broadening of the transition and a finite coherence time, whereas the coherence times in (a) and (c) are much longer due to small momentum spreads in the  $z$  direction and could in principle be infinite.

blocking due to scattering into already occupied states is absent. If this assumption is not made, a part of the cloud becomes inactive, and our discussion would apply only to the atoms near the Fermi surface.

The previous paragraph generalized the bosonic *Fock state* ensemble to nondegenerate and fermionic clouds. We now come back to the *coherent superposition* state. For bosons, it can be produced from a Bose-Einstein condensate in the  $\vec{k} = 0$  state by applying a (so-called Bragg) pulse of two laser beams which differ in wave vector by  $\vec{q}$  and in frequency by the recoil frequency  $\hbar q^2/2m$ . Those beams resonantly drive the transition between momentum states  $\vec{k} = 0$  and  $\vec{k} = \vec{q}$  [14,15] and prepare the superposition state discussed above. Similarly, in a thermal (or fermionic) cloud, the Bragg pulse creates a modulated density distribution with wavelength  $2\pi/q$  which has the same contrast as in the bosonic case and will diffract light or atoms at the same rate. However, due to the thermal motion with velocity  $\hbar k_{th}/m$ , this grating decays during a time  $m/\hbar k_{th} q = 1/\Gamma$  (for the fermionic case,  $k_F$  has to be substituted for  $k_{th}$ ). Thus the Dicke picture and the diffraction picture agree.

*Coherence time.*—The Doppler broadening discussed above seems to imply a fundamental limit to the coherence time of a Fermi system. However, at least in principle, one can prepare a Fermi system with infinite coherence time by starting out with a cloud which is in a single momentum state along the  $\hat{z}$  axis, but occupies many momentum states along  $\hat{x}$  and  $\hat{y}$ . With a Bragg pulse transferring momentum  $q\hat{z}$ , one can prepare a system which shows collective behavior for scattering particles or light with momentum transfer  $q\hat{z}$  with an infinite coherence time (Fig. 1c). Therefore, there is no direct connection between a long coherence time and a high phase-space density. In this ensemble, the scattering is between the states  $|k_z = 0\rangle \otimes |k_x, k_y\rangle$  and  $|k_z = q\rangle \otimes |k_x, k_y\rangle$ . Therefore, we have enhanced scattering into the  $|k_z = q\rangle$  quantum state, but the atoms may differ in other quantum numbers. What matters is only the symmetrization of the many-body wave function along  $\hat{z}$ . The other quantum

numbers ensure that there is no conflict with the Pauli blocking for fermionic systems. This is analogous to the separation of electronic wave functions into a symmetric part (e.g., the spin part) and an antisymmetric part (e.g. the spatial part) where the coupling to an external field (e.g., electron spin resonance experiment) depends only on the symmetric part.

*Experiments.*—The experiments both on superradiance [1] and four-wave mixing [2] in Bose-Einstein condensates have in common that a matter wave grating formed by two macroscopically occupied momentum states is probed, either by light or by atoms. Both experiments create the coherent superposition state discussed above using a Bragg pulse. In the limit of low intensity of the probe beam, the scattering is independent of the nature of the probe particles—one could have used any kind of radiation, bosons or fermions [16]. The bosonic stimulation observed in both experiments demonstrates the dynamic nature of the matter wave grating. Each time a particle or photon is diffracted, the amplitude of the grating grows.

In practice, it is difficult or impossible to carry out these experiments with fermions or thermal atoms. When we observed superradiance of a condensate, we could not observe similar behavior above the BEC transition temperature since the threshold laser intensity for superradiant gain is several orders of magnitude higher (see Ref. [1] for details). Furthermore, the superradiance may be suppressed by heating or other decoherence processes. The shorter coherence time for non-BEC samples should be even more crucial for the four-wave mixing experiment where the matter wave grating is probed by very slow atoms which have a long transit time of about 1 ms through the sample. Another concern is incoherent scattering of the probe particles which accompany the stimulated processes discussed so far. Since the incoherent processes scale linearly with the number of atoms, whereas the stimulated process is proportional to  $N^2$ , there is in principle always a regime where the stimulated process dominates [17].

*Discussion.*—Coming back to the initial question: Is matter wave amplification possible for fermions? The answer is yes, if the system is prepared in a cooperative state and the amplification occurs in a time shorter than the coherence time. However, this amplification does not pile up atoms in a single quantum state, but rather in states which are in the same (or approximately the same) momentum state along  $\hat{z}$ , but differ in other quantum numbers. Therefore, this amplification can be regarded as amplification of a density modulation or as amplification of spatial bunching of atoms. Alternatively, one can regard the density modulation as a collective excitation of the system which involves bosonic quasiparticles (e.g., phonons). Superradiance and four-wave mixing (both with bosons and fermions) can then be ascribed to bosonic stimulation by those quasiparticles.

The phase-coherent matter wave amplification for fermions would start with a short Bragg pulse which puts

some of the atoms into a recoil state which is then amplified. This superposition of two momentum states creates a matter wave grating. This can be regarded as the interference pattern of each atom with itself with all the individual interference patterns being exactly in phase. Matter wave amplification occurs when a single laser beam is diffracted off this grating, increasing the amplitude of each atom to be in the recoiling state. Therefore, the matter wave amplification scheme of Refs. [3,4] would work for fermions, provided the whole process can be done in the short coherence time of the fermionic matter wave grating.

Of course, there is a fundamental difference between bosons and fermions which is reflected in the symmetry of the total wave function. A bosonic system with two macroscopically occupied quantum states is *always* in a fully symmetric and maximally cooperative state. In other words, if two independent Bose condensates cross each other, there is always a macroscopic interference pattern (as observed experimentally [18]), which is reflected in  $S(q, \omega)$  being proportional to  $N^2$  (or to  $N_+N_-$ , to be more precise). It is this density modulation which can be amplified by the dynamic diffraction discussed in this paper. If two beams of fermions overlap, there is no macroscopic interference, unless the two beams were prepared in a symmetric way, e.g., by generating one of the beams by a Bragg pulse from the other one.

Our discussion of scattering without change of the internal state can be generalized. For example, if atoms scatter into the condensate through a spinflip process, the density grating has to be replaced by a polarization or coherence grating. Such gratings were experimentally studied for laser-cooled atoms in Ref. [19].

This paper has focused on bosonically enhanced scattering. Similarly, bosonic enhancement of spontaneous emission can be equally well described by a cooperative initial state without invoking quantum statistics. For scattering, the relevant coupling strength is density fluctuation. For spontaneous emission, it is the electric dipole moment. Both are enhanced by the presence of a Bose condensate, in the latter case because the excited atom corresponds to a Dicke vector of spin  $s = N/2, m = -N/2 + 1/2$  which couples more strongly to the vacuum fluctuations of the electromagnetic field than an individual atom.

In conclusion, we have shown that bosonically enhanced scattering is related to density fluctuations and matter wave gratings. The analogy with Dicke superradiance emphasizes that matter wave amplification and atomic

four-wave mixing are possible for fermionic or nondegenerate samples if they are prepared in a cooperative state which shows coherent and collective behavior.

We are grateful to A. Aspect, C. Cohen-Tannoudji, S. Haroche, K. Helmerson, D. Kleppner, P. Meystre, W. D. Phillips, D. E. Pritchard, S. Rolston, M. O. Scully, D. Snoke, D. M. Stamper-Kurn, and E. Wright for helpful discussion, and to A. Görlitz, C. Raman, A. P. Chikkatur, and S. Gupta for valuable comments on the manuscript. This work was supported by NSF, ONR, ARO, NASA, and the David and Lucile Packard Foundation.

*Note added.*—After submission of this paper we learned of similar work by Moore and Meystre [20] which agrees with our conclusions.

- 
- [1] S. Inouye *et al.*, *Science* **285**, 571 (1999).
  - [2] L. Deng *et al.*, *Nature (London)* **398**, 218 (1999).
  - [3] S. Inouye *et al.*, *Nature (London)* **402**, 641 (1999).
  - [4] M. Kozuma *et al.*, *Science* **286**, 2309 (1999).
  - [5] A. Griffin, *Excitations in a Bose-Condensed Liquid* (Cambridge University Press, Cambridge, 1993).
  - [6] J. Javanainen and S. M. Yoo, *Phys. Rev. Lett.* **76**, 161 (1996).
  - [7] M. Naraschewski *et al.*, *Phys. Rev. A* **54**, 2185 (1996).
  - [8] Y. Castin and J. Dalibard, *Phys. Rev. A* **55**, 4330 (1997).
  - [9] K. Mølmer, *Phys. Rev. A* **55**, 3195 (1997).
  - [10] R. H. Dicke, *Phys. Rev.* **93**, 99 (1954).
  - [11] M. Sargent III, M. O. Scully, and W. E. Lamb, Jr., *Laser Physics* (Addison-Wesley, Reading, Massachusetts, 1974).
  - [12] J. J. Sakurai, *Modern Quantum Mechanics* (Addison-Wesley, Reading, Massachusetts, 1994).
  - [13] H. Wallis, *Appl. Phys. B* **65**, 707 (1997).
  - [14] M. Kozuma *et al.*, *Phys. Rev. Lett.* **82**, 871 (1999).
  - [15] J. Stenger *et al.*, *Phys. Rev. Lett.* **82**, 4569 (1999).
  - [16] P. Villain *et al.*, *cond-mat/0005417*.
  - [17] In the case of a fermionic sample, the density of particles can be increased only by increasing the momentum spread of the sample. This can increase the incoherent “background” for four-wave mixing. For the ensemble in Fig. 1c, an increase in  $N$  at constant volume requires the transverse velocity spread to increase as  $N^{1/2}$ . Therefore, for large  $N$ , the incoherent elastic scattering rate increases as  $N^{3/2}$ , still slower than the stimulated scattering.
  - [18] M. R. Andrews *et al.*, *Science* **275**, 637 (1997).
  - [19] A. Kumarakrishnan, S. B. Cahn, U. Shim, and T. Sleator, *Phys. Rev. A* **58**, R3387 (1998).
  - [20] M. G. Moore and P. Meystre, preceding Letter, *Phys. Rev. Lett.* **86**, 4199 (2001).

## Appendix H

# Observation of vortex phase singularities in Bose-Einstein condensates

This appendix includes the following preprint [24]: S. Inouye, S. Gupta, T. Rosenband, A.P. Chikkatur, A. Görlitz, T.L. Gustavson, A.E. Leanhardt, D.E. Pritchard, and W. Ketterle, “Observation of vortex phase singularities in Bose-Einstein condensates,” *cond-mat/0104444* (2001).

## Observation of vortex phase singularities in Bose-Einstein condensates

S. Inouye, S. Gupta, T. Rosenband, A.P. Chikkatur,  
 A. Görlitz, T.L. Gustavson, A.E. Leanhardt, D.E. Pritchard, and W. Ketterle  
*Department of Physics, Research Laboratory of Electronics, and MIT-Harvard Center for Ultracold Atoms,  
 Massachusetts Institute of Technology, Cambridge, MA 02139, USA*  
 (April 23, 2001)

We have observed phase singularities due to vortex excitation in Bose-Einstein condensates. Vortices were created by moving a laser beam through a condensate. They were observed as dislocations in the interference fringes formed by the stirred condensate and a second unperturbed condensate. The velocity dependence for vortex excitation and the time scale for re-establishing a uniform phase across the condensate were determined.

Quantized vortices play a key role in the dynamics of superfluid flow [1]. The nucleation of vortices determines the critical velocity for the onset of dissipation at zero temperature. In liquid helium, vortices are a source of friction between the normal fluid and the superfluid. Multiple interacting vortices can form a lattice or vortex tangle, depending on their geometry and charge.

Bose-Einstein condensates of dilute atomic gases offer a unique opportunity to study quantum hydrodynamics. The low density of the gas allows direct comparison with first principle theories. A condensate is characterized by a macroscopic wavefunction  $\psi(\vec{r}) = \sqrt{\rho(\vec{r})} \exp(i\phi(\vec{r}))$ , which satisfies a non-linear Schrödinger equation. The density  $\rho(\vec{r})$  and the velocity field  $\vec{v}_s(\vec{r})$  in the hydrodynamic equations can now be replaced by the square of the wavefunction ( $\rho(\vec{r}) = |\psi(\vec{r})|^2$ ) and the gradient of the *phase* of the wavefunction

$$\vec{v}_s(\vec{r}) = \frac{\hbar}{m} \nabla \phi(\vec{r}), \quad (1)$$

where  $m$  is the mass of the particle.

Recently, vortices in a Bose-Einstein condensate have been realized experimentally and are currently under intensive study [2–5]. In most of this work, vortices were identified by observing the density depletion at the cores. The velocity field was inferred only indirectly, with the exception of the work on circulation in a two-component condensate [2]. The flow field of a vortex can be directly observed when the phase of the macroscopic wavefunction is measured using interferometric techniques. In this work, we created one or several vortices in one condensate and imaged its phase by interfering it with a second unperturbed condensate which served as a local oscillator.

Interferometric techniques have previously been applied either to simple geometries such as trapped or freely expanding condensates [6–8], or to read out a phase imprinted by rf- or optical fields [2,9,10]. Here we apply an interferometric technique to visualize turbulent flow.

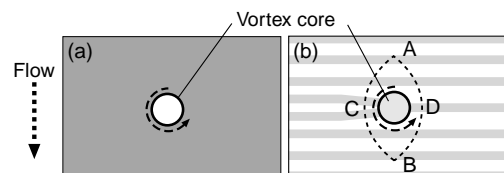


FIG. 1. Density (a) and phase (b) profile of a moving condensate with singly-charged ( $n = 1$ ) vortex. The density profile shows the vortex core, whereas the phase pattern features a fork-like dislocation at the position of the vortex. Interference between two initially separated, freely expanding condensates produces exactly the same pattern as shown in (b), if one of the condensate contains a vortex.

The line integral of Eq. (1) around a closed path gives the quantization of circulation:

$$\int \vec{v}(\vec{r}) \cdot d\vec{r} = \frac{\hbar}{m} (\phi(\vec{r}_f) - \phi(\vec{r}_i)). \quad (2)$$

If the path is singly connected, there is no circulation. If the path is multiply connected (like around a vortex core) the circulation can take values  $nh/m$  (integer multiples of  $h/m$ ), since the phase is only defined modulo  $2\pi$ . As a result, the phase accumulated between two points A and B can be different depending on the path (Fig. 1). The integer quantum number  $n$  is called the charge of the vortex. When the phase gradient is integrated along a path to the left of the vortex (path ACB), the accumulated phase differs by  $2n\pi$  from the path to the right (ADB).

This phase difference can be visualized with interferometric techniques. When two condensates with relative velocity  $v$  overlap, the total density shows straight interference fringes with a periodicity  $h/mv$ . If one of the condensates contains a vortex of charge  $n$ , there are  $n$  more fringes on one side of the singularity than on the other side (Fig. 1b). The change in the fringe spacing reflects the velocity field of the vortex. An observation of this fork-like dislocation in the interference fringes is a clear signature of a vortex [11].

Our setup for the interferometric observation of vortices is essentially a combination of two experiments conducted in our lab in the past [6,12]. Briefly, laser cooled sodium atoms were loaded into a double-well potential and further cooled by rf-induced evaporation below the BEC transition temperature. The double-well potential was created by adding a potential hill at the center of a cigar-shaped magnetic trap. For this, blue-detuned far off-resonant laser light (532 nm) was focused to form an elliptical  $75\ \mu\text{m} \times 12\ \mu\text{m}$  (FWHM) light sheet and was aligned to the center of the magnetic trap with the long axis of the sheet perpendicular to the long axis of the condensate. The condensates produced in each well were typically  $20\ \mu\text{m}$  in diameter and  $100\ \mu\text{m}$  in length. The height of the optical potential was  $\sim 3\ \text{kHz}$ , which was slightly larger than the chemical potential of the condensate. A more intense light sheet would have increased the distance between the condensates, thus reduced the fringe spacing [6].

After two condensates each containing  $\sim 1 \times 10^6$  atoms in the  $F = 1, m_F = -1$  state were formed in the double-well potential, we swept a second blue-detuned laser beam through one of the condensates using an acousto-optical deflector (Fig. 2). The focal size of the sweeping laser beam ( $12\ \mu\text{m} \times 12\ \mu\text{m}$ , FWHM) was close to the width of the condensate. The alignment of this beam was therefore done using an expanded condensate in a weaker trap where the beam profile created a circular “hole” in the condensate density distribution.

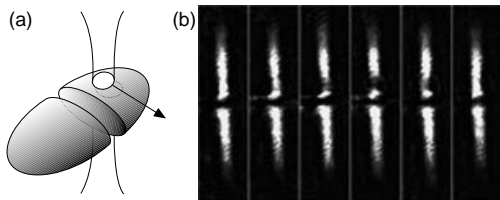


FIG. 2. Schematic (a) and phase-contrast images (b) of the condensates used for the experiment. A blue-detuned laser beam (not shown in the figure) was focused into a light sheet separating the two condensates in the magnetic trap. Another tightly focused laser beam was swept through one of the condensates (the upper one in image (b)) to excite vortices. The intensity of each laser beam was a factor of four higher than in the experiments to enhance the depleted regions in the images. The images in (b) have a field of view of  $100\ \mu\text{m} \times 380\ \mu\text{m}$ . For each image, the stirrer was advanced from left to right by  $5\ \mu\text{m}$ .

After sweeping the beam once across the “sample” condensate, the magnetic and optical fields were switched off and the two condensates expanded and overlapped during 41 ms time-of-flight. The atoms were then optically pumped into the  $F = 2$  hyperfine ground state for  $80\ \mu\text{s}$  and subsequently probed for  $20\ \mu\text{s}$  by absorption imaging

tuned to the  $F = 2$  to  $F' = 3$  cycling transition.

Obtaining high contrast interference fringes ( $\sim 70\%$ ) across the whole cloud required attention to several key factors. First, standard absorption imaging integrates along the line of sight, which was vertical in our experiment. Any bending or distortions of the interference fringes along the direction of observation would result in a loss of contrast. This was avoided by restricting the absorption of the probe light to a thin horizontal slice. The optical pumping beam was focused into a light sheet of adjustable thickness (typically  $100\ \mu\text{m}$ , which is about 10% of the diameter of the cloud after the time-of-flight) and a width of a few millimeters. This pumping beam propagated perpendicularly to the probe light and parallel to the long axis of the trap. Second, the number of atoms in the condensates had to be reduced to about  $1 \times 10^6$  (corresponding to a chemical potential  $\mu \sim 2.5\ \text{kHz}$ ). Higher numbers of atoms resulted in a severe loss of contrast, even if we detuned the probe beam to reduce optical density. We suspect that at high density, the two condensates do not simply interpenetrate and interfere, but interact and collide. Third, high spatial homogeneity of the probe beam was important to obtain absorption images with low technical noise. In some of our experiments, the probe beam position was actively scanned to smooth the beam profile. Fourth, the intensity of the sweeping blue-detuned beam was adjusted so that the height of the optical potential was a fraction (typically one half) of the chemical potential of the condensate. Higher intensity of the sweeping beam resulted in reduced interference fringe contrast, probably due to other forms of excitations.

Images of interfering condensates show a qualitative difference between stirred (Fig. 3(b-d)) and unperturbed states (Fig. 3(a)). Fork-like structures in the fringes were often observed for stirred condensates, whereas unperturbed condensates always showed straight fringes. The charge of the vortices can be determined from the fork-like pattern. In Fig. 3(b), vortices were excited in the condensate on top, and the higher number of fringes on the left side indicates higher relative velocity on this side, corresponding to counterclockwise flow. Fig. 3(c) shows a vortex of opposite charge. The double fork observed in Fig. 3(d) represents the phase pattern of a vortex pair. Multiply charged vortices, which are unstable against the break-up into singly charged vortices, were not observed.

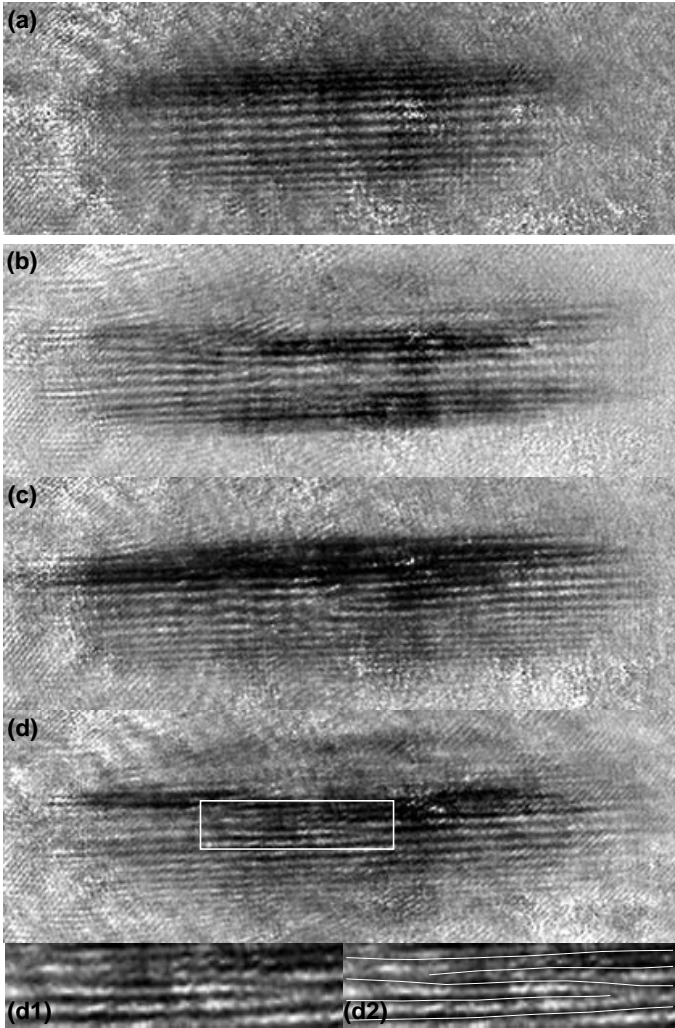


FIG. 3. Observation of the phase singularities of vortices created by sweeping a laser beam through a condensate. Without the sweep, straight fringes of  $\sim 20 \mu\text{m}$  spacings were observed (a), while after the sweep, fork-like dislocations appeared (b-d). The speed of the sweep was  $1.1 \mu\text{m}/\text{ms}$ , corresponding to a Mach number of  $\sim 0.18$ . The field of view of each image is  $1.1 \text{ mm} \times 0.38 \text{ mm}$ . Fig. (d) shows a pair of dislocations with opposite circulation characteristic of a vortex pair. At the bottom, magnified images of the fork-like structures are shown (d1) with lines to guide the eye (d2). The orientation of the condensates is the same as in Fig. 2(b).

Theoretical studies of the superfluid flow around moving objects predict dissipationless flow below a critical velocity [1]. Above this velocity, vortices of opposite circulation are created on the two sides of the moving object and give rise to a drag force [13]. A recent experiment in our group found the onset of dissipation at a critical Mach number of  $v_c/c_s \sim 0.1$  [14]. Dissipation at low velocities can not only occur by vortex shedding, but also by the creation of phonons in the low density regions of

the condensate [15]. The direct observation of vortices at similar Mach numbers (Fig. 3) provides strong evidence that vortices play a major role in the onset of dissipation at the critical velocity.

By varying the speed of the laser beam sweep, we determined the velocity dependence of the vortex nucleation process. Due to the turbulent nature of the flow, every image was different even if they were taken under the same experimental conditions. Thus the images were classified by counting the number of vortices and the fractions were plotted versus the speed of the sweep (Fig. 4). The classification was done after putting images in random order to eliminate a possible “psychological bias.” The plot suggests that the nucleation of vortices requires a velocity of  $\sim 0.5 \mu\text{m}/\text{ms}$ , corresponding to a Mach number  $v_c/c_s \sim 0.08$ , consistent with our previous measurement [14]. However, a direct comparison is not possible due to different geometries—in the present experiment, the stirrer was swept along the radial direction of the condensate and almost cut the cloud completely, whereas in the previous experiment, the stirrer moved along the axial direction of an expanded condensate.

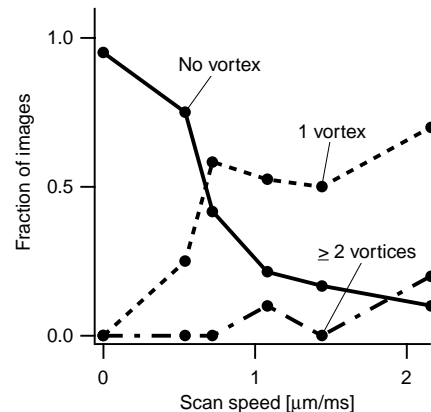


FIG. 4. Velocity dependence of vortex excitation. The fraction of images with zero (solid line), one (dashed line), and two or more vortices (dash-dotted line) are plotted versus the speed of the sweep. After the sweep, the atoms were released from the trap without delay. The total number of evaluated images was 50. Ambiguous low contrast images were excluded; therefore, the sum of the fractions is less than one.

Previous experiments have dramatically demonstrated the robustness of the long-range coherence of the condensate [6,9]. The interferometric technique used here is a sensitive way to assess whether a condensate has the assumed ground state wave function which is characterized by a uniform phase. Sweeping through the condensate excites turbulent flow. By delaying the release of the atoms from the trap by a variable amount of time, we can study the relaxation of the condensate towards its ground

state. Fig. 5 shows that the condensate completely recovers its uniform phase after 50 – 100 ms. Vortices have disappeared after  $\sim 30$  ms. Of course, these measurements depend crucially on the specific geometry of the cloud, but they do indicate typical time scales. The sensitivity of this method was illustrated by the following observation: in a weaker trap, we saw an oscillation in time between images with straight high contrast fringes and images with low contrast fringes. This was probably due to the excitation of a sloshing motion along the weak axis of the condensate.

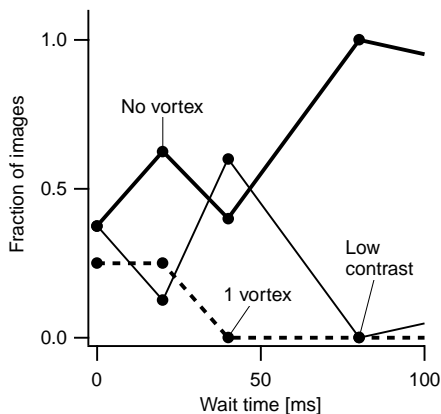


FIG. 5. Relaxation of a condensate towards uniform phase. The fraction of images with zero (thick solid line) and one (dashed line) vortex and with low contrast (thin solid line) are plotted versus the waiting time after the laser beam sweep ( $v/c_s \sim 0.09$ ). The total number of images used for creating this plot was 33.

For interferometric detection of vortices, two different techniques have been discussed. The one employed here uses a separate condensate as a local oscillator. The other alternative is to split, shift and recombine a single condensate with vortices. In this case, the interference pattern is more complicated because all singularities and distortions appear twice. The simulations in Ref. [16] show that the self-interference technique produces more complicated fringe patterns. After completion of this work, we learned that this second technique was used in ENS, Paris to observe the phase pattern of a single vortex [17].

In conclusion, we have studied vortex excitation in Bose-Einstein condensates using an interferometric technique. This technique is suited for the study of complicated superfluid flows, e.g., when multiple vortices with opposite charges are present. We have obtained a clear visualization of vortices as topological singularities, confirmed the role of vortices in the onset of dissipation near the critical velocity, and observed the relaxation of a stirred condensate towards a state with uniform phase.

The field of Bose-Einstein condensation combines atomic and condensed matter physics. This aspect is

illustrated by this work where an atomic physics technique, matter wave interferometry, was used to probe the nucleation of vortices, a problem of many-body physics. There are many issues of vortex physics which remain unexplored, including vortices in two-dimensional condensates (condensates in lower dimensions were recently realized in our laboratory [18]), pinning of vortices by additional laser beams, and interactions between vortices.

This work was supported by NSF, the ONR, ARO, NASA, and the David and Lucile Packard Foundation. A.E.L. and A.P.C. acknowledge additional support by fellowships from NSF, and JSEP, respectively.

- 
- [1] R.J. Donnelly, *Quantized Vortices in Helium II* (Cambridge University Press, Cambridge, England, 1991); P. Nozieres and D. Pines, *The Theory of Quantum Liquids* (Addison-Wesley, Redwood City, CA, 1990).
  - [2] M.R. Matthews *et al.*, Phys. Rev. Lett. **83**, 2498 (1999).
  - [3] K.W. Madison, F. Chevy, W. Wohlleben, and J. Dalibard, Phys. Rev. Lett. **84**, 806 (2000).
  - [4] B.P. Anderson *et al.*, Phys. Rev. Lett. **86**, 2926 (2001).
  - [5] J.R. Abo-Shaeer, C. Raman, J.M. Vogels, and W. Ketterle, Science, in press.
  - [6] M.R. Andrews *et al.*, Science **275**, 637 (1997).
  - [7] J.E. Simsarian *et al.*, Phys. Rev. Lett. **85**, 2040 (2000).
  - [8] I. Bloch and T. W. Hänsch and T. Esslinger, Nature **403**, 166 (2000).
  - [9] D.S. Hall, M.R. Matthews, C.E. Wieman, and E.A. Cornell, Phys. Rev. Lett. **81**, 1543 (1998).
  - [10] J. Denschlag *et al.*, Science **287**, 97 (2000).
  - [11] M.R. Andrews, Ph.D. Thesis (MIT, Cambridge, MA, 1998); E.L. Bolda and D.F. Walls, Phys. Rev. Lett. **81**, 5477 (1998); J. Tempere and J.T. Devreese, Solid State Commun. **108**, 993 (1998).
  - [12] C. Raman *et al.*, Phys. Rev. Lett., **83** 2502 (1999).
  - [13] T. Frisch, Y. Pomeau, and S. Rica, Phys. Rev. Lett. **69**, 1644 (1992); T. Winiecki, J.F. McCann, and C.S. Adams, Phys. Rev. Lett. **82**, 5186 (1999). See C. Raman, R. Onofrio, J.M. Vogels, J.R. Abo-Shaeer, and W. Ketterle, J. Low Temp. Phys. **122**, 99 (2001) for further discussions.
  - [14] R. Onofrio *et al.*, Phys. Rev. Lett. **85**, 2228 (2000).
  - [15] P.O. Fedichev and G.V. Shlyapnikov, preprint cond-mat/0004039.
  - [16] L. Dobrek *et al.*, Phys. Rev. A, **60**, R3381 (1999).
  - [17] J. Dalibard, private communication.
  - [18] A. Görlitz *et al.*, to be published.

# Bibliography

- [1] M. H. Anderson, J. R. Ensher, M. R. Matthews, C. E. Wieman, and E. A. Cornell, "Observation of Bose-Einstein Condensation in a Dilute Atomic Vapor," *Science* **269**, 198 (1995).
- [2] C. C. Bradley, C. A. Sackett, J. J. Tollet, and R. G. Hulet, "Evidence of Bose-Einstein Condensation in an Atomic Gas with Attractive Interactions," *Phys. Rev. Lett.* **75**, 1687 (1995).
- [3] K. B. Davis, M.-O. Mewes, M. R. Andrews, N. J. van Druten, D. S. Durfee, D. M. Kurn, and W. Ketterle, "Bose-Einstein Condensation in a Gas of Sodium Atoms," *Phys. Rev. Lett.* **75**, 3969 (1995).
- [4] K. Huang, *Statistical Mechanics* (Wiley, New York, 1987).
- [5] M. O. Mewes, M. R. Andrews, N. J. van Druten, D. M. Kurn, D. S. Durfee, and W. Ketterle, "Bose-Einstein condensation in a tightly confining DC magnetic trap," *Phys. Rev. Lett.* **77**, 416 (1996).
- [6] M. R. Andrews, C. G. Townsend, H.-J. Miesner, D. S. Durfee, D. M. Kurn, and W. Ketterle, "Observation of interference between two Bose condensates," *Science* **275**, 637 (1997).
- [7] D. M. Stamper-Kurn, M. R. Andrews, A. P. Chikkatur, S. Inouye, H.-J. Miesner, J. Stenger, and W. Ketterle, "Optical confinement of a Bose-Einstein condensate," *Phys. Rev. Lett.* **80**, 2027 (1998).
- [8] S. Inouye, M. R. Andrews, J. Stenger, H.-J. Miesner, D. M. Stamper-Kurn, and W. Ketterle, "Observation of Feshbach resonances in a Bose-Einstein condensate," *Nature* **392**, 151 (1998).
- [9] J. Stenger, S. Inouye, M. R. Andrews, H.-J. Miesner, D. M. Stamper-Kurn, and W. Ketterle, "Strongly enhanced inelastic collisions in a Bose-Einstein condensate near Feshbach resonances," *Phys. Rev. Lett.* **82**, 2422 (1999).
- [10] J. Stenger, S. Inouye, D. M. Stamper-Kurn, H.-J. Miesner, A. P. Chikkatur, and W. Ketterle, "Spin domains in ground-state Bose-Einstein condensates," *Nature* **396**, 345 (1998).
- [11] M. R. Andrews, D. M. Kurn, H.-J. Miesner, D. S. Durfee, C. G. Townsend, S. Inouye, and W. Ketterle, "Propagation of sound in a Bose-Einstein condensate," *Phys. Rev. Lett.* **79**, 553 (1997).

- [12] D. M. Stamper-Kurn, H.-J. Miesner, S. Inouye, M. R. Andrews, and W. Ketterle, "Collisionless and hydrodynamic excitations of a Bose-Einstein condensate," *Phys. Rev. Lett.* **81**, 500 (1998).
- [13] H.-J. Miesner, D. M. Stamper-Kurn, J. Stenger, S. Inouye, A. P. Chikkatur, and W. Ketterle, "Observation of metastable states in spinor Bose-Einstein condensates," *Phys. Rev. Lett.* **82**, 2228 (1999).
- [14] D. M. Stamper-Kurn, H.-J. Miesner, A. P. Chikkatur, S. Inouye, J. Stenger, and W. Ketterle, "Quantum tunneling across spin domains in a Bose-Einstein condensate," *Phys. Rev. Lett.* **83**, 661 (1999).
- [15] H.-J. Miesner, D. M. Stamper-Kurn, M. R. Andrews, D. S. Durfee, S. Inouye, and W. Ketterle, "Bosonic stimulation in the formation of a Bose-Einstein condensate," *Science* **279**, 1005 (1998).
- [16] D. M. Stamper-Kurn, H.-J. Miesner, A. P. Chikkatur, S. Inouye, J. Stenger, and W. Ketterle, "Reversible formation of a Bose-Einstein condensate," *Phys. Rev. Lett.* **81**, 2194 (1998).
- [17] J. Stenger, S. Inouye, A. P. Chikkatur, D. M. Stamper-Kurn, D. E. Pritchard, and W. Ketterle, "Bragg spectroscopy of a Bose-Einstein condensate," *Phys. Rev. Lett.* **82**, 4569 (1999).
- [18] S. Inouye, A. P. Chikkatur, D. M. Stamper-Kurn, J. Stenger, D. E. Pritchard, and W. Ketterle, "Superradiant Rayleigh scattering from a Bose-Einstein condensate," *Science* **285**, 571 (1999).
- [19] S. Inouye, T. Pfau, S. Gupta, A. P. Chikkatur, A. Grilitz, D. E. Pritchard, and W. Ketterle, "Observation of phase-coherent amplification of atomic matter waves," *Nature* **402**, 641 (1999).
- [20] S. Inouye, R.F.Lw, S. Gupta, T. Pfau, A. Grilitz, T. L. Gustavson, D. E. Pritchard, and W. Ketterle, "Amplification of Light and Atoms in a Bose-Einstein Condensate," *Phys. Rev. Lett.* **85**, 4225 (2000).
- [21] W. Ketterle and S. Inouye, "Does matter wave amplification work for fermions?," *Phys. Rev. Lett.* **86**, 4203 (2001).
- [22] D. M. Stamper-Kurn, A. P. Chikkatur, A. Grilitz, S. Inouye, S. Gupta, D. E. Pritchard, and W. Ketterle, "Excitation of phonons in a Bose-Einstein condensate by light scattering," *Phys. Rev. Lett.* **83**, 2876 (1999).
- [23] A. P. Chikkatur, A. Grilitz, D. M. Stamper-Kurn, S. Inouye, S. Gupta, and W. Ketterle, "Suppression and enhancement of impurity scattering in a Bose-Einstein condensate," *Phys. Rev. Lett.* **85**, 483 (2000).
- [24] S. Inouye, S. Gupta, T. Rosenband, A. Chikkatur, A. Grilitz, T. Gustavson, A. Leanhardt, D. Pritchard, and W. Ketterle, "Observation of vortex phase singularities in Bose-Einstein condensates," (2001), preprint cond-mat/0104444.
- [25] D. M. Stamper-Kurn, Ph.D. thesis, Massachusetts Institute of Technology, 1999.

- [26] A. Pais, *Subtle is the Lord, The Science and the Life of Albert Einstein* (Clarendon Press, Oxford, 1982).
- [27] K. Gavroglu, *Fritz London: A Scientific Biography* (Cambridge University Press, Cambridge, 1995).
- [28] A. Griffin, in *A Brief History of Our Understanding of BEC: From Bose to Beliaev, Proceedings of the International School of Physics Enrico Fermi, Course CXL*, edited by M. Inguscio, S. Stringari, and C. Wieman (IOS Press, Amsterdam, 1999), pp. –.
- [29] T. J. Greytak, in *Bose-Einstein Condensation*, edited by A. Griffin, D. Snoke, and S. Stringari (Cambridge University Press, Cambridge, 1995), pp. 131–159.
- [30] S. Chu, “The manipulation of neutral particles,” *Rev. Mod. Phys.* **70**, 685 (1998).
- [31] C. N. Cohen-Tannoudji, “Manipulating atoms with photons,” *Rev. Mod. Phys.* **70**, 707 (1998).
- [32] W. D. Phillips, “Laser cooling and trapping of neutral atoms,” *Rev. Mod. Phys.* **70**, 721 (1998).
- [33] E. A. Cornell, J. R. Ensher, and C. E. Wieman, in *Bose-Einstein condensation in atomic gases, Proceedings of the International School of Physics Enrico Fermi, Course CXL*, edited by M. Inguscio, S. Stringari, and C. Wieman (IOS Press, Amsterdam, 1999), pp. 15–66.
- [34] W. Ketterle, D. S. Durfee, and D. M. Stamper-Kurn, in *Bose-Einstein condensation in atomic gases, Proceedings of the International School of Physics Enrico Fermi, Course CXL*, edited by M. Inguscio, S. Stringari, and C. Wieman (IOS Press, Amsterdam, 1999), pp. 67–176.
- [35] L. deBroglie, Ph.D. thesis, 1923.
- [36] S. N. Bose, “Plancks Gesetz und Lichtquantenhypothese,” *Z. Phys.* **26**, 178 (1924).
- [37] A. Einstein, “Quantentheorie des einatomigen idealen Gases. II,” *Sitzungsberichte der preussischen Akademie der Wissenschaften Bericht* **1**, 3 (1925).
- [38] E. Fermi, *Z. Physik* **36**, 902 (1926).
- [39] W. H. Keesom and M. Wolfke, “Two liquid states of helium,” *Konink. Akad. Wetensch. Amsterdam, Proc.* **31(190b)**, 90 (1928).
- [40] F. London, “The  $\lambda$  -phenomenon of liquid helium and the Bose-Einstein degeneracy,” *Nature* **141**, 643 (1938).
- [41] H. Wolf, *Some strangeness in the Proportion: a Centennial Symposium on Albert Einstein* (Addison-Wesley, New York, 1980).
- [42] F. London, “On the Bose-Einstein Condensation,” *Phys. Rev.* **54**, 947 (1938).
- [43] L. Tisza, “Transport Phenomena in Helium II,” *Nature* **141**, 913 (1938).
- [44] L. Tisza, *Journal de Physique et Radium* **1**, 164,350 (1940).

- [45] L. D. Landau, “The theory of superfluidity of helium II,” *J. Phys. (USSR)* **5**, 71 (1941).
- [46] P. Kapitza, “Viscosity of liquid helium below the  $\lambda$ -point,” *Nature* **141**, 74 (1938).
- [47] J. F. Allen and A. D. Misener, “Flow of liquid helium II,” *Nature* **141**, 75 (1938).
- [48] J. F. Allen and H. Jones, “New Phenomena Connected with Heat Flow in Helium II,” *Nature* **141**, 243 (1938).
- [49] L. D. Landau, *J. Phys. (USSR)* **11**, 91 (1947).
- [50] N. N. Bogoliubov, “On the theory of superfluidity,” *J. Phys. (USSR)* **11**, 23 (1947).
- [51] V. P. Peshkov, *J. Phys. (USSR)* **10**, 389 (1946).
- [52] D. W. Osborne, B. Weinstock, and B. M. Abraham, *Phys. Rev.* **75**, 988 (1949).
- [53] R. P. Feynman, *Phys. Rev.* **91**, 1301 (1953).
- [54] R. P. Feynman, *Phys. Rev.* **94**, 262 (1954).
- [55] O. Penrose and L. Onsager, “Bose-Einstein condensation and liquid helium,” *Phys. Rev.* **104**, 576 (1956).
- [56] J. Bardeen, L. N. Cooper, and J. R. Schrieffer, *Phys. Rev.* **108**, 1175 (1957).
- [57] L. P. Pitaevskii, *Sov. Phys. JETP* **12**, 155 (1961).
- [58] A. L. Schawlow and C. H. Townes, “Infrared and Optical masers,” *Phys. Rev.* **112**, 1940 (1958).
- [59] J. L. Yarnell, G. P. Arnold, P. J. Bendt, and E. C. Kerr, *Phys. Rev.* **113**, 1379 (1959).
- [60] D. G. Henshaw and A. D. B. Woods, *Phys. Rev.* **121**, 1266 (1961).
- [61] W. F. Vinen, “The detection of a single quantum of circulation of superfluid helium,” *Proc. Roy. Soc.* **A260**, 218 (1961).
- [62] G. A. Williams and R. E. Packard, “Photographs of quantized vortex lines in rotating He II,” *Phys. Rev. Lett.* **33**, 280 (1974).
- [63] B. C. Crooker, B. Hebral, E. N. Smith, Y. Takano, and J. D. Reppy, “Superfluidity in a Dilute Bose Gas,” *Phys. Rev. Lett.* **51**, 666 (1983).
- [64] J. D. Reppy, “ $^4\text{He}$  as a dilute Bose Gas,” *Physica B* **126**, 335 (1984).
- [65] D. G. Fried, T. C. Killian, L. Willmann, D. Landhuis, S. C. Moss, D. Kleppner, and T. J. Greytak, “Bose-Einstein Condensation of Atomic Hydrogen,” *Phys. Rev. Lett.* **81**, 3811 (1998).
- [66] J. L. Lin and J. P. Wolfe, “Bose-Einstein Condensation of Paraexcitons in Stressed  $\text{Cu}_2\text{O}$ ,” *Phys. Rev. Lett.* **71**, 1222 (1993).
- [67] C. E. Hecht, *Physica* **25**, 1159 (1959).

- [68] W. C. Stwalley and L. H. Nosanow, "Possible "new" quantum systems," *Phys. Rev. Lett.* **36**, 910 (1976).
- [69] T. W. Hansch and A. L. Schawlow, "Cooling of gases by laser radiation," *Optics Comm.* **13**, 68 (1975).
- [70] D. J. Wineland and H. Dehmelt, "Proposed  $10^{14}\Delta\nu < \nu$  laser fluorescence spectroscopy on  $\text{TI}^+$  mono-ion oscillator III," *Bulletin of the American Physical Society* **20**, 637 (1975).
- [71] D. Wineland, R. Drullinger, and F. Walls, "Radiation-pressure cooling of bound-resonant absorbers," *Phys. Rev. Lett.* **40**, 1639 (1978).
- [72] W. Neuhauser, M. Hohenstatt, P. Toschek, and H. Dehmelt, "Optical-sideband cooling of visible atom cloud confined in parabolic well," *Phys. Rev. Lett.* **41**, 223 (1978).
- [73] I. F. Silvera and J. T. M. Walraven, "Stabilization of atomic hydrogen at low temperature," *Phys. Rev. Lett.* **44**, 164 (1980).
- [74] H. F. Hess, D. A. Bell, G. P. Kochanski, R. W. Cline, D. Kleppner, and T. J. Greytak, "Observation of 3-body Recombination in Spin-polarized Hydrogen," *Phys. Rev. Lett.* **51**, 483 (1983).
- [75] H. F. Hess, "Evaporative cooling of magnetically trapped and compressed spin-polarized hydrogen," *Phys. Rev. B* **34**, 3476 (1986).
- [76] N. Masuhara, J. M. Doyle, J. C. Sandberg, D. Kleppner, T. J. Greytak, H. F. Hess, and G. P. Kochanski, "Evaporative Cooling of Spin-Polarized Atomic Hydrogen," *Phys. Rev. Lett.* **61**, 935 (1988).
- [77] J. Prodan, A. Migdall, W. D. Phillips, I. So, H. Metcalf, and J. Dalibard, "Stopping Atoms with Laser Light," *Phys. Rev. Lett.* **54**, 992 (1985).
- [78] W. Ertmer, R. Blatt, J. L. Hall, and M. Zhu, "Laser Manipulation of Atomic Beam Velocities: Demonstration of Stopped Atoms and Velocity Reversal," *Phys. Rev. Lett.* **54**, 996 (1985).
- [79] A. L. Migdall, J. V. Prodan, W. D. Phillips, T. H. Bergeman, and H. J. Metcalf, "First Observation of Magnetically Trapped Neutral Atoms," *Phys. Rev. Lett.* **54**, 2596 (1985).
- [80] S. Chu, L. Hollberg, J. E. Bjorkholm, A. Cable, and A. Ashkin, "Three-Dimensional Viscous Confinement and Cooling of Atoms by Resonance Radiation Pressure," *Phys. Rev. Lett.* **55**, 48 (1985).
- [81] S. Chu, J. E. Bjorkholm, A. Ashkin, and A. Cable, "Experimental Observation of Optically Trapped Atoms," *Phys. Rev. Lett.* **57**, 314 (1986).
- [82] E. L. Raab, M. Prentiss, A. Cable, S. Chu, and D. E. Pritchard, "Trapping of Neutral Sodium with Radiation Pressure," *Phys. Rev. Lett.* **59**, 2631 (1987).
- [83] P. D. Lett, R. N. Watts, C. I. Westbrook, W. D. Phillips, P. L. Gould, and H. J. Metcalf, "Observation of Atoms Laser Cooled below the Doppler Limit," *Phys. Rev. Lett.* **61**, 169 (1988).

- [84] J. Dalibard and C. Cohen-Tannoudji, “Laser cooling below the Doppler limit by polarization gradients: simple theoretical models,” *J. Opt. Soc. Am. B* **6**, 2023 (1989).
- [85] J. M. Doyle, J. C. Sandberg, I. A. Yu, C. L. Cesar, D. Kleppner, and T. J. Greytak, “Hydrogen in the Submillikelvin Regime: Sticking Probability on Superfluid 4He,” *Phys. Rev. Lett.* **67**, 603 (1991).
- [86] O. J. Luiten, H. G. C. Werij, I. D. Setija, M. W. Reynolds, T. W. Hijmans, and J. T. M. Walraven, “Lyman- $\alpha$  Spectroscopy of Magnetically Trapped Atomic Hydrogen,” *Phys. Rev. Lett.* **70**, 544 (1993).
- [87] V. Bagnato, D. E. Pritchard, and D. Kleppner, “Bose-Einstein condensation in an external potential,” *Phys. Rev. A* **35**, 4354 (1987).
- [88] A. Ashkin, “Trapping of atoms by resonance radiation pressure,” *Phys. Rev. Lett.* **40**, 729 (1978).
- [89] Bjorkholm, J. R. Freeman, A. Ashkin, and D. Pearson, “Observation of focusing on neutral atoms by the dipole forces of resonance-radiation pressure,” *Phys. Rev. Lett.* **41**, 1361 (1978).
- [90] D. E. Pritchard, K. Helmerson, and A. G. Martin, in *Atomic Physics 11*, edited by S. Haroche, J. Gay, and G. Grynberg (World Scientific, Singapore, 1989), p. 179.
- [91] C. Monroe, W. Swann, H. Robinson, and C. Wieman, “Very Cold Trapped Atoms in a Vapor Cell,” *Phys. Rev. Lett.* **65**, 1571 (1990).
- [92] W. Ketterle, K. B. Davis, M. A. Joffe, A. Martin, and D. E. Pritchard, “High-Densities of Cold Atoms in a Dark Spontaneous-Force Optical Trap,” *Phys. Rev. Lett.* **70**, 2253 (1993).
- [93] J. Vigu, “Possibility of applying laser-cooling techniques to the observation of collective quantum effects,” *Phys. Rev. A* **34**, 4476 (1986).
- [94] T. Walker, D. Sesko, and C. Wieman, “Collective Behavior of Optically Trapped Neutral Atoms,” *Phys. Rev. Lett.* **64**, 408 (1990).
- [95] H. J. Lee, C. S. Adams, M. Kasevich, and S. Chu, “Raman cooling of atoms in an optical dipole trap,” *Phys. Rev. Lett.* **76**, 2658 (1996).
- [96] H. Katori, T. Ido, Y. Isoya, and M. Kuwata-Gonokami, “Magneto-optical trapping and cooling of strontium atoms down to the photon recoil temperature,” *Phys. Rev. Lett.* **82**, 1116 (1999).
- [97] A. J. Kerman, V. Vuletic, C. Chin, and S. Chu, “Beyond optical molasses: 3D Raman sideband cooling of atomic cesium to high phase-space density,” *Phys. Rev. Lett.* **84**, 439 (2000).
- [98] D.-J. Han, S. Wolf, S. Oliver, C. McCormick, M. T. DePue, and D. S. Weiss, “3D Raman Sideband Cooling of Cesium Atoms at High Density,” *Phys. Rev. Lett.* **85**, 724 (2000).

- [99] S. L. Cornish, N. R. Claussen, J. L. Roberts, E. A. Cornell, and C. E. Wieman, “Stable  $^{85}\text{Rb}$  Bose-Einstein Condensates with Widely Tunable Interactions,” *Phys. Rev. Lett.* **85**, 1795 (2000).
- [100] A. Robert, O. Sirjean, A. Browaeys, J. Poupard, S. Nowak, D. Boiron, C. I. Westbrook, and A. Aspect, “A Bose-Einstein Condensate of Metastable Atoms,” *Science* **292**, 461 (2001).
- [101] F. P. D. Santos, J. Leonard, J. Wang, C. J. Barrelet, F. Perales, E. Rasel, C. S. Unnikrishnan, M. Leduc, and C. Cohen-Tannoudji, “Bose-Einstein Condensation of Metastable Helium,” *Phys. Rev. Lett.* **86**, 3459 (2001).
- [102] J. V. Prodan, W. D. Phillips, and H. Metcalf, “Laser Production of a Very Slow Monoenergetic Atomic Beam,” *Phys. Rev. Lett.* **49**, 1149 (1982).
- [103] S. Chu, in *Laser Manipulation of Atoms and Ions, Proceedings of the International School of Physics Enrico Fermi, Course CXVIII*, edited by E. Arimondo, W. Phillips, and F. Strumia (North-Holland, Amsterdam, 1992), pp. 239–287.
- [104] D. E. Pritchard and W. Ketterle, in *Laser Manipulation of Atoms and Ions, Proceedings of the International School of Physics Enrico Fermi, Course CXVIII*, edited by E. Arimondo, W. Phillips, and F. Strumia (North-Holland, Amsterdam, 1992), pp. 473–496.
- [105] P. D. Lett, W. D. Phillips, S. L. Rolston, C. E. Tanner, R. N. Watts, and C. I. Westbrook, “Optical Molasses,” *J. Opt. Soc. Am. B* **6**, 2084 (1989).
- [106] D. S. Weiss, E. Riis, Y. Shevy, P. J. Ungar, and S. Chu, “Optical molasses and multilevel atoms: Experiment,” *J. Opt. Soc. Am. B* **6**, 2072 (1989).
- [107] K. B. Davis, M.-O. Mewes, M. A. Joffe, M. R. Andrews, and W. Ketterle, “Evaporative Cooling of Sodium Atoms,” *Phys. Rev. Lett.* **74**, 5202 (1995).
- [108] W. Petrich, M. H. Anderson, J. R. Ensher, and E. A. Cornell, “A Stable, Tightly Confining Magnetic Trap for Evaporative Cooling of Neutral Atoms,” *Phys. Rev. Lett.* **74**, 3352 (1995).
- [109] M. A. Joffe, Ph.D. thesis, Massachusetts Institute of Technology, 1993.
- [110] T. E. Barrett, S. W. Dapore-Schwartz, M. D. Ray, and G. P. Lfyatis, “Slowing Atoms with (sigma-minus) Polarized Light,” *Phys. Rev. Lett.* **67**, 3483 (1991).
- [111] M. A. Joffe, W. Ketterle, A. Martin, and D. E. Pritchard, “Transverse Cooling and Deflection of an Atomic-Beam Inside a Zeeman Slower,” *Journal of the Optical Society of America B-Optical Physics* **10**, 2257 (1993).
- [112] M.-O. Mewes, Ph.D. thesis, Massachusetts Institute of Technology, 1997.
- [113] P. J. Martin, B. G. Oldaker, A. H. Miklich, and D. E. Pritchard, “Bragg scattering of atoms from a standing light wave,” *Phys. Rev. Lett.* **60**, 515 (1988).
- [114] D. M. Giltner, R. W. McGowan, and S. A. Lee, “Atom Interferometer based on Bragg scattering from light waves,” *Phys. Rev. Lett.* **75**, 2638 (1995).

- [115] S. Bernet, M. K. Oberthaler, R. Abfalterer, J. Schmiedmayer, and A. Zeilinger, “Coherent frequency shift of atomic matter waves,” *Phys. Rev. Lett.* **77**, 5160 (1996).
- [116] M. Kozuma, L. Deng, E. W. Hagley, J. Wen, R. Lutwak, K. Helmerson, S. L. Rolston, and W. D. Phillips, “Coherent splitting of Bose-Einstein condensed atoms with optically induced Bragg diffraction,” *Phys. Rev. Lett.* **82**, 871 (1999).
- [117] J.-Y. Courtois, G. Grynberg, B. Lounis, and P. Verkerk, “Recoil-induced resonances in cesium: An atomic analog to the free-electron laser,” *Phys. Rev. Lett.* **72**, 3017 (1994).
- [118] M. Kasevich, D. S. Weiss, E. Riis, K. Moler, and S. Chu, “Atomic Velocity Selection Using Stimulated Raman Transitions,” *Phys. Rev. Lett.* **66**, 2297 (1991).
- [119] J. Stenger, S. Inouye, A. P. Chikkatur, D. M. Stamper-Kurn, D. E. Pritchard, and W. Ketterle, “Erratum: Bragg Spectroscopy of a Bose-Einstein Condensate [*Phys. Rev. Lett.* **82**, 4569 (1999)],” *Phys. Rev. Lett.* **84**, 2283 (2000).
- [120] E. W. Hagley, L. Deng, M. Kozuma, M. Trippenbach, Y. B. Band, M. Edwards, M. Doery, P. S. Julienne, K. Helmerson, S. L. Rolston, and W. D. Phillips, “Measurement of the Coherence of a Bose-Einstein condensate,” *Phys. Rev. Lett.* **83**, 3112 (1999).
- [121] I. Bloch, T. W. Hansch, and T. Esslinger, “Measurement of the spatial coherence of a trapped Bose gas at the phase transition,” *Nature* **403**, 166 (2000).
- [122] J. E. Simsarian, J. Denschlag, M. Edwards, C. W. Clark, L. Deng, E. W. Hagley, K. Helmerson, S. L. Rolston, and W. D. Phillips, “Imaging the Phase of an Evolving Bose-Einstein Condensate Wave Function,” *Phys. Rev. Lett.* **85**, 2040 (2000).
- [123] J. Javanainen, “Spectrum of Light Scattered from a Degenerate Bose Gas,” *Phys. Rev. Lett.* **75**, 1927 (1995).
- [124] R. H. Dicke, “Coherence in Spontaneous Radiation Processes,” *Phys. Rev.* **93**, 99 (1954).
- [125] R. H. Dicke, in *Quantum Electronics, Proceedings of the third international congress*, edited by P. Grivet and N. Bloembergen (Columbia University Press, New York, 1964), p. 35.
- [126] N. E. Rehler and J. H. Eberly, “Superradiance,” *Phys. Rev. A* **3**, 1735 (1971).
- [127] M. G. Moore and P. Meystre, “Theory of superradiant scattering of laser light from Bose-Einstein condensates,” *Phys. Rev. Lett.* **83**, 5202 (1999).
- [128] M. Holland, K. Burnett, C. Gardiner, J. I. Cirac, and P. Zoller, “Theory of an atom laser,” *Phys. Rev. A* **54**, R1757 (1996).
- [129] M. Olshanii, Y. Castin, and J. Dalibard, in *Laser Spectroscopy XII*, edited by M. Inguscio, M. Allegrini, and A. Sasso (World Scientific, Singapore, 1996), pp. 7–12.
- [130] R. J. C. Spreeuw, T. Pfau, U. Janicke, and M. Wilkens, “Laser-like scheme for atomic-matter waves,” *Europhys. Lett.* **32**, 469 (1996).

- [131] H. M. Wiseman and M. J. Collett, “An atom laser based on dark-state cooling,” *Physics Letters A* **202**, 246 (1995).
- [132] P. R. Berman, *Atom Interferometry* (Academic Press, New York, 1996).
- [133] J. Schmiedmayer, M. S. Chapman, C. R. Ekstrom, T. D. Hammond, S. Wehinger, and D. E. Pritchard, “Index of Refraction of Various Gases for Sodium Matter Waves,” *Phys. Rev. Lett.* **74**, 1043 (1995).
- [134] G. E. Stedman, “Ring-laser tests of fundamental physics and geophysics,” *Rep. Prog. Phys.* **60**, 615 (1997).
- [135] T. L. Gustavson, P. Bouyer, and M. A. Kasevich, “Precision Rotation Measurements with an Atom Interferometer Gyroscope,” *Phys. Rev. Lett.* **78**, 2046 (1997).
- [136] L. Casperson and A. Yariv, “Pulse Propagation in a High-Gain Medium,” *Phys. Rev. Lett.* **26**, 293 (1971).
- [137] S. Chu and S. Wong, “Linear Pulse Propagation in an Absorbing Medium,” *Phys. Rev. Lett.* **48**, 738 (1982).
- [138] L. V. Hau, S. E. Harris, Z. Dutton, and C. H. Behroozi, “Light speed reduction to 17 meters per second in an ultracold atomic gas,” *Nature* **397**, 594 (1999).
- [139] D. F. Phillips, A. Fleischhauer, A. Mair, R. L. Walsworth, and M. D. Lukin, “Storage of Light in Atomic Vapor,” *Phys. Rev. Lett.* **86**, 783 (2001).
- [140] C. Liu, Z. Dutton, C. H. Behroozi, and L. V. Hau, “Observation of coherent optical information storage in an atomic medium using halted light pulses,” *Nature* **409**, 490 (2001).
- [141] C. Cohen-Tannoudji, J. Dupont-Roc, and G. Grynberg, *Atom-Photon Interactions* (Wiley, New York, 1992).
- [142] M. Gross and S. Haroche, “Superradiance: An Essay on the Theory of Collective Spontaneous Emission,” *Phys. Rep.* **93**, 301 (1982).
- [143] M. P. van Exter, S. J. M. Kuppens, and J. P. Woerdman, “Theory for the linewidth of a bad-cavity laser,” *Phys. Rev. A* **51**, 809 (1995).
- [144] R. Bonifacio and L. D. Salvo, “Collective atomic recoil laser (CARL) optical gain without inversion by collective atomic recoil and self-bunching of two-level atoms,” *Nuclear Instruments and Methods in Physics Research A* **341**, 360 (1994).
- [145] G. L. Lippi, G. P. Barozzi, S. Barbay, and J. R. Tredicce, “Spontaneous Generation of a Longitudinal Atomic Density Grating in Sodium Vapor,” *Phys. Rev. Lett.* **76**, 2452 (1996).
- [146] P. R. Hemmer, N. P. Bigelow, D. P. Katz, M. S. Shahriar, L. DeSalvo, and R. Bonifacio, “Self-Organization, Broken Symmetry, and Lasing in an Atomic Vapor: The Interdependence of Gratings and Gain,” *Phys. Rev. Lett.* **77**, 1468 (1996).

- [147] W. J. Brown, J. R. Gardner, D. J. Gauthier, and R. Vilaseca, “Amplification of laser beams propagating through a collection of strongly driven, Doppler-broadened two-level atoms,” *Phys. Rev. A* **55**, R1601 (1997).
- [148] M. G. Moore and P. Meystre, “Optical control and entanglement of atomic Schrödinger fields,” *Phys. Rev. A* **59**, 1754 (1999).
- [149] P. R. Berman, “Comparison of recoil-induced resonances and the collective atomic recoil laser,” *Phys. Rev. A* **59**, 585 (1999).
- [150] H. A. Haus, *Waves and Fields in Optoelectronics* (Prentice-Hall, Englewood Cliffs, NJ, 1984).
- [151] S. E. Harris and L. V. Hau, “Nonlinear Optics at Low Light Levels,” *Phys. Rev. Lett.* **82**, 4611 (1999).
- [152] M. Kozuma, Y. Suzuki, Y. Torii, T. Sugiura, T. Kuga, E. W. Hagley, and L. Deng, “Phase coherent amplification of matter waves,” *Science* **286**, 2309 (1999).
- [153] M. R. Andrews, Ph.D. thesis, Massachusetts Institute of Technology, 1998.
- [154] E. Bolda and D. Walls, “Detection of Vorticity in Bose-Einstein Condensed Gases by Matter-Wave Interference,” *Phys. Rev. Lett.* **81**, 5477 (1998).
- [155] J. Tempere and J. T. Devreese, “Fringe pattern of interfering Bose-Einstein condensates with a vortex,” *Solid State Commun.* **108**, 993 (1998).
- [156] C. Raman, M. Khl, R. Onofrio, D. S. Durfee, C. E. Kuklewicz, Z. Hadzibabic, and W. Ketterle, “Evidence for a critical velocity in a Bose-Einstein condensed gas,” *Phys. Rev. Lett.* **83**, 2502 (1999).
- [157] R. Onofrio, C. Raman, J. M. Vogels, J. Abo-Shaeer, A. P. Chikkatur, and W. Ketterle, “Observation of Superfluid Flow in a Bose-Einstein Condensed Gas,” *Phys. Rev. Lett.* **85**, 2228 (2000).
- [158] B. Jackson, J. F. McCann, and C. S. Adams, “Dissipation and Vortex Creation in Bose-Einstein Condensed Gases,” *Phys. Rev. A* **61**, 051603(R) (2000).
- [159] M. R. Matthews, B. P. Anderson, P. C. Haljan, D. S. Hall, C. E. Wieman, and E. A. Cornell, “Vortices in a Bose-Einstein Condensate,” *Phys. Rev. Lett.* **83**, 2498 (1999).
- [160] K. W. Madison, F. Chevy, W. Wohlleben, and J. Dalibard, “Vortex formation in a stirred Bose-Einstein condensate,” *Phys. Rev. Lett.* **84**, 806 (2000).
- [161] J. R. Abo-Shaeer, C. Raman, J. M. Vogels, and W. Ketterle, “Trapping of atoms by resonance radiation pressure,” *Science* **292**, 476 (2001).
- [162] L. Dobrek, M. Gajda, M. Lewenstein, K. Sengstock, G. Birkl, and W. Ertmer, “Optical generation of vortices in trapped Bose-Einstein condensates,” *Phys. Rev. A* **60**, R3381 (1999).
- [163] F. Chevy, K. W. Madison, V. Bretin, and J. Dalibard, “Interferometric detection of a single vortex in a dilute Bose-Einstein condensate,” (2001), preprint cond-mat/0104545.

- [164] M. G. Moore and P. Meystre, “Generating Entangled Atom-Photon Pairs from Bose-Einstein Condensates,” *Phys. Rev. Lett.* **85**, 5026 (2000).
- [165] A. Gorlitz, J. M. Vogels, A. E. Leanhardt, C. Raman, T. L. Gustavson, J. R. Abo-Shaeer, A. P. Chikkatur, S. Gupta, S. Inouye, T. Rosenband, D. E. Pritchard, and W. Ketterle, “Realization of Bose-Einstein condensates in lower dimensions,” (2001), preprint, cond-mat/0104549.
- [166] C. Chin, V. Vuletic, A. J. Kerman, and S. Chu, “High Resolution Feshbach Spectroscopy of Cesium,” *Phys. Rev. Lett.* **85**, 2717 (2000).
- [167] F. K. Fatemi, K. M. Jones, and P. D. Lett, “Observation of Optically Induced Feshbach Resonances in Collisions of Cold Atoms,” *Phys. Rev. Lett.* **85**, 4462 (2000).
- [168] E. Timmermans, P. Tommasini, R. Cote, M. Hussein, and A. Kerman, “Rarified Liquid Properties of Hybrid Atomic-Molecular Bose-Einstein Condensates,” *Phys. Rev. Lett.* **83**, 2691 (1999).
- [169] S. J. J. M. F. Kokkelmans, H. M. J. Vissers, and B. J. Verhaar, “Formation of a Bose condensate of stable molecules via a Feshbach resonance,” *Phys. Rev. A* **63**, 031601 (2001).
- [170] F. A. van Abeelen and B. J. Verhaar, “Time-Dependent Feshbach Resonance Scattering and Anomalous Decay of a Na Bose-Einstein Condensate,” *Phys. Rev. Lett.* **83**, 1550 (1999).
- [171] F. H. Mies, E. Tiesinga, and P. S. Julienne, “Manipulation of Feshbach resonances in ultracold atomic collisions using time-dependent magnetic fields,” *Phys. Rev. A* **61**, 022721 (2000).
- [172] V. A. Yurovsky, A. Ben-Reuven, P. S. Julienne, and C. J. Williams, “Atom loss from Bose-Einstein condensates due to Feshbach resonance,” *Phys. Rev. A* **60**, R765 (1999).
- [173] J. L. Yarnell, G. P. Arnold, P. J. Bendt, and E. C. Kerr, “Atom loss and the formation of a molecular Bose-Einstein condensate by Feshbach resonance,” *Phys. Rev. A* **62**, 043605 (2000).
- [174] J. L. Roberts, N. R. Claussen, S. L. Cornish, and C. E. Wieman, “Magnetic Field Dependence of Ultracold Inelastic Collisions near a Feshbach Resonance,” *Phys. Rev. Lett.* **85**, 728 (2000).